POLITECNICO DI TORINO
Repository ISTITUZIONALE

Aeroacoustics of Propellers under Unsteady Inflow

Original
Aeroacoustics of Propellers under Unsteady Inflow / Ali, M., Piccolo, A., Zamponi, R., Ragni, D., Avallone, F. - In: A Vertical Future: eVTOL Insights, Challenges, and Directions from DICUAM (2022-2026) / Ragni D., Wang S., Zamponi R., Pedretti O., Monteleone F., Abergo L., Casablanca M., Mangrini A., Aldao Pensado E., Combey K., Elsayed O. A., Bassimir B., Schuchardt B. I., Pavel M.,Kirste A.. - [s.l] : TU Delft OPEN Books, 2026. - ISBN 9789465184746. - pp. 49-66

Availability:
This version is available at: 11583/3017732 since: 2026-11-10T10:47:45Z

Publisher:
TU Delft OPEN Books

Published
DOI:

Terms of use:

This article is made available under terms and conditions as specified in the corresponding bibliographic description in the repository

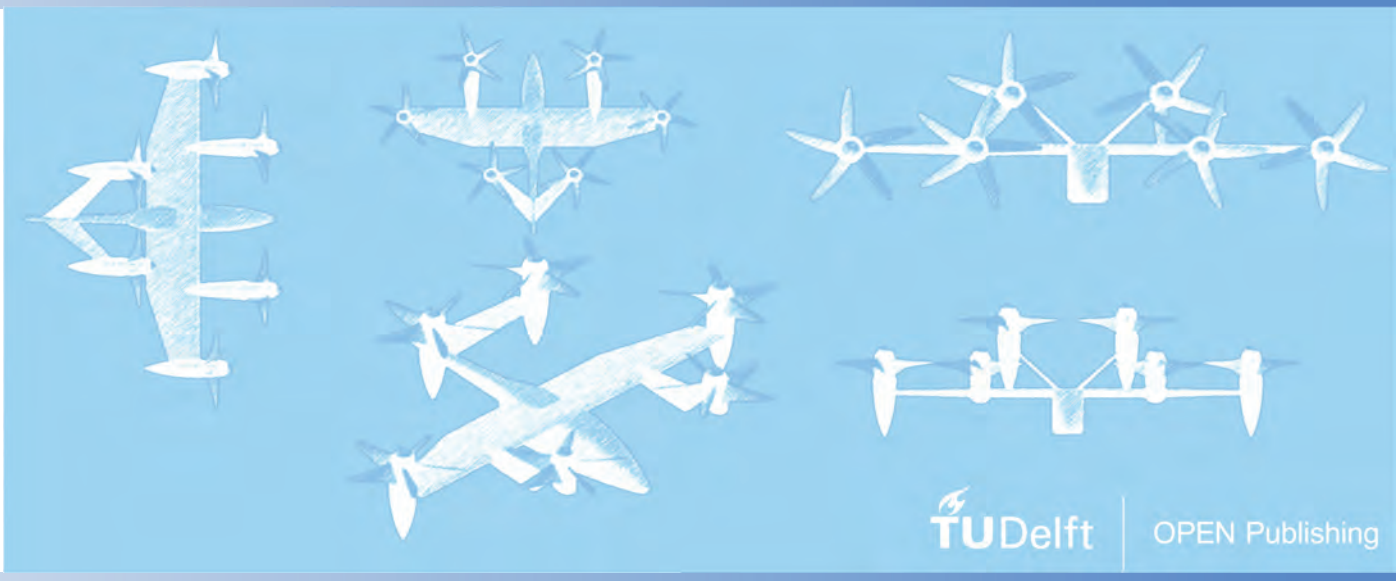
Publisher copyright

(Article begins on next page)

19 November 2026

A Vertical Future

eVTOL Insights, Challenges, and Directions from DICUAM (2022–2026)



TU Delft | OPEN Publishing

Edited by: Daniele Ragni, Sen Wang, Riccardo Zamponi, Ottavio Pedretti, Francesca Monteleone, Luca Abergo, Manuel Casablanca, Andrea Magrini, Enrique Aldao Pensado, Kangni Combey, Omer Ali Elsayed, Bernd Bassimir, Bianca Isabella Schuchardt, Marilena Pavel, Ansgar Kirste

A Vertical Future

eVTOL Insights, Challenges, and Directions from DICUAM (2022–2026)

Edited by: Daniele Ragni, Sen Wang, Riccardo Zamponi, Ottavio Pedretti, Francesca Monteleone, Luca Abergo, Manuel Casablanca, Andrea Magrini, Enrique Aldao Pensado, Kangni Combey, Omer Ali Elsayed, Bernd Bassimir, Bianca Isabella Schuchardt, Marilena Pavel, Ansgar Kirste

Colophon

A Vertical Future | eVTOL Insights, Challenges, and Directions from DICUAM (2022–2026)

Editors:

Daniele Ragni[1]*, Sen Wang[2], Riccardo Zamponi[3], Ottavio Pedretti[4], Francesca Monteleone[4], Luca Abergo[5], Manuel Casablanca[6], Andrea Magrini[6], Enrique Aldao Pensado[7], Kangni Combey[8], Omer Ali Elsayed[8], Bernd Bassimir[9], Bianca Isabella Schuchardt[9], Marilena Pavel[10], Ansgar Kirste[11]

[1]* Corresponding Author, Department of Flow Physics and Technology, Faculty of Aerospace Engineering, Delft University of Technology, The Netherlands, d.ragni@tudelft.nl; 0000-0002-8014-5650

[2] School of Civil, Aerospace, and Design Engineering, University of Bristol, United Kingdom; 0009-0004-4649-8219

[3] Environmental and Applied Fluid Dynamics Department, von Karman Institute for Fluid Dynamics, Belgium; 0000-0001-5172-6109

[4] Department of Architecture and Urban Studies, Politecnico di Milano, Italy; 0009-0000-7197-7327; 0009-0004-5215-8958

[5] Department of Aerospace Science and Technology, Politecnico di Milano, Italy; 0000-0001-8372-7181

[6] Department of Industrial Engineering, Università degli Studi di Padova, Italy; 0009-0009-9984-5233; 0000-0002-3539-149X

[7] AEROLAB, Institute of Physics, Computation, and Aerospace Science, University of Vigo, Spain; 0000-0001-8676-4455

[8] School of Aerospace and Automotive Engineering, International University of Rabat, Morocco; 0009-0008-6784-0086; 0000-0002-7203-4846

[9] Institute of Flight Guidance, German Aerospace Center (DLR), Germany; 0000-0002-7258-5584; 0000-0003-1251-3594

[10] Department of Control and Operations, Faculty of Aerospace Engineering, Delft University of Technology, The Netherlands; 0000-0002-0943-4898

[11] Institute of Aerospace Systems, RWTH Aachen University, Germany; 0000-0003-0638-6840

Keywords: urban; mobility; eVTOL; vertiport; aeroacoustics

Published by:

TU Delft OPEN Publishing | Delft University of Technology, The Netherlands

DOI: https://doi.org/10.59490/mt.269

eISBN: 978-94-6518-474-6

print ISBN: 978-94-6563-070-0

Copyright statement:

This work is licensed under a Creative Commons Attribution 4.0 International (CC BY 4.0) license unless otherwise stated

©2026 published by TU Delft OPEN Publishing on behalf of the authors

Electronic version of this book is available at: https://books.open.tudelft.nl.

Cover design made by Daniele Ragni

Copyright clearance made by the TU Delft Library copyright team.

Conflict of Interest: No conflict of interest to disclose.

Data Access Statement: Existing data: this book brings together existing research data which can be obtained upon request from the editors. Full details of how the data were obtained are also available by contacting the editors.

Peer Review: This book has been peer reviewed. The peer review was triple anonymous. The Editors or Authors and the Publisher would like to thank the reviewers for their time and effort. The peer review was carried out by the Members of the Scientific Committee of the DICUAM2026 Event.

Disclaimer: Every attempt has been made to ensure the correct source of images and other potentially copyrighted material was ascertained, and that all materials included in this book have been attributed and used according to their license. If you believe that a portion of the material infringes someone else's copyright, please contact d.ragni@tudelft.nl.

Table of Contents

Contributing authors 8

Abstract 10

1 Framing a Vertical Future 11

1.1 DICUAM 2022–2026 and the evolution of eVTOL research 11

1.2 From proceedings to synthesis 11

1.3 Scope, themes, and perspective 11

2 Reference Vehicles and Common Models for UAM 13

2.1 Conceptual Design of the Urban Air Mobility Common Model Lift+Cruise Aircraft 13

Vehicle sizing method 14

Model Layout and Sizing Results 16

Aerodynamic Results 18

Hover Flight Condition 18

Climb Flight Condition 19

2.2 Urban Air Mobility Tiltrotor Variant 21

Top-Level Aircraft Requirements (TLARs) and Operational Mission Profile 21

Development of geometric configuration 26

2.3 UAM Common Model, the Multicopter Configuration 27

Power and performance estimation 31

Benchmarking against representative public-domain multicopters 33

Configuration and Model Development 34

3 Rotor Aerodynamics and Aeroacoustics 36

3.1 Fast Aerodynamic Assessment of Propellers 36

Application of the BFM for the propeller aerodynamic characterization 37

3.2 Rotor blade concepts explored in DICUAM 39

Swept Blades 39

Toroidal Joined Blade Tips Propeller 44

3.3 Aeroacoustics of Propellers under Unsteady Inflow 49

Numerical setup 49

Propeller under single vortical gust 51

3.4 Acoustic design optimization of propeller-pylon subsystems 56
Blade loading and thickness noise 57
3.5 Numerical Analysis of Multirotor Aerodynamic Interactions 66
Propeller Performance Analysis 68
3.6 Transformer-Based Prediction of Small-Scale Rotor Aeroacoustics 69
Simulation results and discussion 71
3.7 Assessing Dynamic Rollover Hazards in Multirotor eVTOL Aircraft 74
4 Urban Emission Mapping, Vertiports, and Urban Integration 80
4.1 Noise with Vision Transformers: A Generalized Deep Learning Framework 80
4.2 A Holistic Approach to Urban Air Mobility Vertiport Design and Assessment in Urban Environments 85
Vertiport Demand and Capacity Analysis 87
FATO Congestion (Platform Access) 87
Parking Saturation and Fleet Availability (Arrival/Departure Constraint) 88
Vertiport localization and design 89
Vertiport operations and Noise Assessment 93
4.3 Vertiport Localization for Urban Air Mobility: The Role of Intermodality and Urban Wind Conditions 96
The role of intermodality in vertiport localization 98
Existing public transportation system through the regulatory planning frameworks 98
Urban Wind Simulations and Analyses 101
Microscale wind simulation results and analysis 102
5 Operations, U-space, and Scalable Air Mobility 106
5.1 High Density Vertiports Operations in Advanced U-space 106
Vertiport availability in the strategic phase 107
Slot allocation 108
Approach and departure procedures 109
Weather information and vertiport availability in tactical phase 110
Discussion 110
5.2 U-space Services as a Necessity for Scalable Vertiport Operations 111
Roadmap for the Establishment of an Innovative Air Mobility Control Center Research Lab 112

Operational Scenarios and Research Applications 113
5.3 Autonomous Conflict Resolution for Drones using Deep Reinforcement Learning 113
Simulation environment, RL methodology and Baseline 114
Experimental setup and results 115
5.4 Profitability Potential of Urban Air Mobility Operations across Metropolitan Regions 117
Motivation and scope 117
Demand simulation, surrogate modeling, and profit optimization 117
Key findings and implications 119
6 Cross-Cutting Challenges and Directions Toward a Vertical Future 121
6.1 The value is in the connections 121
6.2 Three cross-cutting challenges 121
Interaction, scalability and commonality 121
6.3 The societal dimension 122
Community noise and acceptance 122
Safety, equity and sustainability 122
6.4 Directions 123
6.5 Outlook toward the next cycle 123
Bibliography 125

Contributing authors

Author	*Affiliation*	*Country*
Hasan Çınar	Department of Aeronautical Engineering, Necmettin Erbakan University	Turkey
Süleyman Tunçel	Department of Electronics and Communication Engineering, Turkish Military Academy, National Defense University	Turkey
Riccardo Zamponi Julien Christophe Christophe Schram	Environmental and Applied Fluid Dynamics Department, The von Karman Institute for Fluid Dynamics	Belgium
Nithya Dhamodharasamy Sundarraj	Department of Aerospace Science and Technology, Politecnico di Milano Department of Aerospace Engineering, RMIT University	Italy Australia
Ottavio Pedretti Francesca Monteleone Fabrizia Berlingieri Giuseppe Quaranta	Department of Architecture and Urban Studies, Politecnico di Milano	Italy
Luca Abergo Alberto Guardone Alex Zanotti	Department of Aerospace Science and Technology, Politecnico di Milano	Italy
Vincenzo Muscarello	Department of Aerospace Engineering, RMIT University	Australia
Daniele Ragni Lourenço Tércio Lima Pereira Fulvio Scarano Damiano Casalino Andrea Piccolo	Department of Flow Physics and Technology, Faculty of Aerospace Engineering, Delft University of Technology	The Netherlands
Francesco Avallone Mario Ali	Department of Mechanical and Aerospace Engineering, Politecnico di Torino	Italy
Lukas Biesalski	Institute of Flight Systems and Automatic Control, Department of Mechanical Engineering, Technical University of Darmstadt	Germany
Manuel Casablanca Andrea Magrini Ernesto Benini	Department of Industrial Engineering, Università Degli Studi di Padova	Italy
Kangni Combey Omer Ali Elsayed Khaoula Qaissi Mohamed Achraf El Gadi Hajar Chouiyakh Mustapha Faqir	LERMA laboratory, School of Aerospace and Automotive Engineering, International University of Rabat	Morocco
Arinze Ndubisi Eze	Aerial MECHANICA Inc. Aerial Industries, Pte.Ltd.	USA Singapore
Federico Nahuel Ramírez	CMT - Clean Mobility & Thermofluids, Universitat Politècnica de València	Spain
Joost Ellerbroek	Department of Control and Operations, Faculty of Aerospace Engineering, Delft University of Technology	The Netherlands

Jacco Hoekstra Marilena Pavel		
Sasha Vlaskin Călin Andrei Badea Emmanuel Sunil Dennis Nieuwenhuisen	Air Traffic Architecture, Validation and Integration Department, The Royal Netherlands Aerospace Center NLR	The Netherlands
Sen Wang	School of Civil, Aerospace, and Design Engineering, University of Bristol	United Kingdom
Enrique Aldao Pensado Fernando Veiga López Higinio González Jorge	AEROLAB, Institute of Physics, Computation, and Aerospace Science, University of Vigo	Spain
Ansgar Kirste Eike Stumpf	Institute of Aerospace Systems, RWTH Aachen University	Germany
Bernd Bassimir Marzia Corsi Enno Nagel Bianca Isabella Schuchardt	Institute of Flight Guidance, German Aerospace Center DLR	Germany
Prajwal Prakasha	Institute of System Architectures in Aeronautics | Aviation System Design and Assessment, German Aerospace Center DLR	Germany

Abstract

The Delft International Conference on Urban Air Mobility (DICUAM) brought together researchers and industry practitioners between 2022 and 2026 around a single organizing question: what will it take for electric vertical take-off and landing (eVTOL) aircraft to operate safely, quietly, and acceptably over cities?

The question is no longer whether electric vertical flights are technically feasible. Prototypes are airborne, certification programs are underway in the United States, Europe, and Asia, and the fundamental physics of distributed electric propulsion are well understood. What remains open and contested is integration: how eVTOL operations are woven into existing airspace, urban infrastructure, and community life. The acceptance of urban air mobility by communities and regulators depends on silent overflights, safe operations, and fares that make the service genuinely accessible rather than a premium curiosity.

The use cases are identifiable. Urban air mobility can bypass road congestion across large metropolitan areas, link underserved districts to employment centers, shorten trips to hospitals and emergency sites, and connect islands and mountain communities where surface infrastructure is thin or absent. It can deploy rapid first responses at disaster sites. None of these benefits arrive automatically. The costs are real: noise overhead, new structures on rooftops and transport hubs, added risk, and regulatory frameworks that must be built from scratch. Whether urban air mobility becomes a useful piece of urban infrastructure or an unwanted intrusion depends as much on the choices made by aircraft designers, aerodynamicists, acousticians, urban planners, and policymakers as well as on the aircraft themselves.

DICUAM was designed to keep those disciplines in conversation. Its editions connected researchers in rotor aerodynamics and aeroacoustics with specialists in flight operations, air traffic management, control engineering, and urban planning, alongside the industry pioneers who are building these vehicles and the operational systems around them.

This book does not reproduce the conference proceedings. It organizes the contributions by theme so that the collective knowledge reads as a coherent argument rather than a sequence of papers. The chapters cover vehicle design and common reference models, propeller aerodynamics at low Reynolds numbers, aerodynamic and aeroacoustic interaction effects, novel rotor concepts, urban noise prediction, vertiport design and localization, and airspace operations including U-space integration and autonomous conflict resolution.

The book serves two readerships. **Scientists and engineers** will find methods, benchmarks, and results across all these domains; the chapters are written to be technically self-contained. **Policymakers, planners, and infrastructure owners** will find in each chapter, and especially in the closing one, a plain account of what technology can do today, what remains uncertain, and which decisions are theirs to make.

A caution on timescale is warranted. The fields covered here move quickly, and some technical specifications, particularly around battery energy density, vehicle autonomy, and early regulatory frameworks, may evolve before this volume reaches all its readers. However, a vertical future will not be delivered by technology alone. It is a decision that cities, communities, and regions will make.

This book is intended to inform that decision.

1 Framing a Vertical Future

1.1 DICUAM 2022–2026 and the evolution of eVTOL research

Urban Air Mobility (UAM) has moved from concept to engineering practice. Electric vertical take-off and landing (eVTOL) aircraft are flying as prototypes, with certification programs underway. Across academia, industry, and regulators, the question is no longer whether eVTOL will enter service, but how to integrate it into cities safely, efficiently, and acceptably.

The Delft International Conference on Urban Air Mobility (DICUAM) was created for this purpose. Between 2022 and 2026 it brought together aerodynamicists, flight-operations researchers, urban planners, control and aeroacoustics specialists, and industry around one problem: enabling the next generation of urban flight. The emphasis shifted across editions from component-level studies in 2022 (rotor aerodynamics, low Reynolds-number effects, aerodynamic interactions, propeller noise) to system-level work by 2026 (common reference vehicles, fast prediction methods, vertiport design, U-space integration, and conflict resolution).

A central outcome of DICUAM has been a common reference model linking vehicle design to vertiport operation. This edited book builds on that idea, synthesizing the work across editions into a structured reference for researchers, engineers, policymakers, and industry.

1.2 From proceedings to synthesis

The material collected across DICUAM 2022-2026 captures a research community addressing one of the central challenges of future aviation: how to make vertical urban flight technically viable, operationally scalable, and socially acceptable. The contributions span aerodynamics, low Reynolds-number propellers, forward-swept and unconventional blades, tandem and distributed-propulsion effects together with aeroacoustic prediction under unsteady inflow, data-driven surrogate models, and multi-fidelity tonal-noise methods, and, at the system level, common UAM reference vehicles, vertiport design and localization, urban noise propagation, U-space integration, and conflict resolution. Rather than organizing this knowledge paper by paper, A Vertical Future is structured around themes, moving from isolated findings to collective interpretation across six chapters. **Chapter 2** introduces the common UAM reference models, the lift+cruise, tiltrotor, and multicopter configurations, that serve as shared platforms for benchmarking aerodynamic, acoustic, and operational studies. **Chapter 3** addresses the rotor aerodynamics and aeroacoustics of eVTOL propulsion, where small propellers at low Reynolds numbers behave unlike conventional rotorcraft; it spans body-force modeling, novel blade and propeller concepts, propeller–pylon acoustic optimization, multirotor interactions, data-driven aeroacoustic prediction, and vehicle-level rollover safety. **Chapter 4** carries noise from the source into the city, combining transformer-based urban noise mapping with vertiport design and localization to bridge source-level prediction and urban environmental assessment. **Chapter 5** turns to operations, examining high-density vertiport operations, U-space services, and autonomous conflict resolution for dense airspace. **Chapter 6** closes the edited book by drawing out the cross-cutting challenges and directions toward a vertical future.

1.3 Scope, themes, and perspective

The edited book is driven by a system perspective. Three themes recur across the DICUAM contributions. The first is **interaction**. eVTOL aircraft are interaction-driven: propellers operate in disturbed inflow, often near other rotors, wings, pylons, and fuselages, and vertiports are not isolated pads but nodes embedded in dense urban environments and intermodal networks. Performance depends less on optimizing components in isolation than on how they influence one another. The second is **scalability**. Solutions that work at prototype scale often fail in dense operation:

a quiet rotor is not enough if vertiport throughput collapses under demand peaks, and a robust conflict-resolution algorithm is insufficient if U-space integration cannot support human oversight and certification. The move from demonstration to deployment demands scalable models, operations, and infrastructure. The third is **commonality**. Shared reference vehicles: lift+cruise, tiltrotor, and multicopter, give aerodynamic, acoustic, and operational studies a common language, as do shared benchmark cases for installed propellers, tandem configurations, and urban noise prediction. A vertical future is therefore at once a design problem, an operational challenge, and an urban question; solving it requires not only better aircraft but better integration between disciplines.

2 Reference Vehicles and Common Models for UAM

Most industrial eVTOL designs remain proprietary, while academic studies often need standardized and general geometries, mission profiles, propulsion architectures, and certification constraints. This allows international cross-comparison between aerodynamic, aeroacoustic, operational, and certification studies possible. The Urban Air Mobility Common Model (UCM) initiative addresses this gap by proposing openly available, modular, and scalable at component and full-system level reference eVTOL configurations that can serve as shared research platforms. Three presented configurations for the UCM are: a tiltrotor, a lift+cruise configuration and a multicopter. These architectures represent distinct solutions to the same mission problem and expose fundamentally different trade-offs between hover efficiency, cruise efficiency, redundancy, certification complexity, and community noise. To ensure comparability, the three UCM configurations are derived from mission-driven preliminary design procedures based on representative urban transport missions. The common mission assumptions include:

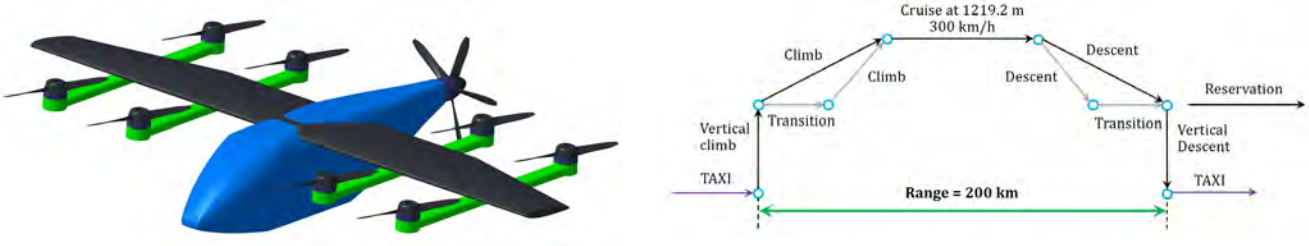
- short-range urban transport and point-to-point vertiport operations;
- battery-electric propulsion and explicit reserve energy requirements;
- certification-oriented safety margins.

The tiltrotor baseline targets longer-range regional connectivity (200 km, 300 km/h, 5 occupants), while the multicopter baseline adopts a shorter-range mission (55 km, 100 km/h, 3 occupants) optimized for dense urban operations. The lift+cruise configuration occupies the intermediate space between these two operational extremes.

2.1 Conceptual Design of the Urban Air Mobility Common Model Lift+Cruise Aircraft

Matteo Malavolti, Luca Abergo, Kangni Combey, Sen Wang, Alberto Guardone, Alex Zanotti

The lift+cruise configuration occupies the middle ground between multicopter simplicity and tiltrotor efficiency. Separate propulsion systems are used for: vertical lift rotors, dedicated cruise propulsors. This architecture avoids the complexity of tilt mechanisms while preserving fixed-wing cruise efficiency. The aerodynamic performance of the isolated propeller is first evaluated and subsequently used to iteratively update the vehicle dimensions, accounting for installation effects and their impact on performance. In DICUAM, the UCM architecture is validated through mid-fidelity aerodynamic simulations, carried out using DUST, an open-source vortex particle method solver developed at Politecnico di Milano (Tugnoli et al., 2021).



(a) (b)

Figure 2.1: (a) UCM lift+cruise (UCM-LC) configuration; (b) conceptual mission profile adopted in the Open UAM Consortium.

The resulting configuration is intended to serve as an open-access baseline for future aerodynamic, aeroacoustic, and multidisciplinary studies within the UAM research community. The focus is placed on the sizing of the vertical lift system, to determine disk loading and rotor dimensions for a prescribed number of propellers required to perform vertical flight phases such as take-off, hover, and climb. Concurrently, the energy consumption, battery mass, and overall vehicle weight are updated. For a predefined wing-fuselage geometry and mission profile, the proposed

methodology is applied to two lift+cruise eVTOL concepts featuring four and eight vertical rotors, respectively, each investigated in three different layouts. The mission requirements are defined based on publicly available UAM design targets and current eVTOL development trends. In particular, the study by Combey et al. (2026) is used to map the mission with respect to existing eVTOL concepts in terms of design range, cruise speed, and passenger capacity. Within the DICUAM initiative, a single reference mission profile has been defined and adopted for both the UCM lift+cruise and the UCM Tiltrotor configurations. The mission parameters selected for the UCM-LC configuration are identical to those of the UCM Tiltrotor model and are summarized in Table 2.1.

Parameter	*Value*	*Parameter*	*Value*
Passengers + pilot	5	Climb vertical velocity [m/s]	9.14
Design range [km]	200	Climb angle [deg]	20
Cruise speed [km/h]	300	Take-off time interval [s]	30
Cruise altitude [m]	1219	Hover time interval [s]	20
Take-off velocity [m/s]	1.52	Climb time interval [s]	125

Table 2.1: Reference mission parameters for the UCM and simplified detailed table for take-off, hover and climb phases.

The reference mission is defined at a conceptual level and consists of a vertical take-off and climb phase, a transition to forward flight, a cruise segment at constant altitude and speed, followed by a transition to vertical descent and landing (Figure 2.1-b). This mission profile captures the primary operational phases relevant to UAM applications while remaining independent of certified operational procedures or air traffic management constraints. The defined mission profile constitutes the primary driver for the preliminary sizing of the propulsion system, energy storage, and overall vehicle mass. All mission parameters are treated as design targets within a first-order conceptual design framework, and no performance validation or optimization is performed at this stage.

Although the same reference mission parameters are adopted, the actual execution of the mission differs slightly between the lift+cruise and Tiltrotor configurations due to their fundamentally different propulsion architectures. In the lift+cruise case, a dedicated hover phase is present after take-off, during which the vehicle remains in near-vertical attitude before pitching forward and engaging the cruise pusher to initiate the climb in forward flight. Conversely, the Tiltrotor configuration performs a conversion maneuver, during which the tilting propellers progressively transition from vertical lift to forward thrust while simultaneously providing lift and propulsion. During the cruise phase of both configurations, once the wing-generated lift becomes sufficient beyond a certain forward speed, the vertical lift propellers are shut down, and the aircraft operates in a wing-borne condition.

In the following, the sizing activity is limited to the vertical propulsion system. The reference mission profile has been simplified by explicitly accounting only for the take-off, hover, and climb phases, which are the most relevant for the sizing of the vertical propellers. The cruise and descent phases are instead included through a fixed percentage with respect to the initial mission energy requirement.

Vehicle sizing method

The strategy that has been developed consists in two macro steps. The first one concerns the creation and the simulation of the isolated rotor geometry, for simplicity without considering the installation effects. The second one consists in the analysis of the full geometry. Both steps have been developed as an iterative process. When the geometry of the rotor is established, the radius R is assumed, and the disk loading DL is extrapolated through mid-fidelity simulation. The value of DL is then given as input to the preliminary design code and a new value of the rotor radius R^* is obtained through momentum-balance considerations (i.e. the rotors should balance the vehicle weight). The loop closes when R^* converges to R. The second step involves the full geometry built with rotors

having a radius equal to the output R^*. An iterative process like the first one is now set up on the entire vehicle, to assess the rotors-wing-fuselage interaction effects on the disk loading value DL^*. The effective downforce which acts on the fuselage and on the wing of the vehicle during the climb phase is computed and added to the weight of the aircraft in contributing to the vertical forces balance inside the preliminary design code. The final R^{final} obtained is the design output. This procedure has been developed for dimensioning the vertical rotors, but the same could be done for the pusher(s) considering the cruise phase.

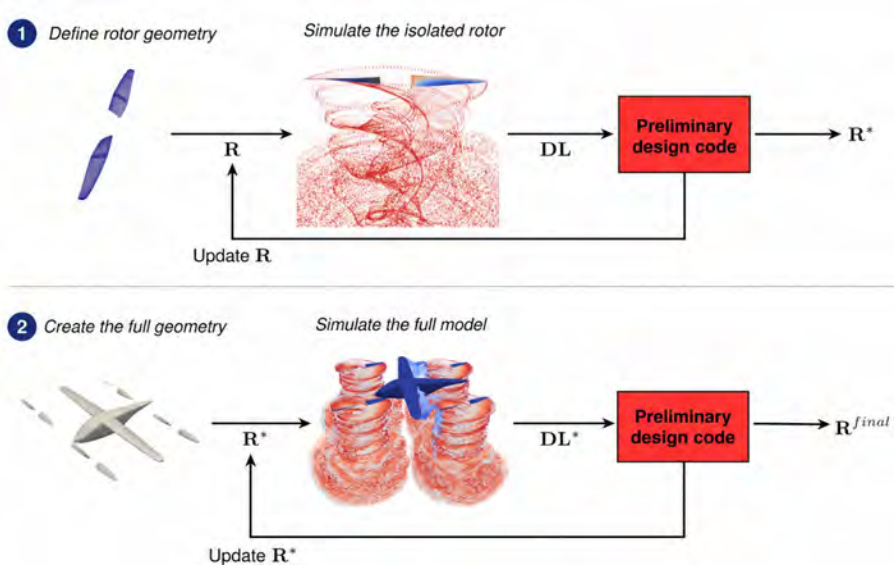


Figure 2.2: Design methodology for the vehicle based on the isolated and interacting rotors.

As previously anticipated, the preliminary design code takes as input the mission profile, the performance requirements, the design parameters and an initial total mass guess and gives as output the mass decomposition of the vehicle, the energy consumption and the batteries mass, to select one setup among the others. The *DL* in each flight phase for each vehicle setup must be given as input such as the vertical downforce acting on the vehicle during climb. The design constraints are the climb angle, the battery energy density, the payload mass, the motors mass and the number of propellers. The value for the battery energy density is assigned to 230 Wh/kg, while the payload mass and the motor mass are respectively 450 kg and 375 kg.

The airframe component masses, such as fuselage, wing-landing-gear-tail compound and propellers, are estimated to lay on established mass ratios for similar category aircraft. These mass ratios are obtained from exemplary aircraft components made from aerospace-grade aluminum, since at the current stage no data for mass ratios based on composite materials for comparable aircraft is available. Formulas for the computations refer to the design of a lightweight Cessna vehicle and summarized in Table 2.2 (Roskam, 1987). To estimate the battery's mass pack, it is possible to rely on the definition of power loading *PL* for each flight phase: it is a function of disk loading *DL* and figure of merit *FM*, as specified below. Since the battery mass is given as a function of battery energy density, state of charge, and required power and time for each flight phase, the total mass is obtained iteratively through a bisection method. The bisection method iteratively reduces the interval between a lower limit (equal to payload mass) and an upper limit (4000 kg, based on the eVTOL from Beta Technologies) until a solution is found. The ending iterations bring to a payload mass of 450 kg, and a motor mass of 375 kg (cumulative) once considering a battery energy density of 230 Wh/kg. The remaining part of the analysis is carried out with DUST (Tugnoli et al.,

2021) integrating different aerodynamic models for solid bodies, such as actuator disks, surface panels, vortex lattice elements and lifting line elements.

Parameter	*Design formula*
Fuselage	$m_f=14.86 m_{tot}^{0.144}\left(\frac{l_f}{P_{max}}\right)^{0.778} l_f^{0.383} N_{pax}^{0.455}$
Propeller	$m_{\text{prop}}=k_{\text{prop}} N_{blades}^{0.391} \frac{D_{\text{prop}} P_{clb}^{0.782}}{N_{\text{prop}} 1000}$
Wing and landing gear	$m_{wtl}=0.04674 m_{tot}^{0.397} S_w^{0.36} \eta_w^{0.397} AR_w^{1.712}+(40 m_{tot})^{0.67} N_{wheels}^{0.54}$
Battery	$m_{bat}=\frac{1}{e_{bat} SOC}\sum P_i t_i=\frac{g}{e_{bat} SOC}\sum \frac{t_i}{PL_i}$
Total mass	$m_{tot}=m_{tot}+m_{fus}+m_{wtl}+m_{bat}+m_{\text{prop}}+m_{mot}+m_{payload}$
Condition	*Design formula*
Hover phase	$PL=FM\sqrt{\frac{2\rho}{DL}}$
Climb phase vertical component	$PL=\frac{1}{V_z-\frac{k}{2}V_z+\frac{k}{2}\sqrt{V_z^2+\frac{2DL}{\rho}}}$
Climb phase horizontal component	$PL=\frac{\eta_{\text{prop}} WL}{0.5\rho C_D V_x^3}$

Table 2.2: Equations for weight estimate based on aircraft design rules (Roskam, 1987).

The DUST vortex particle method is divided into three main modules: a pre-processor, a solver and a post-processor. In the pre-processor module, geometric components can be imported from existing meshes or generated parametrically. Solid bodies are represented using a surface distribution of singularities; thus, a DUST model requires surface discretization only. It is possible to choose between a structured vortex lattice wake, vortex particles wake or a mixed one: its intensity is obtained enforcing the Kutta condition at the trailing edges at each time step. The solution process involves generating a sequence of singularities with varying intensities to represent the solid bodies and their resulting wakes. The mathematical formulation relies on a vorticity–velocity mixed aerodynamic problem based on the Helmholtz decomposition of the velocity field and a Lagrangian description of the vorticity field. In this work, the rotor blades have been modeled as (linear) vortex lattice elements and the wing and the fuselage as surface panels. Each blade of the rotors was represented by 400 vortex lattice elements, with a spanwise discretization of 40 panels and a chordwise discretization of 10 panels. For all simulations, a half-cosine refinement was applied to surface elements in the chord-wise direction, similarly in the spanwise direction a refinement is applied at the blade tip.

Model Layout and Sizing Results

The design process has been applied to two lift+cruise eVTOL concepts, with four and eight propellers arranged in three different layouts. Different layouts share same fuselage, wing and blades geometries, but different rotor positions. The dimension of the wing has been scaled to correctly fit the fuselage according to other examples from literature (e.g. the NASA reference model (Katz & Plotkin, 2001)).

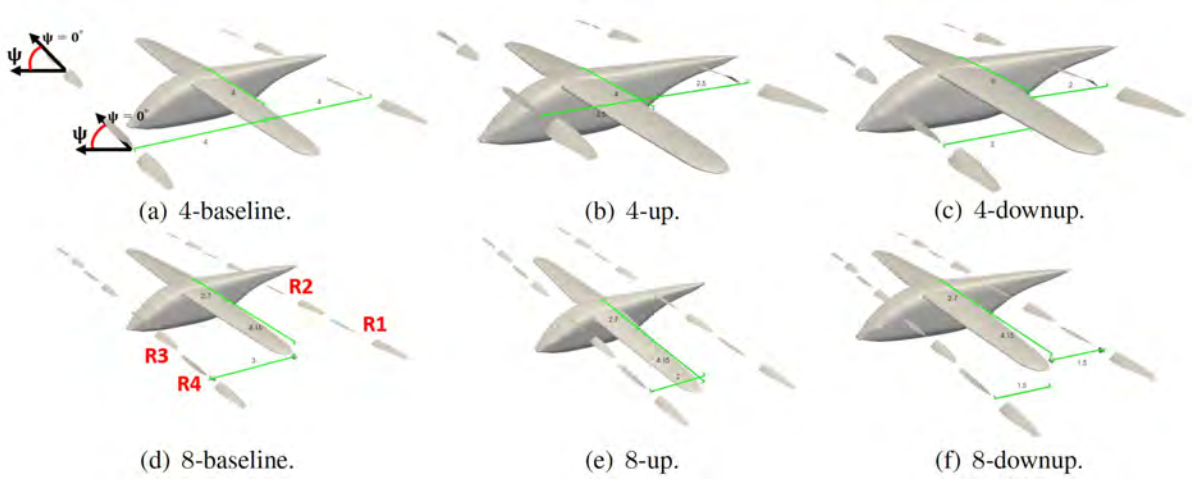


Figure 2.3: lift+cruise models: (a) 4-baseline; (b) 4-up; (c) 4-downup; (d) 8-baseline; (e) 8-up; (f) 8-downup.

Figure 2.3 shows the different configurations. The baseline configurations present the rotors located on the same plane as the wing. In the up configurations, the rotors are positioned 0.7 m above the wing plane and closer to the wing with respect to the baseline case. In the downup configurations, the front rotors are placed 0.35 m below the wing, while the rear rotors are positioned 0.35 m above it. Compared to the up setup, the longitudinal distance between the front and rear rotors is reduced. For the subsequent analysis of the results, it is important to specify that all rotor blades rotate counterclockwise. Therefore, a reduction in the distance between the rotors and the wing/fuselage is expected to intensify aerodynamic interaction effects. As previously discussed, the preliminary design code primarily outputs the rotor disk radius, total mass, and battery mass. The data reported in Table 2.3 represent the outcome of the double iterative process, including installation effects.

Configuration	*D [m]*	m_{tot} *[kg]*	m_{bat} *[kg]*
4-baseline	4.9	2226	847
4-up	5	2228	845
4-downup	4.87	2245	862
8-base	3.4	2250	853
8-up	3.54	2259	857
8-downup	3.42	2267	866

Table 2.3: Design results for sizing.

For each layout, three rotor diameters were obtained and each of them represents the ideal value for each flight phase (take-off, hover and climb). Since the climb phase is the most demanding one because of the additional contribution given by the airframe drag to the aircraft weight, the design must be based on that corresponding value, reported in Table 2.3. It is interesting to specify that the “downup” layout is the one which leads to the smallest increase in the rotor radius value with respect to the outcome from the first step of the design procedure. It emerges that none of the investigated configurations can be identified as unequivocally preferable over the others.

This outcome can be attributed to several modeling assumptions and simplifications. In particular, the total motor mass has been assumed to be identical for both the four- and eight-rotor configurations. Furthermore, the mass of the pylons connecting the rotors to the wing has not been included in the model. Additionally, the propeller geometry, number of blades, and rotational speed have not been optimized with respect to the different flight phases. Moreover, the cruise phase has not been explicitly modeled; instead, it has been accounted for through a safety

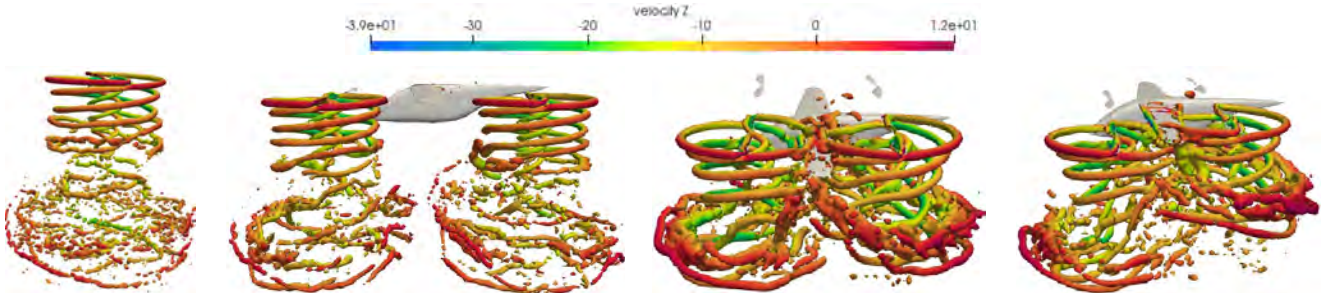
factor that assumes a battery discharge consistent with typical values applied uniformly to all eVTOL configurations.

Aerodynamic Results

The analysis characterized the dominant interaction mechanisms between the propulsion system, wing, and fuselage, concentrating on rotor-wake evolution in hover and climb, which are the most critical phases for sizing the vertical propulsion system. Beyond global thrust and power, the aim was to understand how rotor placement relative to the wing and fuselage reshapes the wake, alters the induced velocity at the rotor disks, and affects aerodynamic efficiency. Flow topology and wake coherence were examined through three-dimensional Q-criterion visualizations contoured by vertical velocity. A prior convergence and validation campaign on the isolated rotor established a numerical setup that reproduced thrust and torque at acceptable computational cost. The isolated rotor simulations were performed in hover conditions, representing the most demanding case in terms of wake stability and convergence requirements. A sensitivity study was carried out by varying both the blade discretization and the temporal resolution. The number of spanwise elements was fixed at 40, while the number of chordwise panels progressively increased to evaluate mesh convergence effects on thrust and torque predictions. Stable values of thrust and torque were obtained as the number of chordwise elements increased, while the relative error progressively decreased. A temporal convergence analysis was also performed considering azimuthal resolutions of 1, 2, 3, and 5 degrees per time step. The results demonstrated that the dependence of thrust and torque predictions on the time-step size remained limited, with the coarsest resolution producing errors below 1% relative to the finest one. Based on this trade-off between numerical accuracy and computational effort, a resolution of 3° per time step was selected for all vehicle simulations. The isolated rotor analysis also provided an important physical reference case. In the absence of installation effects, the rotor wake developed into a stable and coherent helical structure characterized by ordered tip vortices and relatively smooth induced velocity distributions. This isolated behavior later served as a baseline for evaluating how rotor-wing-fuselage interactions progressively altered the wake topology in the complete aircraft configurations.

Hover Flight Condition

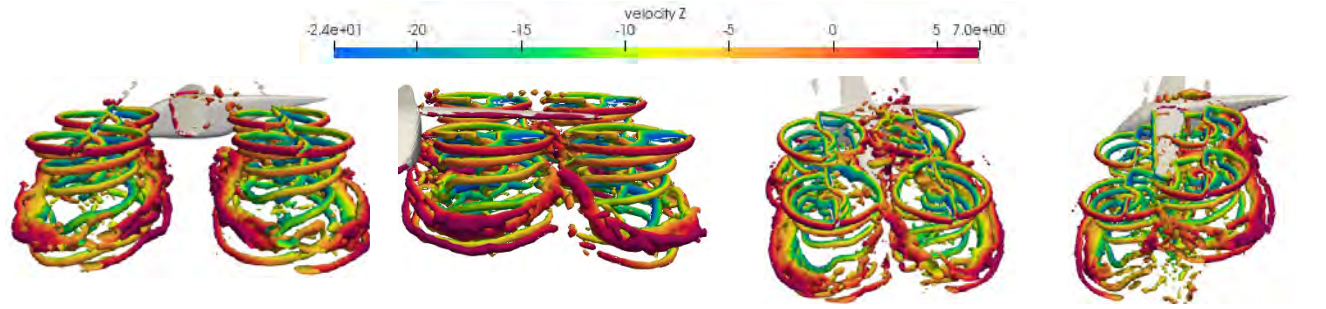
The hover condition revealed the strongest sensitivity to rotor placement and installation effects. From the flow-field analysis the aerodynamic behavior of the lift+cruise aircraft changes substantially as the distance between the rotors, wing, and fuselage is modified. For the four-rotor configurations, the baseline arrangement showed relatively weak interaction effects. Since the rotors were positioned farther from the wing plane and sufficiently separated from one another, the helical wakes remained coherent and evolved similarly to the isolated rotor case. Rotor-rotor interactions were minimal, and the wake structures maintained their ordered organization over a significant downstream distance. The flow field therefore suggested that the four propellers operated almost independently from an aerodynamic perspective. A markedly different behavior emerged for the 4-up and 4-downup layouts. In these configurations, the reduced distance between the rotor disks and the wing intensified the interaction between the rotor wakes and the lifting surface. The helical wake structures rapidly lost coherence below the wing plane, leading to a more turbulent and diffused flow topology. The progressive destruction of the tip vortices altered the induced velocity distribution at the rotor disk, which in turn affected the effective angle of attack experienced by the blades and modified the thrust distribution along the span. For the eight-rotor configurations, more numerous and smaller rotors reduced the spacing between adjacent wakes, so rotor-rotor interaction became substantially stronger than in the four-rotor cases (Figure 2.4). In the 8-baseline layout the frontal and rear wakes stayed relatively clear of the wing, but neighboring tip vortices already showed clear merging.



(a) Isolated-hover (b) 4-baseline (c) 4-up (d) 4-downup

Figure 2.4: Hover flight, Q-criterion visualizations contoured by vertical velocity.

The 8-up and 8-downup layouts were more complex, with individual helical structures merging into larger collective wake systems; in 8-downup the asymmetric interaction between the rear rotor wakes and the wing-induced vortices broke the symmetry about the wing center plane, and the rear tip vortices rolled up beneath the rotor plane into strongly disturbed regions of wake breakdown. Hover performance of distributed propulsion is therefore governed by installation effects: isolated-rotor estimates are useful, but the complete vehicle behaves substantially differently once wakes interact with surfaces and neighboring propellers.

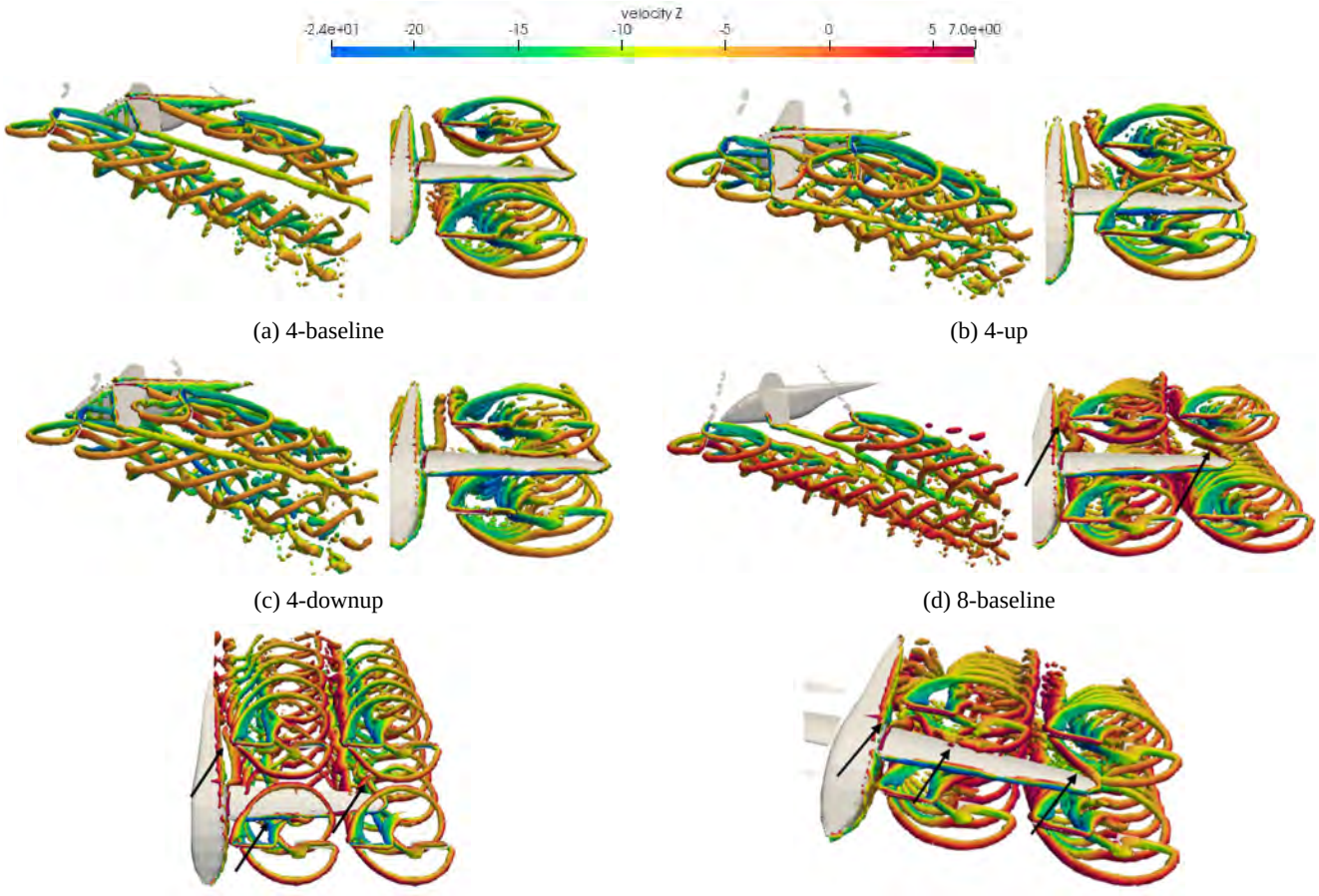


(a) 8-baseline: side (b) 8-baseline: frontal (c) 8-up (d) 8-downup

Figure 2.5: Hover flight, Q-criterion visualizations contoured by vertical velocity.

Climb Flight Condition

During climb, rotor-induced flow combines with forward-flight effects, shifting the dominant interaction from rotor-rotor to rotor-wing coupling (Figure 2.6). The four-rotor baseline wakes stayed relatively stable, convecting downstream without significantly impinging on the wing and largely preserving their helical structure. The 4-up and 4-downup configurations instead showed clear wake impingement on the wing. The frontal rotor wakes directly interacted with the lifting surface, causing the lower portion of the helical wake to lose coherence shortly after the interaction region. The wake breakdown was particularly visible in the vicinity of the wing leading-edge and near the fuselage-wing junction. For the 4-downup arrangement, an additional interaction mechanism appeared between the wing tip vortex and the wake generated by the rear rotor. The two vortex systems partially merged, producing more complex wake structures and increasing the level of flow distortion downstream of the vehicle. These effects illustrate how even relatively small variations in rotor vertical positioning can significantly alter the aerodynamic environment experienced by the vehicle. The climb analysis of the eight-rotor configurations revealed the strongest interaction effects of the entire study. Due to the high rotor density and reduced spacing between propulsion units, the wakes became highly coupled with both the wing and the fuselage-generated vortices. The 8-up configuration produced the largest interaction region among all investigated layouts. Because the frontal rotors were positioned above the wing plane, their wakes impinged directly on the wing leading edge, generating highly disturbed flow structures and rapid vortex breakdown.



(a) 4-baseline (b) 4-up

(c) 4-downup (d) 8-baseline

(e) 8-up (f) 8-downup

Figure 2.6: Climb flight, Q-criterion visualizations contoured by vertical velocity.

At the same time, the wing tip vortices merged with the wakes generated by the rear external rotors, producing a strongly coupled vortex system. The 8-downup arrangement displayed similarly strong interaction effects, although the evolution of the frontal and rear wakes differed due to the asymmetric rotor placement. In this case, the wing tip vortices became almost fully embedded within the rotor wake structures, leading to extensive wake merging and substantial loss of vortex coherence downstream of the aircraft. Overall, the climb simulations demonstrated that the aerodynamic environment of lift+cruise eVTOL aircraft is governed by a delicate balance between rotor placement, wake convection, and wing-generated vortex structures. Compact distributed propulsion architectures can significantly intensify aerodynamic interactions, potentially affecting not only thrust generation and efficiency, but also aeroacoustic behavior and flight stability.

Installation effects therefore cannot be neglected in the conceptual design of lift+cruise eVTOL aircraft: rotor wakes interact strongly with the wing and fuselage, especially in compact distributed-propulsion layouts where aerodynamic surfaces and propulsion units sit close together. Key trends:

- Increasing the number of rotors intensifies rotor–rotor interaction effects and promotes wake merging phenomena.
- Rotor placement relative to the wing strongly influences wake coherence and vortex stability.
- Compact layouts produce larger interaction regions and more disturbed flow structures.
- Wake impingement on the wing leads to rapid destruction of helical vortex organization.

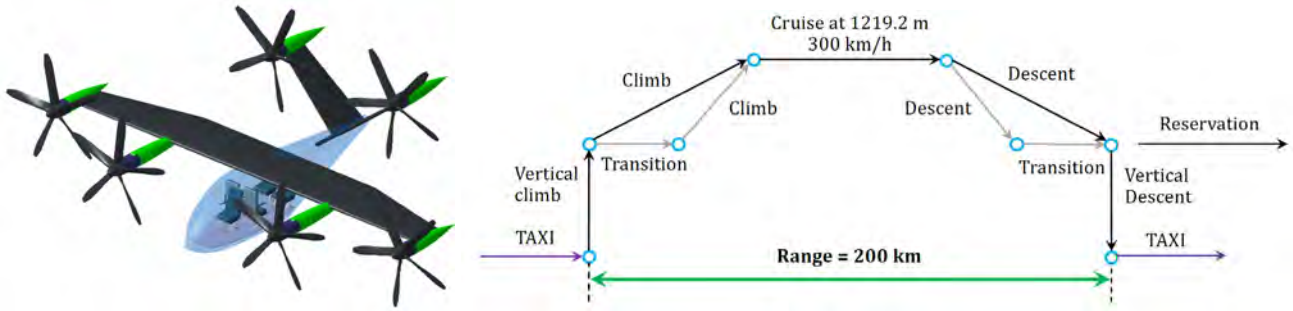
- Installation effects significantly modify the induced velocity field at the rotor disks and therefore alter thrust generation mechanisms.

More broadly, the results highlight that aerodynamic interactions represent one of the defining characteristics of future eVTOL aircraft. Understanding and controlling these interactions will be essential not only for improving aerodynamic efficiency, but also for reducing noise generation, optimizing energy consumption, and ensuring stable and predictable vehicle behavior across all flight phases.

2.2 Urban Air Mobility Tiltrotor Variant

Andrea Magrini, Anna Palacio Castro, Kangni Combey, Manuel Casablanca

Among the primary UAM configuration families, the tiltrotor *TR* architecture presents instead a highly efficient vectored-thrust strategy where the same propulsive mechanisms provide both vertical lift and forward propulsive force, eliminating parasitic weight from inactive engines during cruise flight. Most prominent eVTOL frameworks exploit Distributed Electric Propulsion DEP, mounting multiple compact, electrically driven rotors across lifting surfaces to enhance redundancy, control authority, and aerodynamic efficiency. However, DEP introduces highly complex aerodynamic interactions, challenging aeroacoustic signatures, complex structural integration issues, and uncharted certification pathways, all magnified by strict urban operational requirements concerning community noise limits and safety margins. Moreover, the absence of predetermined propulsive layouts and the sensitive subsystems interactions greatly widen the design space, making the conceptual vehicle design particularly complex. In the frame of the collaborative UAM model development, this section presents the preliminary tiltrotor configuration established through initial design assumptions.



(a) (b)

Figure 2.7: (a) UCM Tiltrotor aircraft (UCM-TR) configuration; (b) conceptual mission profile adopted in the Open UAM Consortium.

Top-Level Aircraft Requirements (TLARs) and Operational Mission Profile

The TR configuration follows a mission-driven approach aimed at point-to-point intra-urban transport. Its Top-Level Aircraft Requirements (TLARs) set a payload for five occupants (one pilot, four passengers), about 500 kg; the main operational parameters are listed in Table 2.4.

Parameter	*Value*	*Parameter*	*Value*
Passengers + pilot	5	Rate of climb [m/s]	8
Design range[km]	200	Lift-off time [s]	10
Cruise speed [km/h]	300	Initial descent velocity [m/s]	30
Cruise altitude [m]	1219	Final descent velocity [m/s]	5

Table 2.4: Reference mission parameters for the UCM TR model.

The sizing mission profile (Figure 2.7) comprises ground taxi, vertical take-off and climb, a transient transition to forward flight, cruise at constant altitude and speed, an approach transition back to vertical thrust, vertical descent to touchdown and taxi, and a hover reserve. Similarly to the previous design approach, the preliminary design framework employs an iterative, lumped-parameter sizing workflow where initial subsystem masses are estimated, performance maps are analyzed across all flight segments, and the final vehicle mass is sequentially updated until convergence is achieved. The framework avoids detailed subsystem modeling, focusing on producing a conceptual design to obtain a preliminary geometric configuration for further aerodynamic assessments, as schematized in Figure 2.8.

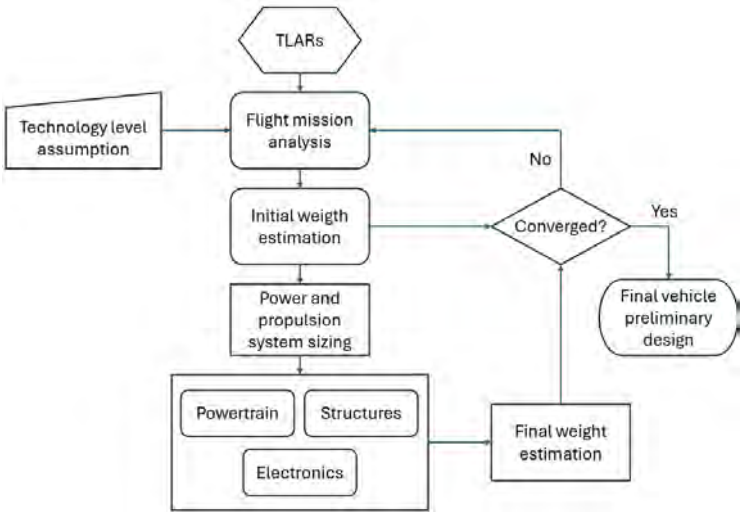


Figure 2.8: Tiltrotor preliminary design workflow.

To model propulsive behavior during forward flight, the aerodynamic and power coefficients are extracted from characteristic maps corresponding to a representative four-blade NACA 5868 propeller layout, yielding an efficiency of 0.86 at an advance ratio of 1.08. To maintain conservative first-order design margins, this efficiency is applied globally across all standard flight segments, while the purely vertical components are characterized via classic helicopter momentum considerations. The technological state-of-the-art for propulsive and energy systems relies on contemporary yet realistic metrics, derived from analysis of existing systems. The chosen values for the current configurations are:

- Battery Pack Specific Energy Density: 230 Wh/kg
- Powertrain Mechanical Efficiency: 0.97
- Motor Power-to-Weight Ratio: 0.4 kW/kg

The baseline geometric parameters of the airframe structure are defined uniformly to align with a shared reference fuselage layout within the broader UCM initiative, as reported in Table 2.5.

Parameter	*Value*	*Parameter*	*Value*
Wing span [m]	10.7	Fuselage aspect ratio	1.5
Fuselage length [m]	8	Fuselage diameter [m]	1.5
Fuselage nose length [m]	2.3	Landing gear height [m]	2
Fuselage tail length [m]	4		

Table 2.5: Tiltrotor reference fuselage parameters.

The sizing loop is initialized by establishing a historical baseline derived from successful legacy and modern tiltrotor configurations presented in Table 2.6. An empirical evaluation of vehicles encompassing the Bell XV-15, the Leonardo AW609, the Joby S4, and the 7-seater Lilium Jet establishes normalized design bounds. The aggregated database yields an average Payload-to-Maximum Take-Off Weight ratio *PL/MTOW* of 0.234 and an Operating Empty Weight-to-Maximum Take-Off Weight ratio (*OEW/MTOW*) of 0.628. Factoring in the strict 500 kg payload mandate, these ratios seed the iterative solver with an initial estimated *MTOW* of 2137 kg and an initial *OEW* of 1342 kg.

Aircraft	*MTOW (kg)*	*OEW (kg)*	*OEW/MTOW*	*PL (kg)*	*PL/MTOW*
XV-15 (NASA)	6804	4341	0.638	1327	0.195
AW609 (Leonardo)	8165	4765	0.584	2722	0.333
Joby S4 (Joby Aviation)	2404	1950	0.811	453	0.188
Lilium Jet (7-seater)	3175	1524	0.480	700	0.220

Table 2.6: Existing tiltrotors weight from literature.

Analogous to the previous configuration, to formulate the power requirements across each mission segment, the instantaneous thrust and lift requirements must be calculated. The vertical ascent profile defines an initial 10-second acceleration phase designed to transition the vehicle from rest to a steady Rate of Climb *ROC* of 8 m/s. Aerodynamic drag forces acting opposite to the vertical flight path are numerically integrated using the projected fuselage and wing planform areas. The drag force in the vertical trajectory was computed from the assumed fuselage and wing planform, based on the study of Wang et al. (2025). Conversely, forward cruise drag is modeled via classic finite wing theory, incorporating an Oswald efficiency factor of 0.85 to define the induced drag component (Roskam, 1987). It is important to mention that, since the selected descent rate does not fall within the applicability limits of helicopter momentum theory, an empirical polynomial model was adopted to estimate the induced velocity and the corresponding power requirement during descent.

Parameter	*Design formula*
Induced velocity in hover	$v_{ih}=\sqrt{\frac{T/N_{rotors}}{2\rho\pi(D_{rotor}/2)^2}}$
Induced velocity in climb (in function of the rate of climb ROC)	$v_i=-\frac{ROC}{2}+\sqrt{\frac{ROC^2}{4}+v_{ih}^2}$
Induced velocity during descent	$\underline{v_i}=\kappa+k_1\underline{v_z}+k_2\underline{v_z^2}+k_3\underline{v_z^3}+k_4\underline{v_z^4}$
Non dimensional descent velocity	$v_{ih}=\sqrt{\frac{T/N_{rotors}}{2\rho\pi(D_{rotor}/2)^2}}$

Table 2.7: Sizing formulas for the TR configuration.

All the sizing equations are reported in Table 2.7, where the induced velocity in hover is v_{ih}, the induced velocity during climb or descent is v_i, T the total rotor thrust needed in that flight phase, N_{rotors} the number of rotors, ρ the air

density, and D_{rotor} the rotor diameter. The parameter *ROC* represents the rate of climb, *P* the required power, $\underline{v_z}$ the nondimensional descent velocity defined as V_d/v_{ih}, and V_d the vertical descent velocity. The coefficients k_i are empirical constants used to estimate the induced velocity during descent.

The vertical descent phase is designed to execute from an initial vertical speed of 30 m/s, followed by a managed deceleration phase reducing the velocity to 5 m/s directly prior to final touchdown. Because a descent rate of 30 m/s creates highly turbulent vortex-ring states that violate the standard applicability limits of classic 1D helicopter momentum theory, an empirical polynomial velocity model is implemented. This formulation computes the real induced velocity and localized power penalties during steep descent profiles.

Motor		*Power (kW)*	*Weight (kg)*	*Battery Voltage (L-M-HV)*
Emrax	188	37	7.1	160-390-660
	208	56	9.4	170-420-690
	228	75	12.9	250-630-830
	268	117	21.4	340-830-830
	348	140	43.1	610-830-830
Joby	JM1S	8.2	1.8	–
	JM2	14	4	–
T-MOTOR	U15XXL	28	5.13	50-100
	U15XL	23	4.41	50-100
	U15L	16	3.6	50-100

Table 2.8: Selection of electric motors suitable for eVTOL and tiltrotor applications.

The propulsion subsystem masses encompass the electric motors, propellers, nacelle structures, and ancillary electrical distribution systems. Motor sizing is governed by the peak power demand identified during mission analysis, which occurs during vertical take-off and hover conditions. A regression analysis was executed using technical data from a commercial electric motor catalog reported in Table 2.8 (including Emrax 188, 208, 228, 268, 348 models, Joby JM1S/JM2 units, and T-Motor U15 series), creating a polynomial model that links continuous and peak rated power directly to motor mass. The mass of the high-voltage copper wiring harness is calculated using empirical correlations that scale with the geometric layout of the aircraft and the spatial distribution of the power units. Auxiliary power electronics and converters are integrated via consolidated lump-sum mass allowances. Avionics and flight control actuation utilize a component-based methodology, summing the specific masses of safety-critical elements, such as redundant flight control computers, navigation suites, communication transceivers, air-data sensors, and rotary actuators, extracted from manufacturer datasheets.

Airframe component weights for wings, fuselage, landing gear, and tail structures are computed using semi-empirical correlations optimized for general aviation aircraft, specifically the Cessna Method. General aviation weights serve as an appropriate proxy due to comparable geometric envelopes, speed vectors, and load factors. While these historical equations were derived based on traditional materials, they yield conservative mass estimates for modern composite structures. This conservatism is beneficial during preliminary conceptual sizing to avoid underestimating structural loads and cross-coupling weight penalties.

The iterative multi-disciplinary sizing loop successfully converges with a final vehicle MTOW of 2738 kg. A comprehensive mass fraction and performance breakdown of the final converged configuration is detailed in Table 2.9. To assess the physical validity of the model, the specific power requirements across the hover, climb, and cruise

regimes were compared against validated commercial equivalents, specifically the Joby S4 tiltrotor and the Lilium Jet.

Sizing Parameter	*Value*	*Sizing Parameter*	*Value*
Cruise Power [kW]	238.7 kW	Hover Power [kW]	502.0
Specific Cruise Power [W/kg]	87.1 W/kg	Specific Hover Power [W/kg]	183.4
Number of rotors	6	Rotor Diameter [m]	3.0
Rotor Disk Loading [kg/m²]	64.6	Wing Loading [kg/m²]	222.6
Total Battery Mass [kg]	933 (34.0%)	Total Powertrain Mass [kg]	328 (12.0%)
Total Structural Mass [kg]	920 (33.6%)	Design Payload Mass [kg]	500 (18.3%)

Table 2.9: Final weight breakdown of the preliminary tiltrotor configuration.

Despite the simplified lumped-parameter nature of the sizing loop, the specific power curves in Figure 2.9 show close alignment with commercial baselines. This verification confirms the plausibility of the sizing methodology and supports the use of the TR as a reliable open reference model.

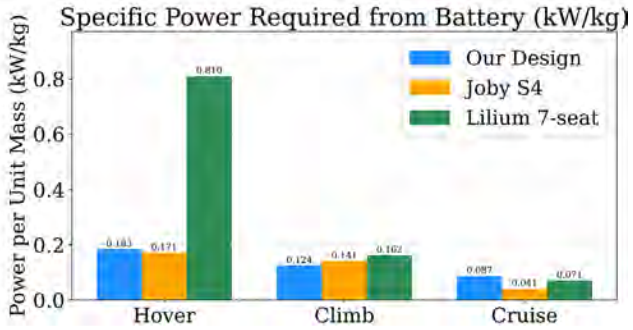


Figure 2.9: Specific power during main mission phases for the present and existing tiltrotor configurations.

Given that the electrochemical energy storage system represents the single largest mass component (34% of total MTOW), a sensitivity analysis was performed to evaluate how variations in battery performance impact the overall vehicle mass, see Figure 2.10. The analysis reveals a highly non-linear relationship between battery energy density and total aircraft mass due to compounding weight penalties. Under the baseline assumptions (230 Wh/kg specific energy), the aircraft requires a total battery mass of 933 kg to meet the 200 km range and 10-minute hover requirements. Sweeping the specific energy density from 200 Wh/kg up to 500 Wh/kg highlights the compounding benefits of battery technology advancement. For example, a 30% improvement in pack-level specific energy density relative to the baseline triggers an approximate 20% reduction in the converged MTOW of the vehicle. This compounding mass reduction occurs because a lighter battery pack reduces structural load requirements, which decreases the required wing and fuselage mass, subsequently lowering the thrust and power requirements during vertical flight. This cascading sizing loop emphasizes that battery performance remains a primary driver for the operational viability and weight optimization of modern eVTOL tiltrotor designs.

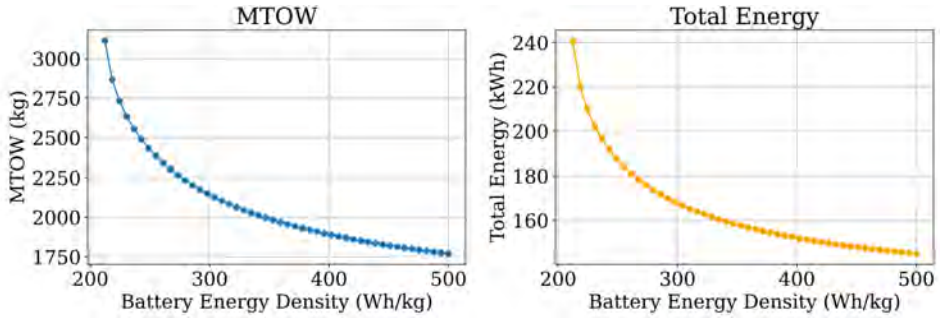


Figure 2.10: Variation of tiltrotor MTOW with battery energy density

Development of geometric configuration

Once the primary parameters converged, a three-dimensional CAD model was generated as the baseline TR airframe, that is a geometrically consistent translation of the conceptual sizing results.

The architectural layout combines several distinct structural design elements:

- ***Fuselage Cabin Envelope:*** Sized to match standard ergonomics and layout constraints for five occupants, assuming a single pilot and four passengers.
- ***Lifting Surfaces:*** A fixed-wing architecture with a moderate aspect ratio and a span of 10.7 m, providing high lift-to-drag ratios during forward cruise.
- ***Empennage Stability:*** A symmetric V-tail configuration designed to provide combined longitudinal and directional stability while minimizing aerodynamic drag and structural weight penalties.
- ***Distributed Symmetrical Propulsion Layout:*** Six identical electrically driven 3 m diameter propellers mounted within tilting nacelle assemblies. Four rotors are spaced symmetrically along the span to provide uniform lift distribution, while two additional rotors are mounted on the aft V-tail assembly. This layout maintains a balanced thrust center during vertical lift maneuvers and transition corridors.

Figure 2.11 shows the reference fuselage and the preliminary geometric UCM-TR configuration with its dimensions.

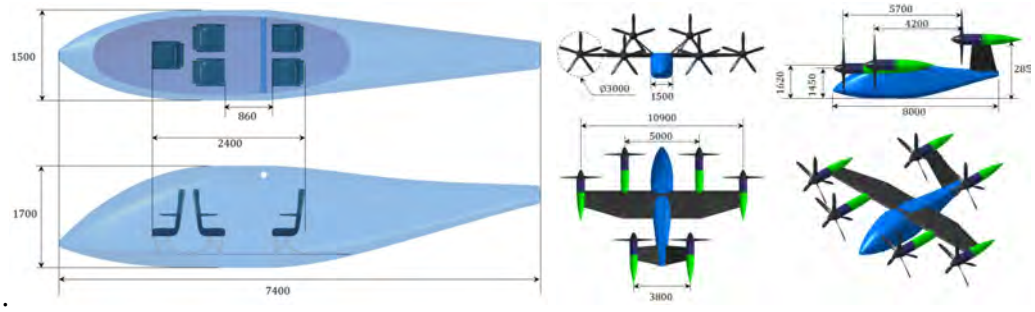


Figure 2.11: UCM-TR preliminary geometric model.

The CAD models capture the tilting-nacelle states in hover and cruise, giving the community a standardized mesh baseline for aerodynamic and structural modeling. The resulting 2738 kg vehicle meets its targets — five occupants over 200 km at 300 km/h cruise. Future work can replace the lumped-parameter mass assumptions with higher-fidelity structural and powertrain models to support formal Multidisciplinary Design Optimization (MDO) across alternative layouts, aimed at reducing energy consumption. Because aerodynamic and aeroacoustic interaction is decisive in eVTOL aircraft, the available geometry also enables CFD studies of wing-rotor slipstream coupling and blade-vortex interaction during transition, while lower-fidelity methods such as vortex-lattice methods (VLM) offer

faster assessment. The preliminary UCM-TR thus provides the community with an open starting point for these studies.

2.3 UAM Common Model, the Multicopter Configuration

Arinze Ndubisi Eze, Kangni Combey, Federico Nahuel Ramírez, Sen Wang

The multicopter reference configuration completes the UAM Common Model (UCM) family alongside the lift+cruise and tiltrotor baselines, as a direct realization of distributed lift. In this paper the term multicopter is defined as any crewed or uncrewed vehicle in which multiple rotors provide all thrust and lift required for vertical take-off, forward flight, and landing, without the use of a fixed wing for sustained aerodynamic lift. Multicopter concepts range from small quadrotors to large, highly redundant passenger-carrying vehicles. Notably, aerodynamic interaction and performance penalties can be significant in rotor–on–body and rotor–rotor interactions, motivating careful modeling even at the conceptual stage (Combey et al., 2025). For example, computational studies of a NASA quadrotor urban air taxi concept highlight the sensitivity of rotor performance to aerodynamic interference and operating condition (Diaz & Yoon, 2020). Multicopters also provide a natural testbed for research in over–actuated flight control. With the number of rotors N_r exceeding four, control allocation becomes central to design and verification.



(a) (b)

Figure 2.12: a) UCM Multicopter (UCM-MC) configuration. The analyzed baseline is an 18-propeller conventional radial multicopter. b) Preliminary sizing workflow. The loop couples mission energy, mass estimation, and an electrical feasibility / parts selection roll–up into a reproducible process.

The vehicle can tolerate limited rotor failures, redistribute thrust to manage loads, and enforce actuator limits while tracking desired forces and moments. Because UAM operations occur close to communities, multicopters are also relevant for investigations on distributed–propulsor noise signatures and developing noise-aware trajectories and rotor operating schedules (Pereira et al., 2024). The UCM–Multicopter configuration is not proposed as a certifiable product design; rather, it serves as a reference that reflects relevant certification drivers and enables early "certification–thinking" sizing studies. In both FAA and EASA frameworks, the emerging regulations for powered–lift and VTOL aircraft emphasize system safety, continued safe flight and landing under failures, and special considerations for novel energy sources. For instance, EASA Means of Compliance (MOC) material for SC–VTOL provides dedicated guidance on propulsion and energy storage safety, including battery thermal runaway considerations (European Union Aviation Safety Agency (EASA), 2026b). FAA has also published guidance on certification approaches and operational considerations for powered–lift aircraft (Federal Aviation Administration (FAA), 2024). These drivers motivate explicit margins, redundancy assumptions, and an electrical–architecture feasibility layer even in early sizing. This section describes the preliminary sizing workflow used to develop the UCM–Multicopter baseline. The workflow is designed to be *parametrized*, which permits modifications on rotor

count, mission, and technology assumptions without restructuring the model. Figure 2.12-b summarizes the sizing loop.

Parameter	*Symbol*	*Baseline value*
Range [km]	R	55
Cruise speed [km/h]	V_{cr}	100
Cruise altitude (MSL) [km]	h_{cr}	1.2
Occupancy (passengers + pilot)	N_{occ}	3 (2 pax + 1 pilot)
Propulsion	–	Electric / hybrid capable
Propeller count	N_r	18

Table 2.10: Representative TLARs used in this work.

Conceptually, the loop enforces consistency among mission energy, battery mass, empty mass, and total mass, while verifying propulsion and electrical architecture feasibility (i.e., the selected components can deliver the required power and current at the chosen voltage). The UCM-Multicopter is intended to represent a short-range urban/peri-urban mission. The TLARs adopted in this work are summarized in Table 2.10. Values are representative rather than prescriptive; the objective is to define a coherent baseline that can be modified by users. A simple mission model is adopted to support energy estimation and reserve accounting. The mission is discretized into segments indexed by i, each with duration Δt_i, representative airspeed V_i, and required shaft power $P_{sh,i}$:

$$E_{req}=\sum_i \left(\frac{P_{sh,i}}{\eta_{all}}\right)\Delta t_i$$

where η_{all} is a lumped efficiency capturing electrical and mechanical conversion losses.

For a representative UAM mission, the segments include: (i) take-off and initial climb; (ii) climb to cruise altitude; (iii) cruise; (iv) descent and approach; (v) landing hover; and (vi) reserve. Reserve is represented as an additional energy quantity:

$$E_{req}^{\star}=E_{req}(1+f_{res})$$

where f_{res} is a reserve fraction (e.g. 20% for conceptual studies) or can be defined as a time-based loiter depending on the operational assumptions. The UCM–Multicopter is parametrized by a set of geometry and architecture variables for early sizing, downstream load, and flight dynamics modeling. A body-fixed frame B is defined with origin at the vehicle's CG: x_B forward, y_B right, and z_B down (standard aerospace convention). Each propeller $j \in \{1, \dots, N_r\}$ is assigned a position vector $r_j=[x_j, y_j, z_j]^T$ from the CG, and a unit thrust direction n_j (typically aligned with $-z_B$ in hover). The thrust generated by each propeller is denoted $T_j \geq 0$. For the baseline $N_r=18$ configuration, the propellers are arranged in a radial multicopter layout and distributed circumferentially around the fuselage. The total lifting area A is the sum of 18 independent propeller disks, each with a diameter of D_r. Similarly, the total thrust T is the sum of per-propeller thrust T_r. A first–order weight closure is used to connect empty mass m_e to total mass m_0 through an empty–mass fraction model. Classical aircraft conceptual design often uses log-log regression models of the form (Roskam, 1987):

$$log(m_0)=Alog(m_e)+B$$

where A and B are empirically fitted coefficients for a vehicle class and technology level. For the UCM-Multicopter, this equation is treated as an initial closure relationship, not as a definitive prediction. The coefficients

should be updated when a community dataset of multicopter designs becomes available. The total mass is decomposed into empty mass (m_e), payload mass (m_{pl}), and energy storage mass (m_{bat}):

$$m_0 = m_e + m_{pl} + m_{bat}$$

Substituting the mass decomposition into the closure relationship yields the nonlinear equation in m_e,

$$f(m_e) = A\log(m_e) + B - \log\left(m_e + m_{pl} + m_{bat}\right) = 0$$

This equation is solved iteratively using Newton's method (Algorithm 1). The iteration is robust for positive masses if the initial guess is chosen conservatively (e.g., $m_e^{(0)} \approx 2\left(m_{pl} + m_{bat}\right)$). Newton's method updates m_e as:

$$m_e^{(k+1)} = m_e^{(k)} - \frac{f\left(m_e^{(k)}\right)}{f'\left(m_e^{(k)}\right)}$$

where:

$$f'(m_e) = \frac{A}{m_e} - \frac{1}{m_e + m_{pl} + m_{bat}}$$

The key multicopter adaptations relative to conventional airplane/tilt–rotor methods are: (1) fixed lifting surfaces (wing and tail) are omitted ($m_w = m_t = 0$) for a wingless multicopter baseline; (2) landing gear is treated as skid gear by default, with retractable gear left as an optional increment; (3) propulsion and electrical masses are replicated across N_r rotors, and feasibility checks are applied at the per–rotor level. The UCM workflow uses the first–order solver for rapid closure and the second–order build–up for diagnostic mass breakdowns and identification of key drivers (arms/booms, wiring, and propulsor replication). In future work, the empty mass fraction coefficients (A, B) can be re–estimated from an open dataset of multicopter designs to reduce epistemic uncertainty. In practice, the stopping criterion is expressed as a relative tolerance scaled by ($m_{pl} + m_{bat}$) to avoid over-solving under uncertain input assumptions. Battery mass is not an independent input; it depends on mission energy, which in turn depends on total mass through required thrust. To maintain a simple coupling, battery mass is computed from a pack–level specific energy e_{bat} (including packaging overheads) as:

$$m_{bat} = \frac{E_{req}^{\star}}{e_{bat}}$$

with e_{bat} expressed in Wh/kg or J/kg. The second–order model decomposes m_e into major component groups:

$$m_e = m_{str} + m_{\text{prop}} + m_{elec} + m_{av} + m_{\int} + m_{misc}$$

where m_{str} is the structural mass (fuselage + arms/booms + landing gear), m_{prop} is propulsor hardware (rotors/propellers, hubs, mounting), m_{elec} is electrical powertrain hardware (motors, inverters/ESCs, distribution, wiring), and the remaining terms represent avionics, interiors, and miscellaneous systems. For a wingless UAM multicopter, the fuselage is treated as a pressure-less cabin shell with crashworthiness and occupant protection drivers. A fuselage scaling relationship can be adapted from empirical transport formulations by interpreting the cabin length and perimeter as proxy measures of shell area. The baseline model therefore retains the structure of Roskam–style regressions [9] while using multicopter–appropriate margins:

$$m_{fus} \propto (m_0)^{\alpha_f} \left(\frac{l_f}{p_{max}}\right)^{\beta_f} l_f^{\gamma_f} N_{occ}^{\delta_f}$$

where l_f is fuselage length, p_{max} is maximum cross–section perimeter, and N_{occ} is occupant count. For the UCM baseline we treat this relation as a calibrated placeholder: coefficients are documented and can be replaced by future

community calibration. To reflect crashworthiness and certification conservatism at conceptual stage, a structural margin factor $k_{cr} \in [1.05,1.20]$ may be applied:

$$m_{fus}^{\star}=k_{cr}m_{fus}$$

Multicopter arms/booms carry rotor thrust and the mass of motors/propellers at offsets from the fuselage. A first–principles sizing proxy is derived by modeling each arm as a cantilever beam of length l_b with a tip load F_b and tip mass m_{tip}. The root bending moment is approximated as:

$$M_b \approx F_b l_b + m_{tip} g l_b$$

where F_b is the rotor thrust load routed into the arm. For a simple thin–walled circular tube of outer radius R and wall thickness t, bending stress is:

$$\sigma_b \approx \frac{M_b R}{I}, I \approx \pi R^3 t$$

assuming $t \ll R$. Selecting an allowable stress σ_{allow} yields a required thickness:

$$t \approx \frac{M_b}{\pi R^2 \sigma_{allow}}$$

The corresponding mass of one boom is $m_b=\rho_{mat}(2\pi Rt)l_b$, and total boom mass is the sum over booms. This physics–based proxy allows explicit scaling with rotor thrust and arm length. It is also worth noting that the possible radial component of the thrust and the torsional loads generated during rotor operation are neglected, as they are considered significantly smaller than the bending stresses. The potential buckling on the compressive side of the arm is also neglected to simplify the preliminary design of the boom.

The UCM–Multicopter baseline adopts skid landing gear by default for simplicity and reduced weight. Landing gear mass is modeled as a function of gear length l_{lg} and load factor n_{lg} with an empirical regression:

$$m_{lg} \propto l_{lg}^{\alpha_{lg}} \left(m_0 n_{lg}\right)^{\beta_{lg}}$$

Retractable gear and fairings can be introduced later as optional increments.

For conceptual sizing, propeller mass is related to diameter and transmitted power. A commonly used regression form is

$$m_{\text{prop}} \propto \left(\frac{D_r P_{per}}{N_{blade}}\right)^{\alpha_p}$$

where P_{per} is per–rotor power and N_{blade} is blade count. The constant and exponent are treated as tunable parameters reflecting manufacturing technology (composite blades vs metal).

Electrical powertrain mass includes motors, inverters/ESCs, and wiring. Here, they are expressed as:

$$m_{mot}=N_r m_{mot,1}\left(P_{rated,1}\right)$$
$$m_{esc}=N_r m_{esc,1}(I_{max}, V_{bus})$$
$$m_{wire} \approx \rho_{Cu} \sum_k A_k L_k$$

where $m_{mot,1}$ and $m_{esc,1}$ are selected from a component database with a consistent schema documenting each component's attributes, and wiring is computed from conductor cross–section A_k and length L_k for each harness segment k. The explicit wiring expression supports load and thermal checks and improves reproducibility compared with a single lumped "electrical fraction".

Power and performance estimation

Performance modeling is kept low-order but physically interpretable, emphasizing hover power, climb power, and cruise power. Based on actuator disk momentum theory, ideal induced power in hover is:

$$P_{ind,ideal}=\frac{T_r^{3/2}}{\sqrt{2\rho A_r}}$$

where $N_r T_r \approx W$ in hover, ρ is air density, and A_r is the propeller disk area. The actual induced power is corrected by a figure of merit (hover efficiency) FM:

$$P_{ind}=\frac{P_{ind,ideal}}{FM}$$

FM depends on rotor design and interference; conceptual studies typically assume $FM \in [0.65, 0.80]$ for small, distributed rotors, with lower values reflecting higher profile and interaction losses. A simple profile power approximation for a set of N_r rotors is:

$$P_{pro} \approx N_r \left(\frac{\sigma C_{d0}}{8}\right) \rho A_r (\Omega R)^3$$

where σ is rotor solidity, which is a function of number of blades, blade chord, and rotor radius. C_{d0} is the blade section drag coefficient, Ω is rotor angular speed, and $R=D_r/2$. Parasite power (fuselage and exposed structures) in forward flight is modeled using an equivalent flat plate area A_f:

$$P_{par}=\frac{1}{2}\rho V^3 A_f$$

In multicopters, parasite drag can be significant due to exposed booms and landing skids; therefore A_f is treated as an explicit calibration parameter rather than being embedded in a generic drag coefficient. For a wingless multicopter in steady, level forward flight, the thrust vector must provide both weight support and drag balance. If the net thrust magnitude is T and drag is D, the force balance implies:

$$T=\sqrt{W^2+D^2}, D \approx \frac{1}{2}\rho V^2 f$$

This relation links cruise power to airframe drag and makes clear that improving drag area has a direct impact on energy consumption. The total shaft power is evaluated by using segmented power models. For the present baseline, the following segment models are used:

Hover/take-off/landing: $P_{hover} \approx P_{ind}+P_{pro}$

Climb: $P_{climb} \approx P_{hover}+WV_c$ where V_c is the climb rate.

Cruise: $P_{cr} \approx P_{ind,ff}+P_{pro}+P_{par}$

with thrust from the cruise force balance. In the absence of a detailed edgewise-inflow model for forward flight, the induced-power term is approximated as a fixed fraction of hover induced power:

$$P_{ind,ff}=k_{ff}P_{ind}, k_{ff}=0.35$$

The value $k_{ff}=0.35$ is adopted as a conservative low-order approximation for the present baseline, reflecting the reduction in induced power once the multicopter is in translating flight. For the worked example, this gives a forward-flight induced-power term on the order of 45 kW.

Reserve can be represented as either a fixed fraction f_{res} or as a prescribed time t_{res} at a specified power (hover, cruise, or loiter). For electrical architecture, reserve definition has a strong impact on feasibility: time-based hover reserves can dominate the battery mass. This paper therefore reports sensitivity to reserve policy in Section 3.

A key feature of the UCM baseline is an electrical feasibility layer that translates power requirements into a physically consistent electrical architecture. The purpose is twofold: (1) enforce that currents, voltages, and component ratings remain within reasonable bounds for the selected technology assumptions; (2) provide reproducibility: an explicit component database and selection algorithm ensure that other users can recreate the same architecture and mass roll–up. Let the peak electrical power required per rotor be $P_{el,1}$ (including margins). For a DC bus voltage V_{bus}, the per–rotor current is approximately:

$$I_1 \approx \frac{P_{el,1}}{V_{bus}}$$

The total current drawn from the battery bus depends on the architecture (central bus vs. segmented buses). High currents motivate higher bus voltages to reduce conductor cross–section and resistive loss. For safety and certification considerations, voltage selection is constrained by insulation requirements, connector technology, and maintainability. The UCM–Multicopter adopts a deterministic parts selection approach: given required per–rotor power and a design bus voltage, the algorithm selects the lightest feasible combination of (battery modules, motors, ESCs/inverters, and PDB hardware) from a database, subject to constraints. The deterministic nature is central to reproducibility: the same inputs must yield the same selected set. The selection approach can later be replaced by optimization (e.g., integer programming) without changing the surrounding aircraft-sizing framework, provided the interface remains stable. With N_r>4, a multicopter is typically over-actuated: there are more independent thrust actuators than controlled degrees of freedom. Control allocation maps a desired force/moment vector $u \in \mathbb{R}^6$ to propeller thrust commands $T \in \mathbb{R}^{N_r}$.

For the baseline N_r=18 radial configuration, the 18 propellers are distributed around the fuselage and provide independent thrust channels. Assuming each rotor produces thrust T_j along direction n_j and a reaction torque τ_j about its axis, the net force and moment of the CG are:

$$F = \sum_j T_j\, n_j$$

$$M = \sum_j r_j \times \left(T_j n_j\right) + \sum_j \tau_j n_j$$

The minimum-norm allocation is

$$T^{\star} = B^{\dagger} u$$

where $B \in \mathbb{R}^{6\times 18}$ is the control effectiveness matrix. In practice, constrained allocation handles actuator limits and failure cases:

$$\min_T \| W(T - T_0) \|^2 \; s.t. \; BT = u, T_{min} \le T \le T_{max}$$

This section presents a worked example for the UCM–multicopter baseline with N_r=18 propellers in a conventional radial multicopter layout. The numerical values are illustrative: they demonstrate how the sizing workflow closes and how key assumptions propagate into mass and energy, rather than representing a validated product configuration. Before examining the worked-example closure, the baseline is positioned against representative public-domain multicopter demonstrators for context and comparison.

Input	*Symbol*	*Value*
Propeller count	N_r	18
Rotor diameter [m]	D_r	2.3

Input	*Symbol*	*Value*
Figure of merit (hover)	FM	0.75
Equivalent flat plate area [m²]	f	3.0
Occupants (passengers + pilot)	N_{occ}	3 (2 pax + 1 pilot)
Mass per occupant (incl. baggage) [kg]	m_{occ}	90
Payload mass [kg]	m_{pl}	270
Reserve fraction	f_{res}	0.20
Pack specific energy [Wh/kg]	e_{bat}	230
Overall efficiency	η_{all}	0.85

Table 2.11: Baseline modeling assumptions and outputs.

Table 2.11 summarizes the baseline assumptions to generate the worked example, and the resulting vehicle attributes. Unless stated otherwise, the mission is assumed to be a short UAM mission with a reserve fraction f_{res}=20% and an overall drivetrain efficiency η_{all}=0.85 (battery to rotor). The pack-level battery specific energy is set to 230 Wh/kg, reflecting a near-term achievable value once packaging, thermal management, and battery-management-system (BMS) overheads are included. The mission timing is parametrized such that cruise time is approximately R/V_{cr} and VTOL segments represent a few minutes of combined take-off, climb, approach, and landing hover. For this example, the resulting required mission energy including reserve is approximately $E^{\star}_{req} \approx$ 121 kWh.

Benchmarking against representative public-domain multicopters

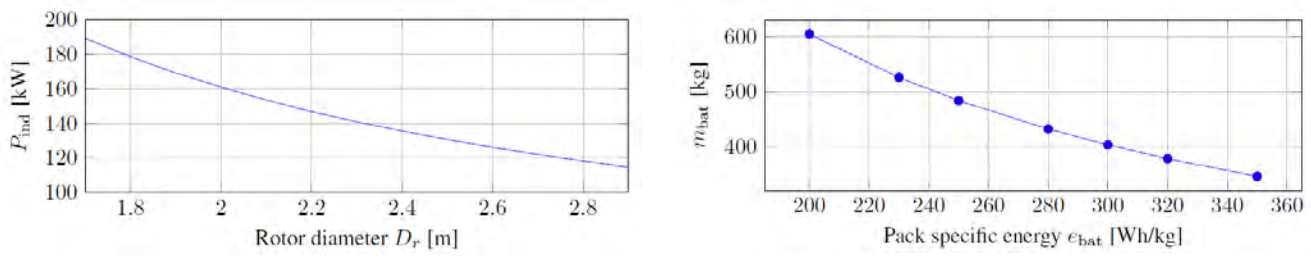
To situate the UCM baseline, its mission and top-level characteristics are compared in Table 2.12 against two well-known multicopter demonstrators, the Volocopter VoloCity and the EHang 184, not to rank them, but to place the baseline within the current multicopter UAM design space and to show how its mission assumptions differ from short-range certified air-taxi and earlier single-occupant concepts. Public specifications vary across sources and prototype revisions, so these values are contextual references rather than certification-grade benchmarks: published range may be operational (with reserves) or best-case nominal, and published power may be installed peak electrical rather than sustained shaft power.

Vehicle	*Pilot*	*Pax*	*Propellers*	*Range [km]*	*Cruise [km/h]*	*MTOM [kg]*
UCM-MC baseline	1	2	18	55	100	1210
VoloCity	0-1	1-2	18	20-35	90	900-1000
EHang 184	0	1	8	30-40	100-130	360-620

Table 2.12: Benchmark comparison between the UCM multicopter baseline and representative public-domain multicopter demonstrators.

The comparison shows that the UCM baseline is more ambitious than both demonstrators in nominal mission range while retaining a multicopter configuration. Relative to VoloCity, the UCM baseline assumes one additional occupant and a significantly longer mission, which helps explain the stronger battery-mass sensitivity observed in the worked example. Relative to EHang 184, the UCM baseline moves from a single-occupant demonstrator class toward a multi-occupant UAM baseline and therefore should not be interpreted as a one-to-one product analogue. This positioning reinforces the role of the UCM as a common reference model: it is intended to sit within the demonstrated multicopter design space while remaining sufficiently extensible to support future variants and mission-driven scaling studies. Using the sizing loop within the corrected radial baseline produces a converged notional mass closure of $m_0 \approx$ 1210 kg, $m_{bat} \approx$ 525 kg, $m_{pl} \approx$ 270 kg, $m_e \approx$ 415 kg. Two first–order sensitivities are

reported here: rotor diameter (disk loading) and battery specific energy. Figure 2.13-a shows hover power as a function of rotor diameter for fixed m_0=1210 kg, N_r=18, and FM=0.75, with a constant profile loss placeholder. Larger rotors reduce induced power by increasing total disk area, but may increase structure, noise footprint, and packaging constraints.



(a) (b)

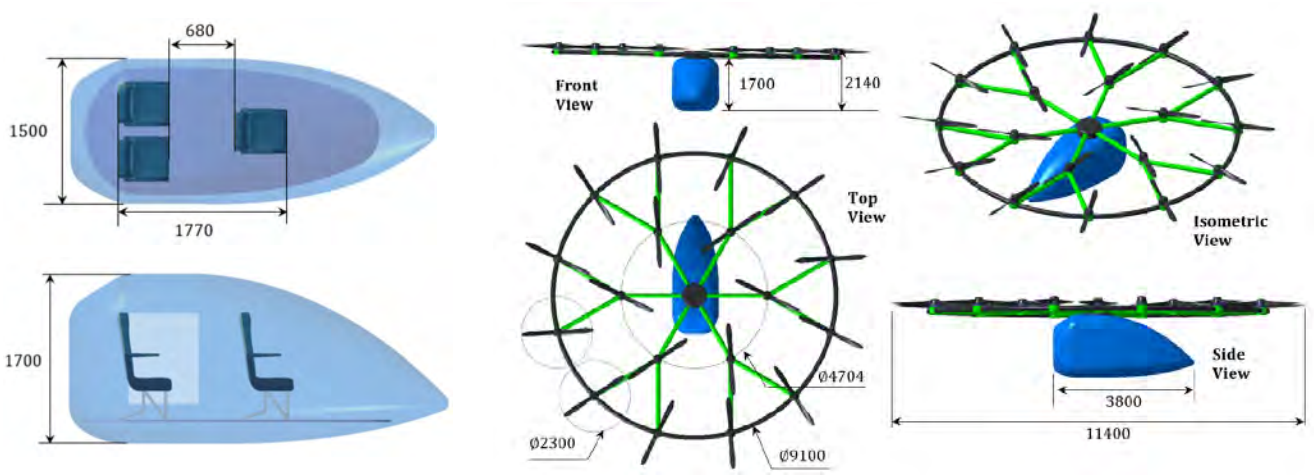
Figure 2.13: a) Sensitivity of induced hover power to rotor diameter for the 18-propeller radial multicopter baseline, with m_0= 1210 kg and FM= 0.75. Larger propellers reduce induced power by increasing total disk area, but may increase structure, noise footprint, and packaging constraints; b) Battery mass required for a fixed mission energy $E^{\star}_{req}$ 121 kWh as a function of pack-level specific energy. The present baseline adopts e_{bat}230 Wh/kg, which gives $m_{bat} \approx$ 525 kg.

Battery mass scales inversely with pack specific energy. Figure 2.13-b shows the battery mass required for $E^{\star}_{req}$=121 kWh across a plausible near–term range of pack specific energies. The N_r=18 configuration is over-actuated for 6-DOF control. The control effectiveness matrix, $B \in \mathbb{R}^{6\times 18}$, is exported in the aircraft specification interface so that downstream simulation environments can reproduce the same allocation behavior. In the conventional radial layout, each propeller contributes through a distinct position vector and spin direction, and redundancy arises from the availability of 18 independent thrust channels. A practical design implication is that redundancy can be used in multiple ways, including fault tolerance, load management, and noise management. Regarding fault tolerance, if one rotor fails (T_j=0), the remaining rotors can often satisfy the desired u with small performance degradation. For load management, constrained allocation can reduce peak boom/root loads by avoiding high thrust on rotors with large moment arms. Moreover, the distributed thrust design gives flexibility in shaping thrust distribution to avoid high tip Mach numbers and the following strong interaction tone, consistent with the motivation of noise-aware design frameworks [6]. These control–allocation DOFs further motivate the necessity of treating rotor layout and effectiveness as first–class data, not as an implicit “multicopter mixer”.

Configuration and Model Development

Following the sizing results, a three-dimensional geometric model of the UCM multicopter (UCM-MC) was developed (Figure 2.14) as a simplified, physically consistent CAD model reflecting the principal parameters from the conceptual phase. Fuselage dimensions were set from the cabin volume needed for one pilot and two passengers, giving a first-order cabin envelope compatible with typical UAM ergonomic and layout constraints.

As previously mentioned, the resulting UCM-MC configuration features eighteen electrically driven propellers arranged in a distributed propulsion architecture using a conventional radial multicopter layout. The propulsive units are distributed circumferentially around the fuselage to provide a balanced lifting footprint and symmetric control authority. Figure 2.14 presents the overall configuration of the proposed multicopter aircraft along with the principal geometric dimensions. The vehicle is designed to accommodate two passengers in addition to the pilot while maintaining a compact configuration suitable for short-range UAM operations. Under the UCM framework, the same fuselage forebody will be used in parallel vehicle designs featuring lift+cruise and tiltrotor architectures.



(a) (b)

Figure 2.14: a) Preliminary fuselage sizing based on the cabin capacity requirement for three occupants (2 pax + 1 pilot); b) Overall configuration and principal geometric dimensions of the proposed UCM-Multicopter (UCM-MC) aircraft in its conventional radial 18-propeller layout. Dimensions are in millimeters (mm).

3 Rotor Aerodynamics and Aeroacoustics

This chapter examines the aerodynamic and aeroacoustic behavior of eVTOL propulsion systems, with a focus on rotor–airframe interactions, noise generation mechanisms, and fast prediction methods. Building on the common reference vehicles introduced in Chapter 2, the contributions collected here explore how rotor performance, wake development, and acoustic signatures are affected by installation effects, unconventional blade geometries, and unsteady inflow conditions. Rather than addressing isolated propellers, the studies emphasize interaction-driven behavior, where aerodynamic performance and noise are shaped by the proximity of other rotors, lifting surfaces, pylons, and the surrounding flow environment.

3.1 Fast Aerodynamic Assessment of Propellers

Manuel Casablanca, Andrea Magrini, Ernesto Benini

These vehicle designs rely on tightly integrated propeller-airframe architectures, necessitating precise aerodynamic modeling at reasonable computational cost. Within the DICUAM framework, several contributions therefore focus on reduced- and mid-fidelity approaches capable of capturing the main flow features at a fraction of the computational cost. A central approach explored is the body-force method (BFM), implemented through a RANS/BET formulation. In this method, the propeller is not geometrically resolved; instead, its aerodynamic effect is introduced as distributed source terms within a rotating region of the computational domain. These source terms are computed using Blade Element Theory (BET), which evaluates local lift and drag based on tabulated airfoil data and the instantaneous inflow conditions. The influence of the propeller on the flow is then incorporated by adding such source terms to the right-hand side of the RANS equations in the subsequent CFD iteration. This is schematically represented in Figure 3.15.

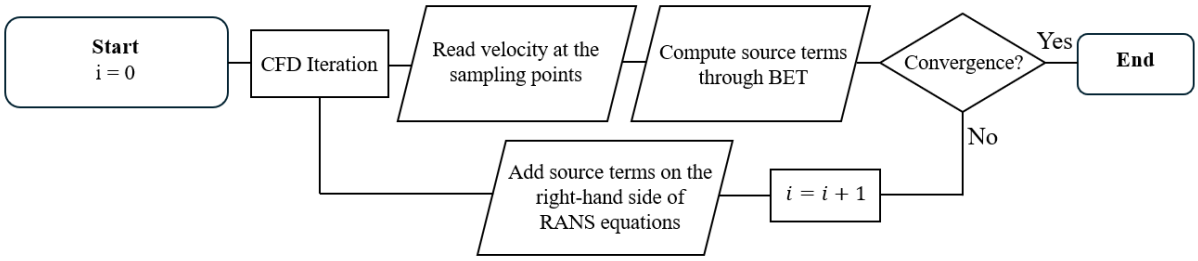
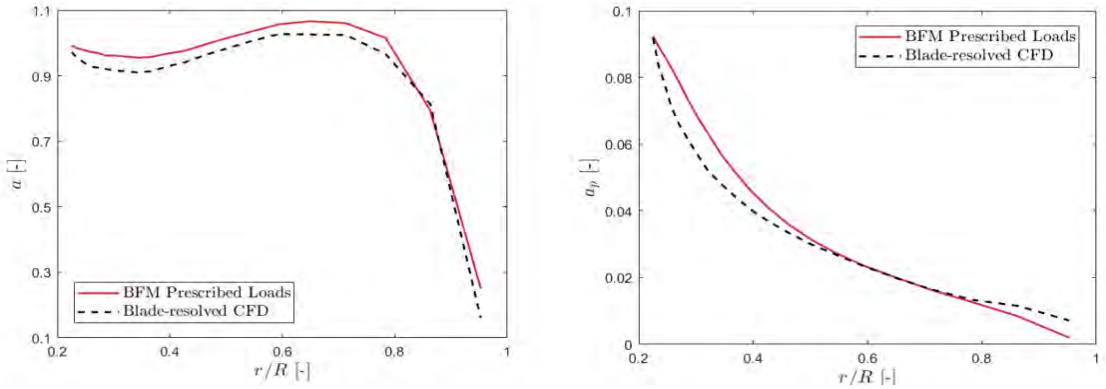


Figure 3.15: RANS/BET body-force workflow.

The local load at a given radial and azimuthal position *(r, θ)* is computed using the velocity vectors evaluated at a fixed number of sampling points on the propeller plane to determine the local angle of attack *AoA*. The corresponding lift and drag coefficients are then extracted from tabulated airfoil polars. The resulting lift and drag forces are subsequently projected onto the Cartesian coordinate system to obtain the local Cartesian force vector. Finally, after scaling the Cartesian force vector, the source terms are computed by distributing the force vector along the axial direction. Compared to blade-resolved CFD, the flow field predicted by the RANS/BET approach can be regarded as representative of the time-averaged solution over a complete propeller revolution, making it suitable for performance estimation and preliminary design. Additionally, this approach allows the simulation of non-uniform inflow conditions at the propeller, such as those resulting from incidence angles or installation effects. To assess the reliability of the proposed approach, the method is applied to a reference APC 9×6 propeller.

Application of the BFM for the propeller aerodynamic characterization

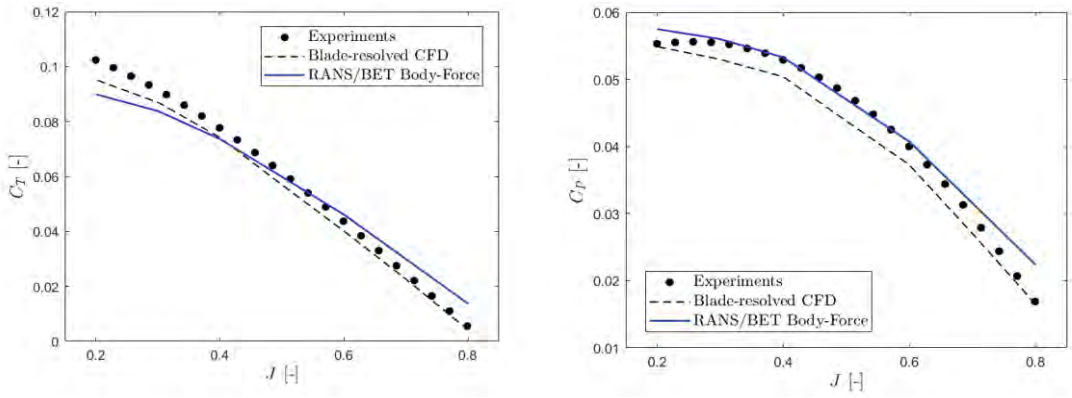
To assess the reliability and predictive capability of the RANS/BET body-force methodology, a small-scale APC 9×6 propeller is selected as the reference test-case. The first investigation is intended to examine the ability of the model to accurately reconstruct the resulting flow field when the exact propeller load distribution is supplied. To this end, the spanwise distributions of the axial and tangential loads were extracted from a blade-resolved CFD solution and supplied to the RANS/BET body-force framework. As a result, the momentum source terms at each RANS iteration are directly imposed from these data. As shown in Figure 3.16, the RANS/BET formulation successfully captures the behavior observed in the blade-resolved simulations for both axial and tangential induction factors, thus confirming that the body-force approach can reconstruct the velocity field with high fidelity when the exact spanwise load distribution is imposed. Specifically, $a=\frac{V_{x,CFD}-V_\infty}{V_\infty}$ and $a_P=\frac{V_{t,CFD}}{\Omega r}$.



(a) (b)

Figure 3.16: Comparisons of spanwise distribution of axial (a) and tangential (b) induction factors for RANS/BET body-force with prescribed loads and 3D blade resolved CFD, at J = 0.2.

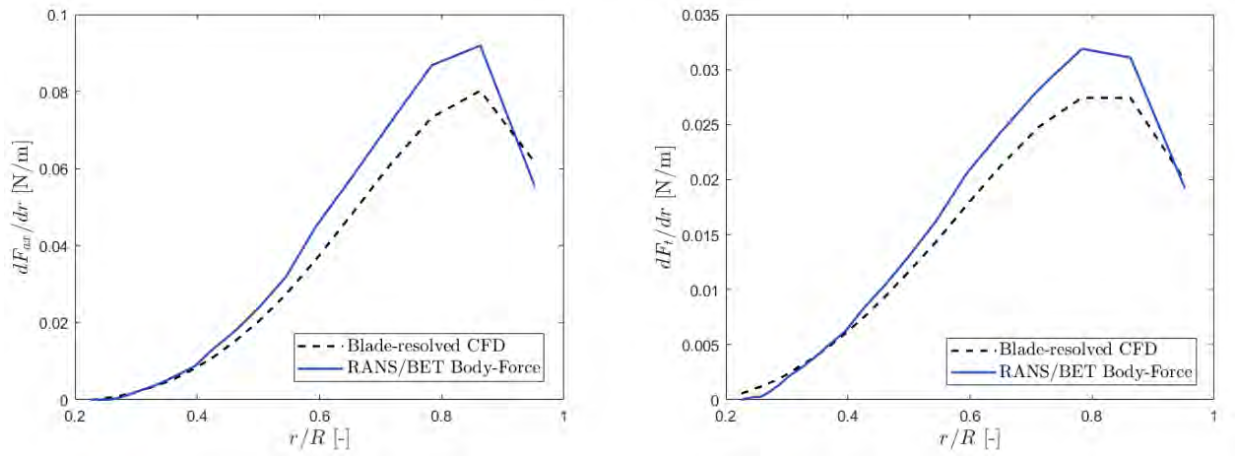
Nonetheless, a key advantage of the body-force method lies in its applicability without the need for high-fidelity data from blade-resolved CFD simulations. A crucial aspect in assessing the effectiveness of this approach is the investigation of its performance when the source terms are computed using the BET routine, thereby relying on tabulated 2D airfoil polar data. In this regard, the BFM prediction of the variation of the thrust coefficient with advance ratio is in good agreement with both experimental data and blade-resolved CFD, as shown in Figure 3.17.



(a) (b)

Figure 3.17: Comparisons of performance parameters C_T (a) and C_P (b) versus advance ratio for RANS/BET body-force implementation versus blade-resolved CFD and experimental data.

Specifically, the body-force method slightly underestimates the thrust coefficient compared to blade-resolved CFD at low advance ratios. Similarly, the body-force method closely reproduces the experimental power coefficient. To further investigate the discrepancies between the solutions provided by the body-force method and the blade-resolved CFD, it is relevant to compare the spanwise distributions of axial and tangential loads. Figure 3.18-a shows that the present body-force method reproduces the spanwise distribution of the axial load with sufficient fidelity at $J = 0.2$. However, the body-force method slightly underpredicts the total thrust compared to the blade-resolved CFD results. This underestimation can be attributed primarily to the deficit in the inboard region of the blade. These findings suggest that the BET routine should include a model that accounts for the lift augmentation near the blade hub, resulting from the strong three-dimensionality of the flow, particularly for highly-loaded operating conditions. As shown in Figure 3.18-b, although the body-force method underestimates the tangential force in the inner portion of the blade, the integral tangential force is overestimated compared to the blade-resolved CFD results, leading to an overprediction of both torque and power. In this regard, the overestimation is primarily driven by the overprediction of the load in the outboard region of the blade.



(a) (b)

Figure 3.18: Comparison of the spanwise distributions of axial and tangential forces at J = 0.6 for RANS/BET body- force implementation versus blade-resolved CFD: (a) axial force spanwise distribution, (b) tangential force spanwise distribution.

Figure 3.18 presents the spanwise distributions of the loads at $J = 0.6$, corresponding to an operating condition close to the design point. Under such conditions, the body-force method does not exhibit any underprediction of either the axial or the tangential loading in the inboard region of the blade. This behavior is consistent with the negligible lift augmentation phenomenon when the rotor operates under less heavily loaded conditions. Additionally, Figure 3.18 highlights that the overestimation of both axial and tangential load distributions in the outer blade region is still observed at $J = 0.6$. This result can be attributed to an inadequate correction method for tip-loss effects within the BET routine. Although the present body-force framework incorporates the Glauert correction for tip-loss modeling, such a correlation corrects only the induction factors. Therefore, the present investigation suggests that it would also be necessary to correct the aerodynamic coefficients extracted from the airfoil polars in order to properly model the load reduction in the outer blade region toward the tip. Nevertheless, this approach already proves to be highly reliable for the analysis of propeller aerodynamic performance. Owing to its capability to handle both uniform and non-uniform inflow conditions, as well as isolated and installed operating configurations, the present approach represents a valuable tool for the design and optimization of propellers featuring tight geometric integration with the airframe, where current state-of-the-art low-fidelity methods still present notable limitations.

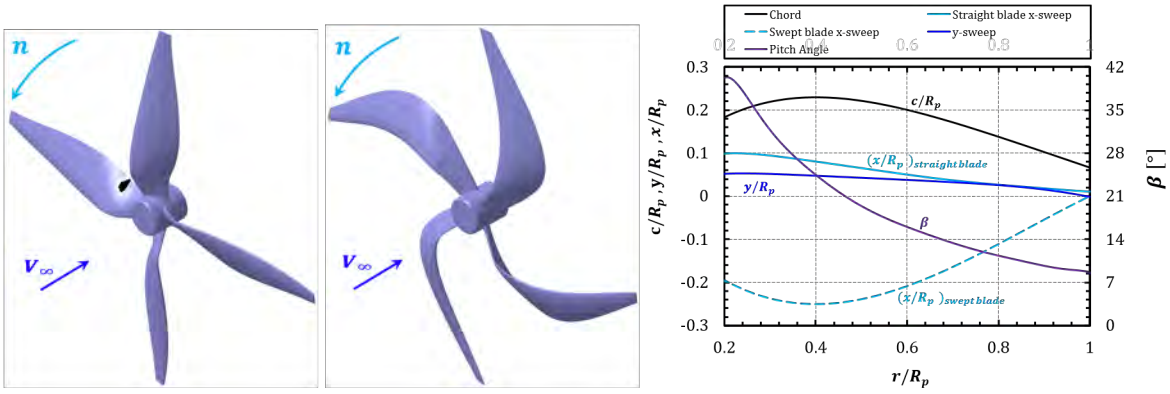
3.2 Rotor blade concepts explored in DICUAM

Kangni Combey, Omer Ali Elsayed, Khaoula Qaissi, Mohamed Achraf El Gadi, Hajar Chouiyakh, Mustapha Faqir

Propeller-driven configurations are favored for their superior performance at low altitudes and in low Reynolds number regimes (Bergmann et al., 2024; Riboldi & Gualdoni, 2016). Propeller design adapted to UAM missions is a central topic. Among the several explored concepts, swept and toroidal propellers have been central.

Swept Blades

Starting from swept blades, the concept has been recently investigated for eVTOL applications. Backward-swept blades have dominated propeller designs because of their proven aerodynamic benefits at higher speeds and favorable noise characteristics (Hwang et al., 2024; Jeracki et al., 1979; Jeracki & Mitchell, 1981). However, for eVTOL operations characterized by low-to-moderate speeds and stringent noise constraints, the aerodynamic trade-offs of backward sweep may not always be optimal. In contrast, forward-swept blades have received limited attention in propeller applications. Although forward-swept is often considered disadvantageous based on conventional swept-wing theory, several studies (Krone, 1980; Seitz et al., 2011) indicate potential aerodynamic benefits that warrant investigation for propellers. In this section, analysis of the aerodynamic performance of a forward-swept propeller operating at low Reynolds number is presented as from the DICUAM framework. A numerical investigation is conducted on a forward-swept four-bladed propeller and compared with a conventional straight-bladed configuration, evaluating aerodynamic performance and wake characteristics to assess its potential for UAM applications. A straight four-bladed propeller in Figure 3.19-a was designed to deliver the same thrust as a previous benchmarked study for low-Reynolds number from TUD (Grande et al., 2021) at identical operating condition, while keeping identical chord distribution, and diameter. The blade is connected to the hub via elliptical sections for $r/R_p < 0.2$. The blade geometry characteristics, chord, sweep and pitch angle distributions are shown in Figure 3.19-c, with $\beta_{0.75Rp} = 12.3°$ and $c_{max} = 0.034$ m. The forward-swept 4-bladed propeller (Figure 3.19-b) was therefore design from the straight 4-bladed propeller, by applying tangential sweep to the blade as shown in the Figure 3.19-c.



(a) (b) (c)

Figure 3.19: Propeller Configurations: (a) Straight blade propeller (b) Forward-swept blade propeller (c) Blade characteristics.

For the present study aerodynamic performance were evaluated using a three-dimensional unsteady Reynolds-averaged Navier-Stokes (URANS) solver, with a *k–ω* SST turbulence model (Menter et al., 2003). The propeller rotation was modeled using a sliding mesh approach with a timestep defined as $\Delta t = 2\pi/(\omega B \Delta d)$, with $\Delta d = 15$, yielding $\Delta t = 2.5\times10^{-4}$ s, which corresponds to 6° rotation per time step and 60 timesteps per revolution. The rotational speed was fixed at 4,000 rpm, while the inflow velocity was varied between 0 and 12 m/s. The computational domain consisted of a rotating inner domain containing the propeller and a stationary outer domain

extending 15 R_p downstream with a diameter of 12.2 R_p (Figure 3.20). Boundary conditions included a velocity inlet, pressure outlet, zero-shear far-field boundaries, and no-slip blade surfaces. Domain coupling between rotating and stationary regions was enforced using sliding interfaces. An unstructured mesh with 20 inflation layers was generated to adequately resolve near-wall gradients. A mesh independence study was carried out but omitted for conciseness reasons. The final mesh Figure 3.20-b-c) consisted of approximately 7.4 million elements, with near-wall resolution maintained at $y^+ < 1$ over the blade surface. Each simulation was run for at least 10 propeller revolutions, and convergence was verified based on thrust and torque histories.

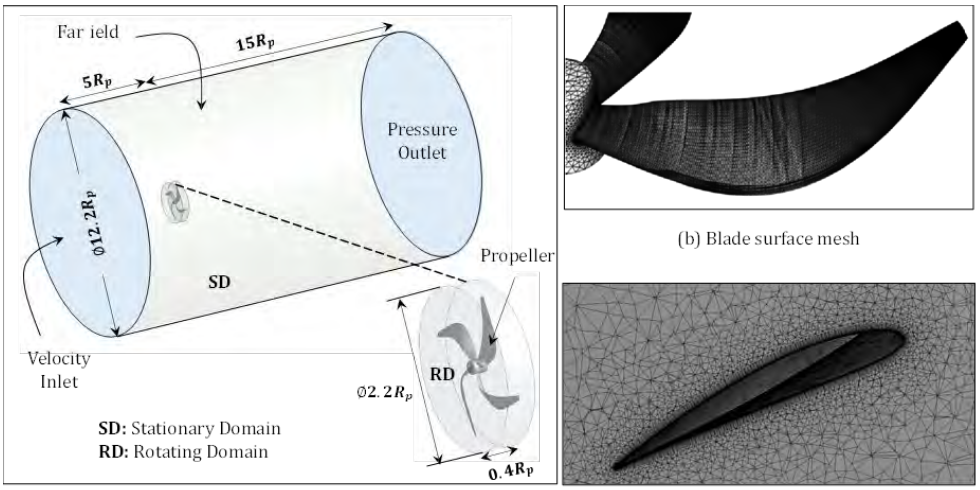


Figure 3.20: Computational domain and grid resolution showing the blade surface mesh and inflation layers around the blade section.

The propeller performance is characterized using non-dimensional parameters, namely the advance ratio $J = V_\infty/(nD_p)$, thrust coefficient $C_T = T/(\rho_\infty n^2 D_p^4)$, power coefficient $C_P = P/(\rho_\infty n^3 D_p^5)$ and propeller efficiency $\eta_{prop} = JC_T/C_P$.

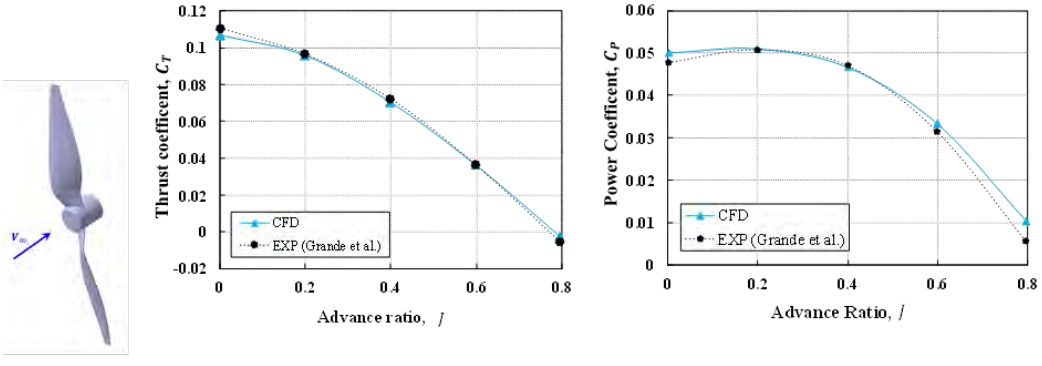
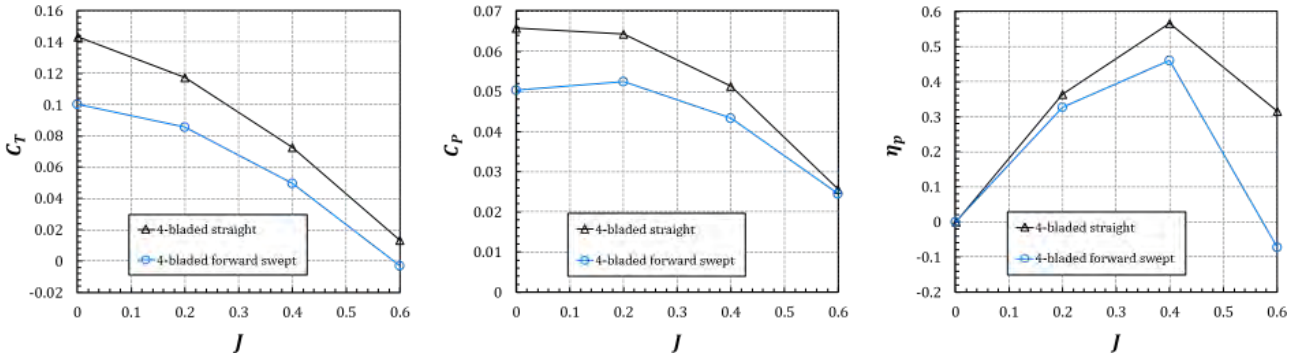


Figure 3.21: Comparison of numerical and experimental (Grande et al. [22]) results of the (a) Two-bladed propeller: (b) Thrust Coefficient, C_T and (c) Power coefficient, C_P versus advance ratio, J at 4000 rpm.

The thrust coefficient (C_T) and power coefficient (C_P) are presented in Figure 3.21 as functions of the advance ratio J. As evidenced by the comparison, the numerical predictions show good agreement with the experimental measurements, confirming the capability of the present numerical setup to accurately predict the aerodynamic performance of low Reynolds number propellers. Consistent with classical propeller performance theory, the thrust coefficient exhibits a parabolic trend with respect to the advance ratio, which is characteristic of small-scale propellers (see Figure 3.21-b). With increasing advance ratio, the thrust coefficient decreases due to the reduction

in the blade local effective angle of attack. Similarly, as shown in Figure 3.21-c, the power coefficient decreases with increasing advance ratio. This occurs because the blade-section angle of attack becomes progressively smaller, reducing aerodynamic effectiveness and generating less drag-induced torque. Consequently, the power required to drive the propeller decreases. The aerodynamic performance of the 4-bladed straight and tangentially forward-swept propellers is evaluated in terms of thrust coefficient (C_T), power coefficient (C_P), and propulsive efficiency (η_p). As shown in Figure 3.22-a, across the entire operating range, the forward-swept blade propeller exhibits lower thrust coefficients than the straight blade configuration. The difference is most pronounced at low advance ratios, corresponding to near-hover conditions. This behavior indicates that tangential forward-swept leads to a reduction in aerodynamic loading. By sweeping the blade, the inflow effective angle of attack changes and therefore decreasing the effective portion of the blade that may contribute to the thrust generation. As the advance ratio J increases, the thrust coefficient decreases for both propellers due to the increase in axial inflow velocity. In addition, the difference in C_T between the two propellers progressively decreases, suggesting a gradual unloading of the blades as axial inflow becomes dominant. The power coefficient (Figure 3.22-b) trends show that the forward-swept propeller consistently absorbs less power than the straight blade for a given advance ratio. This reduction in C_P reflects a modified aerodynamic loading distribution with reduced induced and profile losses typically associated with strong tip loading. The propulsive efficiency (Figure 3.22-c) curves show that despite the lower power coefficient of the forward-swept propeller, it is less efficient than the straight blade propeller. The aerodynamic mechanisms underlying the integral performance trends are clarified by the radial blade loading distributions at J = 0.4 shown in Figure 3.23. The straight blade exhibits a classical loading distribution, characterized by a gradual increase from the root to approximately r/R_p = 0.75–0.80, followed by a moderate unloading near the tip. This behavior is consistent with near-optimal circulation distributions predicted by momentum and lifting-line theories, enabling efficient thrust production while maintaining acceptable induced losses. In contrast, the tangential forward-swept blade displays a markedly different loading pattern.



(a) (b) (c)

Figure 3.22: Aerodynamic performance comparison between the forward-swept and straight propellers: (a) thrust coefficient C_T; (b) power coefficient C_P; (c) Propulsive efficiency η_p as functions of advance ratio J at n = 4000 rpm.

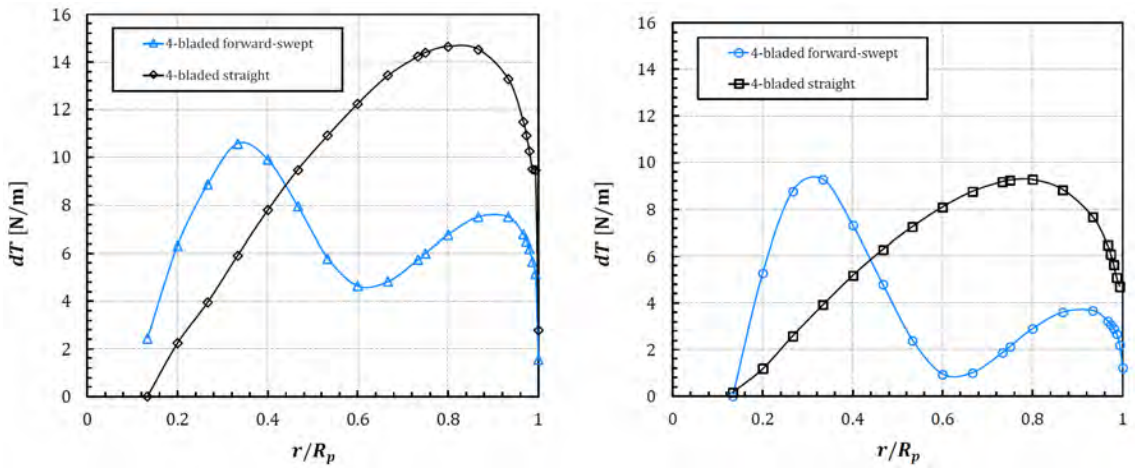


Figure 3.23: Spanwise distribution of sectional thrust for the forward-swept and straight blades at: (a) J = 0.2 and (b) J = 0.4.

A pronounced loading peak is observed in the inboard region ($r/R_p \approx 0.25$–0.35), followed by a significant mid-span unloading and a limited reloading toward the tip. The near-tip loading remains substantially lower than that of the straight blade. It is evident that the observed redistribution of aerodynamic loading results from the tangential sweep in the direction of rotation, which modifies the local relative inflow angles and produces spanwise pressure gradients along the blade. These effects promote induced flow components that shift circulation toward the blade root, thereby reducing the aerodynamic contribution of the outer blade sections.

Figure 3.24 illustrates the pressure coefficient (C_p) contours together with the corresponding chordwise sectional C_p profiles for the forward-swept and straight blades at four radial stations. At $r/R_p = 0.33$ (Figure 3.24-a, Figure 3.24-c), the forward-swept blade exhibits a significantly stronger suction peak on the suction side compared to the straight blade, as evidenced by both the higher low-C_p region in the contour plot and the deeper minimum in the sectional distribution. The pressure-side C_p is also higher, resulting in a larger pressure differential across the section. This indicates increased sectional loading in the inboard region for the forward-swept configuration. At $r/R_p = 0.44$ (Figure 3.24-d, Figure 3.24-f), the loading behavior changes markedly. The forward-swept blade exhibits clear attenuation of the suction peak. The contour plot shows a redistribution of the low- C_p region toward the lower surface, and the sectional distribution reveals a substantial reduction in pressure differential. The integrated area between the C_p distributions on the upper and lower surfaces of the two blade sections becomes similar, consistent with the sectional thrust in Figure 3.23, indicating convergence of the pressure loading. However, at $r/R_p = 0.60$ (Figure 3.24-g, Figure 3.24-i), the forward-swept blade exhibits a nearly inverted pressure distribution relative to the straight blade, indicating reduced local thrust in the mid-span region and lower C_p levels. At the outermost station, $r/R_p = 0.80$ (Figure 3.24-j, Figure 3.24-l), the distribution recovers a more conventional form but with weaker suction and pressure peaks than the straight blade, leading to a reduced pressure differential; the contour plots confirm a less concentrated suction region near the leading edge. Overall, the results demonstrate that while the forward-swept blade increases loading in the inboard region, it induces a substantial mid-span load inversion and a persistent reduction in outboard sectional loading. The cumulative effect of these mid- and outboard penalties explains the overall thrust deficit observed in the global performance and radial loading distributions. The forward-swept propeller (Figure 3.25-a-c) consistently shows a more compact high velocity core compared to the straight propeller (Figure 3.25-d-f) at all three non-dimensional axial positions $y/R_p = 0$, 0.5, and 1. With increasing downstream distance, the peak velocity magnitude decreases, and the contours become more diffused for both

configurations; however, the straight propeller maintains a wider radial extent of elevated velocity magnitude across the disk.

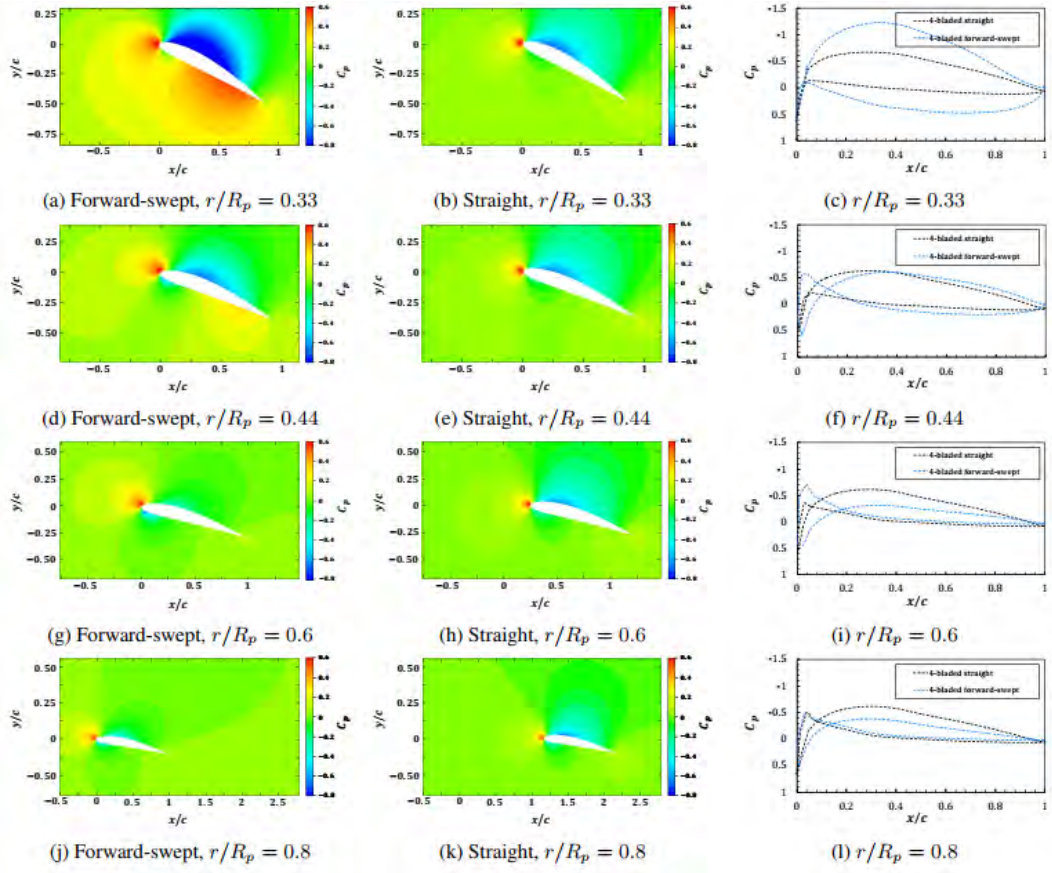


Figure 3.24: Pressure coefficient (Cp) distributions along the blade cross sections for the forward-swept and straight blades at (a–c) r/R_p = 0.33, (d–f) r/R_p = 0.44, (g–i) r/R_p = 0.60, and (j–l) r/R_p = 0.80.

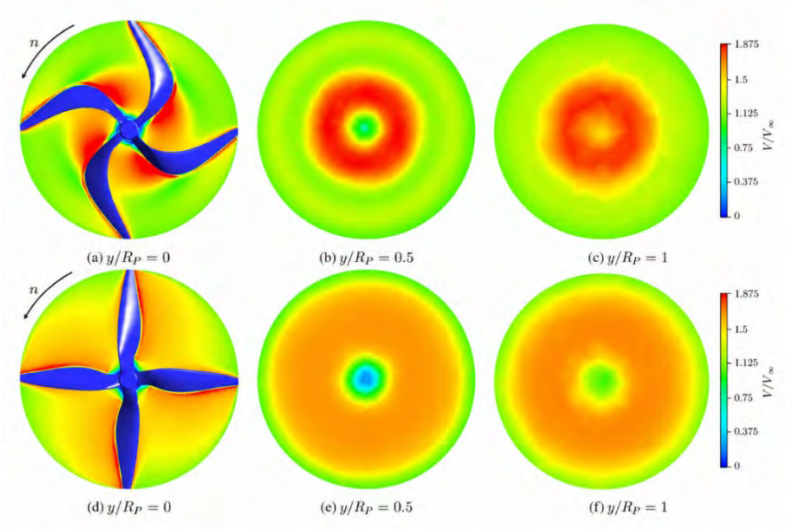


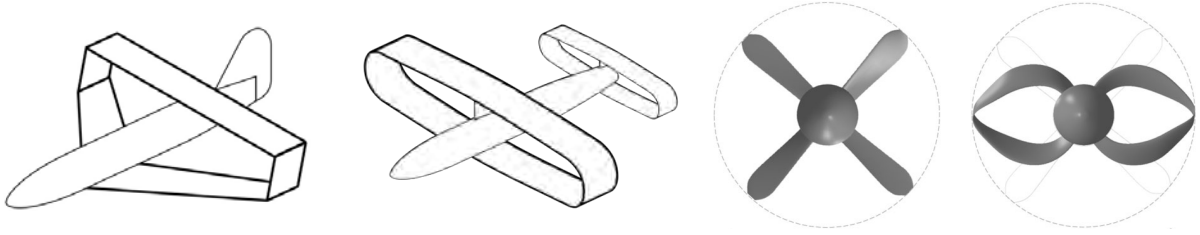
Figure 3.25: Velocity magnitude contours in downstream planes of the four-bladed forward-swept (a-c) and straight (d-e) propellers at non-dimensional axial positions y/R_p = 0.0, 0.5, and 1.0 at J = 0.4 and n = 4000 rpm.

The focus in DICUAM on the numerical aerodynamic investigation shows how tangential sweep modifies the local inflow direction and effective angle of attack, inducing spanwise pressure gradients that shift circulation toward the root. Although this redistribution has structural load alleviation aeroacoustic advantages associated with the dephasing effect of the scattering of the loading and thickness sources in the azimuthal direction, the sweep effect causes a pronounced inboard loading peak, mid-span unloading, and reduced outer-span contribution. Successful integration of forward-swept blades requires coordinated aerodynamic redesign, particularly spanwise twist and pitch optimization in the outer blade region to restore efficient loading and prevent reversed thrust tendencies. Overall, this work clarifies the aerodynamic mechanisms responsible for performance degradation in tangentially forward-swept propellers at low Reynolds numbers and provides a foundation for future optimization studies aimed at reconciling aerodynamic efficiency with structural and acoustic considerations in UAM propulsion systems.

Toroidal Joined Blade Tips Propeller

One of the primary sources of aerodynamic inefficiency and noise generation in propeller installation is the impingement of the coherent blade-tip vortices on the downstream structures. In the DICUAM2026 framework unconventional rotor concepts aimed at mitigating tip-vortex formation while maintaining or improving aerodynamic performance are explored. Among these emerging solutions, toroidal or tip-joined-blade propellers have attracted significant attention, suggesting potential noise reduction capabilities. By connecting adjacent blade tips into a continuous loop, these designs may eliminate the free blade tip responsible for vortex roll-up and modify the aerodynamic interactions occurring around the rotor. In the following, the aerodynamic characteristics of a novel toroidal tip-joined blade (T-JBT) propeller developed for potential eVTOL and Urban Air Mobility applications. Particular attention is given to understanding the flow mechanisms responsible for its performance relative to a conventional propeller. The T-JBT propeller originates from concepts previously explored in closed-wing and box-wing aircraft configurations, as shown in Figure 3.26-a-b, where connecting lifting surfaces increase the aerodynamic efficiency by reducing the strength of wingtip vortices and their associated induced losses. Extending this principle to rotating wings results in a looped-blade architecture in which adjacent blades are connected at their tips, forming a toroidal geometry. The investigated T-JBT configuration consists of two looped blades created by joining pairs of conventional propeller blades (Figure 3.26-d). Each loop comprises a forward blade and a rearward blade relative to the direction of rotation of the propeller. The resulting geometry eliminates free blade tips and introduces additional aerodynamic interactions between the forward and rearward sections of the loop.

The underlying hypothesis is that suppressing tip-vortex formation can reduce induced losses while simultaneously modifying the local flow field in a manner that maintains or enhances thrust generation. In addition, the closed-loop structure may provide increased structural rigidity compared with conventional cantilevered blades, potentially offering benefits for future lightweight eVTOL propulsion systems.



(a) (b) (c) (d)

Figure 3.26: Conceptual Design of a) Box Wing and b) Ring Wing. Comparison between c) Conventional F29 Propeller; d) T-JBT Propeller.

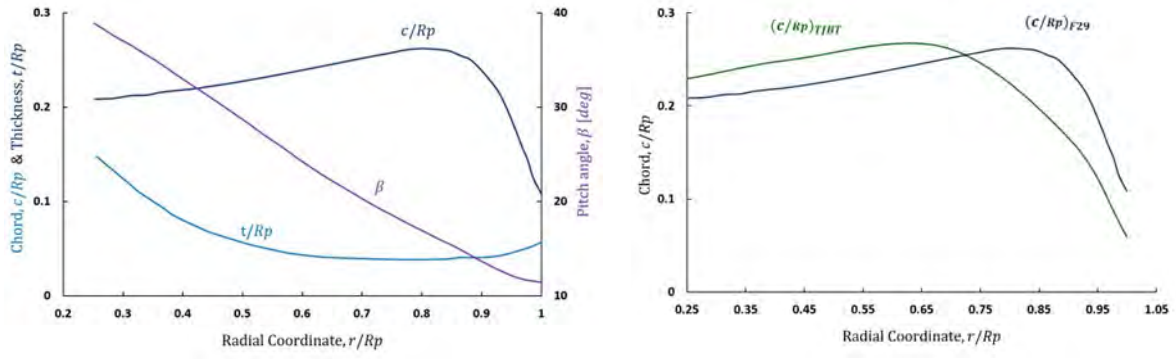
The novel T-JBT propeller, derives its name from the distinctive shape obtained by joining the tips of two conventional blades to create a looped blade in a toroidal form. The process involves connecting the tips of two

adjacent blades of a conventional propeller (see in Figure 3.26-c) at their mid-plane, resulting in the looped blade with no tip, as illustrated in Figure 3.26-d. This innovative design aims to mitigate the wasteful effects associated with wingtip vortices typically occurring at the tips of conventional blades. In this conceptual design, the geometry of the F29 propeller serves as the reference propeller for comparison purposes in order to assess the performance improvements introduced by the T-JBT propeller.

Value	J	V_∞ *[m/s]*	D_p *[m]*	R_h/R_p	$\beta_{0.7R_p}$ *[deg]*	$(c/R_p)_{Root}$	$(c/R_p)_{Tip}$
T-JBT	0.4	20	0.3048	0.28	20	0.21	0.23
F29					30	0.10	0.06

Table 3.13: Parameters of the two F29 and T-JBT propellers.

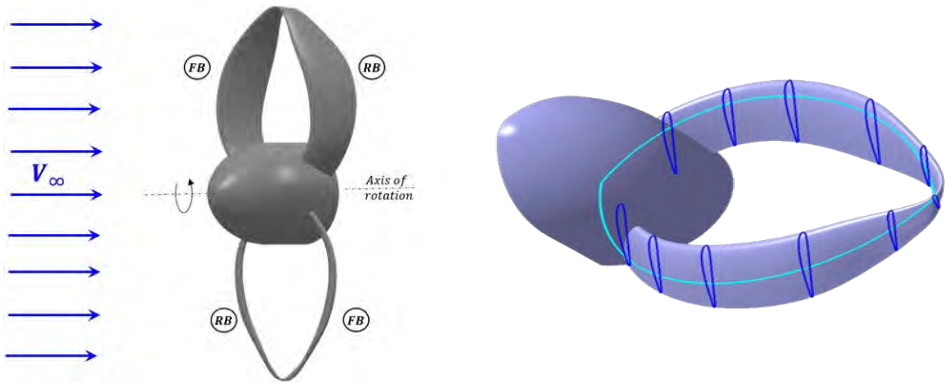
The propeller geometry employed in this study as baseline is the F29 propeller which has four blades with a diameter D_p = 304.8 mm and blade pitch of $\beta(0.7R_p)$ = 20 deg (Table 3.13). The propeller blade geometry characteristics are illustrated in Figure 3.27. The hub radius is $R_h = 0.28R_p$. This geometry was defined by the Fokker Aircraft Company for their internal F29 project (Stokkermans et al., 2021).



(a) (b)

Figure 3.27: Propellers characteristics: a) F29 Blade characteristics b) Chord distribution comparison.

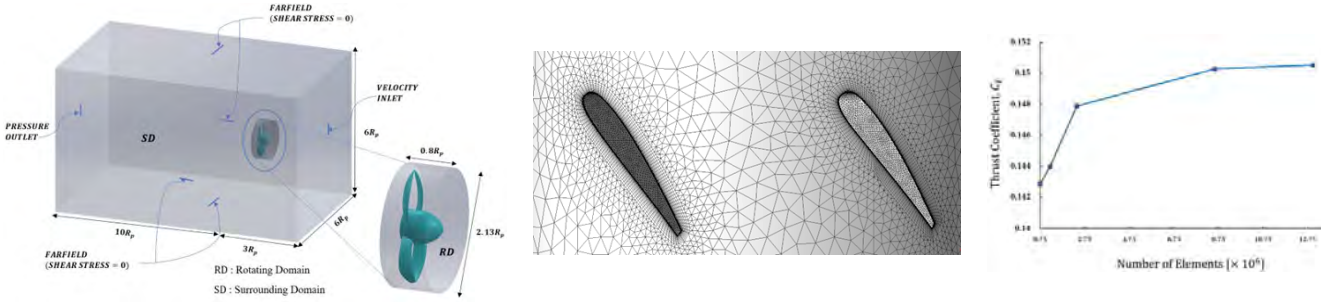
The T-JBT configuration consists of two looped blades with a constant pitch angle. Each looped blade is formed by joining two conventional blades at their mid-plane, resulting in a forward blade (FB) and a rearward blade (RB) relative to the direction of propeller rotation, as illustrated in Figure 3.28. For comparative study, the initial configuration employs two looped blades, which is equivalent to four conventional blades. The airfoils are distributed along predefined stacking lines and are characterized by specific chord, thickness, and pitch distributions. The aerodynamic center of each airfoil determined using XFOIL, was aligned with the stacking line. The airfoils were oriented such that they faced the incoming airflow directly, with no geometric incidence other than the local aerodynamic angle of attack, as illustrated in Figure 3.28-b. A symmetric airfoil was employed at the blade tip. At this stage of the investigation, no optimization was performed on either the blade geometric parameters or the number of blades. Furthermore, the pitch and chord distributions were intentionally kept identical for both the forward and rearward blades.



(a) (b)

Figure 3.28: T-JBT propeller with (a) airflow and propeller rotation. Forward blade (FB) and rearward blade (RB) relative to the direction of rotation; (b) Airfoils positioning along the blade.

To evaluate the aerodynamic behavior of the proposed concept, CFD simulations were performed for the T-JBT propeller and compared with those of the well-documented F29 propeller, which served as the reference configuration. Both propellers were analyzed under identical operating conditions, corresponding to a freestream velocity of 20 m/s and an advance ratio of J = 0.4. The numerical framework employed an unsteady Reynolds-Averaged Navier–Stokes (URANS) approach coupled with the *k-ωSST* turbulence model (Menter et al., 2003). A sliding-mesh technique was adopted to accurately capture the unsteady flow structures generated by the rotating blades. The computational domain is illustrated in Figure 3.29. The inlet and outlet boundaries were prescribed as a velocity inlet and pressure outlet, respectively, while the remaining boundaries of the stationary domain (SD) were defined as far-field conditions with zero shear stress. All propeller surfaces were treated as no-slip walls.



(a) (b) (c)

Figure 3.29: (a) Computational domain and boundary conditions; (b) Unstructured mesh, showing the inflation layers around the blade section; (c) Mesh convergence study for isolated propeller.

An unstructured mesh was generated, with grid density was controlled by face sizing and body refinement to accurately resolve near-wall and wake-flow structures. A mesh independence study was conducted and thrust coefficient was monitored as shown in Figure 3.29 demonstrated that an 8.6 million-element mesh provided an optimal compromise between numerical accuracy and computational cost. For the final adopted mesh, the blades were surrounded by 20 inflation layers with growth rate of 1.2 and first layer thickness, which serves the purpose of setting the y^+ value of 0.8, as depicted in Figure 3.29. The aerodynamic analysis employed URANS coupled with *k-ωSST* turbulence model, enabling the resolution of both the mean flow field and the dominant turbulent structures within the interacting slipstreams. The computational setup was first validated against available experimental measurements for the F29 propeller, providing confidence in the numerical predictions. The analysis focused on

both global performance metrics and detailed velocity flow-field characteristics to identify the aerodynamic mechanisms governing the observed behavior. The numerical results indicate a substantial increase in aerodynamic loading for the T-JBT configuration compared to the conventional F29 propeller. At the investigated operating condition, the T-JBT propeller achieves a 42% higher thrust coefficient (C_T = 0.212 vs 0.149), accompanied by a significant increase in torque coefficient (C_Q = 0.039 vs 0.018). The increase in thrust is primarily associated with the higher overall blade loading, which results from a combination of geometric and aerodynamic factors. In particular, the higher constant pitch angle of the T-JBT configuration contributes to an increased effective angle of attack, leading to higher sectional loading along the blade span. In addition, the looped blade topology potentially modifies the spanwise flow and induced velocity field, resulting in a redistribution of aerodynamic loading compared to the conventional finite-blade configuration.

However, the increase in torque is proportionally larger than the gain in thrust, which results in a significant reduction in propulsive efficiency. Based on the computed values, efficiency decreases from 52.7% for the F29 propeller to 34.6% for the T-JBT, corresponding to a relative reduction of approximately 34%. This reduction in efficiency indicates that the additional thrust is achieved at the expense of increased power requirement. From an aerodynamic perspective, this behavior can be attributed to higher blade loading, which increases profile and induced losses or blade-blade interaction between the forward and rearward segments of the loop. Therefore, while the T-JBT configuration demonstrates improved thrust-generation capability, it operates at a higher energy cost, highlighting a clear trade-off between thrust augmentation and propulsive efficiency (Table 3.14).

	C_T	C_Q	η
F29	0.149	0.018	52.7
T-JBT	0.212	0.039	34.6

Table 3.14: Performance parameters.

The flow structures obtained for both propellers reveal clear differences in blade aerodynamics and wake development. For the conventional F29 propeller (Figure 3.30-a–b), the flow remains largely attached over the suction side at both considered radial locations. The velocity distribution shows a smooth acceleration over the suction surface, with no significant flow irregularities observed. This behavior is characteristic of a moderately loaded blade operating under stable conditions. In contrast, the T-JBT configuration (Figure 3.30-c–d) exhibits a more complex flow topology. A strong interaction region is observed between the forward blade (FB) and rearward blade (RB), where locally elevated velocity levels are present. The flow is significantly accelerated along the suction sides of both blade segments, indicating increased aerodynamic loading compared to the conventional configuration. This acceleration is particularly pronounced in the region between the FB suction side and the RB pressure side, where the flow passage appears constricted.

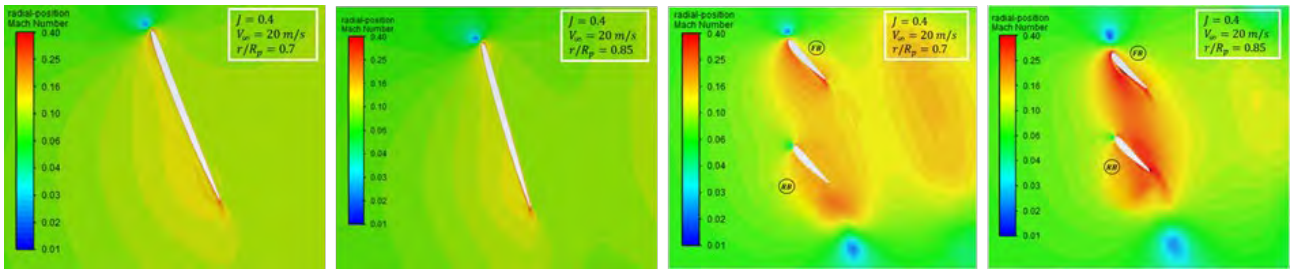


Figure 3.30: Mach number distribution for (a) F29 at r/R_p = 0.7; (b) F29 at r/R_p = 0.85; (c) T-JBT at r/R_p = 0.7; (d) T-JBT at r/R_p = 0.85.

At higher radial position (r/R_p=0.85, Figure 3.30-d), small, localized regions of reduced velocity are visible on the suction side of the forward blade, consistent with the presence of limited flow separation, followed by reattachment downstream. Despite these localized features, the flow remains globally attached to most of the blade surface. The wake development further highlights the differences between the two propellers. As shown in Figure 3.31, the velocity magnitude downstream of the T-JBT propeller is consistently higher than that of the F29 at all investigated axial positions (x/R_p = 0, 0.5, and 1). Near the rotor plane x/R_p = 0), the T-JBT wake exhibits a complex structure associated with the looped blade geometry, while the F29 wake reflects the blade passage pattern. Further downstream (x/R_p = 0.5), the T-JBT wake transitions into a more continuous high-velocity region with reduced azimuthal variation. At x/R_p=1, the wake of the T-JBT remains more spatially concentrated with higher velocity magnitude compared to the F29 propeller. These observations indicate that the T-JBT configuration produces a stronger and more axial velocity field in the near wake, consistent with its higher thrust coefficient.

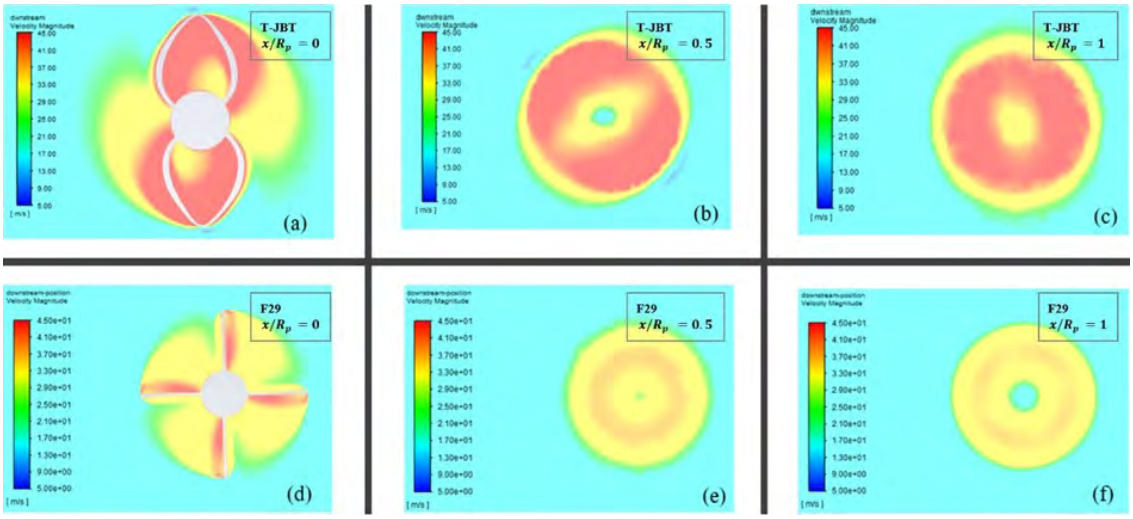


Figure 3.31: Velocity distribution at different positions behind the propellers: (a) r/R_p = 0, (b) r/R_p = 0.5, (c) r/R_p = 1 for the T-JBT propeller and (d) r/R_p = 0, (e) r/R_p = 0.5 (f) r/R_p = 1 for the F29 propeller.

This study investigated the aerodynamic characteristics of a novel Toroidal Joined Blade Tips (T-JBT) propeller using numerical simulations, with comparison to a conventional four-bladed F29 propeller at a fixed operating condition. The results demonstrate that the T-JBT configuration produces a significantly higher aerodynamic loading, achieving approximately 42% higher thrust coefficient. This increase is accompanied by a substantial rise in torque coefficient, indicating that higher thrust is obtained at the expense of increased power consumption. Flow field analysis revealed notable differences in blade aerodynamics and wake development between the two configurations. The T-JBT propeller exhibits strong aerodynamic interaction between the forward and rearward blade segments, along with a more accelerated and spatially concentrated wake compared to the conventional propeller. These features are consistent with the observed increase in thrust generation. However, the higher torque demand results in a marked reduction in propulsive efficiency, with efficiency decreasing from 52.7% to 34.6%. This highlights a clear trade-off between thrust augmentation and energy efficiency in the present design. The observed performance differences are therefore influenced not only by toroidal topology but also by geometric parameters such as pitch and chord distribution. Further work is required to fully assess the potential of the T-JBT concept, including geometric optimization, wake and energy analysis, aeroacoustic evaluation, and structural considerations. Such investigations are necessary to determine the viability of toroidal propellers for future eVTOL and urban air mobility applications.

3.3 Aeroacoustics of Propellers under Unsteady Inflow

Mario Ali, Andrea Piccolo, Riccardo Zamponi, Daniele Ragni, Francesco Avallone

Urban environments are characterized by a wide range of turbulence scales, originating from the atmospheric boundary layer, obstacles, and temperature gradients (Vahdat-Nejad et al., 2016). When rotors and propellers operate in such conditions, their interaction with unsteady inflow becomes one of the main noise-generation mechanisms, commonly referred to as vortex-impingement noise. The acoustic response to incoming turbulence strongly depends on its characteristics, including spectral content, intensity, and integral length scales (Raposo & Azarpeyvand, 2024).

It has been shown that leading-edge noise is the dominant noise source in the frequency range spanning from the second blade passing frequency (BPF) up to approximately the twentieth harmonic (Wojno et al., 2002). More specifically, turbulence interaction increases the broadband noise floor and may introduce spectral humps around the higher BPF harmonics (Amiet, 1978; Raposo & Azarpeyvand, 2024). The latter effect occurs when the integral length scale is sufficiently large to promote blade-to-blade correlation of the aerodynamic loading (Stewart Glegg & William Devenport, 2017). In addition, small propellers typically operate at low Reynolds numbers, where the laminar boundary layer developing over the blade surface may separate and subsequently reattach, forming a laminar separation bubble (LSB), a phenomenon characteristic of this flow regime (Casalino et al., 2021). The dynamics of the LSB influence the properties of the turbulent boundary layer impinging on the trailing edge and therefore affect trailing-edge noise generation. In experimental studies, turbulence is commonly generated using turbulence grids (Go et al., 2024; Jamaluddin et al., 2021; Sikirica et al., 2019), which typically produce inflows dominated by small-scale turbulence. In the first part of this work, we reproduce the setup of an experimental campaign conducted at TU Delft (Piccolo et al., 2025). In DICUAM, it is demonstrated that even mild inhomogeneities in the mean inflow, caused by the grid footprint, can lead to dominant tonal noise within the same frequency range affected by turbulence. Furthermore, it is investigated how the laminar separation bubble interacts with the ingested turbulent inflow. In the second part of the work, the interaction between the propeller and a single-frequency vortical gust is investigated.

Numerical setup

The numerical setup in Figure 3.32 reproduces the experimental configuration described in Ref. (Piccolo et al., 2025). The flow exits a cylindrical pipe of diameter 0.6 m, whose walls are treated as frictionless. The turbulence grid is located inside the pipe, 0.6 m upstream of the exit and 1 m upstream of the propeller plane. The propeller corresponds to the reference configuration used in previous studies (Casalino et al., 2021), with a diameter of 0.3 m and a NACA 4412 airfoil profile. The rotational speed is set to 6000 rpm. The total pressure p_0 computed by accounting for the local pressure losses introduced by the grid, is prescribed as an upstream boundary condition to match the reference free-stream velocity V_∞ = 9 m/s. Twenty probes are distributed upstream of the propeller plane to characterize the inflow. Surface pressure is sampled at f_s = 367 kHz, with a spatial averaging of 0.4 mm over the propeller and nacelle surfaces and used as input for the solid formulation of the Ffowcs Williams–Hawkings (FWH) analogy to obtain the acoustic spectra. Data, sampled over 10 propeller revolutions, are then divided into four Welch blocks with 50% overlap, resulting in a frequency resolution of Δf = 20 Hz. The clean-inflow configuration is obtained by removing the turbulence grid and resetting the prescribed total pressure. The validation of the numerical setup has been presented by the authors in a previous work (Ali et al., 2025)

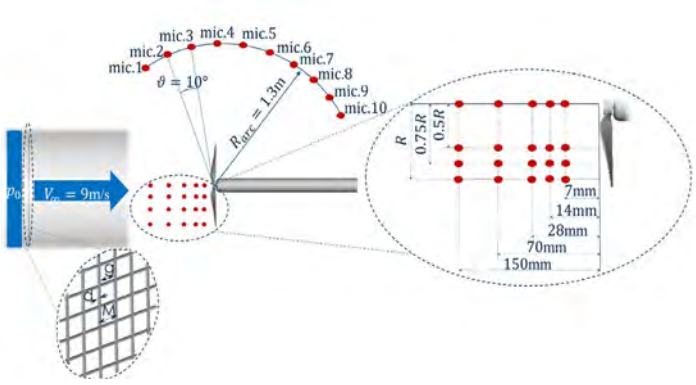


Figure 3.32: Numerical setup, reproducing the reference experiment.

Analysis of the mean flow shown in the presence of the grid in Figure 3.33-a, the inflow exhibits a regular spatial pattern, which is expected to generate peaks at the BPF harmonics in the unsteady loading spectrum. In particular, periodic components at the 2nd and 4th harmonics are expected at the inner and outer radial positions, respectively. This behavior is confirmed in Figure 3.34, where the sectional phase-averaged unsteady loading is reported at r/R = 0.5, 0.75 and 1 over one revolution. Here, ϕ denotes the phase angle, ranging from 0 to 360°. At the inner radial location, the unsteady loading exhibits a periodicity corresponding to the 2nd harmonic, whereas moving toward the blade tip the dominant periodicity shifts to the 4th harmonic.

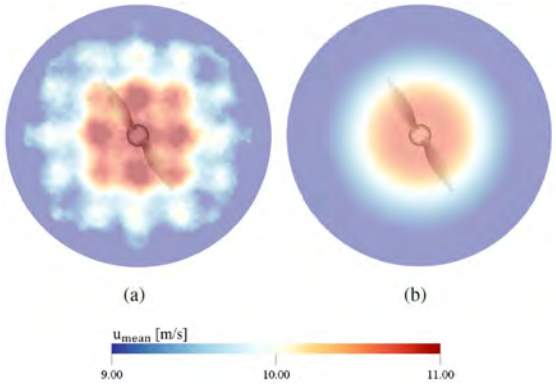


Figure 3.33: Mean streamwise velocity u_{mean} upstream of the propeller plane (a) with and (b) without the grid.

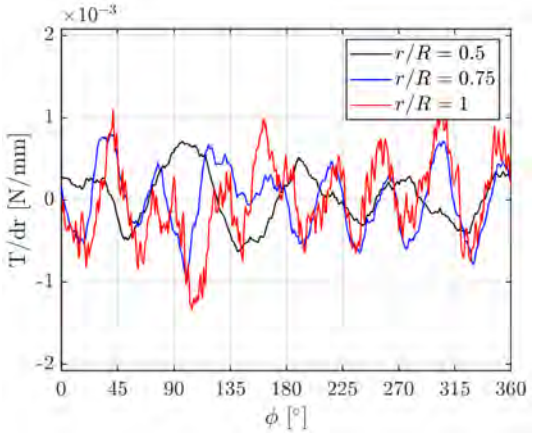


Figure 3.34: Sectional phase-averaged unsteady loading.

The average computed properties close to the propeller plane of u = 12 m/s, TI = 3.6% and Λ = 15 mm are then used as input to the Amiet's model (Piccolo et al., 2025) to identify the effect of turbulence and inhomogeneity.

From an acoustic perspective, an inhomogeneous inflow introduces tonal components at higher BPF harmonics in the acoustic spectrum. This behavior arises because the periodic blade loading induced by the inflow inhomogeneity introduces an additional periodicity in the acoustic response, which is modulated by the BPF. In other words, this additional periodicity is carried by the fundamental frequency. As a result of this modulation, the Fourier representation of the acoustic signal inherently contains a series of higher harmonics.

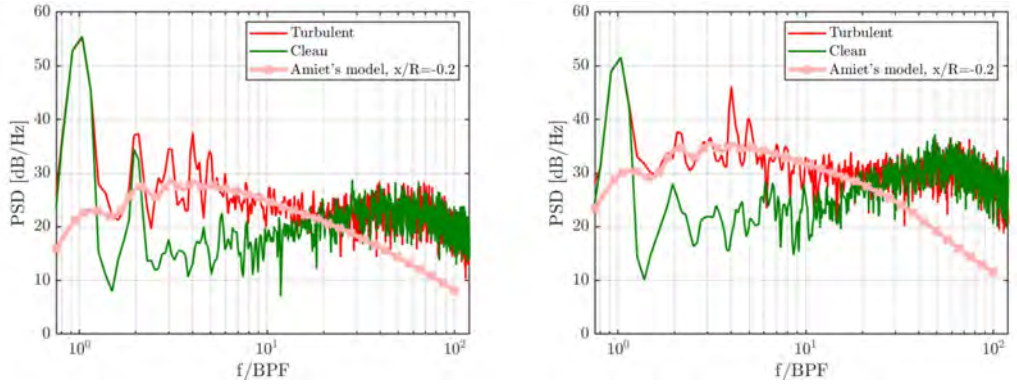


Figure 3.35: Acoustic spectra at (a) Mic.1 and (b) 8.

The acoustic spectra at Mic.1 and 8 are shown in Figure 3.35. Predictions of turbulence-ingestion noise obtained using Amiet's model are reported on the same plots to identify the effects of turbulence–blade interaction and to separate them from those associated with inflow inhomogeneity. Indeed, Amiet's model relies on a prescribed turbulence spectrum to predict the noise generated by blade–turbulence interaction and thus provides a reference for noise associated with turbulent inflow. It can be observed that the primary effect of turbulence is to raise the broadband noise floor, whereas the strong peaks observed in the mid-frequency range are attributed to inflow inhomogeneity. Moreover, the influence of the inhomogeneity on the 2nd and 3rd harmonics decreases from upstream to downstream of the propeller. Finally, no pronounced quasi-tonal noise is observed, as the value of $\Lambda_{uu,x}$ is not sufficiently large to ensure blade-to-blade correlation in the unsteady loading. At frequencies higher than the 20th harmonic, trailing edge noise is the dominant noise source. This section highlights the importance of ensuring a high-quality mean inflow over the entire propeller plane in both experiments and numerical simulations aimed at characterizing the acoustics of low-Reynolds-number propellers under turbulent inflow, since even localized and unintended inhomogeneities can periodically modulate the blade unsteady loading, generating dominant tonal noise within the same frequency range in which turbulence ingestion affects the acoustic spectrum.

Propeller under single vortical gust

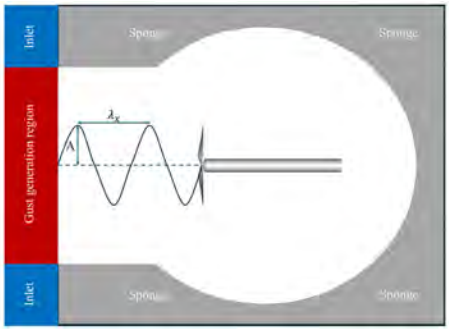


Figure 3.36: Schematic of the numerical setup.

The numerical setup is sketched in Figure 3.36. The vortical gust is generated using an unsteady inlet boundary condition, in which the velocity components are prescribed. Specifically, following the formulation in Ref. (Zhong et al., 2018), the inlet velocity field is defined as:

$$u(x,y,t)=-g(y)h(z)\frac{Ak_y}{\sqrt{k_x^2+k_y^2}}sin\left(k_x x+k_y y-\omega t\right)$$

$$v(x,y,t)=g(y)h(z)\frac{Ak_x}{\sqrt{k_x^2+k_y^2}}sin\left(k_x x+k_y y-\omega t\right)$$

$$w(x,y,t)=0$$

where A is the gust amplitude, k_x and k_y are the streamwise and transverse wavenumbers, and $\omega = U_\infty k_x$ denotes the gust angular frequency. The functions $g(y)$ and $h(z)$ are C^∞ shape functions that confine the gust to a finite region of the inlet.

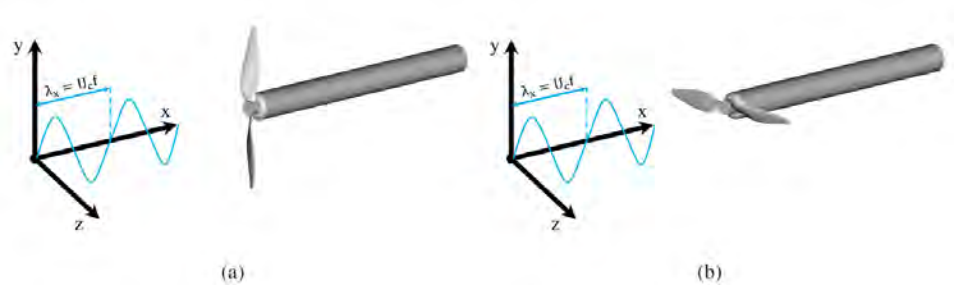


Figure 3.37: Directionality of the gust.

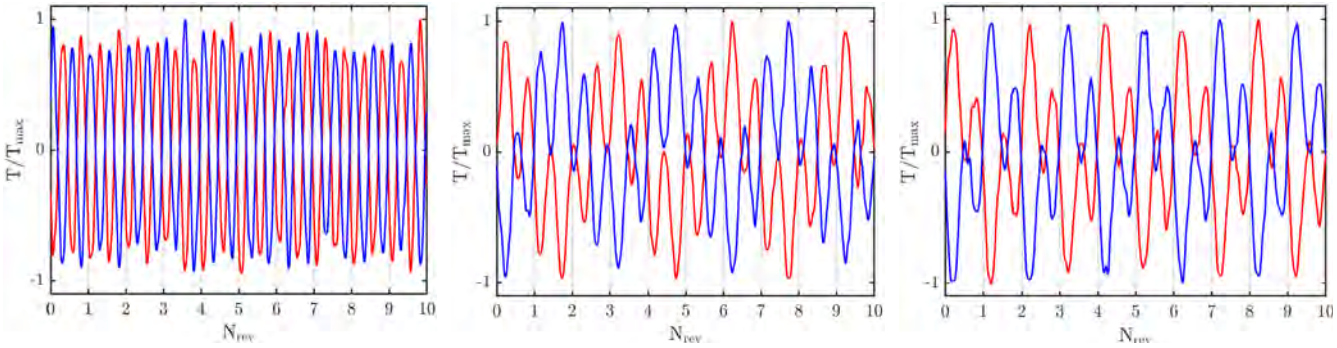
This formulation ensures the free-divergence condition of the velocity field, preventing the formation of spurious acoustic waves. Sponge zones are applied near the domain boundaries to minimize reflections; however, they are not applied in the gust-producing region of the inlet, allowing the gust to be generated by the unsteady inlet boundary condition without damping. The mean inflow velocity is V_∞ = 10 m/s. In addition, because the gust is directional, the initial phase, along with the gust frequency and direction, is also expected to influence the interaction process as shown in Figure 3.37. This effect is investigated only for the gust frequency 100 Hz. The angular phase at which the propeller encounters the gust is determined by the distance from the inlet plane, the gust velocity, and the initial phase of the propeller. The gusts tested are reported in Table 3.15.

Gust case	$k_x/2\pi$ [cm^{-1}]	$k_y/2\pi$ [cm^{-1}]	f_{gust}/f_{rot}	ϕ_0
1	1/10	0	1	0
2	1/15	0	2/3	0
3	1/20	0	1/2	0
4	1/10	0	1	90

Table 3.15: Gusts tested in the current study.

The time history of the unsteady loading on the two blades, reported in Figure 3.38 for the three tested cases, shows that the unsteady velocity field modulates the blade loading. In addition, it can be observed that, under all tested conditions, the unsteady loading on the two blades is in phase opposition. Consequently, this effect cannot be observed in the overall thrust as the contributions from the two blades cancel each other out. The phase difference arises from the fact that the two blades are spaced by 180° and that the gust acts on the propeller plane. As a result, when one blade experiences an increase in tangential velocity and loading, the other experiences a corresponding

reduction. In ascending flight, this corresponds to an increase/reduction in the tangential velocity implies an increase/reduction in the angle of attack and thrust.



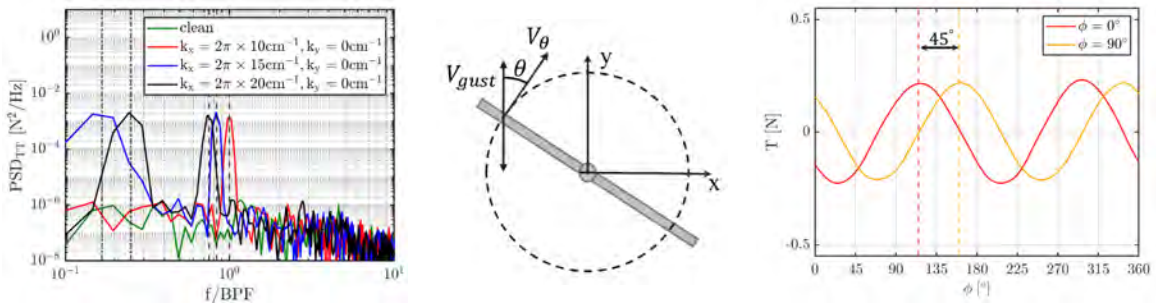
(a) (b) (c)

Figure 3.38: Time-history of the blade unsteady loading under the gusts with frequencies (a) f_{gust}/f_{rot} = 1, (b) 2/3 and (c) 1/2. The two colors correspond to the two blades.

The frequency content of the unsteady loading is shown in Figure 3.39-a. It can be observed that the interaction with the gust generally introduces two peaks in the unsteady loading spectrum at $f_{rot} \pm f_{gust}$. For f_{gust}/f_{rot} = 1, only the peak at $f_{rot} + f_{gust}$ is visible, since the other peak occurs at *f/BPF*=0. The appearance of the peaks at these specific locations indicates a non-linear interaction between the rotational and gust frequencies, which can be explained as follows. In the following, the angular frequency $\omega = 2\pi f$ will be used for convenience, as it leads to a more compact notation in the analytical developments. Referring to the sketch in Figure 3.39-b, the effective tangential velocity $V_{\theta,eff}$ of a point with a rotational frequency f_{rot} can be written as:

$$V_{\theta,eff}(t) = V_{\theta} + V_{gust}\cos(\theta) = \Omega r + \frac{A}{2}\left(\cos\left(\left(\omega_{gust}+\omega_{rot}\right)t+\phi_0\right)+\cos\left(\left(\omega_{gust}-\omega_{rot}\right)t-\phi_0\right)\right)$$

and by performing the Fourier transform it is shown that the non-linear interaction between the two frequencies produces the peaks at the discussed frequencies $f_{rot} \pm f_{gust}$. Figure 3.39-c shows the unsteady loading for a gust frequency of f_{gust}/f_{rot} = 1 and two initial phases, ϕ_0 = 0° and 90°, over one revolution. A phase shift of 45° is observed in the time history of the unsteady loading. Consequently, the time-derivative of the loading is also shifted by 45°. Since the unsteady loading is one of the main noise sources, this phase shift is expected to influence the noise directivity.



(a) (b) (c)

Figure 3.39: Frequency gust effect on the blade unsteady loading spectrum (a) and explanatory sketch (b). The dash-dot lines in (a) identify $f_{rot} - f_{gust}$, while the dashed lines identify $f_{rot} + f_{gust}$. (c) Initial phase effect on the unsteady loading.

The acoustic spectrum measured at Mic. 1 is shown in Figure 3.40. For clarity, the low- and high-frequency ranges are reported in two separate panels: the left panel shows the range from 0.1 BPF to the 5th harmonic, where a high

frequency resolution is retained to highlight the tonal components introduced by the gust, while the right panel presents the higher-frequency range, for which the frequency resolution is partially sacrificed to reduce the variance of the spectrum. While the high-frequency range does not exhibit any influence of the gust, the low-frequency range, particularly up to the 2nd harmonic, shows that the interaction with the simulated gusts introduces tonal components both at the gust frequency f_{gust}, and around BPF, at BPF ± f_{gust}.

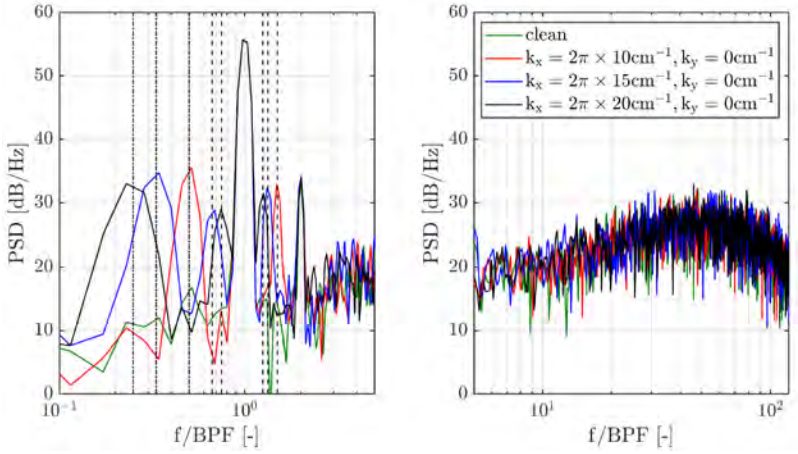


Figure 3.40: Effect of the gust frequency on acoustic spectra at Mic.1. The vertical dash-dot lines identify f_{gust} whereas the dashed lines identify the BPF ± f_{gust}. For f_{gust}/f_{rot} = 1, f_{gust} coincides with BPF - f_{gust}.

The origin of the tonal noise generated by the interaction with the gust can be explained using Lowson's theory, Lowson (1965), and by relating it to the unsteady loading spectrum observed. Again, in the following, the angular frequency $\omega = 2\pi f$ will be used for the sake of a more compact notation. In particular, ω_{rot} is the rotational frequency, ω_{load} is the harmonic in the unsteady loading, and ω_{ac} is the acoustic harmonic. The $\hat{(\cdot)}$ denotes the Fourier coefficients of the generic quantity. Lowson (1965) provided the following expression for the far-field acoustic pressure due to a point force in motion:

$$p(\vec{x},t)=\left[\frac{(x_i\text{-}y_i)}{4\pi a_0 r^2(1\text{-}M_r)^2}\left(\frac{\partial F_i}{\partial t}+\frac{F_i}{1\text{-}M_r}\frac{\partial M_r}{\partial t}\right)\right]_{t=\tau}, i=1,2,3$$

Here, a_0 is the sound speed; x and y denote the observer and source coordinates, respectively, and r is the source-observer distance; M_r is the component of the relative Mach number in the observer direction; and F_i is the ith force component on the fluid and concentrated at a representative point of the blade. The expression in the square brackets must be evaluated at the retarded time τ, i.e. the emission time of the acoustic wave, which is defined as:

$$\tau = t\text{-}\frac{r}{a_0}$$

where t is the reception time and r is the source-observer distance evaluated at the retarded time τ. The far-field acoustic pressure equation contains contributions from two terms: the first arises from the time rate of change of the force, while the second arises from the acceleration associated with the circular motion, which generates acoustic pressure even when the force does not fluctuate. In other words, the second term is present even under clean inflow conditions. Since the observed peaks occur only in the presence of the gust, and thus of an unsteady force, it is reasonable to attribute these peaks primarily to the first term. Thus, in the next the second term will be neglected. Since it is periodic, the unsteady loading and its time-derivative can be written as the Fourier series expansion:

$$F_i=\sum_{\lambda=1}^{N_h}\hat{F}_{i,\lambda}\,e^{i\omega_{\lambda,load}t}\text{ and }\frac{\partial F_i}{\partial t}=\sum_{\lambda=1}^{N_h} i\,\omega_{\lambda,load}\hat{F}_{i,\lambda}e^{i\omega_{\lambda,load}t}$$

where N_h is the number of harmonics in the loading spectrum and $\omega_{\lambda,load}$ is the λ^{th} unsteady loading harmonic. Since in a circular motion $(x_i\text{-}y_i)$ and r are periodic, the ratio:

$$q(t)=\frac{x_i\text{-}y_i}{4\pi a_0 r^2}$$

can be written in general in terms of the Fourier expansions:

$$q(t)=\sum_{-\infty}^{\infty} \hat{q}_n \, e^{\mathrm{in}\omega_{rot}t}$$

In addition, in the limit of low Mach numbers, the following geometric expansion can be used:

$$\frac{1}{(1\text{-}M_r)^2}=\sum_{n=1}^{\infty} n\, M_r^{n\text{-}1}=1+2M_r+o(M_r^2)$$

Substituting these expansions in 5 and keeping the leading term gives:

$$p_1(\vec{x},t) \approx \left[\frac{(x_i\text{-}y_i)}{4\pi a_0 r^2}\sum_{\lambda=1}^{N_h} i\,\omega_\lambda \hat{F}_{i,\lambda} e^{i\omega_{\lambda,load}t}\right]_{t=\tau}$$

where the acoustic frequencies received are:

$$\omega=\omega_{\lambda,load}+n\omega_{rot},\ n\in\mathbb{Z}$$

This result agrees with the exact solution for a rotating dipole in the frequency domain provided by Mao et al. (2012). However, in the previous figures only the harmonics corresponding to $n = 1$ are observed. This is due to the destructive interference shown in the following. The acoustic pressure previously presented corresponds to the contribution from the first blade. The second blade is located 180° apart and, in addition, its unsteady loading is in phase opposition with respect to the first blade. Consequently, the acoustic signal radiated by the second blade can be expressed as:

$$p_2(\vec{x},t) \approx \left[\sum_{n=0}^{\infty}\sum_{\lambda=1}^{N_h} i\,\omega_{\lambda,load}\hat{q}_n\hat{F}_{i,\lambda} e^{i(\omega_{\lambda,load}+n\omega_{rot})t} e^{i(n+1)\pi}\right]_{t=\tau}, i=1,2,3$$

and the overall signal will be:

$$p(\vec{x},t)=p_1+p_2 \approx \left[\sum_{n=0}^{\infty}\sum_{\lambda=1}^{N_h} i\,\omega_{\lambda,load}\hat{q}_n\hat{F}_{i,\lambda} e^{i(\omega_{\lambda,load}+n\omega_{rot})t}\left(e^{i(n+1)\pi}+1\right)\right]_{t=\tau}$$

Where:

$$e^{i(n+1)\pi}+1=\begin{cases}0 & \text{if } n \text{ is even}\\ 1 & \text{if } n \text{ is odd}\end{cases}$$

Therefore, only the frequencies with odd n survive:

$$\omega_{ac}=\omega_{\lambda,load}+n\omega_{rot},\ n=1,3,5,\ \ldots$$

The last equation highlights that the peaks in the acoustic spectrum are directly linked to the unsteady tonal loading introduced by the gust and its modulation through the rotational frequencies. In particular, terms with even n cancel out due to destructive interference between the acoustic waves radiated by the two blades. To conclude, in DICUAM, we have shown how, under turbulent inflow conditions, the presence of mild unintended inflow inhomogeneity can lead, in the acoustic spectrum, to dominant tonal noise in the same range of frequency where

turbulence increases the broadband floor, however leaving unchanged the trailing-edge noise. This highlights the importance of ensuring high quality of the inflow over the entire propeller plane in experiments and numerical simulations aiming at characterizing the aeroacoustics of propellers under turbulent inflow. In the second part of the study, we conducted the first set of high-fidelity numerical simulation to systematically investigate the effects of a vortical gust on the aeroacoustics of the same propeller. More in detail, the focus is on the roles of wavelength and initial phase of the gust. It was shown that the interaction with the vortical gust modulates the unsteady loading of the propeller but this cannot be observed in the overall thrust, because the unsteady loading is in phase-opposition in the two blades. The peaks in the unsteady loading spectrum are observed regularly at $f_{rot} \pm f_{gust}$, and this was shown to arise from the non linear interaction between the rotational and gust frequencies. The tonal unsteady loading was shown to be radiated at frequencies:

$$\omega_{ac}=\omega_{load}+n\omega_{rot}, n=1,3,5, \ldots$$

Following a theoretical approach based on the Lowson model, this was shown to be the result of the unsteady loading modulation through the rotational frequency and the canceling effect due to the phase opposition of the blades and their loadings. In the future, other gust conditions will be introduced to explore the effects of the gust direction, together with a detailed analysis of the noise directivity, a time–frequency analysis of the acoustic signals, and an acoustic source identification.

3.4 Acoustic design optimization of propeller-pylon subsystems

Riccardo Zamponi, Ewann Passelac Estrada, Julien Christophe, Christophe Schram

Early-stage design of emerging electric vertical take-off and landing (eVTOL) aircraft requires the rapid assessment of many competing configurations and technological options. In DICUAM, decisions regarding propulsion layout, vehicle architecture, and operational strategy are often made before detailed analyses are available, creating a strong need for computational or analytical tools that can provide timely and reliable performance estimates (Silva et al., 2018). Public acceptance of urban air mobility services will depend heavily on the ability of eVTOL vehicles to operate with minimal acoustic impact on surrounding communities (Rizzi et al., 2026). As a result, integrating acoustic considerations from the outset of the design cycle is essential to avoid costly redesigns and ensure compliance with future regulatory and environmental constraints. This places significant emphasis on the development of efficient prediction methods capable of guiding low-noise design choices at the conceptual level. In eVTOL aircraft, noise is primarily generated by the propulsion system, with major contributions arising from rotor self-noise and aerodynamic installation effects (Ffowcs Williams & Hawkings, 1969). The distributed propulsion architectures typical of eVTOL concepts lead to strong interactions between rotors and nearby structural elements, such as pylons and wings. These interactions give rise to additional noise mechanisms that generate pronounced tonal components at the blade passing frequency (BPF) and its harmonics, as well as increased broadband noise (H. Lee & Lee, 2020; Tinney & Sirohi, 2018). Among the various installation effects, propeller–pylon subsystems constitute a significant contributor to the overall acoustic signature because propulsion units are often mounted near supporting structures. Investigations by Zawodny & Douglas Boyd Jr (2020) have demonstrated that pylon-induced disturbances can dominate the higher BPF harmonics and substantially modify the radiated acoustic field, with noise levels being highly sensitive to geometric shape, relative positioning, and rotor–pylon spacing. The prediction of potential-interaction noise in a propeller–pylon subsystem in eVTOLs can be effectively based on analytical developments originally carried out for UAV applications. Over the past years, several studies have demonstrated that simplified analytical formulations are able to capture the dominant mechanisms of rotor–pylon acoustic coupling (Roger & Kucukcoskun, 2019; Roger & Moreau, 2020) Vella et al. (2024) applied a similar two-dimensional methodology to experimental configurations from Gojon et al. (2023), successfully reproducing key tonal features and directivity patterns while highlighting the strong sensitivity of noise levels to spacing and

relative phase effects. In DICUAM, the work of Zamponi et al. (2026) that recently proposed a generalized framework for modeling potential interaction noise in generic rotor–pylon arrangements using aerodynamic data from an unsteady panel method is adopted as a design-oriented tool and applies it to the analysis of a propeller–pylon subsystem representative of a realistic eVTOL aircraft configuration.

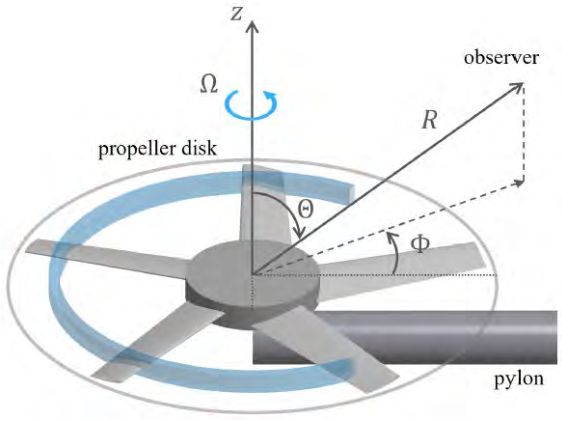


Figure 3.41: Reference system definition for the propeller–pylon setup. In blue an annular strip at the generic radius r. The pylon is here initially approximated as a straight circular cylinder. Image adapted from Zamponi et al. [24].

Blade loading and thickness noise

A propeller operating within the stationary distortion induced by a pylon radiates noise at multiples of the BPF, which depends on the number of propeller blades B and rotational speed Ω and is defined as $mB\Omega/(2\pi)$ (see Figure 3.41). The far-field acoustic pressure at the observer location x and at the m-th harmonic of the BPF, with the convention $e^{-i\omega t}$ for monochromatic waves, is (Hanson, 1993):

$$p_{mB}(x) = -\frac{ik_{mB}Be^{-ik_{mB}R}}{4\pi R}\sum_{s=-\infty}^{\infty} e^{i(mB-s)(\Phi-\pi/2)} \times \int_{r_{root}}^{r_{tip}} J_{mB-s}(k_{mB}r\sin\Theta)\left[\frac{mB-s}{k_{mB}r}F_{b,\varphi}^{(s)}(r)+\cos\Theta F_{b,z}^{(s)}(r)\right]dr$$

where c_0 is the speed of sound, J_n is the Bessel function of the first kind of order n, and $k_{mB} = mB\Omega/c0$ is the wavenumber related to the BPF. $F_{b,\phi}^{(s)}(r)$ and $F_{b,z}^{(s)}(r)$ represent the tangential and axial harmonics of the blade loading, i.e., the complex Fourier coefficients of the periodic force per unit span acting on a blade element at radius r. The components associated with $s = 0$ correspond to the steady aerodynamic loads generated by the propeller. Owing to the assumption of acoustic compactness and zero sweep, the previous equation is integrated only along the radial direction, consistent with the strip-theory approach used in rotor noise modeling. The harmonics of the blade loading result from the stationary flow distortion induced by the pylon downstream of the propeller. This distortion is derived using a two-dimensional model based on the classical incompressible solution for the potential flow around a circle. Considering the unwrapped representation of the annular strip at radius r depicted in Figure 3.42, the propeller blades are idealized as flat plates, consistent with their relatively small thickness, and are separated by a circumferential spacing of $2\pi r/B$. As the propeller rotates, the blades pass in front of a cylindrical pylon of circular cross-section with a tangential speed of Ωr. Each blade is characterized by a chord length c and a pitch angle α, which defines a stagger angle γ relative to the rotor axis. The diameter of the pylon is denoted by D_s, and the propeller plane is located at a distance L from the pylon centerline. The pylon is subjected to the velocity field generated by the propeller, i.e., Ui, which consists of both axial (downwash) and tangential (swirl) components. The corresponding swirl angle is indicated by α_0 and defined according to Figure 3.42. These induced velocities are determined at the rotor plane under the assumption of an isolated propeller, so that any modifications produced by the presence of the pylon are disregarded in accordance with a no-coupling hypothesis (Vella et al., 2024).

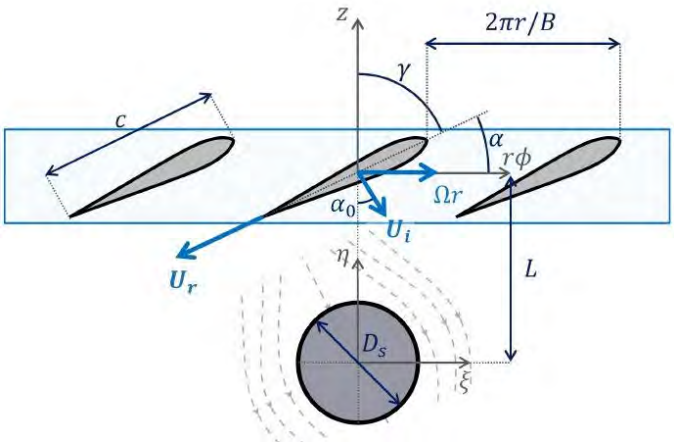


Figure 3.42: Two-dimensional unwrapped representation of the annular strip at arbitrary radius. The pylon is modeled as a circular cylinder subjected to the velocity field induced by an infinite series of blade passages.

The distortion of the flow field over the rotor disk induced by the pylon is represented using a two-dimensional, incompressible potential flow model. The complex potential $f(\zeta)$, expressed in terms of the complex coordinate $\zeta = \xi + i\eta$, describes the flow in a plane centered on the pylon. In this representation, the coordinates on the rotor disk correspond to $\xi = r\varphi$ and $\eta = L$, with φ and L being the azimuthal coordinate in the unwrapped representation in Figure 3.42 and the axial distance from the pylon, respectively. According to the Milne–Thompson circle theorem, the potential associated with a circular cylinder immersed in a uniform stream can be written as:

$$f(\zeta) = \mathrm{i}U_i\left(\zeta e^{-\mathrm{i}\alpha_0} - \frac{D^2 s}{4\zeta}e^{\mathrm{i}\alpha_0}\right)$$

where $U_i = |U_i|$. The local velocity components are obtained from the complex derivative of the potential as $u(\zeta) = \Re\{\partial f/\partial\zeta\}$ and $v(\zeta) = -\Im\{\partial f/\partial\zeta\}$. The upwash velocity w acting on each blade section is then determined by projecting the velocity perturbation onto the direction normal to the chord. The radial dependence of c, α, γ, U_i, and α_0 will be omitted in the subsequent derivations for the sake of clarity.

Even though the upwash velocity field is stationary in the global reference frame, each blade encounters it as a periodic azimuthal disturbance in its rotating reference frame. The s^{th} harmonic component of this distortion at a given radial station r is obtained through Fourier series:

$$w_s(r) = \frac{1}{2\pi}\int_0^{2\pi} w(r,\varphi)e^{is\varphi}\,d\varphi\,, \quad s \geq 1$$

Each harmonic w_s generates a corresponding unsteady loading response on the blade, which can be evaluated using an aerodynamic transfer function based on Sears' theory, under the assumption that the blade chord is aerodynamically compact. For a rotor cascade interacting with the potential field produced by a stator cascade, the generalized lift function takes the form:

$$K(\sigma,\mu) = C(\sigma)[J_0(\mu) - iJ_1(\mu)] + \frac{i\sigma}{\mu}J_1(\mu), \quad where \quad \sigma = \frac{s\Omega c}{2U_r} \quad \wedge \quad \mu = \frac{isc}{2r}e^{-i\gamma}$$

with C denoting the Theodorsen function [19] and U_r the component of the relative velocity aligned with the blade chord. The harmonics of the unsteady lift per unit span are given by:

$$L_s(r) = \pi\,\rho_0 c U_r w_s(r) K^*$$

where ρ_0 is the fluid density, the superscript * denotes complex conjugation, and the negative harmonics follow from the relation $L_{-s} = L_s^*$. These lift harmonics are subsequently resolved into axial and tangential force components:

$$F_{b,\varphi}^{(s)}(r) = L_s(r)\ cos\ \gamma, \qquad F_{b,z}^{(s)}(r) = -\ L_s(r)\ sin\ \gamma$$

Finally, noise from the rotor is also radiated due to the air volume being displaced by the blade motion. Assuming thin propeller blades and under the condition of acoustic compactness and zero sweep, the acoustic pressure in the geometric far-field at the m-th harmonic of the BPF can be expressed as:

$$p_{mB}(x) = -\frac{mk_{mB}Be^{-ik_{mB}R}}{4\pi R} e^{imB(\Phi\ -\ \pi/2)} \int_{r_{root}}^{r_{tip}} \rho_0 c_0 J_{mB}(k_{mB} r\ sin\ \Theta)\ \Omega\ \Delta h\ c\ r\ dr$$

where Δh represents the chordwise integral of the local blade thickness distribution. The acoustic source term associated with thickness is therefore determined exclusively by the blade geometry and does not depend on the angle of attack or camber. Propeller–pylon interaction produces additional loading noise due to the unsteady pressures induced on the pylon by the potential field of the passing blades (Wu et al., 2022). This contribution can be modeled within the rotor–stator framework of Hanson (1985), treating the pylon as a stationary unswept stator with a single unprofiled vane. The complex far-field sound pressure at the m^{th} BPF harmonic reads:

$$p_m(x) = -\frac{ik_m\ Be^{-ik_mBR}}{4\pi R} \sum_{S=-\infty}^{\infty} e^{i(mB-s)(\Phi-\pi/2)} \times \int_{r_{mot}}^{r_{tip}} J_{mB-s}(k_mBr\ sin\Theta) \left[\frac{mB-s}{k_mBr} F_{s,\varphi}^{(m)}(r) + cos\Theta\ F_{s,z}^{(m)}(r)\right] dr$$

In this case, the pylon loading determined by $F_{s,\phi}$ and $F_{s,z}$ is evaluated using a simplified two-dimensional incompressible potential-flow model in which the pylon cross-section is represented as a circular cylinder. Each blade section is modeled as a point vortex carrying a circulation proportional to the sectional lift and convecting past the pylon to represent blade passage. The resulting unsteady pressure distribution on the pylon surface is then obtained from the unsteady Bernoulli equation and integrated over the pylon surface to yield the forces per-unit-span acting on the pylon. For brevity, the detailed derivation of the model is not reported here, and interested readers are referred to the aforementioned studies. The m^{th} harmonics of the resulting force distributions are finally derived:

$$F_{s,\varphi}^{(m)}(r) = \frac{1}{T_b}\int_0^{T_b} F_{s,\varphi}(r,t)e^{imB\Omega t}\ dt\,, \quad F_{s,z}^{(m)}(r) = \frac{1}{T_b}\int_0^{T_b} F_{s,z}(r,t)e^{imB\Omega t}\ dt$$

The two-dimensional potential flow formulation outlined in the previous section was originally derived for a pylon with a circular cross section. Building on these analytical solutions, the flow field around a more realistic, polygonal-shaped cylinder can be determined using conformal mapping. This approach establishes a correspondence between the circular boundary in the reference ζ-plane and the polygonal boundary in the physical plane. Since Laplace's equation, which governs incompressible potential flow, is invariant under conformal transformations, the solution for the circular cylinder can be mapped to the physical domain. The resulting formulation incorporates the geometric influence of the actual pylon shape on the surrounding flow through the superposition principle.

Following the approach of Zamponi et al. (2026), a hypotrochoidal mapping function is employed to represent a range of polygonal geometries with finite corner radii, in accordance with the method proposed by Solanki & Sharma (2022). A hypotrochoid is a cycloidal curve generated by a point located at a distance ρ from the center of a circle of radius R_r that rolls without slipping inside a fixed circle of radius R_d. The related conformal mapping is given by:

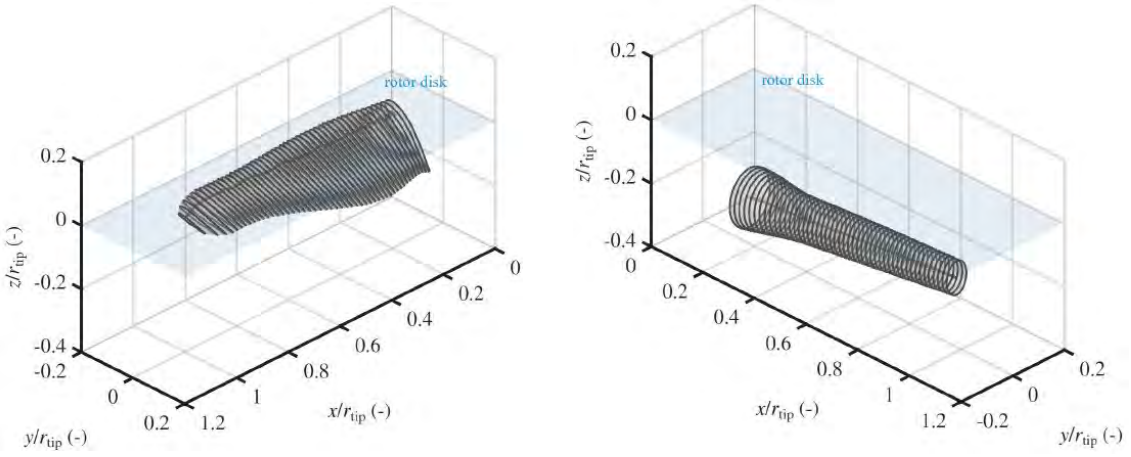
$$Z(\zeta) = R_d \left[\left(1 - \frac{1}{N}\right)\zeta + \frac{\rho}{R_d}\frac{1}{\zeta^{N-1}}\right] e^{i\theta_0}$$

where $N = R_d/R_r$, ζ denotes the complex coordinate defined outside the hypotrochoidal boundary, and θ_0 defines the orientation of the polygonal shape with respect to the positive real axis. A closed polygonal contour is obtained when N is an integer greater than two. The parameter ρ ranges between 0 and R_r, controlling both the curvature of the corners and the degree of straightness of the polygon sides. The flow velocity in the physical plane is obtained by combining the complex potential f, defined as in the following equation, with an hypotrochoidal mapping function. The resulting complex velocity f' is expressed as:

$$f'(Z) = u(Z) - iv(Z) = R_d \left(1 - \frac{1}{N}\right) \frac{\partial f(Z)}{\partial \zeta} \zeta'(Z)$$

where $\zeta'(Z) = d\zeta/dZ$. The prefactor $R_d(1 - 1/N)$ accounts for the velocity scaling introduced by the mapping and is consistent with the previous equation in the limit $\rho \rightarrow 0$ (Solanki & Sharma, 2022). The velocity components along the ζ- and η-directions are obtained from the real and imaginary parts of the previous equation, respectively, and are subsequently used to evaluate the blade upwash in the unsteady loading models.

The geometrical setup considered in this study, along with the low-fidelity computational framework proposed to calculate the aerodynamic inputs required by the predictive model, is outlined in this section. The rotor considered in this study is a representative five-bladed eVTOL propeller manufactured at 1/10 scale and specifically designed for hover operating conditions. An isometric view of the propeller blade is shown in Figure 3.43-a. The rotor was produced from aluminum alloy using computer numerical control machining, achieving a surface finish of 0.8 μm. This manufacturing approach ensures high geometric accuracy and minimizes surface imperfections, which could otherwise degrade the quality of the flow field around the blades and affect the acoustic response. The propeller, with a tip diameter of 304 mm and a hub diameter of 46 mm, was experimentally tested in the ALCOVES anechoic chamber at the von Karman Institute for Fluid Dynamics. The facility complies with ISO 3745 standards and exhibits free-field acoustic behavior for frequencies above 150 Hz (Gallo et al., 2025). The corresponding measurement dataset is publicly available as open-source material (Bresciani et al., 2025).



(a) (b)

Figure 3.43: Isometric views of the (a) propeller blade and (b) pylon, which are discretized into 48 spanwise stations.

The geometry of the pylon downstream of the propeller, sketched in Figure 3.43-b, is also chosen to be representative of a realistic eVTOL aircraft. In the model, the pylon geometry is defined through a spanwise-varying elliptical cross-section obtained via conformal mapping. The major diameter and axial distance from the rotor disk follow prescribed power-law distributions between the root and tip, while the aspect ratio slowly varies along the span to control the sectional shape. A smooth hub-transition blending modifies the diameter, aspect ratio, and

centerline offset in the inner region, introducing a gradual bend located a finite distance from the rotor disk. This ensures a continuous variation of thickness and curvature without geometric discontinuities. The main geometric parameters at five representative spanwise stations are summarized in Table 3.16.

r/r_{tip} [-]	D_S [m]	L [m]	R_d/D_s [-]	R_r/D_s [-]	ρ/R_r [-]	θ_0 [rad]
0.182	0.0280	0.0380	0.9167	0.4583	0.0909	0
0.251	0.0271	0.0368	0.8701	0.4351	0.1493	0
0.506	0.0223	0.0335	0.7948	0.3974	0.2582	0
0.745	0.0202	0.0303	0.8335	0.4168	0.1998	0
0.983	0.0175	0.0272	0.8809	0.4404	0.1352	0

Table 3.16: Pylon geometry at representative spanwise stations.

Here below the model is adapted to reproduce the experimental configuration presented before. The ambient conditions are taken as ρ_0 = 1.20 kgm^{-3} and $c0$ = 340m s^{-1}. The model requires as input the steady aerodynamic loading of the isolated propeller, assuming that the presence of the pylon has a negligible influence on the mean propeller performance in hover. These steady loads are obtained using blade element momentum theory (BEMT), which combines one-dimensional momentum theory with sectional blade–element aerodynamics to estimate the thrust and torque distributions along the blade span. The rotor is modeled as an actuator disk that imparts a pressure jump to the flow, while each blade section is analyzed as a two-dimensional airfoil operating at a local angle of attack. By enforcing the equivalence between the forces predicted by momentum theory and those obtained from blade-element theory, the radial distributions of thrust T and torque Q can be determined iteratively for a given operating condition. A comparison between the BEMT results and the experimental loads measured in the ALCOVES facility is reported in Table 3.17 for different rotational speeds. Overall, the BEMT model predicts thrust and torque with deviations generally within 15% and 20%, respectively, relative to the experimental measurements over the investigated range of rotational speeds. In the results presented in this paper.

	4000	5000	6000	7000	8000	9000
T_{pred} [N]	11.82	18.46	26.59	36.19	47.26	59.82
T_{exp} [N]	10.3	16.2	23.6	32.3	42.3	51.3
Q_{pred} [N·m]	0.312	0.487	0.702	0.955	1.248	1.579
Q_{exp} [N·m]	0.276	0.424	0.610	0.811	1.039	1.275

Table 3.17: Comparison of BEMT predictions and measurements of propeller loads at different rotational speeds.

A positive rotational speed of 8300 rpm is adopted, as it corresponds to the nominal operating condition of the propeller in hover and is therefore representative of its designed performance. From the BEMT loading distributions, the corresponding axial and tangential induced velocities U_i are evaluated through momentum relations. The axial induced velocity and the tangential component obtained from conservation of angular momentum are:

$$U_{i,z}(r) = \sqrt{\frac{dT(r)}{4\pi\rho_0 r dr}}, \qquad U_{i,\varphi}(r) = \frac{dQ(r)}{4\pi\rho_0 r^2 dr U_{i,z}(r)}$$

With the local swirl angle used in the acoustic model computed as $\alpha_0 = arctan(U_{i,\varphi} / U_{i,r})$. The predictive framework proposed in this study is initially validated by reproducing measurements of the isolated propeller under hover conditions acquired in the ALCOVES facility, which is equipped with three linear arrays comprising a total of 24 G.R.A.S. 40PL condenser microphones surrounding the propeller. A schematic of the microphone layout, including their distances from the propeller, is shown in Figure 3.44. The transducers feature an accuracy of ±1 dB over the frequency range from 100 Hz to 10 kHz following individual calibration. The spherical reference frame in the experimental arrangement, which will be used for the presentation of the results, is related to that of the analytical formulation through the transformation $(R, \theta_{exp}, \phi_{exp}) = (R, \pi/2 - \Theta, \pi - \Phi)$. In this coordinate system, the pylon is placed at $(\theta_{exp}, \phi_{exp}) = (0, \pi)$.

For an isolated rotor, noise at the BPF arises primarily from the steady aerodynamic loads and the thickness of the propeller blades. A comparison between the predicted and experimental radiation patterns extracted at $\phi_{exp} = \pi/2$ and normalized for a reference distance between the microphones and the propeller center of 1m is shown in Figure 3.44. On the one hand, the analytical model successfully predicts the noise levels in the vicinity of the rotor disk. On the other hand, it significantly underpredicts the radiated sound as the observer location moves toward the propeller axis. This discrepancy is most likely associated with additional unsteady loading sources generated by the ingestion of turbulence recirculating within the anechoic room (Weitsman et al., 2020), which are not accounted for in the present acoustic model. Nevertheless, the satisfactory agreement in the polar angle region where the acoustic field is primarily governed by steady loading and thickness noise indicates that the BEMT provides aerodynamic force distributions with sufficient accuracy for use in the acoustic predictive method.

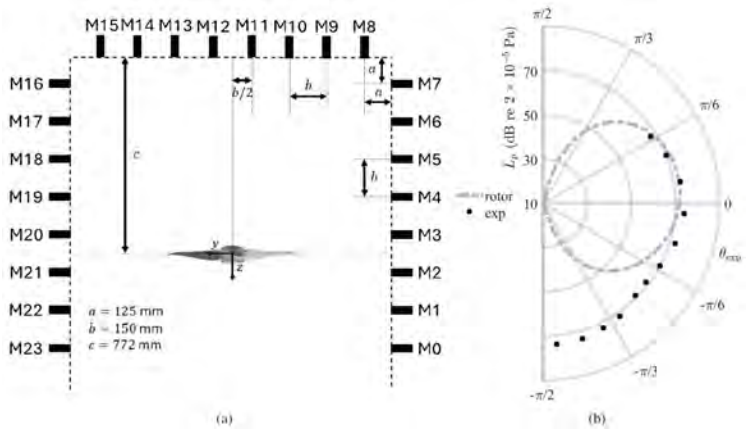


Figure 3.44: (a) Microphone layout in the ALCOVES anechoic chamber and (b) predicted and experimental directivity patterns of the far-field noise radiated by the isolated propeller at the BPF for $\phi_{exp} = \pi/2$.

The upwash disturbance *w* introduced in the previous section directly influences the unsteady lift generated by the blade segment according to Sears' theory. Consequently, examining this velocity component at the rotor disk provides insight into the sources of unsteady loading noise radiated by the blade. To this end, the contour of *w* over the propeller disk induced by the pylon in Figure 3.43 is presented in Figure 3.45. The stationary upwash disturbance produced by an equivalent simplified pylon is also included for comparison. This equivalent geometry consists of a straight pylon with a constant circular cross-section designed to preserve the total volume of the baseline configuration. The cylinder diameter is determined by equating the span-averaged cross-sectional area of the original elliptic cross-section to that of a circle, resulting in a constant diameter of D_s = 0.018 m that maintains the

same integrated volume along the span. The axial distance from the rotor disk is set to a uniform value equal to the mean of the original axial distance distribution, i.e., L = 0.032 m, while the hub transition and centerline offset are removed. This comparison allows the influence of the realistic pylon shaping to be isolated from the overall blockage effect associated with a body of equivalent volume.

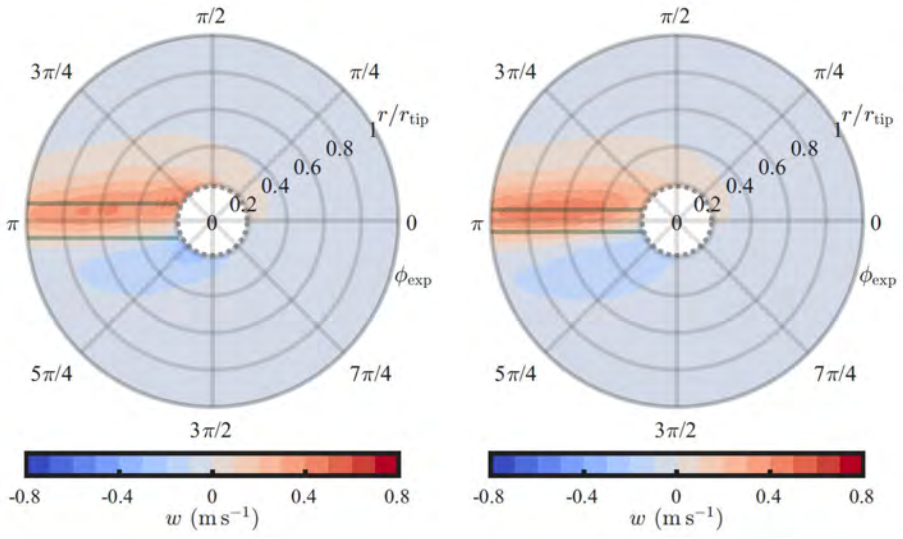


Figure 3.45: Contours of the upwash velocity disturbance induced by (a) the baseline pylon defined in Figure 3.43 and (b)the equivalent straight circular cylinder. The propeller spins in the counter-clockwise direction.

As expected, the inflow distortion induced by the realistic pylon is presented in Figure 3.45 on the rotor disk is concentrated around φ_{exp} = π, i.e., in the region directly upstream of the component. Higher levels of upwash disturbance are observed close to the hub, where the pylon cross-section is wider to accommodate and support the propeller motor. Moving toward the blade tip, w gradually decreases because of the cross-section tapering and the aspect ratio variation of its elliptical shape. Furthermore, due to the flow swirl angle, each blade encounters the blockage imposed by the pylon before passing over the component, whereas a region of increased induced velocity, associated with negative upwash, develops past it. On the contrary, the inflow distortion produced by the equivalent straight cylinder Figure 3.45 exhibits a more uniform distribution, suggesting that the simplified geometry generates a more homogeneous blockage effect along the blade radial direction. The potential–interaction noise radiated by the propeller–pylon arrangement results from the unsteady aerodynamic response of the blades as they encounter the stationary distortion field induced by the pylon. A first overview of this impact is shown in Figure 3.46, which compares the radiation pattern at the BPF of the isolated propeller with that of the propeller operating upstream of the pylon for R = 1 m. The total far-field acoustic pressure is obtained here by incoherently summing the contributions of the rotor, comprising blade loading and thickness noise as in the previous equations. For the isolated propeller (Figure 3.46-a), the emitted noise exhibits the typical toroidal directivity of rotor steady-loading noise, with maximum sound levels radiated sideways in the propeller plane and minima along its axis. When the pylon is accounted for (Figure 3.46-b), the radiation pattern dramatically changes, losing the axisymmetric toroidal shape observed for the isolated configuration.

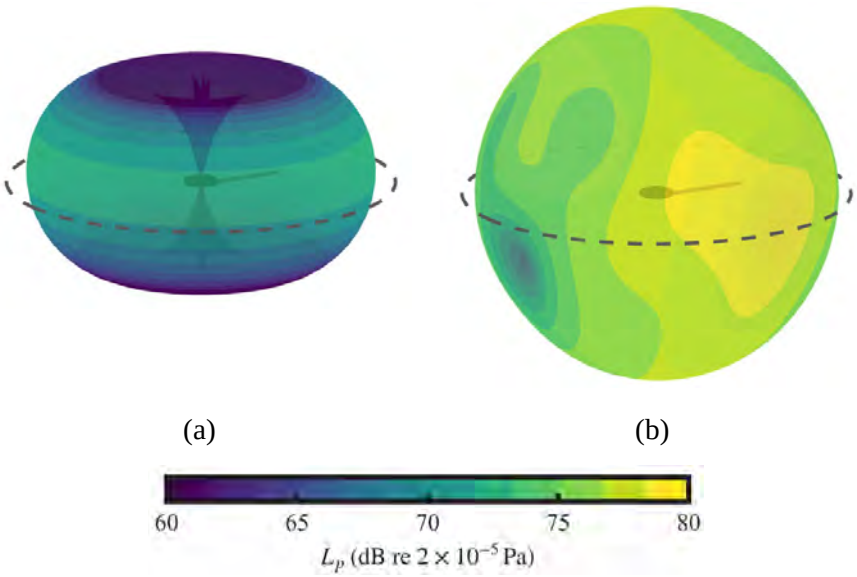
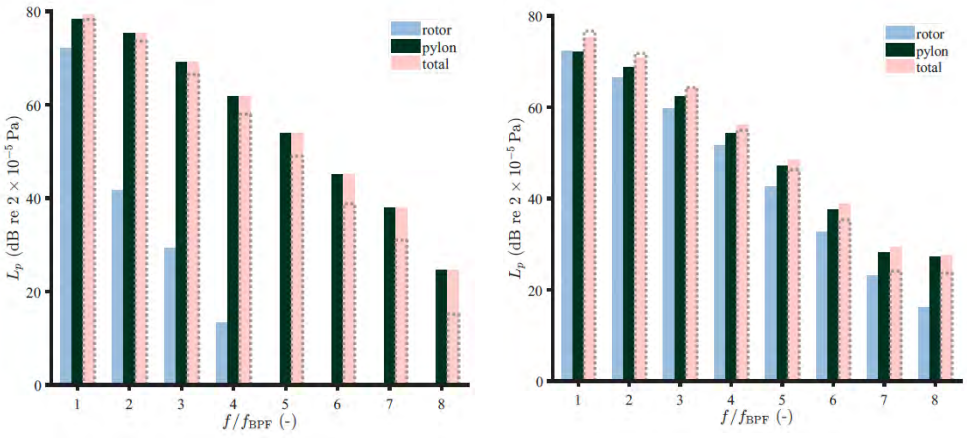


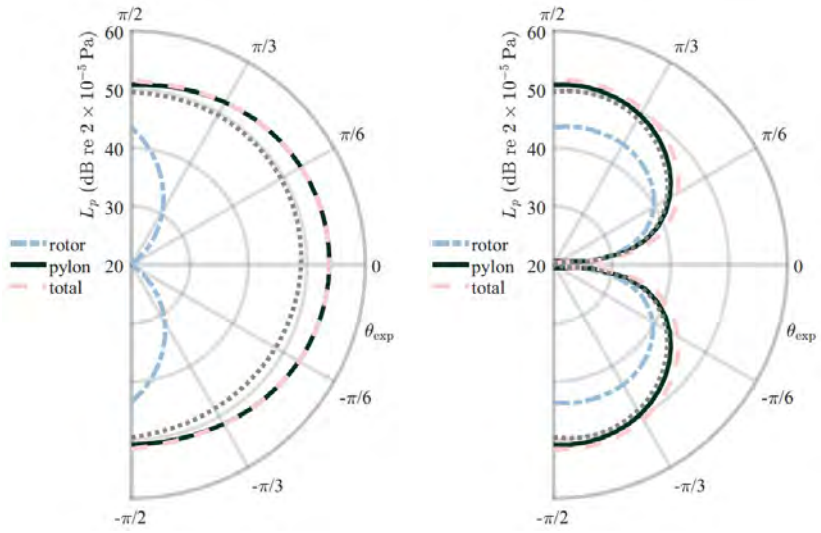
Figure 3.46: Predicted directivity pattern of the far-field sound pressure level radiated at the BPF by (a) the isolated propeller and (b) the propeller operating upstream of the pylon. The observers are located on a sphere at R = 1m.

As a result of the potential interaction, the sound radiation becomes more uniformly distributed over the sphere, with higher sound pressure levels extending toward both upstream and downstream directions. The first eight BPF harmonics of the far-field pressure predicted for the propeller–pylon configuration are shown in Figure 3.47 for several observer locations. The rotor and pylon contributions are reported separately, together with their combined effect. When the observer is located in the propeller plane and normal to the pylon axis (Figure 3.47-a), the radiated noise is dominated by the pylon contribution, consistent with the results of Gojon et al. (2023). In contrast, when the observer is aligned with the pylon axis (Figure 3.47-b), the rotor contribution is comparable to that of the pylon, as the observer is positioned close to the direction of minimum radiation of the dipole associated with pylon loading noise. Compared with the sound pressure level predicted for the equivalent straight cylinder, the realistic configuration produces a general increase in pylon unsteady-loading noise that reaches 9.5 dB at the eighth BPF harmonic for $[\theta_{exp}, \varphi_{exp}] = [0, \pi/2]$, suggesting that realistic details in the pylon architecture cannot be neglected if accurate noise predictions are sought. Conversely, more similar sound pressure levels are generally observed at $[\theta_{exp}, \varphi_{exp}] = [\pi/4, 0]$. The analysis presented above can be further extended by examining the directivity of the unsteady loading noise over the polar angle. The radiation patterns of the far-field pressure, computed at the azimuthal observer positions considered in Figure 3.47, are shown in Figure 3.48 for fifth BPF harmonic, which features the largest deviation between the unsteady-loading noise radiated by the realistic pylon and that predicted for the equivalent straight cylinder. At $\varphi_{exp} = \pi/2$ (Figure 3.48-a), the contribution of rotor noise is maximum along the propeller axis and minimum in the rotor plane, exhibiting a clear dipolar radiation pattern. In contrast, the pylon noise displays a more toroidal directivity and dominates most observer locations. This toroidal shape is more pronounced for the realistic pylon than for the equivalent straight cylinder. At $\varphi_{exp} = 0$ (Figure 3.48-b), the two unsteady-loading contributions have similar directivity patterns, and they do not radiate along the pylon axis. At this azimuthal location, potential-interaction noise levels from the straight cylinder are consistently lower than those from the realistic pylon throughout θ_{exp}, although they exhibit a smaller deviation with respect to the previous observer location.



(a) (b)

Figure 3.47: Predicted harmonics of the far-field noise radiated by the propeller operating upstream of the pylon for (a) [θ_{exp}, φ_{exp}] = [0, $\pi/2$] and (b) [θ_{exp}, φ_{exp}] = [$\pi/4$, 0]. The frequency axis is normalized by the BPF. The dashed bar outlines denote the total acoustic pressure radiated by the equivalent straight cylindrical pylon. The observer is located at R = 1 m.



(a) (b)

Figure 3.48: Predicted directivity patterns of the far-field noise radiated at the fifth harmonic of the BPF by the propeller for (a) φexp = π/2 and (b) φexp = 0. The dashed bar outlines denote the total acoustic pressure radiated by the equivalent straight cylindrical pylon. The observer is located at R = 1 m.

This research work presents an analytical methodology for predicting the potential–interaction tonal noise generated by a propeller–pylon configuration in an eVTOL aircraft with minimal mathematical complexity and low computational cost. The approach combines individual models for blade loading noise, blade thickness noise, and pylon loading noise to describe the acoustic pressure radiated by a propeller in hover that operates upstream of a pylon representative of an eVTOL vehicle. The pylon geometry is modeled using a hypotrochoidal conformal mapping combined with a strip-based approach, enabling the realistic geometric features of the component to be reproduced while retaining analytical tractability. The model uses as input the spanwise distributions of the steady

loads produced by an isolated propeller, which are assumed not to be affected by the presence of the pylon and are estimated through BEMT.

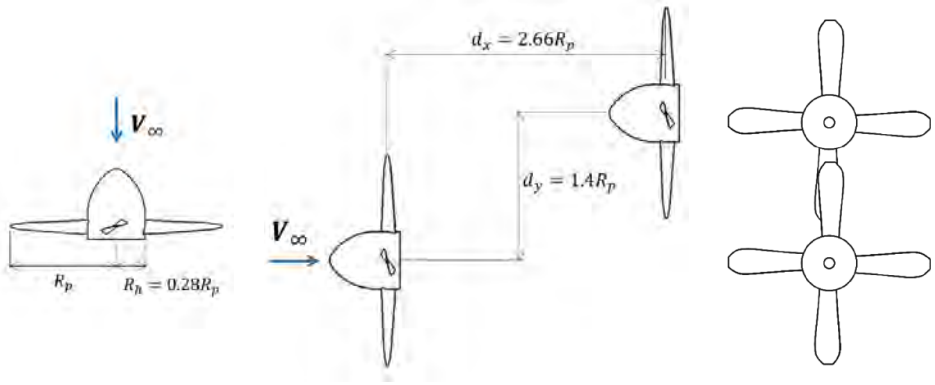
The results presented in this study indicate that, despite its inherent limitations and simplifying assumptions, the proposed analytical approach can capture the main trends and variations associated with changes in the input parameters. In particular, the analysis highlights that realistic geometric details of the pylon can significantly affect the predicted interaction noise levels and therefore cannot be neglected in accurate noise assessments. As such, the proposed methodology provides a level of accuracy suitable for identifying low-noise configurations during the early stages of the design process, when rapid evaluations and reduced computational costs are essential. Future work will include a formal validation of the prediction accuracy of the potential–interaction model.

3.5 Numerical Analysis of Multirotor Aerodynamic Interactions

Kangni Combey, Khaoula Qaissi, Mustapha Faqir, Omer Ali Elsayed

Distributed Electric Propulsion (DEP) has emerged as a defining feature of many modern eVTOL aircraft for UAM applications. By replacing a small number of large rotors with multiple electrically driven propellers, DEP architecture offers several advantages, including enhanced redundancy, improved controllability and increased operational safety (H. D. Kim, 2020; H. D. Kim et al., 2018). In DICUAM, some of the increasingly complex aerodynamic interactions between neighboring propellers are analyzed to explore the balance between advantages and disadvantages. Unlike conventional propulsion systems, eVTOL aircraft often employ closely spaced rotors whose wakes interact during hover, transition, and forward flight. Such interactions modify the inflow conditions experienced by downstream propellers, affecting thrust generation, propulsive efficiency, and overall vehicle performance. Several studies (Stokkermans et al., 2021; Zanotti & Algarotti, 2022) indicated that when a propeller operates in a non-uniform inflow and ingesting the wake of another propeller, it could face a significant thrust loss of up to 80%. Experimental investigation conducted by Atte et al. (2022) further demonstrates that a tandem configuration's aft rotor experiences a significant 24% decrease in thrust coefficient when compared to a single rotor operating at the same rotational speed and airspeed with a hub spacing of 2.1 times the propeller radius. In a numerical study, Piccinini et al. (2020) revealed that side-by-side (SBS) configurations exhibited a slight performance decrease, while tandem configurations experienced a more substantial reduction. Full overlap of propeller disks resulted in a notable 30% thrust loss and a 20% reduction in propulsive efficiency. Stokkermans et al. (2021) found that in SBS configuration, interaction effects become particularly severe as the propeller angle of attack increases, leading to a significant reduction in rear propeller thrust, up to 30%, at a constant advance ratio. Moreover, an extensive investigation carried out by Zarri et al. (2022), highlighted the phenomenon of tip-on-tip interaction. Therefore, an accurate assessment of these interactions during the conceptual design phase is crucial for precise performance predictions. Understanding these mechanisms is therefore essential during the conceptual design phase, when rotor placement decisions can significantly influence aircraft performance. In the following, the analysis of the aerodynamic interactions pertaining to a cascade of two propellers configuration representative of distributed propulsion layouts found in several eVTOL concepts. Attention is given to the performance degradation experienced by the downstream propeller because of wake ingestion. The investigated arrangement consisted of two partially overlapping propellers (OAA) aligned in the streamwise direction. While the upstream propeller operated in relatively undisturbed flow conditions, the downstream propeller was positioned within the evolving wake generated by the front propeller. The wake of a propeller is characterized by a complex combination of axial velocity deficit, swirl velocity, tip vortices, and turbulent structures. To characterize these interaction effects, CFD simulations were performed using two co-rotating F29 propellers arranged in an OAA configuration with longitudinal and lateral spacings of $d_x = 2.66\ R_p$ and $d_y = 1.4\ R_p$, respectively, as shown in Figure 3.49. These values were inspired by the Airbus Vahana eVTOL architecture, although a reduced longitudinal spacing was deliberately

selected to amplify and show propeller-propeller interaction effects. The F29 propeller used as benchmarking reference in aircraft studies is employed in DICUAM (Stokkermans et al., 2021). It has a radius of R_p = 152.4 mm and a blade pitch angle of $\beta(0.7R_p)$ = 20°, and its geometry and sectional airfoil data have been publicly released, making it particularly suitable for validation and comparative studies.

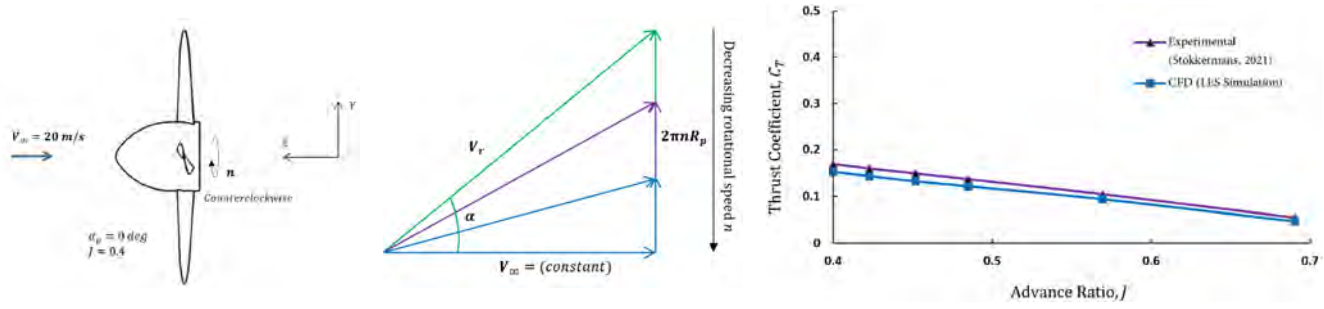


(a) (b) (c)

***Figure 3.49:** Overview of different test configurations, indicating main dimensions: a) Isolated propeller, b) Side view of OAA c) Front view of OAA.*

The computational framework comprised a rotating domain (RD) surrounding each propeller and a stationary domain (SD) representing the external flow field. Simulations were performed at a freestream velocity of 20 m/s. The dimensions of both computational domains are presented in Figure 3.49. The SD was sufficiently large to ensure undisturbed freestream boundary conditions and to minimize the influence of domain boundaries on the flow solution. The isolated propeller was evaluated over an advance ratio range of (J = 0.4-0.7), whereas the OAA configuration was investigated at (J = 0.4). An unstructured mesh was generated using ANSYS Meshing, with local refinements around the blades and rotating domains to accurately resolve near-wall and wake-flow structures. A mesh independence study demonstrated that an 8.6-million-element mesh provided an optimal compromise between numerical accuracy and computational cost. The aerodynamic analysis employed URANS coupled with *k-ωSST* turbulence model, enabling the resolution of both the mean flow field and the dominant turbulent structures within the interacting slipstreams.

To assess the impact of aerodynamic interactions on propeller performance in the OAA configuration, the performance of an isolated propeller was first evaluated and used as a reference case. This baseline serves as the benchmark against which the performance of each propeller in the OAA configuration is compared. Throughout this section, the term propeller plane refers to the plane of rotation of the propeller. The numerical setup was first validated against the experimental measurements (Stokkermans et al., 2021). Simulations were performed using the same F29 propeller under identical operating conditions and non-zero freestream velocity, as illustrated in Figure 3.50-a-b. Figure 3.50-c compares the thrust coefficient obtained from the present numerical simulations with the corresponding experimental data. The results show consistent trends and good overall agreement between the numerical predictions and experimental measurements. The max difference between the experimental and numerical thrust coefficients was found to be about 10%. Overall, the comparison provides confidence in the accuracy and reliability of the adopted numerical methodology.



(a) (b) (c)

Figure 3.50: (a) Isolated Propeller configuration b) Velocity triangle schematics; (c) Comparison of the isolated propeller thrust coefficient, obtained from the numerical simulation with experimental data.

Propeller Performance Analysis

The OAA configuration considered in this study is characterized by the following specific parameters: $\alpha_p = 0$, $d_x/R_p = 2.66$, and $d_y/R_p = 1.4$. The selection of these values was influenced by the design of the Airbus Vahana eVTOL aircraft. However, the choice of $d_x/R_p = 2.66$ corresponds to half of the distance in the Vahana design. This selection was made deliberately to effectively investigate and measure the effects of propeller–propeller interactions within the current configuration. The two propellers operate at the same advance ratio $J = 0.4$ and rotate counterclockwise (observer facing the propeller from the front). The performance of each propeller is described in Table 3.18. The overall thrust generated by the OAA configuration is compared with the combined thrust of two isolated propellers to analyze the ratio of changed performance with respect to design conditions. A computed 7% reduction in thrust and in power ratio in OAA configuration is reported. When compared with a single isolated propeller, the change in advance ratio determined by the slipstream impingement onto the aft propeller reduces the overall performance with respect to design. While the front propeller is located in a region of the flow field where the airflow remains undisturbed, the rear propeller, already with just a partial overlap, experiences a reduction of 12.4% ($\Delta C_{T\ rear/iso} = 0.019$) in thrust coefficient and a 10.43% ($\Delta C_{P\ rear/iso} = 0.011$) decrease in power coefficient. The interaction with the wake reduces the effective inflow velocity and lift generation, ultimately decreasing thrust production. In addition, the presence of the front propeller and its associated wake imposes interference drag on the rear propeller. This drag necessitates a higher power input to maintain the same thrust level, resulting in a reduction in power efficiency.

	Thrust coefficient	$C_{T(RP+FP)}/\ C_{T(2xiso)}$	*Power coefficient*	$C_{P(RP+FP)}/\ C_{P(2xiso)}$
Isolated propeller	0.149	0.93	0.111	0.94
Front propeller (FP)	0.147		0.110	
Rear propeller (RP)	0.130		0.099	

Table 3.18: Comparison of propeller performance in OAA configuration with isolated configuration for the condition where J = 0.4, α_p = 0, d_x/R_p = 2.66 and d_y/R_p = 1.4.

To effectively visualize and analyze the effect of the interaction on velocity distribution, a specific velocity range of 5-45 m/s was deliberately displayed for all cases. The velocity distribution in the front propeller plane, as illustrated in Figure 3.51, is similar to that of the isolated propeller plane. This similarity arises because the front propeller operates in a region that is not affected by presence of the rear propeller. On the other hand, the distribution shown in Figure 3.51, representing the rotational plane of the rear propeller, shows significant differences. In particular, the section of the rear propeller that partially overlaps with the front propeller experiences a non-uniform and disturbed flow from the front. This results in a nonuniform distribution of loads over the rear propeller disc.

Some sections of the rear propeller receive airflow that is more favorable for generating thrust, whereas others experience less favorable conditions. This non-uniform load distribution can result in a decrease in thrust production. The interaction is clearly observed by examining the slipstream of the two propellers in Figure 3.51-d, which is compared with the case of an isolated propeller in Figure 3.51-c.

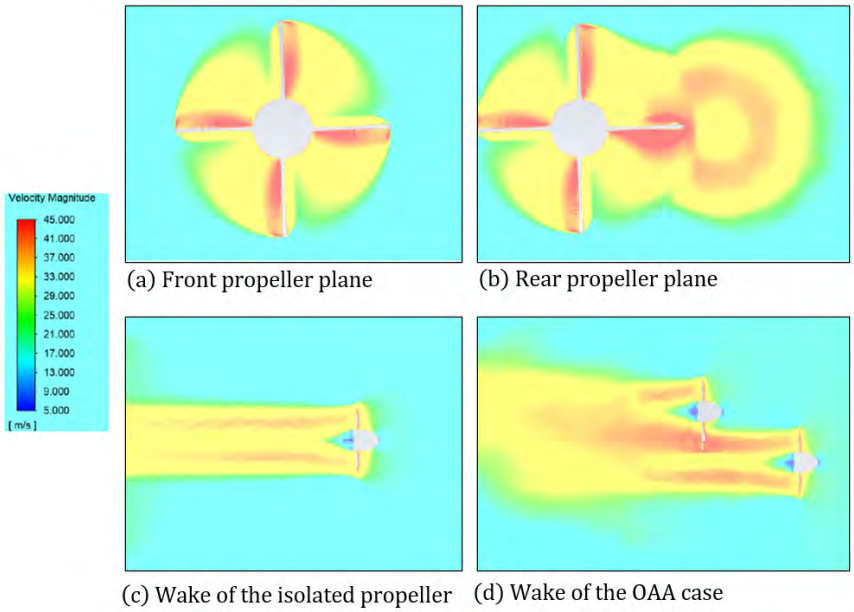


Figure 3.51: Velocity magnitude distributions in the planes of rotation and wake regions, a) Front rotational plane, b) Rear rotational plane c) Wake region of the isolated case and d) Wake region of the OAA case.

From analysis of the tip vortices, the interaction is seen to modify the local vortex dynamics and produces a more complex wake topology. The analysis of the propeller slipstreams and their interactions provides insight into the complex aerodynamic mechanisms governing multirotor systems. In particular, the blockage effect induced by the front propeller modifies the inflow conditions encountered by the rear propeller, resulting in changes to both thrust and torque distributions across the rotor disk. These findings demonstrate that aerodynamic interactions should not be treated as secondary effects during multirotor UAM vehicle conceptual design, as rotor placement directly influences propulsion efficiency, energy consumption, and potentially aeroacoustic performance. Although the present results provide meaningful insight into propeller–propeller interactions for a specific configuration and operating condition, further investigations are required to assess a wider range of geometric parameters, rotor arrangements, and flight regimes. In particular, future studies should examine hover, transition flight, varying rotor spacings, overlap ratios, and rotational directions to better characterize interaction effects across the operational envelope. Future work should also consider additional physical phenomena, including aeroacoustics, structural dynamics, vibrations, and flight-control interactions.

3.6 Transformer-Based Prediction of Small-Scale Rotor Aeroacoustics

Süleyman Tunçel, Hasan Çınar

In DICUAM, attention is also given to techniques which are able to reduce the costs of testing or high-fidelity simulations. In particular, machine learning-based noise prediction models have been found to significantly accelerate the design cycle and evaluation processes also for eVTOL design (Y. Kim & Lee, 2024; S. Li & Lee, 2020). To overcome the high computational cost of conventional methods, Deep Neural Networks (DNN) and hybrid models (NN-BET) have been developed, achieving up to 1800-fold acceleration in rotor noise prediction while maintaining high fidelity (Dabaghian et al., 2025; S. Li & Lee, 2020). In the literature, Gene Expression

Programming (GEP) has been employed to model complex broadband spectra, whereas transfer learning and active learning techniques optimize model accuracy under limited experimental data conditions (Gill & Lee, 2024; Zhou et al., 2025). Physics-informed neural networks and Deep Reinforcement Learning (DRL) algorithms, which offer certifiable accuracy in urban environments, enable the planning of dynamic flight routes that minimize noise impact (Park et al., 2025). In the DICUAM framework, a patch-based transformer integrated self-attention mechanisms for real-time prediction was applied to noise measurements of rotors at relatively low Reynolds number The aim was to obtain a data-driven framework that adapts the Transformer architecture fundamental to Large Language Models to forecast rotor noise generation. The proposed framework employs a patch-based causal transformer architecture for autoregressive time-series forecasting of rotor aeroacoustic pressure envelopes. Input sequences of 256 samples are segmented into non-overlapping patches via a 1D convolutional embedding layer, projected into a 64-dimensional latent space, and augmented with learnable positional embeddings to preserve causal temporal ordering. Two Transformer encoder layers with four multi-head self-attention heads capture long-range dependencies within the acoustic signal, and a linear regression head maps the encoder output to 16-step-ahead envelope predictions. Training was conducted over all microphone locations (1–40) and all grid positions (1–28) using data from three rotor advance ratios (J1–J3), with the fourth (J4 = 0.61) reserved for testing. All trainable parameters were jointly optimized using AdamW, minimizing the Mean Squared Error between predicted and measured envelopes, with weight decay and learning rate applied to mitigate overfitting. All computations were GPU-accelerated. Evaluation on the held-out RSJ4 dataset showed strong prediction performance across many microphone locations; for example, the model achieved $R^2 = 0.966$ at mic19 and $R^2 = 0.830$ at mic39, indicating that the proposed transformer-based framework generalizes effectively to a previously unseen advance ratio.

The acoustic dataset used in this study was published by Baars & Ragni (2024). Measurements were conducted in the anechoic A-Tunnel of Delft University of Technology, using a two-bladed small-scale rotor (D_p = 0.30 m, NACA 4412, 7860 RPM, f_b = 262 Hz, M_{tip} = 0.358, $Re_{c75} = 1.35 \cdot 10^5$. Four advance ratios were tested by varying the freestream velocity while keeping the rotational speed constant: $J = 0$ (hover, U_∞ = 0 m/s), 0.24 (9.6 m/s), 0.41 (16.0 m/s), and 0.61 (24.0 m/s). Acoustic pressure time series were recorded at 1120 microphone positions (28 boom positions × 40 sensors, 60 mm spacing) using GRAS 40PH free-field microphones sampled simultaneously at f_S = 51.2 kHz for T = 40 s. The dataset comprises 157 mat files (≈ 1.5 GB each), each storing a [2’048’000, 41, 3] matrix: the first 40 channels are microphone signals (raw, band-pass filtered, and A-weighted), and channel 41 is the 1/rev encoder signal. Baseline recordings without the rotor (motor-only and tunnel-only) are also included for noise-floor characterization.

Model performance is evaluated using four complementary criteria: Mean Square Error (MSE), Root Mean Square Error (RMSE), Mean Absolute Error (MAE), and the coefficient of determination R^2. In all expressions, N denotes the number of evaluation samples, y_k the k^{th} ground-truth observation, and $\hat{y}_k$ the corresponding model prediction. MSE quantifies the average squared residual, imposing a quadratic penalty that amplifies the influence of large deviations, a desirable property given the impulsive intensity modulations characteristic of small-scale rotor aeroacoustics:

$$MSE=\frac{1}{N}\sum_{k=1}^{N}(y_k-\hat{y}_k)^2,\quad RMSE=\sqrt{\frac{1}{N}\sum_{k=1}^{N}(y_k-\hat{y}_k)^2},\quad MAE=\frac{1}{N}\sum_{k=1}^{N}|y_k-\hat{y}_k|,\quad sMAPE=\frac{100}{n}\sum_{t=1}^{n}\frac{2|y_t-\hat{y}_t|}{|y_t|+|\hat{y}_t|}$$

RMSE recovers the physical unit of the target signal by taking the square root of MSE, enabling direct comparison of prediction errors against the measurement scale. MAE averages absolute residuals without squaring, yielding a linearly proportional and outlier-robust measure of typical prediction discrepancy across the full operational range. To quantify the relative forecast accuracy of the transformer-based supervised deep learning model, we calculate

the symmetric Mean Absolute Percentage Error (sMAPE), which measures the average relative magnitude of errors across n total data points by comparing the actual ground truth value, y_t, against the model's predicted value, $\hat{y}_t$, at each time step t. Finally, R^2 measures the fraction of signal variance explained by the model relative to a mean-value baseline, where $\bar{y}$ is the sample mean of the observations:

$$R^2 = 1 - \frac{\sum_{k=1}^{N}(y_k - \hat{y}_k)^2}{\sum_{k=1}^{N}(y_k - \bar{y})^2}$$

Values of R^2 near unity indicate high model fidelity, while values near zero suggest no improvement over a trivial predictor. As a normalized, scale-independent index, R^2 complements the absolute error metrics and facilitates cross-dataset comparisons of model performance.

Simulation results and discussion

Table 3.19 presents the test performance metrics of the RSJ4 model in both normalized and original scales. The results indicate relatively low prediction errors, with RMSE and MAE values remaining small in the original scale, while the R^2 value of 0.60 suggests a moderate level of predictive capability. Overall, these metrics demonstrate that the model can capture the general behavior of the acoustic signal with reasonable accuracy.

Metric	*Normalized Scale*	*Original Scale*
MSE	1.474796	0.061755
RMSE	1.214412	0.248506
MAE	0.119248	0.024402
R^2	0.603921	0.603921
MAPE (%)	57.789230	6.351521
sMAPE (%)	15.922997	6.314512

Table 3.19: RSJ4 Test Metrics (Normalized and Original Scale).

Table 3.20 presents the prediction performance across different forecasting horizons for the RSJ4 dataset. The results show that the error metrics (MSE, RMSE, and MAE) slightly increase as the prediction horizon extends, while the R^2 values remain relatively stable around 0.60. This indicates that the model maintains consistent predictive capability even for longer forecasting horizons.

Forecast horizon	*MSE*	*RMSE*	*MAE*	*R^2*
t+01	0.061915	0.248828	0.013617	0.603006
t+05	0.061563	0.248120	0.020095	0.605233
t+10	0.061527	0.248046	0.027187	0.605346
t+15	0.062160	0.249320	0.031989	0.601231

Table 3.20: Per-Horizon Metrics on RSJ4 (Original Scale).

The results show that prediction errors decrease substantially after the first few grid positions, while the R^2 values generally increase and remain above 0.8 for most cases. This indicates that the model achieves stable and reliable prediction performance across different grid positions (not reported for conciseness) The RMSE, MAE, and R^2 values for each microphone are also investigated in the RSJ4 dataset. The results show that prediction errors gradually decrease for microphones located further in the array, while the R^2 values generally increase and remain above 0.9 for many microphones. This trend indicates that the model provides increasingly accurate predictions across most microphone positions. Figure 3.52 compares measured and predicted acoustic signal amplitudes at three microphone locations for the foremost grid position (GP01). Here GP01 is at the forefront position among the 28 grid positions, and the same convention applies to Mic 1, Mic 20, and Mic 40 along the microphone array. The plots show 1000 selected points predicted with the transformer-based model. The model generally follows the overall evolution of the signal; however, noticeable differences occur at several high-amplitude peaks, particularly for Microphone 1. For Microphones 20 and 40, the predicted signals align more closely with the measurements, indicating that the model captures the main structure of the acoustic signal despite some limitations in representing sharp variations.

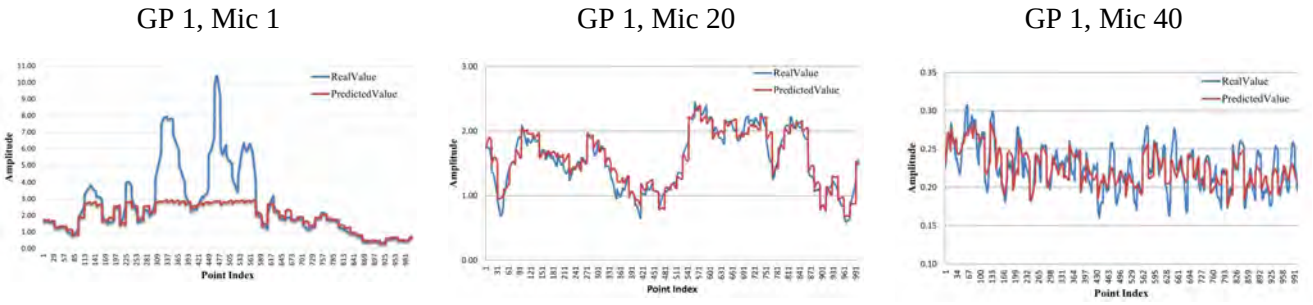


Figure 3.52: Comparison of real measured values and model-predicted values across three microphone positions (Mic 1, Mic 20, and Mic 40) for GP 1, plotted as a function of point index.

Figure 3.53 presents prediction results for the 1000 selected points at GP14, a mid-array position, providing a positional perspective for evaluating model performance. Compared with the previous configuration, the predicted signals exhibit closer alignment with the measured amplitudes at all microphone locations. The model effectively represents both global signal behavior and local fluctuations, suggesting that increasing the number of input features improves the representation of the acoustic dynamics.

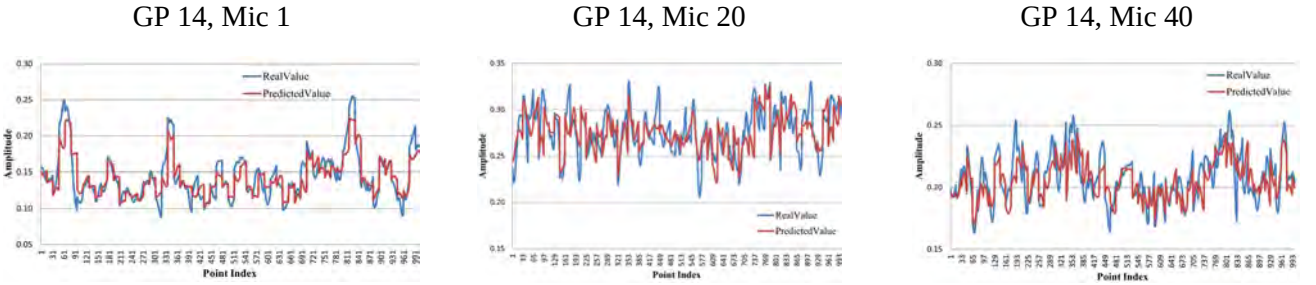


Figure 3.53: Comparison of real measured values and model-predicted values across three microphone positions (Mic 1, Mic 20, and Mic 40) for GP 14, plotted as a function of point index.

The model effectively represents both global signal behavior and local fluctuations, suggesting that increasing the number of input features improves the representation of the acoustic dynamics. Figure 3.54 shows the prediction performance of the proposed model for 3 different mic locations on the y axis at the 28-th position of grid, and 28-th position remains the last in the 28 position of the grid. The proposed Transformer-based model performs multi-

step time-series forecasting of the acoustic envelope signal. Given an input sequence of length L = 256 time steps L=256 time steps, the model predicts the future acoustic envelope over a forecast horizon of H = 16 time steps: H=16 time steps:

$$\{x_{t-L+1}, \dots, x_t\} \rightarrow \{\hat{y}_{t+1}, \hat{y}_{t+2}, \dots, \hat{y}_{t+H}\}$$

Where x_t represents the observed acoustic envelope and $\hat{y}_{t+H}$ denotes the predicted envelope value at horizon h. The original acoustic measurements were recorded at a sampling frequency of 51.2 kHz. After envelope extraction and temporal down-sampling by a factor of 8, the effective sampling frequency becomes 6.4 kHz, corresponding to a temporal resolution of 0.156 ms for a 2.5 ms prediction into the future.

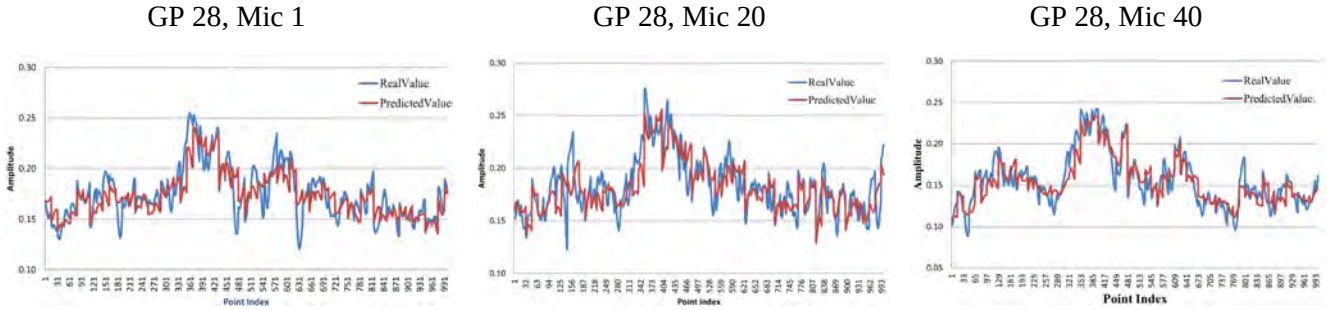


Figure 3.54: Comparison of real measured values and model-predicted values across three microphone positions (Mic 1, Mic 20, and Mic 40) for GP 28, plotted as a function of point index.

Reporting per-horizon metrics enables analysis of how prediction accuracy evolves as the forecast distance increases, which is particularly relevant for real-time aeroacoustic monitoring applications. The prediction error varies across microphone grid positions due to differences in the local acoustic field. As seen in the following table and in the previous figures, the first two grid positions exhibit significantly higher prediction errors (GP < 3). These positions lie closest to the rotor disk and therefore fall within the near-field region, where the measured pressure signal contains strong hydrodynamic pressure fluctuations, blade–vortex interactions, and broadband turbulent components. Such non-stationary effects increase the signal variance and make accurate forecasting more challenging for data-driven models. In contrast, grid positions (GP > 3) correspond to regions progressively farther from the rotor where the acoustic field becomes more dominated by propagating acoustic waves than by hydrodynamic pressure fluctuations. Moreover, the acoustic envelope becomes smoother and more predictable, resulting in substantially lower RMSE values and higher R^2 scores. A gradual decrease in R^2 toward the farthest grid positions can also be observed; this is expected, because the acoustic amplitude decreases with distance from the rotor, which reduces the variance of the signal and makes the coefficient of determination more sensitive to small prediction errors.

From analysis of the forecasted values, it can be deduced that the model preserves a consistent overall predictive capability even for longer forecasting horizons. However, these values represent the cumulative performance over the entire RSJ4 test set. In contrast, the spatially resolved results show that local prediction performance is substantially higher at most grid positions, where R^2 frequently exceeds 0.80 and reaches values above 0.95 in some cases. Therefore, while the global RSJ4 performance is moderate, the local spatial performance is considerably stronger across much of the measurement domain. Overall, the spatial distribution of prediction errors follows the expected aerodynamic and aeroacoustic behavior of rotor noise propagation. Table 3.21 summarizes the prediction error metrics (MSE, RMSE, and MAE) at the three microphone positions for the three representative boom settlements (GP1, GP14, GP28). The single near-field location GP1 & Mic1 dominates the error budget, whereas all remaining location pairs show very small errors, consistent with the spatial trends discussed above.

The model demonstrated stable prediction performance across multiple spatial positions and forecast horizons. Evaluation on the previously unseen RSJ4 operating condition displayed that the model can make a generalization effectively to new flight regimes, achieving an overall coefficient of determination of approximately $R^2 \approx 0.604$. Detailed spatial analysis revealed that prediction accuracy varies systematically with microphone and grid position. Higher prediction errors were observed near the rotor wake region, where hydrodynamic pressure fluctuations and blade–vortex interactions dominate the signal. In contrast, microphones positioned closer to the rotor exhibited significantly enhanced accuracy due to the stronger presence of periodic rotor noise and smoother acoustic envelope dynamics. The results confirm that transformer-based architectures can effectively learn the temporal structure of aeroacoustic signals while enabling fast inference suitable for real-time applications. The proposed approach therefore provides a promising tool for rapid aeroacoustic prediction, with potential applications in active noise monitoring, flight trajectory optimization, and future real-time noise control systems for eVTOL aircraft.

Future work will focus on incorporating additional spatial features, extending the framework to multirotor configurations, and integrating physics-informed constraints to further improve prediction accuracy and generalization.

Microphone and position	*MSE*	*RMSE*	*MAE*
GP1 & Mic1	2.844902	1.686684	0.850684
GP1 & Mic20	0.016526	0.128555	0.095810
GP1 & Mic40	0.000270	0.016433	0.012462
GP14 & Mic1	0.000287	0.016938	0.011815
GP14 & Mic20	0.000339	0.018423	0.013898
GP14 & Mic40	0.000162	0.012747	0.009975
GP28 & Mic1	0.000210	0.014479	0.010476
GP28 & Mic20	0.000255	0.015979	0.011806
GP28 & Mic40	0.000176	0.013285	0.010103

Table 3.21: Prediction error metrics (MSE, RMSE, MAE) for all microphone positions across three boom settlements (GP1, GP14, GP28).

3.7 Assessing Dynamic Rollover Hazards in Multirotor eVTOL Aircraft

Marilena Pavel

Safety is the primary design constraint in aviation, shaping certification requirements, operational procedures, and vehicle architecture. The rapid development of UAM (Doo et al., 2021) technologies has led to a large diversity of eVTOL aircraft (Figure 3.55). These vehicles have unique characteristics that result in difficult design choices and limited design space when considered during design. For example, some configurations use fixed-pitch blades and attempt to use rotor speed for primary flight control. This means that vehicle size and the powertrain now act as the primary flight control actuators, resulting in the need for the flight controls to be tightly integrated with the aircraft size.

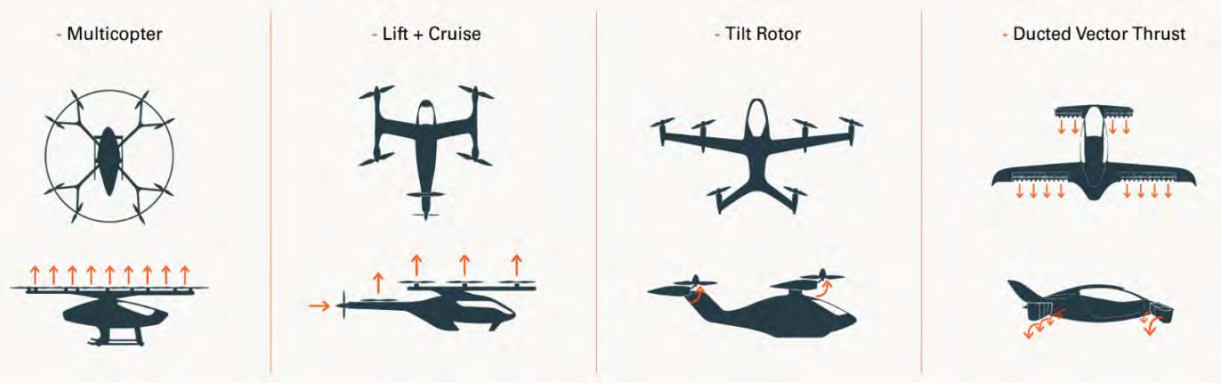


Figure 3.55: The diversity of UAM vehicles integrating multiple rotors and multiple control strategies. Reproduced from Chahba et al., 2023, © 2023 to the authors. Licensee MDPI, Basel, Switzerland. Licensed under CC BY 4.0 (https://creativecommons.org/licenses/by/4.0/).

Also, many of these configurations have multiple, stiff rotors. However, rotors tend to amplify certain aerodynamic instabilities, resulting in a sharper, more jerky response from the vehicle when operating in an atmospheric environment with gusts or turbulence. Having multiple rotors creates multiple sources of vibration in the vehicle but also provides more control effectors. Therefore, it is necessary to understand how the flight dynamics of these vehicles are impacted by their novel configuration.

We also need to understand how these new vehicles behave in relation to past configurations, identifying how past lessons can be effectively applied to these new, emerging concepts. One of the lessons from the past is related to helicopter and auto-gyro accidents involving a dangerous condition that occurs when the aircraft tips onto its side close to the ground and the pilot is unable to stop it. This is known as the dynamic rollover phenomenon. For helicopters, a safety analysis on rollover occurrences in the National Transportation Safety Board (NTSB) database (Pavel et al., 2013) showed that, from a total of 100 helicopter emergency landings, 20.8% (29 cases) involved failed autorotation and 28.8% (39 cases) rollover events. Furthermore, FAA reports indicated that, from approximately 14% accidents involving rollover, 5% caught fire (Palmerton, 2005). This percentage while small is not insignificant making the requirement of “appropriate location of emergency exits a necessity”. While the tendency of rollover accidents in helicopters decreased in the last 10 years, rollover occurrences still correspond to 9% of the accidents (Bills et al., 2026; Saleh et al., 2022; White et al., 2021). According to the NTSB aviation occurrence category definitions, there is a difference between rollover and dynamic rollover. While rollover can be associated with abnormal contact during landing/take-off and can be therefore coded as “Abnormal Runway Contact (ARC)” event, dynamic rollover (especially for helicopters) involves the aircraft losing control around a pivot point and it should be coded as Loss of Control-Ground (LOC-G) event rather than ARC. Heli-offshore industry report describes as 7% as LOC-G occurrences from all 65 accidents included in the database 2013-2024 (HeliOffshore, 2025). Gyroplanes can also experience dynamic rollover especially immediately after landing (Duda et al., 2022).

The objective of this analysis is to investigate the physical principles for the rollover of a eVTOL during pure vertical descent and touch down to rollover. The VTOL vehicle to which the rollover analysis will be performed is an 8-rotor lift+cruise configuration similar to the NASA concept lift+cruise VTOL (Putnam & Littell, 2023).

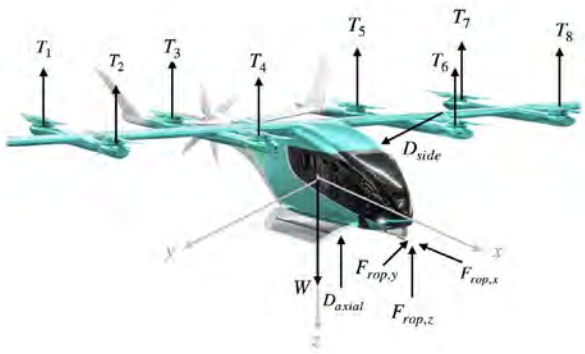


Figure 3.56: The 8-rotor lift+cruise VTOL configuration.

A five DOF model will be developed for this vehicle (u, v, w, p, q). The yaw is neglected in this study being assumed that the vehicle rolls over a pivoting point before yawing, see Figure 3.56. The scenario considered was for a dynamic rollover caused by an obstacle on the ground, occurring while the eVTOL is drifting and descending close to the ground, see Figure 3.57. The vehicle begins in a hovering position, 8 meters above the ground (i.e. the distance between the landing gear and the landing surface). The drift is introduced by a wind gust close to the ground, which contributes to an additional roll angle being initiated. This study will not consider pilot correction of this situation; this will be the objective of future work, which will involve developing pilot strategies to cope with eVTOL rollover.

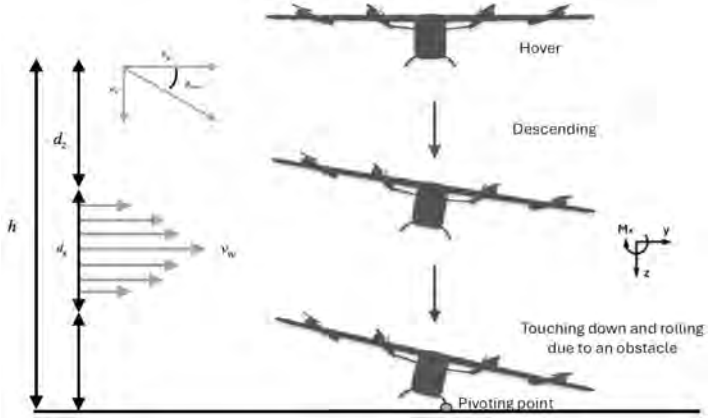


Figure 3.57: The rollover scenario.

It was assumed that when the vehicle has a downwards vertical velocity of 3 m/s or higher, the landing is in danger. The rollover was assumed to happen around a pivoting point. For the vertical descent a PID controller on rotor RPM was implemented to simulate a stable descending flight. As the eVTOL is approaching the ground, a wind gust is encountered. The wind gust profile used in this paper is modeled as the classical 1-cosine shape (Moorhouse & Woodcock, 1982). The methodology used for the rollover scenarios is presented in Figure 3.58. Looking at this figure, it follows that different variations in the scenarios are introduced in the eVTOL vehicle (8 rotors: 4 propellers front and 4 propellers rear) descending. These scenarios will be compared with the rollover tendency of a helicopter (1 rotor).

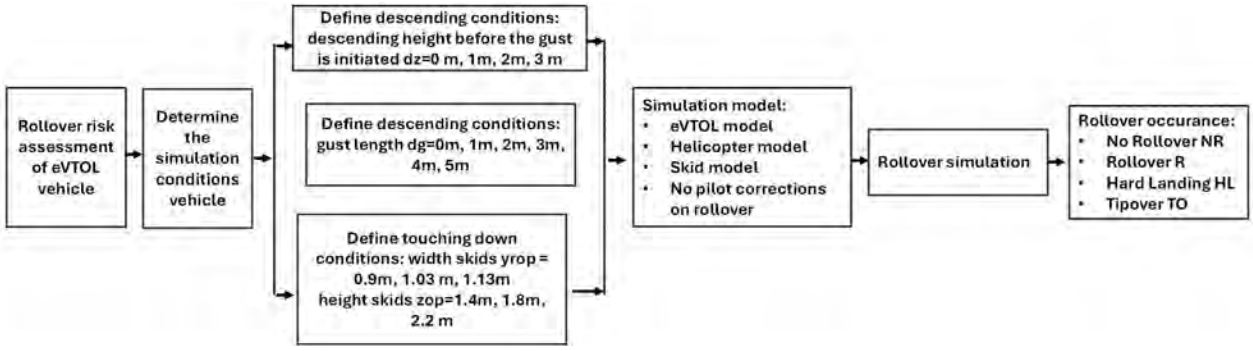


Figure 3.58: Rollover methodology.

The results will be categorized according to Table 3.22:

1) **No rollover:** the simulation results show that the rollover angle is under the critical angle and therefore the vehicle will not rollover at the impact with an obstacle around pivoting point;
2) **Hard landing:** the vehicle descends with a velocity of 3m/s or higher;
3) **Rollover tendency:** the vehicle is expected to rollover as the critical angle is achieved (Note: the pilot controller is not added)
4) **Tipped over:** the rollover results in the vehicle tipping the ground on one of its sides.

Occurence	Depiction
No Rollover	NR
Hard Landing	HL
Rollover	RO
Tipped over	TO

Table 3.22: Scenario cases.

Table 3.23 presents the results of the rollover scenarios when the eight-rotor propeller aircraft encountered different gusts during descending before touching the ground, this in the case of the eVTOL configuration. Looking at this figure, the results show that, for calm to gentle breeze, the critical rolling angle is not reached. If the gust speed increases and in the case of high ϕ_{wind} angles the aircraft will be in danger of hard landing as the extra speed component w_{wind} will accelerate the aircraft descending (Note, it is assumed that the pilot does not control this by increasing the pitch propeller). When the gust speed increases, combined with relatively small values of wind angles (so crosswind), the aircraft is in danger of rolling over. One can see that even for smaller values of crosswinds the aircraft tendency is to tip over as much higher values of critical rollover angle are achieved. This is due to the extra rolling dynamics introduced by the left right propellers. At higher crosswinds the aircraft are somehow only in the region of rollover danger without tipping over. This is due to the higher moment of inertia about the longitudinal axis which resists rapid changes in roll.

EIGHT-PROPELLER EVTOL AIRCRAFT			ϕ_{wind} (deg) EFFECTS OF WIND GUST ON ROLLOVER TENDENCY										
Description	Vg(m/s)	Vg (KTS)	-45	-36	-27	-18	-9	0	+9	+18	+27	+36	+45
Calm (0BFT)	0	0	NR	NR	NR	NR	NR	NR	NR	NR	NR	NR	NR
Light air (1BFT)	2	3.8	NR	NR	NR	NR	NR	NR	NR	NR	NR	NR	NR
Gentle breeze (3BFT)	4	7.9	NR	NR	NR	NR	NR	NR	NR	NR	NR	NR	NR
	6	11.6	HL	HL	NR	NR	NR	NR	NR	NR	NR	NR	NR
Moderate breeze (4BFT)	8	15.5	HL	HL	HL	NR	NR	NR	NR	NR	NR	NR	NR
Fresh breeze (5BFT)	10	19.4	HL	HL	HL	NR	NR	NR	NR	NR	NR	HL	HL
	12	23.3	HL	HL	HL	HL	NR	TO	NR	NR	NR	HL	HL
Strong breeze (6BFT)	14	27.2	HL	HL	HL	HL	TO	TO	TO	TO	NR	HL	HL
Near gale (7BFT)	16	31.1	HL	HL	HL	HL	TO	RO	RO	TO	TO	HL	HL
	18	35	HL	HL	HL	HL	RO	RO	RO	RO	TO	TO	HL
Gale (8BFT)	20	38.8	HL	HL	HL	HL	RO	RO	RO	RO	RO	TO	TO
	22	42.7	HL	HL	HL	TO	RO	RO	RO	RO	RO	RO	TO
Strong gale (9BFT)	24	46.6	HL	HL	TO	TO	RO	RO	RO	RO	RO	RO	TO
	26	50.5	TO	TO	TO	TO	RO	RO	RO	RO	RO	RO	RO

Table 3.23: Rollover tendency for an 8-propeller eVTOL aircraft in different gust scenarios.

HELICOPTER			ϕ_{wind} (deg) EFFECTS OF WIND GUST ON ROLLOVER TENDENCY										
Description	Vg(m/s)	Vg (KTS)	-45	-36	-27	-18	-9	0	+9	+18	+27	+36	+45
Calm (0BFT)	0	0	NR	NR	NR	NR	NR	NR	NR	NR	NR	NR	NR
Light air (1BFT)	2	3.8	NR	NR	NR	NR	NR	NR	NR	NR	NR	NR	NR
Gentle breeze (3BFT)	4	7.9	NR	NR	NR	NR	NR	NR	NR	NR	NR	NR	NR
	6	11.6	NR	NR	NR	NR	NR	NR	NR	NR	NR	NR	NR
Moderate breeze (4BFT)	8	15.5	NR	NR	NR	NR	NR	NR	NR	NR	NR	NR	HL
Fresh breeze (5BFT)	10	19.4	HL	NR	NR	NR	NR	NR	NR	NR	NR	HL	HL
	12	23.3	HL	HL	NR	RO	RO	RO	NR	NR	HL	HL	HL
Strong breeze (6BFT)	14	27.2	HL	HL	HL	RO	RO	RO	RO	TO	HL	HL	HL
Near gale (7BFT)	16	31.1	HL	HL	HL	HL	TO	RO	RO	RO	HL	HL	HL
	18	35	HL	HL	HL	HL	RO	RO	RO	RO	RO	HL	HL
Gale (8BFT)	20	38.8	HL	HL	HL	HL	RO	RO	RO	RO	RO	HL	HL
	22	42.7	HL	HL	HL	HL	RO	RO	RO	RO	RO	RO	HL
Strong gale (9BFT)	24	46.6	HL	HL	RO	RO	RO	RO	RO	RO	RO	RO	HL
	26	50.5	RO	RO	RO	RTO	RO	RO	RO	RO	RO	RO	RO

Table 3.24: Rollover tendency for a helicopter in different gust scenarios.

Table 3.24 presents for comparison the results of rollover scenarios in the case of a helicopter assumed to have a similar mass with the eVTOL aircraft and a much lower disk loading (bigger rotor). This means that the helicopter will have a much smaller moment of inertia around the roll x-axis with a CG position above the ground higher than in the case of eVTOL. Looking at this figure, it follows that, exactly as in the case of eVTOL aircraft, the helicopter will roll over in crosswinds conditions but there is no indication of tip over. This is because the helicopter CG is closer to the ground. With a lower moment of inertia about the longitudinal (roll) axis, the helicopter will tend to respond more quickly to the same amount of rolling moment. This makes the helicopter more sensitive to crosswind disturbances, increasing the likelihood of rapid roll onset. However, although low inertia increases sensitivity, it

will enhance controllability. In contrast, the higher longitudinal axis inertia of the eVTOL aircraft will provide more rolling stability but it will reduce responsiveness and once the bank angle is developing it will take longer to stop. Next, to understand the effect of rotor interferences, a sensitivity analysis is performed on the thrust difference distribution between the four front and four rear rotors. This is achieved by introducing a tip loss factor that was introduced in the thrust of the rear rotors. Looking at Table 3.25 it follows that, once the difference in thrust increases in the rear rotors due to rotor-rotor interferences, the tendency to roll over and tip increases, especially when wind gusts become stronger. This demonstrates the importance of considering the aerodynamic interferences in the case of eVTOL configurations.

Concluding, this work presented an exploratory study for the rollover tendency of eVTOL multirotor aircraft. For this, an 8-propeller lift+cruise eVTOL configuration was selected and the dynamic rollover phenomenon was analyzed during a vertical landing scenario with a wind gust and an obstacle on the ground considered as the pivoting point for roll. A simple lateral flight dynamics model was developed accounting for the different propeller thrust forces of the eVTOL aircraft expressed in momentum theory and corrected to account for ground effect and vortex ring state. A skid-type landing gear model was added now of vehicle touch down and roll over a pivoting point. The eVTOL aircraft results were compared to a helicopter rollover scenario of the same mass as the eVTOL aircraft.

Thrust decrease on the rear rotors (%) EIGHT-PROPELLER EVTOL AIRCRAFT									
Description	Vg(m/s)	Vg (KTS)	-2%	0%	+2%	+4%	+6%	+8%	+10%
Calm (0BFT)	0	0	RO	NR	NR	NR	HL	HL	HL
Light air (1BFT)	2	3.8	RO	NR	NR	NR	HL	HL	HL
Gentle breeze (3BFT)	4	7.9	RO	NR	NR	NR	HL	HL	HL
	6	11.6	RO	NR	NR	NR	HL	HL	HL
Moderate breeze (4BFT)	8	15.5	RO	NR	NR	NR	HL	HL	HL
Fresh breeze (5BFT)	10	19.4	RO	NR	NR	NR	HL	HL	HL
	12	23.3	RO	TO	NR	NR	HL	HL	HL
Strong breeze (6BFT)	14	27.2	RO	TO	TO	TO	HL	HL	HL
Near gale (7BFT)	16	31.1	RO	RO	RO	TO	TO	TO	HL
	18	35	RO	RO	RO	RO	TO	TO	TO
Gale (8BFT)	20	38.8	RO	RO	RO	RO	RO	RO	TO
	22	42.7	RO	RO	RO	RO	RO	RO	RO
Strong gale (9BFT)	24	46.6	RO	RO	RO	RO	RO	RO	RO
	26	50.5	RO	RO	RO	RO	RO	RO	RO

Table 3.25: Sensitivity of rollover tendency to rotor-on-rotor interferences.

It was found that, compared to a helicopter, the eight-propeller eVTOL aircraft was less sensitive to dynamic rollover due to its higher moment of inertia about the longitudinal (roll) axis. However, once it was involved in dynamic rollover, it proved more difficult to recover and exhibited greater persistence to rollover. This demonstrates the need to develop rollover techniques that require good pilot/flight control system anticipation, given that the eVTOL aircraft lags in its response to the rollover phenomenon. For the scenario presented in this study where a crosswind and an obstacle on the ground were used for triggering the rollover condition one could think of crab and/or sideslip combined techniques used in the case of fixed-wing aircraft for maintaining wing-level attitude (Ren et al., 2025). Future work will involve development of pilot controllers during the rollover phenomenon and extension of the database of rollover scenarios.

4 Urban Emission Mapping, Vertiports, and Urban Integration

4.1 Noise with Vision Transformers: A Generalized Deep Learning Framework

Enrique Aldao, Lourenço Tércio Lima Pereira, Sen Wang, Fernando Veiga-López, Daniele Ragni, Higinio González-Jorge

In the context of Urban Air Mobility (UAM), aircraft are expected to operate at low altitudes over densely populated urban areas (Cohen et al., 2021). With the anticipated levels of traffic, these operations can significantly increase noise exposure in sensitive and residential areas, potentially provoking community annoyance, adverse health effects, and public resistance to the deployment of UAM services (Johnson & Silva, 2022). Therefore, for the widespread adoption of this paradigm, comprehensive noise assessments are required to design operational procedures and mitigation strategies that ensure social acceptability and prevent the population from being exposed to excessive noise levels.

These methods typically characterize the sound pressure level at a given distance from the vehicle. However, to assess the impact on the population, another crucial aspect is the simulation of noise propagation. Urban areas feature complex geometries, including high-rise buildings, narrow streets, and varying terrain, all of which can significantly affect acoustic wave propagation through reflection, diffraction, scattering, and absorption. This geometric complexity, combined with the large spatial extent of urban areas, severely limits the applicability of full-wave methods such as the Finite Element Method (FEM) and the Boundary Element Method (BEM). This limitation is particularly critical in the audible frequency range, where fine mesh resolutions are required to resolve short wavelengths. Due to these limitations, instead of solving noise propagation directly as a partial differential equation (PDE), geometric methods are often employed, particularly ray tracing. These methods discretize the acoustic field into narrow rays to simulate propagation, including reflections and atmospheric refraction, enabling efficient estimation of sound pressure levels in complex environments. However, as a purely geometric approach, ray tracing neglects wave effects such as diffraction, interference, and finite wavefront extent, which can lead to non-physical artefacts such as sharp shadow zones and infinite amplitudes at caustics. It also suffers from high computational cost when solving the eigenray problem, making dense receiver field evaluation inefficient. Gaussian Beam Tracing (GBT) addresses some of these limitations by propagating finite-width beams with Gaussian transversal profiles, naturally representing wavefront extent (Porter & Bucker, 1987). The pressure field is obtained through coherent superposition of beam contributions, which inherently captures interference and avoids both caustics and the eigenray problem. Beam spreading also enables a partial representation of diffraction, reducing fully shadowed regions, although it remains less accurate near sharp edges and corners. Overall, GBT has been successfully applied to UAM problems, offering a good trade-off between accuracy and efficiency, with runtimes on the order of minutes (Bao et al., 2025; Yunus et al., 2023a). However, despite their efficiency, these methods remain computationally expensive for applications requiring multiple simulations, such as the optimization of UAM operations. UAM vehicles typically emit noise over a range of frequencies, including multiple blade-passing frequencies (BPFs) and broadband noise. For a single vehicle at a given trajectory point, several simulations are required because noise propagation and attenuation depend on frequency.

Given the limitations of direct simulations, this chapter investigates the use of AI-based surrogate models to accelerate the computation of urban noise propagation. Using a database of precomputed solutions, this information is used to train a Vision Transformer (ViT)-based model, enabling fast inference of noise footprints with minimal computational cost. In DICUAM, this study employs a database of six real city 3D models including the following cities across the world: Amsterdam, São Paulo, New York, Madrid, Hong Kong, and Melbourne (Figure 4.59). Each of these scenarios encompasses an area of $10 \times 10\ \text{km}^2$, thus covering an extensive area with varied urban layouts. In these scenarios, noise propagation is simulated using a Gaussian Beam Tracing (GBT) method, to create a

database of noise propagation simulations in different flight conditions. In these simulations, instead of computing the absolute sound pressure level, the Sound Level Decay (SLD) is calculated. SLD represents the noise intensity level difference between a given point in the environment and a reference noise sphere, located at a radius of 10 m with respect to the vehicle's geometric center.

Figure 4.60 shows the corresponding SLD of one such simulation in a scenario with high-rise buildings. As shown, building occlusions cause significant wave reflections that tend to concentrate the acoustic energy in urban canyons, therefore increasing the overall sound intensity in those areas. With this approach, a database of 120,000 simulations is constructed using the city model database, randomizing the following variables:

1. **Vehicle position:** The UAV position is randomized in all conducted simulations within each city, including its horizontal location and relative altitude with respect to the ground. Altitudes are drawn from typical UAM operational envelopes, ensuring coverage of both low-altitude hover and higher-altitude cruise conditions.
2. **Noise emission frequency:** The GBT model incorporates atmospheric absorption according to ISO 9613-1 (International Organization for Standardization (ISO), 2024), which increases with frequency. To represent this variation, the emission frequency is randomized by selecting frequencies within the range 50 Hz to 2 kHz, covering typical blade passing frequencies and extending into the broadband regime.

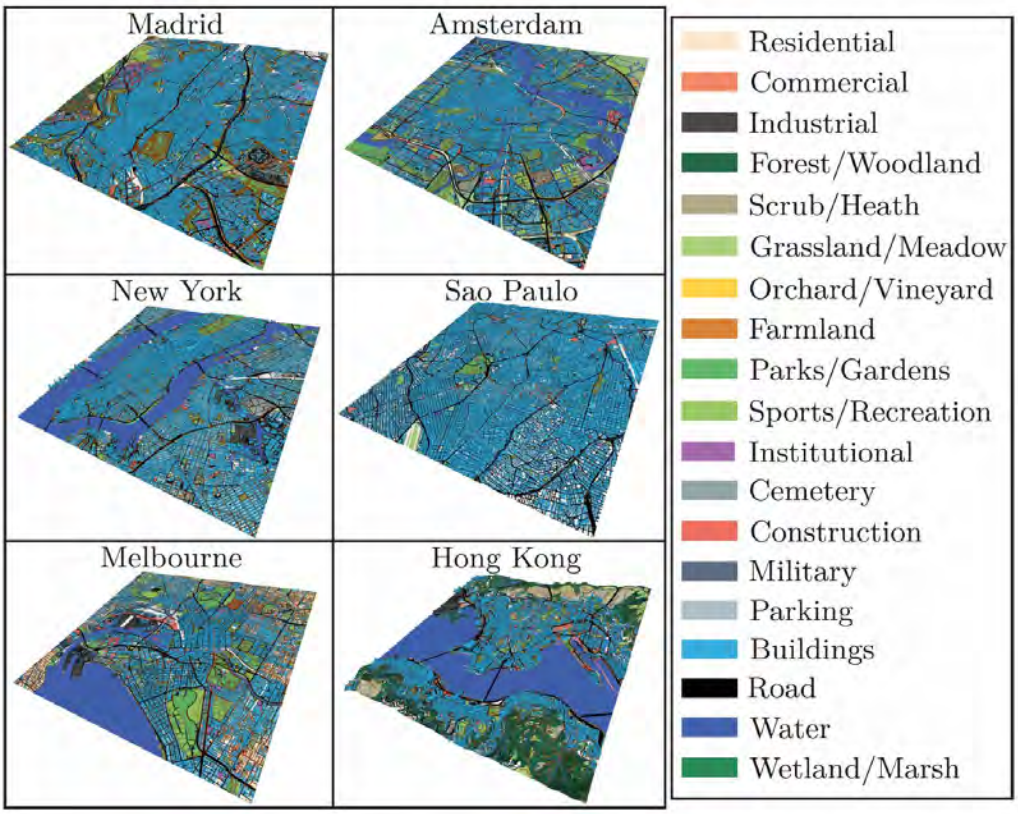
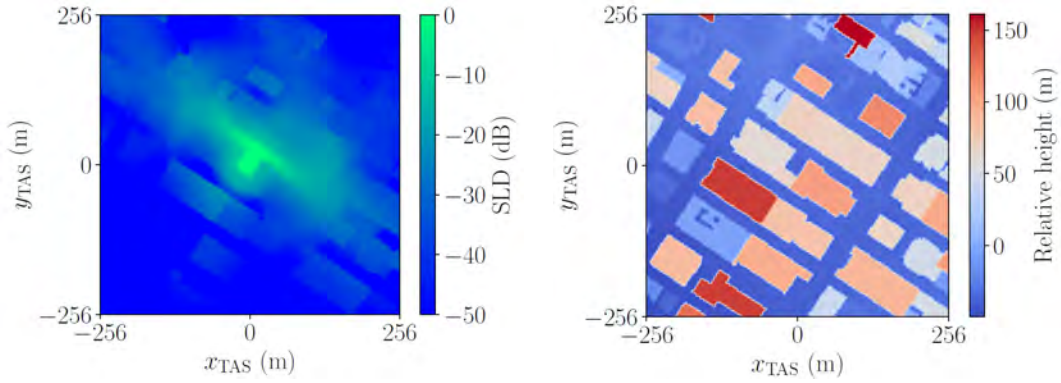


Figure 4.59: Final 3D models of the proposed study case scenarios. Each model represents a 10×10 km square area, covering nearly the entire extent of the respective city. Surface colors correspond to OpenStreetMap categories, Map data © OpenStreetMap contributors, available under the Open Database License (ODbL) v1.0 Copyright and License (OpenStreetMap, 2026).

3. **Vehicle true airspeed**: In the presence of uniform wind or vehicle motion, a relative velocity with respect to the air is induced. This relative motion produces a Doppler effect, modifying the effective frequency. This parameter was randomized within the range of 0-70 m/s, corresponding to typical speeds of UAM vehicles.

In all these simulations, the following information is stored:

1. **SLD of GBT simulations:** This represents the actual sound level decay with respect to the reference sphere that is to be predicted by the neural network (Figure 4.60-a). By default, an array of uniformly spaced points covering a 512 × 512 m domain is chosen, with the vehicle located at the center of the domain. These receiver points are placed at a reference height of 2 m above terrain or building surfaces.
2. **Relative elevation map:** The city geometry model is rasterized and converted to a Digital Elevation Map. The relative elevation with respect to the vehicle altitude is computed to then feed the network with information about building layout and topology (Figure 4.60-b). This map encodes the necessary geometric cues for the network to estimate occlusions and reconstruct the wave propagation.
3. **Free noise propagation map:** This represents the SLD levels that would be achieved if no buildings or terrain were present, i.e., attenuation due solely to atmospheric absorption and spherical spreading. This input encodes information about acoustic viscous dissipation and wavelength variation due to the Doppler effect, effectively decoupling atmospheric and geometric effects.



(a) (b)

Figure 4.60: Gaussian Beam Tracing simulation example. (a) Sound Level Decay map of one scenario with strong wave occlusion. (b) Relative elevation map, outlining building geometry and height with respect to the UAV position.

With this approach, the complete database is generated, comprising 120,000 simulations and generating SLD maps along with their corresponding inputs at a resolution of 256 × 256 pixels. Of these data, 70 % were allocated for training, 20 % for validation, and the remainder for the test set. With these data, a Transformer-UNet model is trained for the rapid reconstruction of noise fields. This model is a customized version of the UNet architecture that incorporates a Vision Transformer at the bottleneck as well as attention gates at the skip connections in the decoder (Papa et al., 2024; Y. Wang et al., 2025). The Vision Transformer applies a cross-attention mechanism, enabling the establishment of global relationships among the different parts of the environment. This is performed at the bottleneck after the encoding stage, which reduces the dimensionality of the embedding space. Such spatial awareness is crucial for noise reconstruction, as purely convolutional networks can only extract information based on local patterns. In the case of noise propagation, building occlusions and sound reflections have an important effect on regions that may be far apart in the image. Regarding the attention gates, they provide high-level information that enhances the reconstruction of the noise fields with highly detailed, salient features, while suppressing irrelevant activations and improving generalization in complex urban environments.

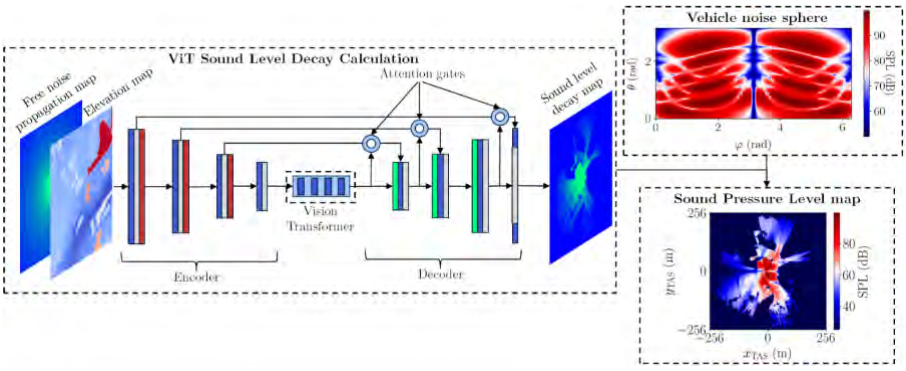


Figure 4.61: Transformer U-Net architecture and proposed workflow for noise intensity prediction combining a noise sphere with an AI surrogate model.

The network takes as input the free noise propagation map, which encodes the atmospheric losses and wave spreading, together with the relative elevation map, which represents building topologies and heights with respect to the UAV position. In this way, the network is capable of predicting the corresponding sound level decays at the different receiver locations. Figure 4.61 illustrates the overall architecture and the information flow. The behavior of the neural network was assessed, and its performance was evaluated to compute the surrogate model errors. Overall, the errors were small, with a root-mean-square error (RMSE) of just 0.81 dB with respect to the GBT solutions. Additionally, the maximum errors were bounded, with the 95th percentile of the error distribution remaining below 2.8 dB, as shown in Figure 4.62.

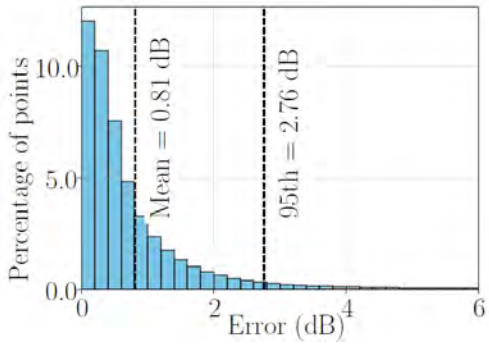
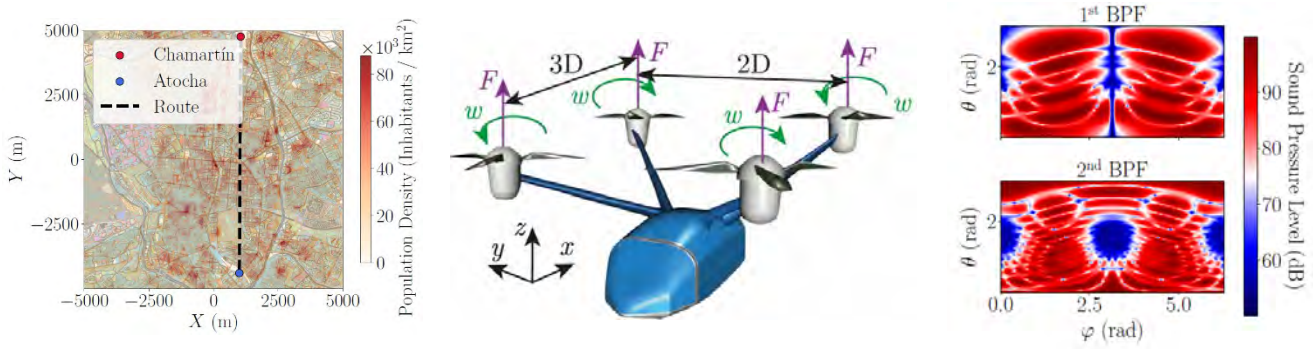


Figure 4.62: Statistical error distribution of the trained model evaluated on the test dataset.

As a practical application, the neural network was applied to a test case in the city of Madrid. The route was defined between the two main train stations of the city, as a representative corridor for a typical UAM use case. For the mission, a straight-line trajectory at different altitudes was simulated, and the peak noise levels were recorded, as shown in Figure 4.63-a. These trajectories are simulated, assuming that flight is conducted exclusively during the cruise phase. In this analysis, the same vehicle as in a previous study by Yunus et al. (2023b) is considered, together with the noise spheres corresponding to the *1st* and *2nd* Blade Passing Frequencies (Figure 4.63-b). Using this configuration, the AI surrogate model is executed to predict the acoustic response along the trajectory, and the overall noise level is computed as the sum of the corresponding linear acoustic intensities.



(a) (b)

Figure 4.63: Considered case study in the city of Madrid. (a) Considered trajectory between the two main train stations of the city overlaid on the population map derived from the Global Human Settlement Population Grid GHS-POP (Pesaresi et al., 2019), CC BY 4.0 (https://creativecommons.org/licenses/by/4.0/). (b) Noise spheres corresponding to the first and second Blade Passing Frequencies (BPF) of the reference UAM vehicle taken from a previous study, adapted and recolored by (Yunus et al., 2023b).

Figure 4.64 shows the peak noise intensity levels for straight-line trajectories flown at constant cruise altitudes. As expected, lower altitudes lead to higher ground-level noise due to reduced atmospheric spreading and viscous dissipation. Very close to the flight path, levels can reach around 100 dB, driven by proximity effects and reflections within urban canyons. At low altitudes, building occlusions tend to concentrate acoustic energy into smaller regions, producing localized noise hotspots. In contrast, higher altitudes yield more dispersed noise footprints with lower peak intensities due to increased atmospheric attenuation and spherical spreading, although the affected area becomes larger.

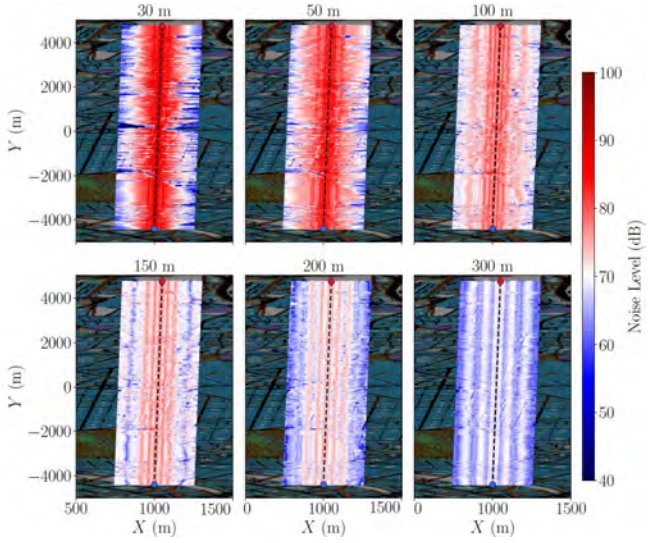


Figure 4.64: Peak noise intensity recorded at ground level during a straight-line trajectory for different flight altitudes above terrain. Background map data © OpenStreetMap contributors, GHS-POP: Global Human Settlement Population Grid. European Commission, Joint Research Center (JRC), CC BY 4.0 (https://creativecommons.org/licenses/by/4.0/).

Finally, Figure 4.65 presents an analysis of the acoustic impact of the operation by quantifying the number of inhabitants exposed to different levels of sound intensity. For this purpose, the peak noise intensities from the previous figures were combined with the GHS-POP population density map of the study area. Overall, the results show that for lower altitude flights (below 150 m), a significant portion of the population is exposed to acoustic levels exceeding 80 dB, which can cause substantial annoyance and may be harmful in the long term. In view of

these findings, special attention should be given to low-altitude flight operations and to the approach and take-off phases, which could lead to a significant acoustic impact on the population if operational frequency is high.

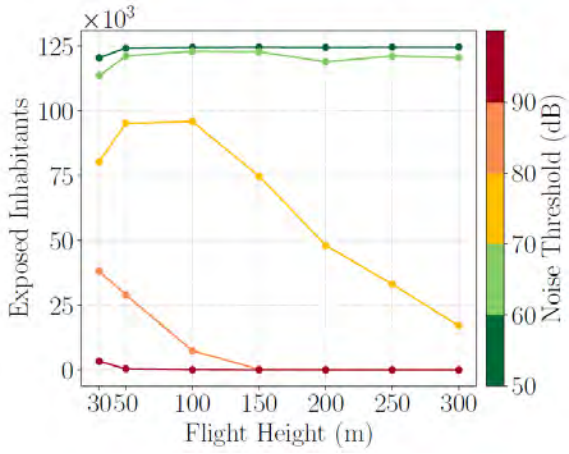


Figure 4.65: Population exposure to different noise levels. Each line shows the number of inhabitants exposed to noise above a specific threshold.

In the study accomplished, simplifying hypotheses were adopted, considering that at all times flight was conducted during the cruise phase and with constant noise emissivity given by the used noise sphere. In reality, this does not fully hold, as vehicle noise and directivity may vary during the different flight phases, being especially relevant during take-off and landing, where the UAV would be flying at a different flight regime and generating different amounts of thrust during the ascent and descent. These phases are especially critical and must be carefully studied, as vehicles would be flying in close proximity to population, potentially causing a significant noise impact. For doing this, future work should implement a digital noise source model, phase-dependent noise emission, broadband noise, and continuous exposure metrics, and these should feed a trajectory optimization framework.

4.2 A Holistic Approach to Urban Air Mobility Vertiport Design and Assessment in Urban Environments

Ottavio Pedretti, Enrique Aldao Pensado, Fernando Veiga Lopez, Francesca Monteleone, Lukas Biesalski, Sen Wang

Beyond the extensive research devoted to developing UAM aircraft, it is important to recognize that the enabling of UAM market also depends on their integration with existing infrastructure (Goyal et al., 2018). A key element of this integration is the vertiport, which is defined as an aerodrome intended for the landing and take-off of VTOL-capable aerial vehicles according to the European Union Aviation Safety Agency (European Union Aviation Safety Agency (EASA), 2021). A market study by the National Aeronautics and Space Administration (NASA) suggests that the initialization of a viable UAM market can benefit from the use of existing helipads and airports (Goyal et al., 2018). Nevertheless, UAM operation differs substantially from existing aviation services. Accordingly, vertiports, as the supporting infrastructure, must be designed to support these modes of operation, yet the current research on their siting and sizing remains limited. Addressing this gap requires a comprehensive understanding of vertiports' operational characteristics. The UAM concept of operation indicates that a vertiport can function as a multimodal transportation hub, supporting a wide range of operations in Visual Flight Rules (VFR), Instrument Flight Rules (IFR), and Advanced Flight Rules (AFR). These operations include cargo delivery, passenger transport, or mixed-use services, with the latter two receiving considerable attention. Therefore, an understanding of public expectations for these operations is essential when considering vertiport design in urban environments. Furthermore, the geographic characteristics of urban environments introduce additional constraints that must be considered in

vertiport design. In light of that, it becomes evident that different scales and configurations of vertiports will be required to support a functional UAM network.

A review of existing vertiport concepts and demonstrations shows that current designs mainly take analytical approaches, e.g., Integer or Mixed-Integer Programming to maximize throughput while maintaining efficient use of surface area and operational performance Parker D Vascik and R John Hansman. Development of vertiport capacity envelopes and analysis of their sensitivity to topological and operational factor (Preis, 2021; Vascik & Hansman, 2019; Zelinski, 2020). Existing vertiport designs generally incorporate several common elements, including the vertipad, gate area, taxiway, final approach and take-off area (FATO), and touch-down and lift-off area (TLOF). With reference to established heliport regulations, the Federal Aviation Administration (FAA), the European Union Aviation Safety Agency (EASA) and the International Civil Aviation Organization (ICAO) have provided guidance on the dimensions of vertipads and taxiways, which scale with the vehicle's dimension. Several generic vertiport topologies arise from arranging these components differently, including single-pad, satellite, linear, and pier configurations. These topologies vary in complexity and sizes, evolving from small-scale layouts to large-scale arrangements as additional elements are integrated. Depending on operational needs, additional elements, such as terminal buildings, maintenance hangars, and commercial blocks, may also be integrated to further expand the functional capabilities of the vertiport. Nevertheless, the design of a vertiport must be carefully tailored to the service types, passenger flows, and spatial constraints imposed by the surrounding environment.

Another important aspect of vertiport design, which is essential for social acceptance yet frequently overlooked, is the noise impact associated with operating eVTOL vehicles at vertiport. For typical UAM services employing tiltrotor vehicles weighting between 1,000 kg to 3,000 kg, both FAA (14 CFR 36.1103) and ICAO (Annex16 Vol.1) (International Civil Aviation Organization (ICAO), 2017) specify that the effective perceived noise level (EPNL) during take-off, approach, and flyover at approximately 150 m above ground level should fall within the range of 90 EPNdB to 95 EPNdB. While these regulations define the noise emission of a single event, they do not fully reflect how noise should be regulated in the vicinity of a vertiport that is expected to experience frequent arrivals and departures. With that said, the environmental noise is typically assessed using a temporal cumulative metrics such as Lden (day-evening-night level), which incorporates the total number of operations over a 24-hour period, and applies penalties for evening and nighttime operations. The cumulative metric is necessary as public health guidance issued by the World Health Organization indicates that prolonged exposure has adverse effects on the well-being of humans. The current guidance suggests that a commercial airport should meet the reference of 55 dB (EU Environmental Noise Directive) if it's situated near a residential area. Similarly, vertiports should also satisfy the threshold, which indicates the throughput should be limited and noise mitigation strategies are necessary.

All of these factors complicate the integration of vertiports and UAM services in the urban environment. A preliminary simulation tool for vertiport demand and capacity analysis has been developed to assess the vertiport capacity according to the local population. At the same time, a city has been selected, São Paulo, for conducting the simulation tool test and for the location and design of the ports. Two locations, Avenida Paulista in the city center, and São Paulo Guarulhos International Airport, have been identified as testbeds to integrate vertiports in different urban conditions. At these locations, the vertiport demand and capacity analysis simulation tool has been adopted to inform the siting choice of the vertiports. In this framework the parameters adopted in the demand and capacity simulation tool were based on preliminary qualitative hypotheses to test the tool in different conditions and in relation to possible vertiport layouts. The vertiport designs are then assessed to ensure that the take-off and landing operations of UAM vehicles do not exceed noise levels that may pose risks to human health.

Vertiport Demand and Capacity Analysis

To determine the appropriate sizing of the vertiport, a statistical capacity analysis is conducted to evaluate the infrastructure's performance under stochastic demand. The analysis begins by modeling demand using the Global Human Settlement Population Grid (GHS-POP), a dataset representing local population density. Based on this data, the population p within the vertiport's area of influence is computed assuming a circular catchment area of radius r = 5 km. Note that the radius of the catchment area can be modified. From this population aggregate, the expected number of hourly vertiport operations N_{ops} is estimated as:

$$N_{ops}=p \times f$$

where f represents the trip generation rate (defined as the ratio between hourly operations and the population). For this analysis, two different population rates have been adopted due to qualitative considerations regarding the possible capacity of the vertiport in relation to its localization. Therefore, a rate of $f = 1 \times 10^{-5}$ is adopted in the city center localization and a rate of $f = 1\times10^{-4}$ is adopted in the airport localization. Although the vertiport localization and design will be discussed in the following section, different population fractions for the demand parameters correspond to a qualitative analysis linked to hypothetical demand. In fact, in the city center, the demand could be linked to business/leisure purpose and lower demand could be expected rather than in the airport localization, where the service would likely be used not only by locals but also as airport shuttle and for many other destinations rather than just the city center. Given that the vertiport would provide on-demand taxi services, the following assumptions are considered for modeling the infrastructure demand:

- **Stochastic arrival process:** To model the lack of a pre-scheduled timetable, passenger and aircraft arrivals are treated as random events with desired timestamps uniformly distributed over the service hour.
- **Coupled demand logic:** The system distinguishes between two interdependent demand streams: passenger arrivals generate a demand for aircraft departures, while aircraft arrivals generate a demand for parking stands.

To formalize this, let N_{dep} denote the number of departures, defining the set $D=\{1, \dots, N_{\text{dep}}\}$, with the remaining operations constituting the set of arrivals $A=\{1, \dots, N_{\text{arr}}\}$. The desired timestamps for a departure $i \in D$ and an arrival $j \in A$ are modeled as independent random variables:

$$\hat{t}^{i}_{\text{dep}} \sim U(0,60), \hat{t}^{j}_{\text{arr}} \sim U(0,60)$$

where U denotes a uniform distribution in minutes. Distinct from these desired values, the actual arrival and departure times are governed by the availability of three critical resources: the FATO platforms, parking stands, and the aircraft fleet.

FATO Congestion (Platform Access)

Each operation requires exclusive access to a FATO area. Let the vertiport operate n_{plat} platforms, indexed by $k \in \{1, \dots, n_{\text{plat}}\}$. When a platform k is utilized starting at time t, it remains unavailable for any other operation during the interval:

$$I_{\text{busy}}=[t, t+\Delta t]$$

where Δt represents the constant service time required for take-off or landing procedures.

If at least one platform is free at the desired time, the operation proceeds immediately. However, if all n_{plat} platforms are occupied, the operation is delayed until the earliest platform becomes available. Let T^{k}_{free} denote the time when platform k next becomes free. The actual realized timestamps for departure i and arrival j are determined respectively as:

$$t^{i}_{\text{dep}}=max$$

Following the assignment, the availability of the selected platform is updated to $T^{k}_{\text{free}}=t+\Delta t$. The delays incurred due to FATO congestion are strictly defined as the take-off wait time ($t^{i}_{\text{wait, take-off}}$) and the landing wait time ($t^{j}_{\text{wait, landing}}$):

$$t^{i}_{\text{wait,take-off}}=t^{i}_{\text{dep}}-\hat{t}^{i}_{\text{dep}},\ t^{j}_{\text{wait,landing}}=t^{j}_{\text{arr}}-\hat{t}^{j}_{\text{arr}}$$

Parking Saturation and Fleet Availability (Arrival/Departure Constraint)

Once an aircraft lands, it requires a parking stand. Let n_{stand} be the total parking capacity and $v(t)$ denote the number of aircraft occupying stands at time *t*. If the vertiport is saturated (i.e., $v(t^{j}_{\text{arr}})=n_{\text{stand}}$) upon the arrival of aircraft *j*, the aircraft cannot dock and must loiter until a spot is liberated by a future departure. Defining $D_{\text{ftr}}=\{i \in D | t^{i}_{\text{dep}}>t^{j}_{\text{arr}}\}$ as the set of subsequent departures, the forced parking wait time is:

$$t^{j}_{\text{wait,park}}=\begin{cases}0 & if\ v(t^{j}_{arr}) < n_{stand}\\ min_{i\in D_{future}}(t^{i}_{dep})-t^{j}_{dep} & if\ v(t^{j}_{arr}) = n_{stand}\end{cases}$$

Conversely, a passenger wishing to depart requires an aircraft to be physically present. If the vertiport is empty of aircraft (i.e., $v(t^{i}_{\text{dep}})=0$) when passenger *i* arrives, the passenger must wait for an incoming aircraft to replenish the fleet. Defining $A_{\text{ftr}}=\{j \in A | t^{j}_{\text{arr}}>t^{i}_{\text{dep}}\}$ as the set of subsequent arrivals, the fleet availability wait time is:

$$t^{i}_{\text{wait,fleet}}=\begin{cases}0 & if\ v(t^{i}_{dep}) > 0\\ min_{j\in A_{future}}(t^{j}_{arr})-t^{i}_{dep} & if\ v(t^{i}_{dep}) = 0\end{cases}$$

In this way, the maximum vertiport delay time, Δ_{max}, represents the worst-case delay experienced by any single operation (arrival or departure) during an hour of service. It is calculated as the maximum of the cumulative delays for all departures and arrivals:

$$\Delta_{max}=max\left(\max_{i\in D}(t^{i}_{\text{wait,fleet}}+t^{i}_{\text{wait,take-off}}), \max_{j\in A}\left(t^{j}_{\text{wait,landing}}+t^{j}_{\text{wait,park}}\right)\right).$$

With these assumptions, N_{sim}=10,000 Monte Carlo simulations of the vertiport are conducted for different configurations of n_{plat} and n_{stand}. The value N_{sim}=10,000 was selected following a sensitivity study analyzing the variability of the results with the number of simulations. This value ensures minimal statistical fluctuation while avoiding prohibitive computational costs. As a measure of operational robustness, the vertiport Delay Rate (DR) is defined as the percentage of simulations in which the maximum delay exceeds a predefined allowable threshold, δ_{limit}:

$$DR=\frac{1}{N_{\text{sim}}}\sum_{s=1}^{N_{\text{sim}}} I(\Delta^{s}_{max} \geq \delta_{\text{limit}}) \times 100$$

where I is the indicator function.

Finally, the optimal infrastructure sizing is determined by identifying the most resource-efficient configuration that maintains operational reliability. The final design for the number of FATO platforms and parking stands is selected as the minimum combination of (n_{plat}, n_{stand}), (n_{plat}, n_{stand}) that satisfies the performance criterion $DR \leq DR_{max}$. For the purposes of this study, a maximum delay rate of DR_{max}=25% considered acceptable. This threshold is chosen based on statistics from the U.S. Bureau of Transportation Statistics (Bureau of Transport

Statistics, 2026), which indicates a delay rate of slightly above 21% for U.S. marketing carrier flights in 2025. Repeated demand and capacity analysis simulations were conducted throughout the study, and a good consistency is observed.

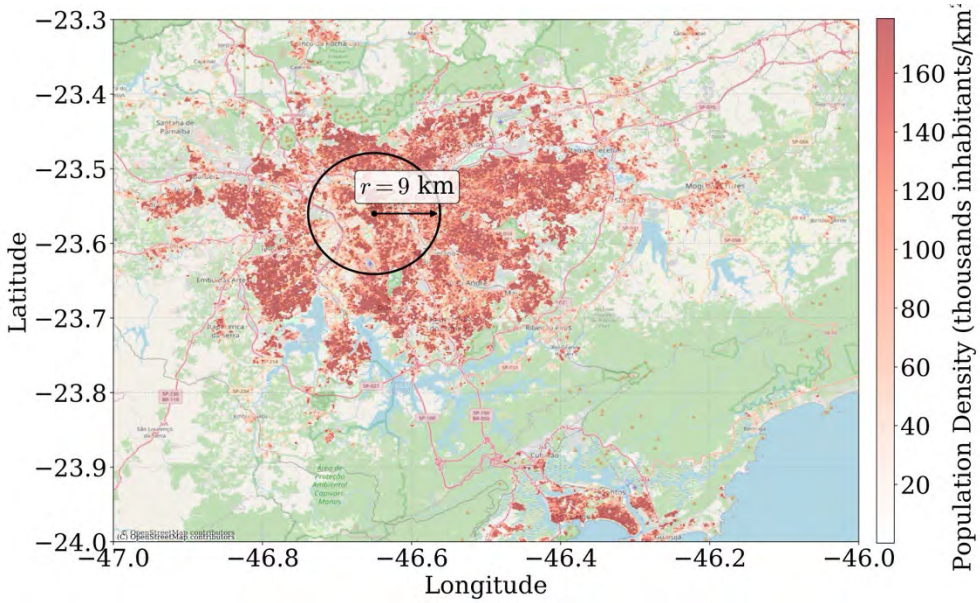


Figure 4.66: Population density of the São Paulo metropolitan area derived from the Global Human Settlement Population Grid GHS-POP (Pesaresi et al., 2019), CC BY 4.0 (https://creativecommons.org/licenses/by/4.0/). Background map data © OpenStreetMap contributors, ODbL v1.0 (Copyright and License).

Vertiport localization and design

Having established the vertiport capacity model, a specific city is selected to test the vertiport design under realistic operational conditions. However, the objective of the UCM is to provide a general framework that can be applied to any location. Therefore, the localization of the city should be interpreted solely as a case study used to demonstrate and apply the proposed methodology. Considering the general applicability, the selected city is São Paulo since it has been widely used as a preliminary testbed case for UAM applications (Figure 4.66). Its consolidated usage of helicopters within the urban environment that could ease the process of social acceptance was a factor considered in the selection. Moreover, operations in São Paulo are expected to reflect a complex management of urban mobility, with high levels of commuting from the outskirts toward the city center (Lopes & Silva, 2023). Therefore, UAM can find fertile ground for possible applications. Selected vertiports' locations have been mapped within São Paulo's metropolitan fabric. The objective is to articulate their mutual relationships, territorial distribution, and interdependencies, identifying how each node contributes to the overall system performance. The strategy of UAM service implementation is articulated in two steps, mirroring the logic of development of UAM per phases. Figure 4.67 represents the two different sets of locations. The first set of locations has been selected as initial set of areas to enter service. In this set, the main airports of the city have been considered, since a typology of service such as an airport shuttle service would be one of the potential use cases to be implemented. The further central location added corresponds to the central business and commercial district of São Paulo and represents a strategic point to be implemented with this typology of service. A second set of locations has been selected as potential follow-up and expansion of the service. Lastly, a regional connection has been hypothesized as a possible further expansion in the whole region.



Figure 4.67: São Paulo vertiport network.

The distinction of different localizations of vertiports according to its connections offers a first guide in the orientation of the vertiports' features to be equipped with. In fact, the vertiport can be developed in a scalable design, privileging small vertipads in the city center for faster connections, equipped with the minimum requirements, and larger hubs serving also for maintenance and storage in the outer areas. Two representative sites have been chosen as testbeds for the subsequent design phase. These two sites are the urban green space in Avenida Paulista located in the city center, and São Paulo Guarulhos International Airport. These sites serve as experimental grounds to evaluate how different spatial and operational conditions affect the architectural articulation of the vertiport. Therefore, the different locations are conceived to be equipped with different typologies of services. Central locations, represented by Avenida Paulista test case, are envisioned as vertistops, where people can quickly embark and disembark, without the provision of further ancillary services. The outer locations, as the case of São Paulo Guarulhos International Airport will be equipped with additional elements such as workshop areas and warehouses. Figure 4.68 illustrates the planned functions that can be inserted in the vertiports design according to their configuration. The dimension of each vertiport is designed based on the size of a tiltrotor UAM vehicle developed within the UCM framework, and the corresponding FATO/stand dimensions. Each vertiport size corresponds to different numbers of FATOs/stands placings that depend on the service. Several trials were carried out through the vertiport demand and capacity analysis, testing vertiport locations with different input of waiting time, adjusting the values according to the envisioned service typology. Minimum safety distances to be respected have been taken from the EASA vertiport's technical prescriptions, since this is one of the early documents that offer guidelines and orientations for the dimensioning of the vertiport and operational safety requirements. In both vertiports, the radius of the FATO has been set to 16 meters.

In the demand and capacity simulations for the target locations, different parameters have been used accordingly to qualitative analysis developed in this work, taking in considerations different typologies these locations may have. As previously mentioned, in the city center and in the airport the demand may be subject to variations due to the passengers' profile and possible operations. It is worth mentioning that the definition of a certain demand and related users' profile is out of scope of the present paper, where separate analysis would be required to address this topic. For this edited book, the focus is not set on the parameters adopted for the simulations, rather the definition of a correspondence and a link between a demand and capacity analysis tool and the design configuration. The aim of this study in fact is to import the tool and the logic of correspondence between the tool's outputs and the design configuration to potential vertiport location and possible parameters, that might vary according to different needs. The input parameters used are an assumption of hypothetical different scenarios and do not correspond to a dedicated analysis. The aim here is to link a specific output of the demand and analysis simulation tool to a corresponding layout configuration. Consequently, varying operating scenarios would require separate analyses.

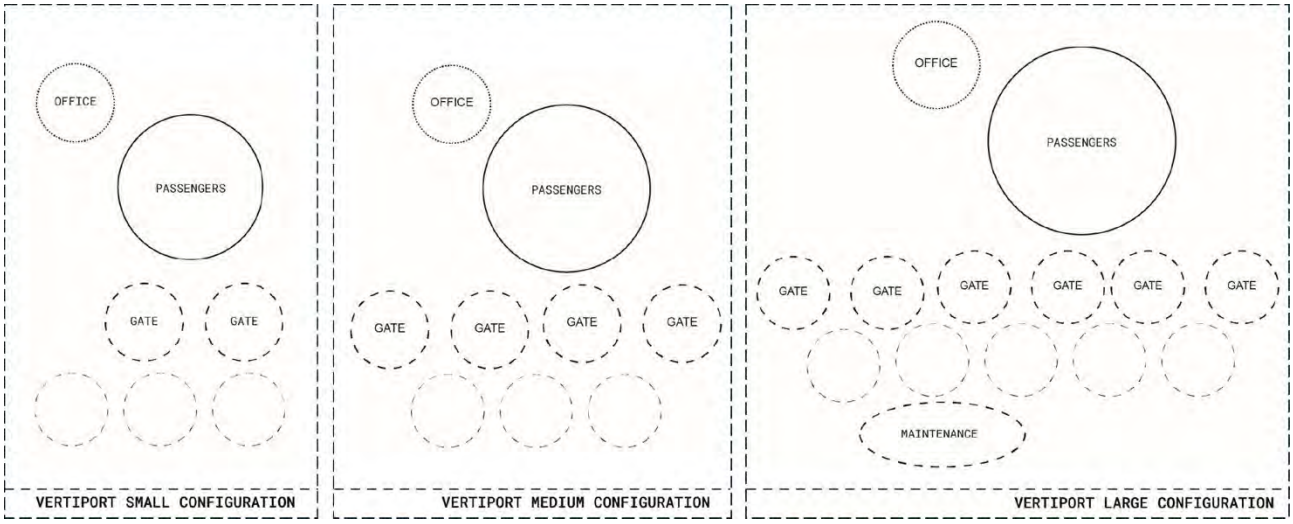


Figure 4.68: Possible vertiport's functional program according to its demand.

Next, the case study of vertiport at different location is presented. The vertiport in Avenida Paulista is located in the urban green space at the center of São Paulo, precisely in correspondence to Square Alexandre De Gusmão, close to the Trianon Park and Mario Covas Park. It is situated in a strategic location, along the metro line two, close to the Metro stop Trianon-Masp. Adjacent to the metro stop a bus stop is also present, serving a range of bus routes. The vertiport can be integrated as a further mobility service in this area. Moreover, the neighborhood consists of several heliports on the rooftop of the surrounding skyscrapers, illustrating the existing use of aerial mobility in the district. The vertiport can represent a viable solution to expand and democratize access to aerial mobility services, supporting both current users while attracting new ones. The urban green space in which the vertiport is inserted lies above Avenida Nove de Julho, one of the main streets connecting the north of São Paulo to the South. Near it stands the São Paulo Art Museum, which is expected to attract a high volume of tourists as potential users.

As shown in Figure 4.69, the vertiport has been placed in the South-East side of the urban green space (enclosed by a red dashed line), in the Square Alexandre De Gusmão. This localization has been selected in order to optimize the distance toward the bus and metro stop present nearby and to minimize the impact of the vertiport in the area, leaving a consistent portion of the urban green space open to the citizens. The design follows the principle of minimizing the needs for unnecessary ancillary elements in the vertiport, to optimize the accessibility to the service in a bus/metro stop-like situation and the corresponding impact in the area. In a closer view shown in Figure 4.69, the gates are equipped only with a small, sheltered waiting area and restrooms for passengers/vertiport operators

(the two volumes at top right corner). A small building dedicated only for operations management (office area) is provided too (smaller volume at the left top corner). This area selected for the vertiport presents a considerable level difference in terrain, that has been adopted in the vertiport configuration to set a safety barrier between the vertiport and the public space. Along the wall marking the change in elevation on the southern side of the vertiport, public spaces serving different purposes have been introduced. These spaces help mitigate the impact of the slope while providing public areas for residents and establishing a connection with the adjacent urban green space. In the area a ventilation duct is also present and is related to the underground street Avenida Nove de Julho. It is assumed that such ventilation duct can be moved close to the vertiport (circular volume in between the two vertiport's blocks) but outside its safety perimeter. On the south side of the area, the entrance to an underground car park exists and it is not modified in the study. Note, the project represents a preliminary hypothesis of the vertiport layout and a deeper analysis of the context would be required as well as further evaluations are needed to assess the real feasibility of such project.

The following input parameters are defined to test the vertiport configuration: fraction of passengers = 1×10^{-5}, population density radius = 5 km, max wait platform = 5 minutes, max wait parking = 5 minutes, and max wait departure = 5 minutes. These parameters give an estimated value of 10 passengers per hour. According to these parameters, the vertiport is composed of one FATO/TLOF and four gates to host the embarkment/disembarkment of the passengers has been obtained. The stands are about 30 meters distant from the FATO. The stands and the FATO/TLOF are arranged in a satellite typology, in order to minimize the footprint of the vertiport in the available space.

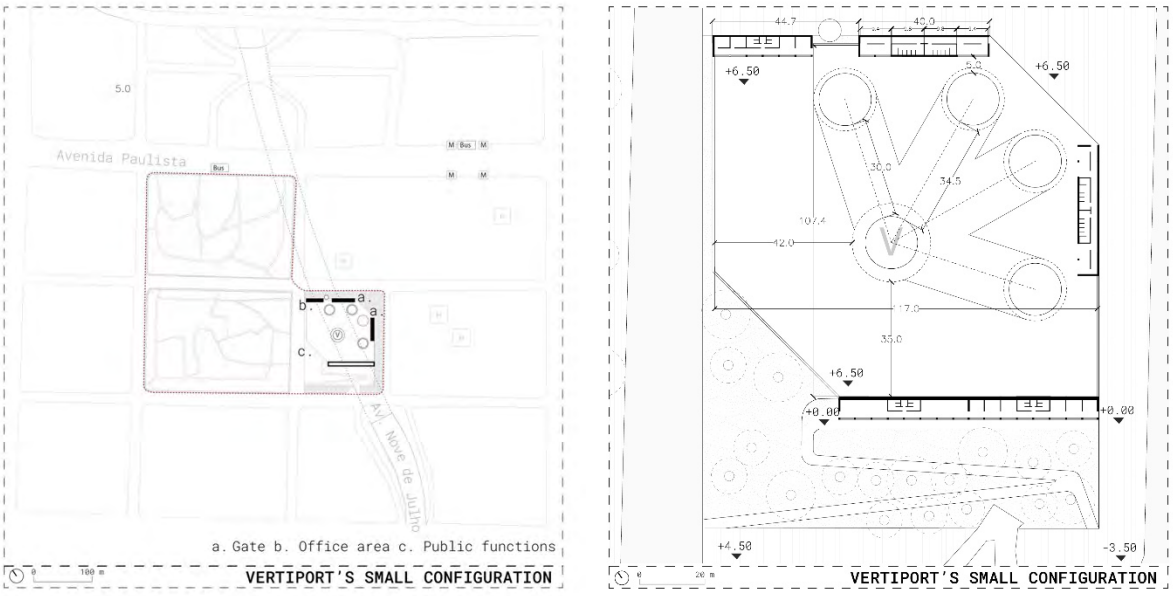


Figure 4.69: Vertiport configuration at Avenida Paulista and detail of the vertiport layout.

Subsequently, the development of a vertiport at São Paulo Guarulhos International Airport exemplifies the integration of UAM infrastructure within an already stratified multimodal transport system. The vertiport layout is illustrated in Figure 4.70. Positioned externally to the main airport terminal complex, the vertiport is located on an elevated platform that partially overlaps the airport's parking structure and is directly adjacent to the railway station connecting the airport to the metropolitan network. This siting strategy establishes a vertically articulated mobility node structured across three superimposed layers: rail at ground level, vehicular circulation within the parking deck, and aerial operations above, thereby optimizing intermodal transfer while maintaining operational autonomy from the primary terminal. The vertiport operates as an independent infrastructural addition. Its elevated condition allows

direct structural integration with the parking deck while preserving clear separation from conventional passenger flows. This configuration produces a compact terminal building that serves as a controlled interface between the landside and airside domains. The landside area accommodates passenger access and security procedures, while the airside operational zone hosts FATO areas and adjacent parking pads for eVTOL aircraft. The spatial organization responds to two constraints simultaneously: regulated passenger flow and high vehicle turnover rates. The dual requirements define the platform's dimensional arrangement and the sizing relationship among waiting areas, circulation corridors, and aircraft stands. Within the broader research framework, this case study serves to validate the simulation tool developed to assess vertiport capacity and operational risk under peak-demand scenarios. Given that the vertiport site presents different characteristics from the one at Avenida Paulista, the vertiport sizing model tests the spatial adequacy of the proposed layout using the following input parameters: maximum waiting time at the platform = 3 minutes, maximum waiting time at the parking stands = 2 minutes, and maximum waiting time at the departure area = 3 minutes. The estimated throughput of vertiport is 31 passengers per hour. As a measure of operational robustness and based on the selected parameters, the optimized configuration, comprising six parking pads and four FATOs, yields a *DR* of 23%. This value indicates that in 77% of simulated scenarios the system maintains delays within acceptable limits, while in the remaining cases congestion primarily emerges in the aircraft ground circulation sequence. The spatial ratio between parking pads and FATOs, therefore, appears as the critical variable influencing overall robustness. The Guarulhos case demonstrates how, within an airport environment, the vertiport is articulated through a dual logic: the landside domain is defined by footprint constraints and architectural choices related to structural integration and passenger access, whereas the airside configuration is dimensioned by aircraft turnaround time and passenger flow synchronization.

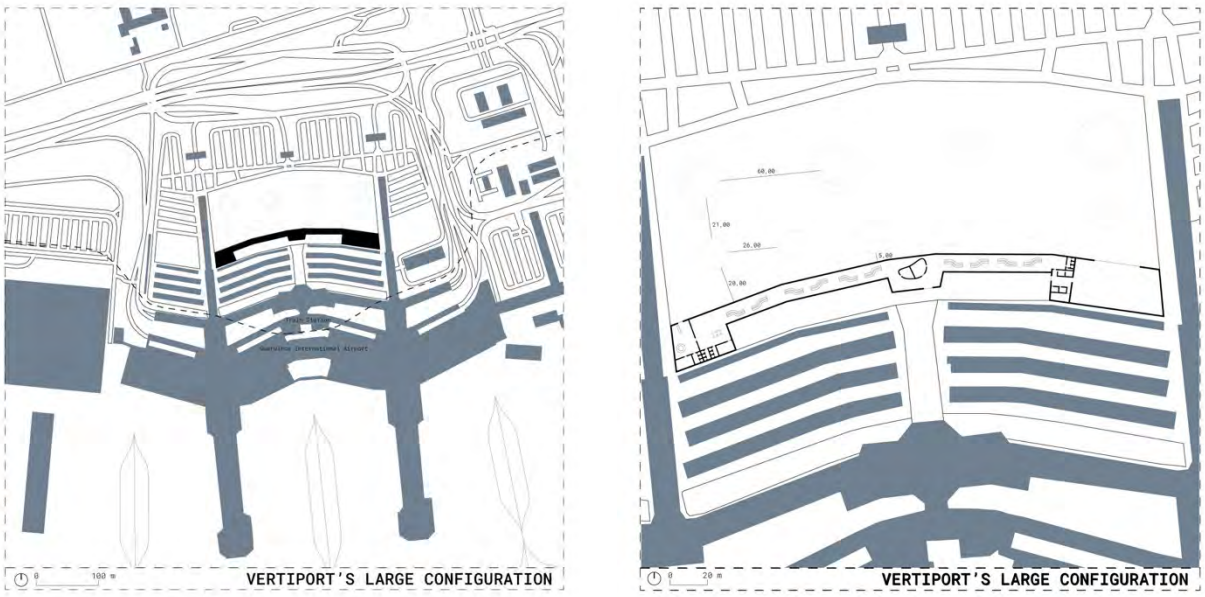


Figure 4.70: Vertiport configuration at Guarulhos International Airport and detail of the vertiport layout.

Vertiport operations and Noise Assessment

In addition to the physical vertiport layout, the proposed design integrates a three-dimensional Obstacle-Free Volume (OFV) that governs all flight operations in compliance with the vertiport framework in the European Union Aviation Safety Agency (EASA). While the omnidirectional OFV configuration defined by EASA provides a standardized geometric safety envelope, it does not adequately reflect the acoustic constraints associated with noise optimized flight trajectories in dense urban environments. To address this limitation, this study proposes an extended framework termed the Noise-Adjusted Obstacle-Free Volume (NAOFV). The NAOFV acts as a

methodological enhancement of the EASA baseline, enabling the simultaneous assessment of obstacle clearance and compliance with local noise regulations and guidelines Federal Aviation Administration (Blanes et al., 2017).

The proposed vertiport layout supports detailed acoustic simulations to quantify the urban impact of approach and departure operations. Initial sound pressure levels are computed assuming spherical propagation and logarithmic decay of acoustic energy according to Eq. (10):

$$L_N = L_{source} - 20log\left(\frac{d_N}{d_{ref}}\right)$$

where L_{source} represents the reference A-weighted source level, d_N is the propagation distance, and d_{ref} corresponds to the reference distance for normalization. A dedicated model evaluates façade exposure at the nearest building surfaces. In both case studies, the resulting peak A-weighted sound pressure levels remain well below the permissible urban noise thresholds established by the Federal Aviation Administration (FAA) (2002). In the Avenida Paulista case study, the peak level reaches 62.2 dBA, while in the case of São Paulo Guarulhos International Airport the resulting peak A-weighted sound pressure level reaches 56.7 dBA. However, additional noise-mitigation measures are required to comply with the healthy exposure thresholds defined by the WHO Environmental Noise Guidelines for the European Region.

The NAOFV extends EASA's omnidirectional OFV by introducing distance-based acoustic boundaries. In the preliminary stage, building heights and reflective surfaces are neglected to isolate the influence of acoustic distance on the flight corridor geometry. Based on Eq. (10), $d_{N,min}$ denotes the minimum separation required to maintain noise levels below the local limit at the nearest building façade.

Figure 4.71 illustrates the geometric principle of the NAOFV: the tangential relationship between the FATO and the spherical noise boundary defines the minimum permissible FATO-to-building distance $d_{FTB,min}$. The resulting boundary conditions, summarized in Table 4.26, constrain the lower and upper altitude limits (h_1, h_2) and ensure that the defined noise contour remains tangent to the safety volume. When $d_{FTB,min} > d_{N,min}$ h_1 becomes an adjustable design parameter that governs the vertical expansion of the NAOFV.

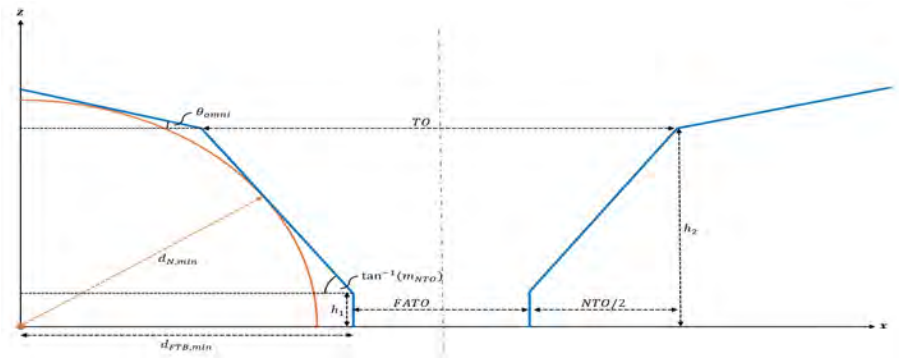


Figure 4.71: Graphical representation of NAOFV.

This approach couples geometric and acoustic design criteria within a unified evaluation framework, allowing designers to preliminarily validate approach and departure trajectories not only for obstacle clearance but also for compliance with noise-abatement policy. Such integration is essential to achieving community acceptance for future UAM infrastructure in high-density city environments. Results from the case studies provide both quantitative outputs, such as capacity data, stand utilization rates, and compliance margins with NAOFV, and qualitative insights into the design implications of noise adaptation, spatial programming, and regulatory compliance. The vertiport configuration of pads has been derived from the output of the vertiport demand and capacity analysis simulation tool. The ratio between parking pads and landing/departing pads can vary according to the parameters set in the

simulation tool. In the simulations conducted, the large-scale prototype at Guarulhos can achieve higher operational throughput. From the simulation tool, in fact, a vertiport configuration comprising 6 parking pads and 4 landing/departure pads emerged. However, merging this configuration with vertiport design specifications required reconfiguring existing airport infrastructure, including partial coverage of parking areas. The urban prototype at Avenida Paulista, instead, is more constrained in scale, being served by 4 parking pads and 1 landing/departing pad. This scale reduction is supported by the integration of the vertiport in a central metropolitan area, facing reduced availability of space. This latter vertiport compared with the former one has stricter noise mitigation requirements, being surrounded by closer buildings. However, the noise levels for the current localization respect the limits. These two factors, availability of space merged with the demand and capacity of the vertiport as well as vertiport displacement, and closeness to buildings to be tested with the noise assessment, complicate the process of identifying suitable locations in the urban environment.

Parameter	*Constraint*	*Condition*
FATO	$\geq max\left[\left(\frac{3}{\sqrt{2}}+0.5\right)D, \frac{3}{\sqrt{2}}D+6m\right]$	-
NTO	$\leq min\left[\frac{7}{\sqrt{2}}D, \frac{2(h_2-h_1)}{\lvert m_{NTO}\rvert}\right]$	-
h_1	$\geq \sqrt{d_{N,min}^2-d_{FTB,min}^2}$	$d_{N,min} \geq d_{FTB,min}$
h_1	-	$d_{N,min} \leq d_{FTB,min}$
h_2	$\geq h_1$	-
m_{NTO}	$\geq \frac{d_{FTB,min}h_2}{d_{FTB,min}^2-d_{N,min}^2}$	-
θ_{omni}	$\geq max\left\{4.5\%, arctan\left[\frac{\left(d_{FTB,min}-\frac{NTO}{2}\right)h_2}{\left(d_{FTB,min}-\frac{NTO}{2}\right)^2-d_{N,min}^2}\right]\right\}$	-

Table 4.26: Boundary conditions of the NAOFV based on the EASA omnidirectional OFV.

The methodological and architectural implications of this work can extend beyond the São Paulo testbed. First, the approach promotes scalability: by testing different conditions and locations, it is possible to systematically compare different vertiport sizes and requirements. Secondly, integrating demand and capacity simulations repositions vertiports not merely as technical landing sites but as socially responsive nodes within an emerging mobility ecosystem. This redefinition is crucial for long-term urban integration and for legitimizing aerial mobility as a public infrastructure category. Therefore, this research establishes a testable and adaptable methodology for vertiport implementation, applicable to both greenfield and brownfield urban contexts. It contributes to supporting design-led UAM research that views vertiports as embedded urban artifacts whose form, function, and spatial logic must be negotiated in situ. Furthermore, coupling technical modeling with noise-sensitive volume opens a new direction in airspace–ground integration, foregrounding public acceptance as a critical parameter in infrastructural design. Overall, the main result achieved in this experimentation is the development of a method able to link the specific population demand in one location with the consequent vertiport stands needed, to test different vertiport configurations in the pathway for implementing and experimenting possible UAM solutions.

This study presented a preliminary framework for vertiport design and assessment that integrates demand–capacity analysis, spatial layout development, and noise-informed operational evaluation within a common workflow. Using São Paulo as a testbed, the framework demonstrates how different urban conditions and service assumptions lead to distinct vertiport configurations and operational requirements. The results show that vertiport design extends beyond technical sizing, as the final layout is shaped by vehicle operations, passenger flows, urban integration, and regulatory constraints, including noise. These findings highlight the need for an interdisciplinary approach combining engineering, architectural, and regulatory considerations. Several limitations should be acknowledged. First, the simulations rely on preliminary assumptions and publicly available data and should therefore be regarded as a demonstration of the framework rather than predictions of specific operating scenarios. The demand and capacity parameters were selected to explore representative conditions and assess the framework under varying assumptions. More reliable applications will require site-specific demand, user, and operational data, enabling more accurate evaluation of vertiport layout, capacity, and performance. In addition, the airport case study uses population density as a proxy for demand, which may underestimate potential users because airports primarily serve transient passenger flows rather than nearby residents. Second, the acoustic assessment is intentionally simplified to enable the integration of noise considerations during the preliminary design stage. More detailed acoustic modeling would be required to capture the effects of flight trajectories, urban morphology, and local sound exposure, while cumulative noise metrics will depend on realistic operational scenarios or surrogate transport models. As representative passenger flow data become available, both operational and acoustic assessments can be refined. Despite these limitations, the proposed framework demonstrates the value of integrating operational modeling, spatial design, and environmental considerations within a unified workflow. By linking demand assumptions to vertiport configuration and operational performance, it provides a flexible tool for supporting preliminary vertiport design and implementation.

4.3 Vertiport Localization for Urban Air Mobility: The Role of Intermodality and Urban Wind Conditions

Francesca Monteleone, Nithya Dhamodharasamy Sundarraj, Fabrizia Berlingieri, Giuseppe Quaranta, Vincenzo Muscarello

Many studies establish vertiport localization strategies by prioritizing UAM network optimization frameworks and demand analysis. While these approaches provide valuable inputs for forecasting UAM networks, they largely overlook the fact that UAM represents a new typology of urban mobility. Consequently, UAM implementation should also be evaluated in relation to the existing urban mobility layer, the spatial configuration of cities, and their future development plans. This perspective merges with regulatory and UAM conceptual frameworks, where intermodality is identified as a fundamental requirement for integrating UAM into existing urban transport systems to align with broader mobility policies, enhance efficiency, reduce costs, and promote societal acceptance. Vertiport placement should therefore be guided by a careful analysis of urban mobility patterns and strategic transport planning to identify potential intermodal hubs capable of supporting UAM operations. In addition, vertiports should be designed to integrate seamlessly with these hubs, ensuring continuity and functional alignment within the broader mobility network.

Beyond urban integration, the local urban environment also has a profound impact on UAM operations through its influence on wind behavior. The complex morphology of cities–tall buildings, narrow streets, and irregular layouts–generates highly localized and multilayered turbulent wind conditions at low altitudes. These microscale wind dynamics will affect take-off, landing, and flight stability near vertiports, posing operational and safety challenges. Thus, local wind conditions must be carefully considered when selecting vertiport locations, as they influence the placement, orientation, and structural layout of Final Approach and Take-Off (FATO) zones and Touchdown and Lift-Off (TLOF) areas.

No studies to date address intermodality and local wind effects simultaneously; doing so requires bridging architecture, urban planning, and aerospace engineering (Stoll et al., 2010). Moreover, UAM demands a three-dimensional spatial configuration understanding of the urban environment, one that encompasses the current urban spatial configuration, existing urban mobility networks and local meteorological conditions (Jia et al., 2026). Hence, interdisciplinary approaches are essential to develop integrated solutions to test, evaluate, and implement UAM infrastructures or vertiports effectively.

Building on the need for an integrated, interdisciplinary approach, this paper presents a methodology for vertiport localization that combines the perspectives from two different fields: Architecture-Urban-Design and Aerospace Engineering stemming from different PhD research areas-through real-case scenarios in the metropolitan area of Milan, Italy. Specifically, three locations are selected according to their intermodal connectivity and urban configuration. Then, microscale wind conditions are simulated for these chosen sites, and each location is evaluated from a dual perspective-intermodality and urban wind dynamics–to assess the feasibility of establishing a vertiport.

The overall methodology involves the process of selecting intermodal hubs within the metropolitan area of Milan, Italy, alongside microscale wind simulation and assessment for the identified sites (see Figure 4.72). The location selection process relies on the analysis of six key aspects (Città Metropolitana di Milano, 2021, 2023; Colleoni, 2019; Comune di Milano, 2020; Regione Lombardia, 2016):

- existing public transportation system with the help of the regulatory planning frameworks.
- settlement typology and intermodal hubs configuration;
- mobility flows and patterns;
- foreseen development of the mobility system considering the trends of evolution;
- proposed urban development projects for the metropolitan area of Milan;
- morphology of the urban form in relation to the mobility system.

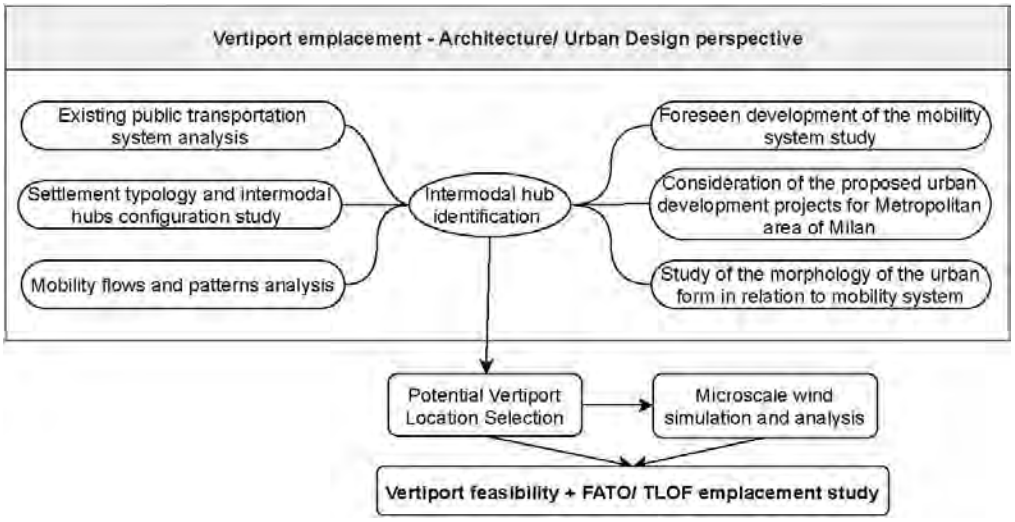


Figure 4.72: High-level workflow of the methodology.

These criteria lead to the identification of three intermodal hubs, namely, the rail–metro exchange at the Rho Fiera Milano and Milano Rogoredo station, and the air–metro exchange at Linate Airport, for testing the vertiport emplacement. Subsequently, the historical wind data for the determined intermodal sites are analyzed to derive the dominant wind speed and wind direction probability distributions. The resulting distributions quantify the likelihood of different inflow wind conditions for the sites and are used to stochastically sample multiple boundary conditions for the wind simulations within the Monte-Carlo framework (Nithya et al., 2025; Zhang, 2021). The microscale wind

simulations are performed using a Stochastic Wind Model (SWM) that is developed by the authors (Nithya, Monteleone, et al., 2025). SWM is a custom urban wind simulator that generates high resolution, quasi-non-stationary wind fields suitable for UAM applications. Then, the outcomes of the wind simulation and intermodal hub identification are assessed in parallel to determine Vertiport emplacement feasibility and development in the chosen sites.

The role of intermodality in vertiport localization

The selection of suitable locations for vertiport emplacement is a key issue in the development of UAM. Vertiport location directly influences service usability and implicitly reflects the strategic vision underlying the network design. This choice has direct implications for the social impact of UAM within urban contexts. The UAM service should complement existing mobility options rather than compete with them; therefore, it should be integrated accordingly (C. Lee et al., 2023). The EU Commission has promoted policies for the sustainable development of mobility that aim to advance an integrated mobility system, fostering multimodality in passenger trips and the coexistence of multiple modes of transportation. In fact, in the last decades, urban mobility has expanded with the emergence of several new modes of transportation, such as on-demand and shared mobility; these new systems must coexist in urban areas without generating additional congestion. Here lies the need for efficient planning and programming of mobility within cities, upon which the EU's Sustainable Urban Mobility Plans have been built. All these mobility options can bring significant benefits when adopted in a multimodal, complementary approach. From this framework, it emerges the need for careful integration of all the different mobility flows at stake across mobility operators, which has led, among other things, to the promotion of Mobility-as-a-Service (MaaS) policies aiming to create a single digital application that integrates mobility options from various mobility operators. These policies are tied to the central EU goal of ensuring a resilient and sustainable transportation system, reducing disparities and enhancing connectivity. It's in this framework that UAM operates. Even though UAM is an air transportation system, it needs supporting infrastructure on the ground to operate. UAM must support the European Transport Policy, which aims for sustainable and efficient mobility. Therefore, in line with the EU SESAR project ConOps (SESAR Joint Undertaking, 2023), intermodality plays a key role in UAM integration, with particular attention to the intersection points of different mobility flows. Intermodal hubs, in fact, are easily accessible from other locations and offer a range of mobility options. Their development follows the pathway for integrated and efficient mobility systems. Their positioning in the mobility network enables exchanges among different mobility options, favoring their complementarity rather than competition. The vertiport locations are the result of an overlay of different factors based on the existing mobility system in the metropolitan area of Milan. The metropolitan area of Milan is part of the Lombardy region in northern Italy and is one of Italy's major metropolitan cities. Its administrative boundary is constituted by the Metropolitan City of Milan (referred to as MCM), bordered by the other Italian provinces of Como, Cremona, Varese, Brescia, Monza, Pavia, Lodi (Lombardy region), and Novara (Piedmont region). To identify suitable locations for testing UAM integration in the selected area, six key aspects have been considered. These aspects have informed the localization selection process outlining the actual and planned mobility system, making it possible to highlight related intermodal hubs.

Existing public transportation system through the regulatory planning frameworks

The regulatory planning framework (Città Metropolitana di Milano, 2021, 2023; Comune di Milano, 2020; Regione Lombardia, 2016) delineate a mobility scenario that is highly interconnected. Milan is located at the intersection of two TEN-T corridors, namely a system of transportation networks (railways, roads, airports, and water) identified by the EU as the main "corridors" to connect all of Europe seamlessly. In this case, Milan is at the crossroads of the Rhine-Alpine Corridor, connecting Amsterdam to Genova, and the Mediterranean Corridor, connecting Portugal with Hungary, passing through Spain and the French coast; therefore, the city is strategically located. MCM, as well

as the Lombardy region, is served by a dense, multimodal public transport system comprising rail and bus services. The road network in and surrounding MCM is highly capillary and composed of several street typologies: highways, national roads, local streets and municipal streets, run by different stakeholders. Milan is surrounded by the Milan Ring Road system of highways, which grants access to the city and connects the area with the rest of the region. The bus lines are evenly distributed across the city of Milan and the other municipalities within MCM. Milan is served by a High-Speed Railway (HSR) line connecting the city with Turin, Bologna, and the rest of Italy. The HSR is also being implemented along the Milan-Venice axis (via Verona). A dense railway network connects Milan with the different municipalities and enters the town via the Milan Suburban Railway (Passante Ferroviario), supported by several tram lines. Milan is served by five metro lines that extend beyond the municipal boundary into nearby municipalities. Milan, as well as the rest of Lombardy, is connected by air through three airports: Forlanini Airport (also known as Linate Airport), Malpensa Airport, and Bergamo Orio al Serio Airport. In addition to this mobility system, various sharing options (bikes, cars, and scooters) are also provided within the Milanese municipal boundary. A critical analysis of the as-is situation reveals that Milan is at the core of a dense mobility network serving the city and its immediate surroundings. The modal split in the region offers different mobility options and is capillary-diffused. MCM is located at the crossing point of an urban conurbation (in the North) and a more agricultural setting (in the South), safeguarded through preservation measures. The Milanese area constitutes one of the significant urban poles of Lombardy. It lies at the center of a densely populated region, where the settlements are concentrated mainly in the North-West and extend toward municipalities located in the Lombard foothill belt. As reported by (Colleoni, 2019; Comune di Milano, 2020; Regione Lombardia, 2016), in fact, MCM is in the midst of a densification process, with settlements forming a growing urban conurbation that includes the municipalities of the Lombard foothill belt, the municipalities situated along the railway line linking Varese to Milano and their surroundings, and the provinces of Bergamo and Brescia. In this scenario, the intermodal hubs in Milan become increasingly important in managing mobility flows. These ones are located in correspondence with metro stops. Moreover, several intermodal exchanges are located outside Milan's administrative boundary, due to the greater conurbation in which the city is inscribed. From this context, it emerges that the Milan region is at the center of a densely populated area, with an evolving settlement typology that is densifying along the pre-alpine axis within a greater urban conurbation extending beyond the administrative boundaries of MCM. In the greater MCM conurbation, the mobility flows are high and frequent. Most mobility demand is directed toward Milan, one of the region's main attractors (Regione Lombardia, 2016). It originates from both municipalities in the MCM and along the Sempione Axis. However, there are also mobility flows from the provinces of Varese, Bergamo, and Brescia. About 80% of mobility demand in Milan is accounted for by mobility flows within MCM municipalities, including Milan. Overall, most mobility flows consist of commuting, and the most congested time slot is from 7.00 to 9.00 a.m., but in the last few years, non-commuting and occasional travel demand mobility has also been increasing. Almost half of the daily population in Milan is composed of city users, so the city's access and exit points are particularly important. The most congested highways are those connecting Milan with the North-West and Eastern areas. The central metro stops are the most congested during the day. The stations with the highest number of passengers, more than 45.000 passengers/day, are Milano Centrale and Milano Porta Garibaldi (Rete Ferroviaria Italiana. Gruppo Ferrovie dello Stato, 2024). However, there are other relevant stations with a high frequency, such as Milan Rogoredo, Milan Suburban Porta Garibaldi, Milan Lambrate, with 20.000 to 45.000 people/day, or Rho Fiera, Milano Greco Pirelli, Sesto San Giovanni, Milano Repubblica, Milano Porta Venezia, Milano Porta Genova, Sesto San Giovanni, Rho, Pioltello Limito, with 10.000 and 20.000 people per day. What emerges is that Milan constitutes the major attractor core of the mobility system in the Lombardy region. Its mobility pattern influences mainly the nearby municipalities, both part and non-part of MCM. In this scenario, the primary mobility demand is displayed along the north-west axis and the eastern part of the city. Mobility demand and patterns are evolving.

Therefore, all the regulatory planning tools reported consider both the existing mobility system and project future mobility evolutions to support regulatory decisions. The study in (Regione Lombardia, 2016) reports the possible expansion of future urban poles, with the configuration of new poles such as Brescia, Bergamo, and Pavia, which may affect the overall demand pattern. (Città Metropolitana di Milano, 2021) envisions the evolution of the mobility system by strengthening public transportation along the axes connecting the nearby MCM municipalities to Milan. The North-West area, between the city boundary of Milan, covers a high-priority intervention in this regard. From this analysis, it emerges that mobility demand and patterns are steady within MCM, and they are expanding and increasing. Particular attention is given to strengthening public transportation systems. The Municipality of Milan is reporting future urban evolutions in the planning tools to inform regulatory decisions. According to this document, several urban developments are ongoing that regard both the outer areas of the city of Milan as well as other MCM municipalities. The proposed development projects regard mainly infrastructural works, such as the reconfiguration of the Bettola node near Monza linked to the proposed extension of the Milanese metro line to Monza, the reconfiguration of the Segrate Railway station to be upgraded with HSR, and the consequent extension of the metro line, in the framework of the Milan East Gate Hub (Giunta Regionale della Lombardia, Delibera n.4962). Further urban redevelopment processes interest Milan as well as MCM, such as the requalification of the former Expo Area close to Rho Fiera Milano railway and metro station. What emerges from this scenario is a consistent number of redevelopment projects going on, both in the areas inside and straddling the Milan Ring Road and outside Milan city. From the analysis carried out, it emerged that the mobility system is capillary and distributed in the selected area. Moreover, urban reconfiguration processes mainly cover the areas outside Milan city center, dealing with an expanding city. Therefore, the Milan Ring Road system constitutes a way of access that also represents an evolution of a possible boundary to the city of Milan, putting in relationship the core of the city with the outer evolving areas and the rest of MCM. In this context, peculiar relevance assumes the intermodal hubs located at the intersection or close to the Milan Ring Road that can enhance the mobility options available to enter in the city of Milan. By merging these six key aspects, it is possible to highlight some focal issues. Milan is at the core of a dense mobility network serving the city and its immediate surroundings, reflecting the high population density present. The settlement typology is densifying along the pre-alpine axis within a greater urban conurbation extending beyond the administrative boundaries of MCM. New urban development processes are at stake, especially in the area straddling the Milan Ring Road. In this context, intermodal hubs play a pivotal role in the access and regulation of mobility demand, providing more options. Several intermodal hubs are located alongside the Milan Ring Road and display relevant modal splits. However, two intermodal metro-rail exchanges cover peculiar relevance due to the closeness to the Ring Road access and for the mobility connections serving the hub, that intersect international, national, regional, and local flows, catching flow demand from the North, North-West, and South-East area: Rho Fiera Milano and Rogoredo. Rho Fiera Milano is inserted in the dense mobility network demands linking the North-West area of Milan. Milano Rogoredo is one of the major hubs of the city and can be equipped to sustain even further mobility demand coming from the envisioned new southern urban pole in Pavia. Considering the evolving demand and the intensification of the relationships with the East side area with respect to Milan, another intermodal hub plays a pivotal role in displaying mobility flows, Linate Airport, which manages air and metro / public transportation mobility. Moreover, the role of this hub will be increased by the foreseen construction of a new HSR station replacing the one in Segrate, enriching the hub modal split. These three locations represent possible suitable localizations for vertiport emplacement in relation to the existing mobility system and future development, as well as to conceive UAM service as a further option and not a competitor of the actual transport modes.

Urban Wind Simulations and Analyses

The microscale wind data for the 3 selected locations in Milan are generated and analyzed using the stochastic microscale wind model, SWM, within a Monte Carlo framework (Owen, 2013) as illustrated in Figure 4.73. SWM is a custom wind model developed by the authors and is based on Reynolds decomposition, where the total wind velocity is expressed as the sum of steady and unsteady wind components. Accordingly, SWM integrates a highly parameterized steady-state microscale wind solver, QUIC-URB (Brown et al., 2016), with a turbulence generator, TurbSim (Kelley & Jonkman, 2007). Although SWM may not achieve the same level of accuracy as computational fluid dynamics (CFD), one of its key advantages is the ability to generate quasi-non-stationary microscale wind data, $U(x, y, z, t)$, within seconds to minutes on a standard laptop. This capability is particularly valuable for vertiport emplacement analyses such as the present study, as SWM can be embedded within a Monte Carlo framework to provide preliminary insights into the prevalent wind conditions above a specific urban region.

The first step in the workflow involves obtaining 1D historical dominant wind speed and direction data at a height of 10 m from the Open Weather API (Meteomatics, 2026) for the period between 1941 and 2025 for the 3 selected locations. These data are then analyzed to determine the correlated wind speed–direction distribution. Subsequently, the full probability distribution is used to construct the cumulative distribution function (CDF). The CDF is then divided into multiple strata to enable stratified Monte Carlo sampling of the inflow wind speed and direction for the SWM simulations. This sampling approach ensures that even rare wind conditions are represented in the simulations, thereby providing a more statistically accurate representation of the wind climate compared to standard random sampling of the historical wind speed–direction distribution.

The SWM Area of Interest (AOI), corresponding to the overall QUIC simulation domain for all 3 locations, is defined as 1×1 km in the *X* and *Y* directions, respectively, with a vertical extent of 100 m in the Z direction. The Region of Interest (ROI) is positioned at the center of the domain, as shown in Figure 4.74. The spatial resolution of the simulation grid is set to 2×2×1 m in the X, Y, and Z directions, respectively.

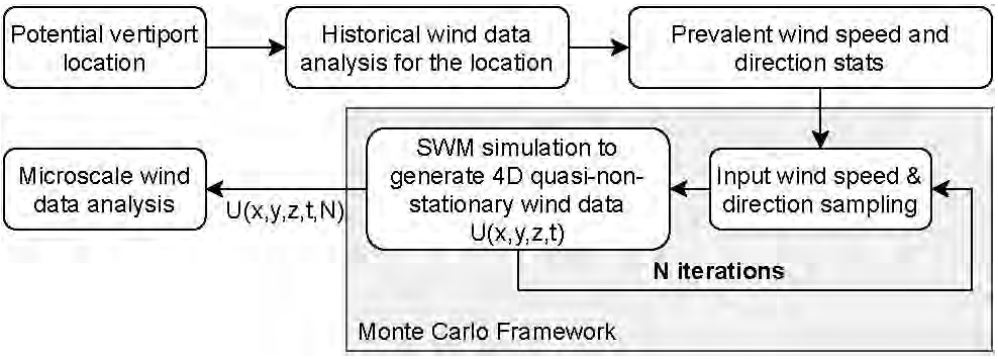


Figure 4.73: Overall microscale wind simulation framework.

The reference height is defined as 10 m, while the reference wind speed and direction are assigned based on the inflow values obtained from the historical data stratified sampling. The inflow wind profile is assumed to follow a uniform logarithmic law profile. Subsequently, the TurbSim simulation setup used to generate the 4D wind field data for the 3 locations is established by dividing the ROI into multiple 2D YZ planes. For the Rogoredo location, the resulting 4D wind data have a spatial resolution of 4×4×1 m and a temporal resolution of 1 s for a total analysis duration of 100 s. The turbulence intensity (TI) is set to 30%, and the fluctuations are configured to follow the Kaimal spectrum with a roughness length of 0.4.



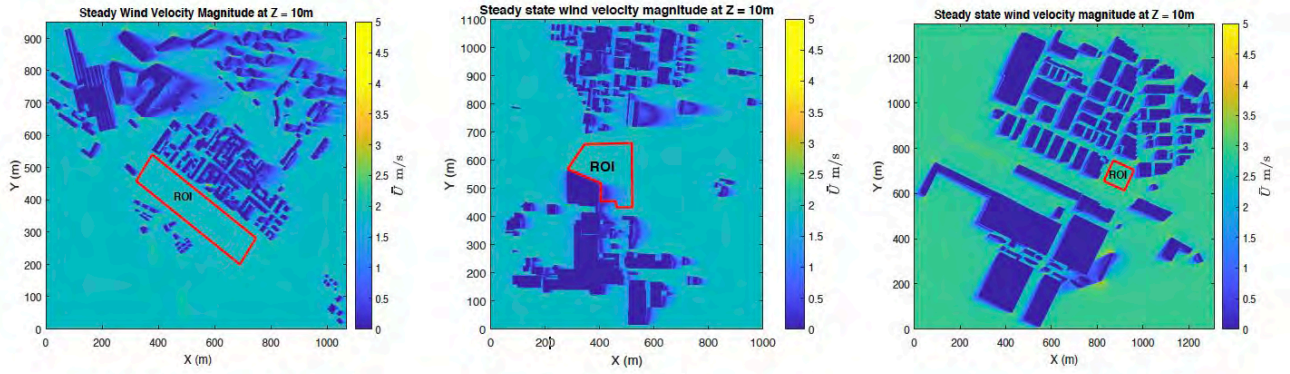
(a) Milano Rogoredo (b) Milano Linate (c) Milano Rho

Figure 4.74: SWM simulation domain or AOI with ROI for the three chosen locations.

For the Linate ROI, the TurbSim data resolution remains the same as in the Rogoredo case; however, the TI is reduced to 15% to represent Kaimal spectrum fluctuation with a roughness length of 0.1. This lower roughness length reflects the relatively open environment of the airport area and the limited number of surrounding buildings within the ROI. For the Rho ROI, the spatial resolution is increased to 2×2×1 m, with a TI of 25% and a roughness length of 0.6 for the Kaimal spectrum fluctuations. Once the simulation setup is finalized, the SWM simulations are executed for 100 iterations using varying inflow wind speed and direction values obtained from the stratified sampling procedure. The total computational time for each location is approximately 27–30 hours for the 100 Monte Carlo iterations when performed on a standard laptop equipped with 16 GB RAM, an 8-core processor operating at 2.8 GHz.

Microscale wind simulation results and analysis

Figure 4.75 presents the steady-state wind velocity magnitude at the 3 locations for a single Monte Carlo iteration, corresponding to one set of inflow wind speed and direction inputs. The inflow conditions used for this iteration are 2 m/s at 276° for Rogoredo and Linate, and 3 m/s at 69° for Rho. From the figure, it can be observed that the wind velocity magnitude range at Rho is higher compared to Rogoredo and Linate, with maximum wind velocities reaching approximately 4 m/s and 3 m/s, respectively. This variation can be attributed to the differences in the surrounding topography and urban morphology. Specifically, Rho represents a dense urban environment characterized by closely spaced buildings, whereas Rogoredo and Linate can be classified as suburban areas with relatively lower building density and larger open spaces. Additionally, the wind flow patterns within the ROI differ significantly across the three locations. In the Rogoredo ROI, the wind flow experiences minimal interference from surrounding buildings, resulting in comparatively smoother flow patterns. In contrast, the Linate ROI lies within the wake and side-wall accelerated flow region of a nearby structure. The Rho ROI, on the other hand, is surrounded by multiple buildings that produce complex localized flow structures. These observations reinforce the fact that wind conditions can vary significantly even between nearby locations within an urban environment due to the urban morphology. They also demonstrate how variations in inflow wind speed and direction can alter the resulting flow field and localized wind patterns in and around ROIs or vertiports. This highlights the importance of understanding wind conditions under multiple inflow scenarios when strategically determining vertiport placement within urban regions.



(a) Milano Rogoredo (b) Milano Linate (c) Milano Rho

Figure 4.75: Steady state wind velocity magnitude at Z = 10 m for all 3 locations for 1 Monte Carlo iteration.

The identification of dominant wind directions and wind speed levels was performed for the 3 selected locations to determine suitable orientations for ideal FATO zones and to assess the types of aircraft that could potentially operate at these sites. For this purpose, wind speeds were classified into three categories: low (0–2 m/s), moderate (2–5 m/s), and extreme wind levels (>5 m/s). It can be observed that, for all 3 locations, the predominant wind speed levels fall within the moderate wind category, although the dominant wind directions vary among the sites. For the Rogoredo region, the prevailing wind directions are between 240–300° and 25–110°, corresponding to easterly, northeasterly, and westerly winds, while the minimum wind occurrence is from the south. This suggests that the ideal FATO orientation should be aligned toward the south. Such an orientation would likely enhance operational availability compared to other directions. Similarly, for the Linate location, the dominant wind directions are from the north and south, while the minimum wind occurrence is observed from the east. This indicates that an eastern FATO orientation would be preferable for this location. In the case of Rho, the predominant wind directions are oriented toward the south, west, and southwest, while the minimum wind occurrence is observed from the east and southeast, suggesting the ideal FATO orientation for this site. The wind rose plots also provide insights into the wind speed–direction combinations associated with extreme wind conditions, thereby indicating directions that should potentially be avoided for FATO placement. However, wind conditions also vary temporally, and these plots represent only the time-averaged mean wind speed and direction distribution obtained from the 100 Monte Carlo iterations. The wind rose plots provide a preliminary understanding of the expected wind speed ranges and directions at the 3 locations, they do not indicate how steady or unsteady the wind conditions are likely to be (Figure 4.76). Therefore, averaged TI heatmaps derived from 100 Monte Carlo iterations were analyzed for the 3 locations at different heights to identify regions experiencing maximum and minimum turbulence levels. The TI magnitude ranges vary across the 3 locations based on the input parameters used in the SWM simulations. Rogoredo experiences TI of up to 34%, Linate up to approximately 15%, and Rho up to approximately 24% at lower altitudes. In the case of Rogoredo, the TI heatmap clearly reveals a strip-like region where the maximum unsteady wind conditions are concentrated. For Linate, the highest TI values occur near the corners of the ROI, primarily due to the influence of nearby structure. In contrast, the Rho ROI exhibits elevated TI across most of the lower altitude region, likely due to the surrounding buildings that generate complex flow interactions. Overall, these plots help identify spatial zones and altitude ranges where the TLOF area should ideally be located. For example, in Rogoredo, the TLOF should be placed within the strip of space where the TI values are minimal. Similarly, for Linate, the TLOF should preferably be located at the far end of the ROI rather than close to the adjacent structure. In the case of Rho, the relatively high TI at lower altitudes suggests that the TLOF may need to be positioned on an

elevated structure. Furthermore, these TI plots provide an estimate of the TI ranges present at each location, which can influence

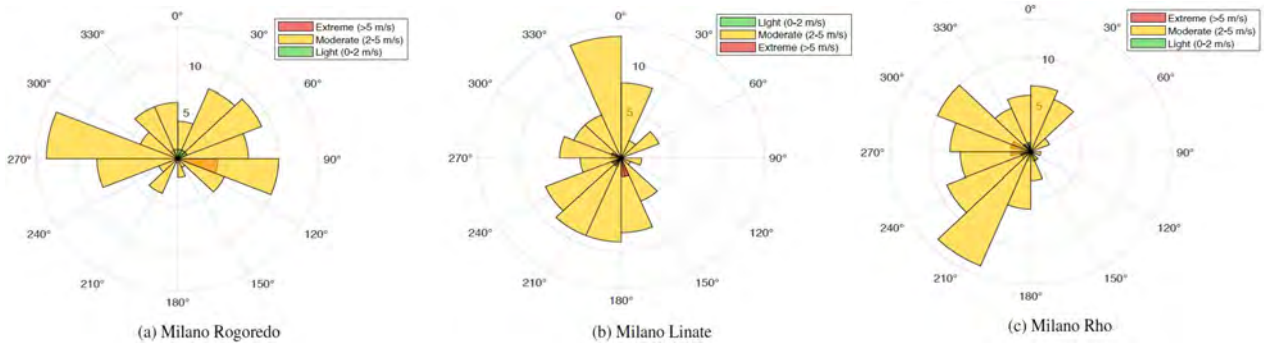


Figure 4.76: Prevalent time-averaged mean wind velocity magnitude and direction distribution for 100 iterations at the 3 selected locations.

the types of UAM aircraft that can safely operate at these sites. Depending on whether a particular UAM aircraft can tolerate the corresponding TI levels, it can be determined whether the vertiport at a given location would be suitable for facilitating a specific UAM aircraft landing/take-off.

In summary, this paper leverages intermodal hubs that intersect international, national, regional, and local mobility flows to identify 3 potential vertiport locations in Milan-Rogoredo, Linate, and Rho. Then, the localized mi-croscale wind flow conditions are simulated for the 3 chosen sites with the help of a stochastic microscale wind model, SWM, within a Monte Carlo framework. The resultant wind data, along with design strategies derived from the existing mobility and urban configuration, are compared and assessed to identify the feasibility of the 3 locations for vertiport emplacements within the metropolitan city of Milan. The analysis indicates that all 3 chosen locations are suitable for vertiport development, with no major discrepancies between the simulated wind conditions and the sites selected from architectural and urban perspectives. However, the study reinforces the fact that the placement of the FATO and TLOF requires particular attention in relation to wind speed, prevailing wind direction, and aircraft type for operational availability, feasibility, and societal acceptance.

On the whole, the interdisciplinary approach introduced in this paper demonstrates that vertiport design cannot be a ”one-size-fits-all” solution. By quantifying how specific urban morphologies dictate local wind behavior, such as the dense building clusters at Rho necessitating elevated landing pads to bypass complex low-altitude wakes, compared to the more open and predictable landscape at Linate, the study provides a technical basis for site-specific architectural requirements (Figure 4.77). Mapping TI and dominant wind roses offers the evidence needed to orient FATOs effectively, ensuring that localized gusts do not unnecessarily restrict the operational window for UAM services. Ultimately, treating UAM infrastructure as a functional component of the existing metropolitan urban

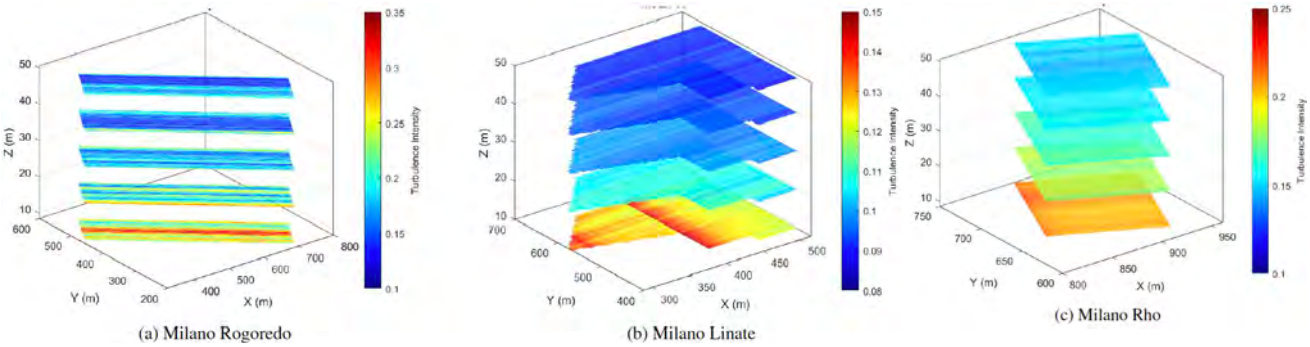


Figure 4.77: Averaged TI heatmap of 100 iterations at different heights (or Z) for the 3 locations.

and transport fabric, rather than an isolated engineering project, promotes seamless integration within cities and accessibility to diverse user groups, including commuters, travelers, and tourists, for better societal acceptance.

5 Operations, U-space, and Scalable Air Mobility

5.1 High Density Vertiports Operations in Advanced U-space

Bernd Bassimir

Vertiports serve as a new type of infrastructure that is specifically designed to facilitate the specific characteristics of the vertical take-off and landing capable aircraft (VCA) with a high level of automation in the involved processes. On a European level, vertiport operations are currently investigated as part of the project EUREKA (Schuchardt et al., 2025), with a focus on initial integration of vertiports into the European air traffic management system. Some of the ideas presented in this paper are based on similar principles which will be presented in that project. Vertiports are envisioned to act as entry and exit, as well as contingency sites for the transport of passengers and goods. To provide these functions, vertiports need to be in different types of environments, e.g., at airports, on top of buildings, and in cities or rural areas. Each type of environment has its own opportunities, challenges and even different involved actors. A vertiport needs to provide a minimum set of infrastructures and services including but not limited to a final-approach and take-off area (FATO), a touchdown and lift-of area (TLOF), as well as rescue and firefighting services (EASA Commission Implementing Regulations 2024/1111). Additionally, to facilitate all UAM scenarios, we need to extend these minimum requirements, at least for bigger vertiports, to include stands/parking spots and taxiways to reach the gates and stands from the FATO/TLOF. For the design and specifications of these infrastructure elements, confer to the EASA prototypical specifications for vertiports (European Union Aviation Safety Agency (EASA), 2022). To facilitate vertiport operations, an operator has to handle the availability of the infrastructure and monitor conformance. In line with the U-space levels, the role of human handling these tasks will change, from more manual control at lower levels of automation to a supervisory role. In the higher U-space levels, the human supervisor is supported by a highly automated vertiport management system handling all tasks, with only manual control in limited emergency situations that cannot be handled by the system itself. We will introduce an initial concept for a vertiport availability service, that is provided by our vertiport management system. This service is designed to answer one specific question: Is the vertiport available to perform an arrival or a departure operation?

An overview of early concepts for vertidrome airside operations can be found in (Schweiger et al., 2022) with a focus on integration into European airspace. For an overview of UTM management as envisioned by the FAA and NASA, we refer to the ConOps (Northeast UAS Airspace Integration Research Alliance (NUAIR), 2021), with a study performed by NASA focusing on the feasibility and scalability of these operations in (Prince, 2025). This study performed by NASA gives a detailed description of the processes involved in VCA operations including the roles and responsibilities of the different actors of UAM. For the vertiport management, this includes the resource allocations, a focus of this paper for the U-space framework, ground handling and the coordination with fleet operators. Additionally, the vertiport operator will continuously monitor the resource allocations, which is also included in the concept introduced in this paper. When handling the availability, most of the scheduling will be handled by this software system. In (J. Li et al., 2025), the authors assess a genetic algorithm for assigning slots and compare the results against a first come first serve algorithm by measuring vertiport capacity and operational delays while considering throughput and passenger satisfaction. For conventional airports, a similar problem needs to be solved. While having less on-demand and more rigorous slot allocations, determining optimal slot assignments in a pre-tactical phase can still improve the runway utilization, see for example (Heidt et al., 2014) for such an optimization using integer program solvers. This performance indicator can be transferred to a vertiport environment where we have to optimize the utilization of the FATOs. As an example of approach designs,

Kleinbekman et al. (2018) introduce a mixed-integer linear program to optimize trajectories for aircraft to reach the vertiport terminal airspace based on remaining battery charge and vertiport capacity.

Vertiport availability in the strategic phase

In this section, we will discuss parts of a vertiport management system that is designed with a high level of automation in advanced U-space levels U3 and U4, and only a human in the supervisory role. In particular, we will be focusing on handling availability of the vertiport. We first give a quick overview of what we consider part of the availability of a vertiport before going more in detail of what is envisioned for each of the different parts of the availability definition, as well as provide a discussion on the challenges involved and addressed by our approach. **Vertiport Availability:** In the concept discussed in this study, availability at a vertiport involves the following points:

- A **Stand** needs to be available for boarding/deboarding or loading/unloading
- A **Taxi-route** needs to be free and, if necessary, the mechanism for the taxiing needs to be available.
- A **FATO** and the corresponding procedure volume need to be free; this includes that the obstacle free volume has no object in it.
- An **approach/departure heading** and its **corresponding route** from the landing decision point to the selected FATO is conflict free.
- The **weather** is within permissible limits as specified by the VCA certification for the planned operation.

Figure 5.78 shows parts 1 to 4 for an approaching flight. For each flight, we need to ensure that one such green path is available from the landing decision point (LDP) to the stand, and the reverse needs to be true for a departing flight, where the LDP is a handover point instead. An integral part of the availability of a vertiport is the definition of a vertiport slot. In the context of this paper, we define a vertiport slot as a time interval with a length supporting the whole operation and for which all five points from the definition above need to be true. The length of the slot can depend on the VCA characteristics but is fixed after the operation is approved. The slots do not adhere to a fixed timetable, instead, the start- and end-time can be freely chosen as long as the requirements for the complete time interval are fulfilled. To be able to perform an operation, either arrival or departure, the aircraft operator needs to book one such slot as part of the generation of a flight plan using a planning service, one of the U-space services provided by a USSP. Slots are requested on demand with low lead times required, but due to their flexible nature, slots are only transmitted on demand to the U-space Service Providers (USSP) and updates in availability are immediately published for affected slot bookings. All the following descriptions are based on a priority system. As such, the discussion in the next sections is valid for flights of the same priority. A flight with a higher priority can always override one of lower priority, e.g., for emergency handling and special operations.

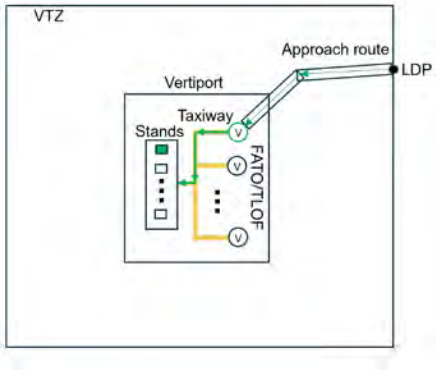


Figure 5.78: Schematic overview of the parts 1 to 4 of the availability definition for an approach operation in the vertiport traffic zone (VTZ). It highlights a route from the landing decision point (LDP) to the deboarding at a stand. Note: The sizes of the elements are not to scale.

Slot allocation

In our approach, we consider two different types of slot allocations. First, we have regular slots that are used for all nominal operations and follow a pre-booking and booking scheme.

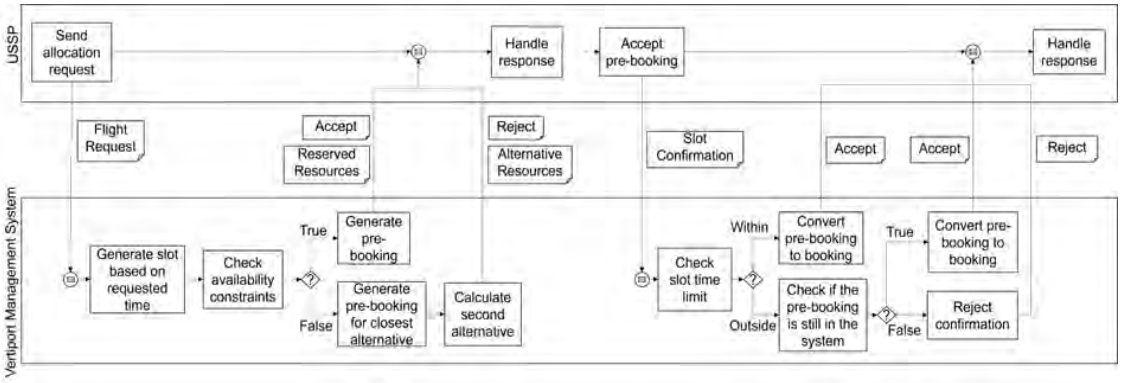


Figure 5.79: Slot allocation flow from the initial flight request sent by the USSP to the response sent after the slot is finally booked. Between the first "Handle response" and the "Accept pre-booking" functions an arbitrary amount of time can pass as represented by the dashed arrow.

Figure 5.79 shows the process envisioned for a single flight request. We start with a pre-booking of a slot, which is generated by the vertiport management system in response to the initial availability request send by the USSP and is based on a submitted flight request. If there are no overlaps with already existing slots, this pre-booking slot is saved in the system. The length is chosen in a way that it allows for the operation to take place at the requested time following all characteristics of the used VCA and the system triggers an "accept" response. The length of the slot includes additional time to allow for small deviations in flight time, however, the actual length of a pre-booking slot will be subject to further research. Otherwise, if it is not possible to perform the requested operation at the requested time, a "reject" response is triggered for the flight request. However, to provide the operator with the information needed to amend the flight request, we generate a list of alternative options. For our initial concept, we will provide the operator with two alternative options. The first alternative option, which will have a pre-booking slot generated, will be the closest possible slot that could accommodate the flight request while minimizing the absolute difference to the requested flight time. The other alternative option provided, which will not have a pre-booking generated, will be the closest slot that is either before or after the initial proposed time depending on the first alternative option.

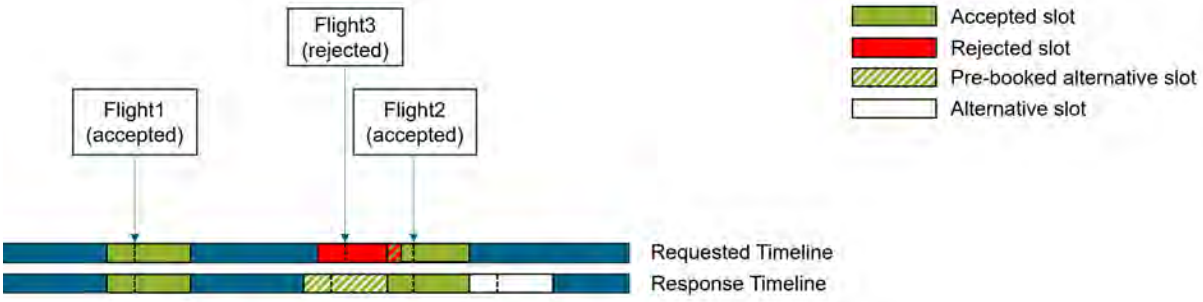


Figure 5.80: Slot pre-bookings showing three flight requests, with Flight1 and Flight2 being accepted and Flight3 being rejected. The red and green striped box shows the overlap in the requested slots. The green boxes show the generated pre-booking slots and the white boxes the alternative options, with the green striped box being the pre-booking.

Figure 5.80 shows the generation of the pre-booking slots for three flight requests being handled sequentially in the order of flight number. Flight1 and Flight2 have pre-booking slots generated based on their requests, as these do not overlap with another slot. However, Flight3 would have an overlap as shown by the box striped red and green

and is therefore rejected. As alternatives, a pre-booking, the box striped white and green, is generated that minimizes the deviation and the second alternative that is sent is shown as a white box.

These alternative options are envisioned to provide a U-space planning service, and the VCA operator, with alternatives to amend the flight plan without having to send further flight requests by blindly changing the requested time until the request is accepted. While the introduced alternatives are based on timings, the vision for further development of the vertiport availability service would include several different objectives that can be selected by the VCA operator, e.g., operational costs or faster turnaround times.

These pre-bookings are reserved for a defined amount of time and only after this time expires can other requests use the time interval of the slot. Until another pre-booking request is sent for the same request or another unrelated request overlaps with the expired pre-booking slot, the pre-booking is kept in the system after exceeding the time limit. To confirm a pre-booking, a confirmation message must be sent through the USSP. If the confirmation message is still within the time limit, the booking is automatically accepted and the pre-booking is converted to a booked slot. Alternatively, if the message is sent after the time limit expired but the pre-booking is still in the system, it will still be accepted. If neither is true, the confirmation is rejected and a new flight request needs to be filed.

A different type of slot is used to comply with regulation 2024/111 for VCA operations. This type of slot is designed to be used in cases of a critical failure of performance (CFP). It follows the same principles of pre-booking and booking previously discussed, however, these slots are allowed to overlap with other contingency slots but they still do not allow overlaps with regular pre-bookings/bookings. This is possible because the regulation forces the rate of a CFP for a single VCA to be at least remote, as such the chance of two aircraft using the booked contingency slot for a CFP at the same time is quite unlikely. In the future, we will further investigate how many VCA can safely use a contingency slot at the same time using an upper bound on the probability of at least one of the VCA that booked a specific contingency slot having a CFP and its impact on capacity and safety. As we cannot predict the exact distance of the VCA to the vertiport for a contingency, there is not a fixed time the aircraft is predicted to land. Therefore, we use slots that are longer to compensate for this unpredictability, as such it allows for more robust operations. Further research will tackle the question of the trade-off between the VCA arriving in the reserved slot and the utilization and capacity of the vertiport.

Approach and departure procedures

To address point 4 of the availability of a vertiport, we introduce our concept of a vertiport traffic zone (VTZ). This zone is not a completely separate airspace, but acts as augmentation to the surrounding airspace, which can be either a controlled or U-space airspace. In this zone, some U-space services will be provided by the vertiport and more direct control of the flight, especially approach and departure routes, will be taken over by the vertiport management system. This allows for more flexible routes to be used, which can lead to an increase in the number of concurrent flights to different FATOs while still ensuring the required level of separation, as well as faster reaction times in case of missed approaches or other failures. Depending on the surrounding airspace, the involved actors will differ. If the vertiport is at an airport, and consequently in controlled airspace, the vertiport will use the collaborative interface to air traffic control (ATC) to exchange information with the air traffic control officer (ATCO) to provide situational awareness about flights arriving to or departing from the vertiport. However, the goal of the approach and departure procedure design is achieving complete separation to all other airspace users. One example of such approaches are the PinS (International Civil Aviation Organization (ICAO), 1993) approaches for rotorcraft at helipads, which can be simultaneous non-interfering (SNI) operations, see (Schmerwitz et al., 2019) for an example of such an approach. It is based on GNSS and combines visual and instrument segments to reach a specific point at a heliport starting from an initial approach fix for arrivals and from a FATO to a PinS location for departures. Unfortunately, the whole procedure cannot be used directly for UAM scenarios as the length of the different approach sections need to be reduced drastically, the defined cloud minima might not apply, and flight procedures for UAM scenarios in higher U-space levels will probably not include visual flight rules. For a vertiport outside of

controlled airspace, these procedures can be simplified, as we do not need to separate from conventional aircraft, however, we still need to have SNI operations between all VCA arriving to, or departing from, the vertiport. Especially in the U-space airspace environment, we can use the omni-directional approach and landing surfaces to minimize the time the FATO cannot be used because of a departing or arriving aircraft. In controlled airspace, this might only be possible to the extend that it does not interfere with the other airspace users at the airport. In both cases, the landing decision point will be at the edge of the VTZ, with multiple of these points connecting to the rest of the route network. As such, we separate the approaching or departing aircraft from the remaining traffic that is not using the vertiport and only the traffic directly affecting the vertiport needs to be separated from each other, a task envisioned for our vertiport management system.

Weather information and vertiport availability in tactical phase

Even if points 1 to 4 of the availability definition are true, for the vertiport to be available for a scheduled operation, the local weather conditions at the vertiport still need to fulfill the specific operational limits of a VCA as specified in the certification processes. These usually include wind, specifically headwinds, tailwinds and crosswinds, cloud minima, and other weather conditions like rain or snow. These need to be taken into account when calculating approach and departure routes and the available headings for a FATO. As such, the vertiport needs to have the required information of an aircraft available for assessing the situation and to provide an estimation on the impact of the operation. This can either be an availability warning or, if exceeding the limits specified by the vertiport for safe operation conditions, a rejection of the availability. As previously introduced, the vertiport availability service is designed to answer one specific question: Is the vertiport available to perform an arrival or a departure operation? This question, however, does not end with the authorization and activation of a U-plan. Even during the tactical phase, the conditions can change enough that one of the points of the availability definition will not be valid anymore. At that point, the vertiport will no longer be available for the aircraft and as such, a change to the U-plan needs to be initiated. This can range from activating a filed contingency to simply booking a new slot at a different FATO. As not all interruptions to the points in the availability definition are significant enough or have a high enough confidence value to actually affect the vertiport availability for a specific U-plan, it still can make sense to inform the VCA operator of a deteriorated availability, which can include information on delays and holding positions, if necessary. Future research will tackle the questions on how such warnings affect throughput of the overall UAM system and potential impacts on business cases. Consequently, this service will be extended to not only include planning elements, but also advisory parts. In practice, we propose the following framework for the advisory part of the availability service.

- Identify a disruption to one of the four points of the availability definition for a U-plan.
- Classify the disruption in regard to severity and probability to affect the scheduled procedure.
- Send an availability change or an availability warning to the USSP depending on the classification.

How to implement step 2 is kept open at this point and is subject to further research, as well as which classifications will trigger an availability warning and which an availability change. There are two goals of this framework, first, the coupling of all aspects concerning availability into a single service to reduce the number of sources for similar information. The second goal is to increase situational awareness during the tactical phase by providing the VCA operator with a clear picture of the vertiport status and providing them with options to amend the U-plan with all information communicated in a timely manner.

Discussion

While we present a concept for the vertiport availability service, which specifically includes considerations for approach and departure procedures, a lot of questions remain to be answered. One of the main open points of discussion when dealing with a high level of automation in the air traffic services is the question of clearances. While in controlled airspace, these can still be given by ATC. However, the process would still need to evolve to

tie into the automation envisioned by the new U-space stakeholders. In full U-space, it remains an open topic which of the U-space stakeholder can and should take on this responsibility. One possible solution would be to have the vertiport management system and the human supervisor provide some related clearances, or at least clearance-like authorizations, e.g., for start-up, taxiing, and a collaborative take-off authorization with air traffic control or the USSP. However, as a result, the vertiport operator needs to include trained and certified personnel, an air traffic control officer or at least someone similarly trained and certified which, therefore, elevates the vertiport operator to a controlling authority. Furthermore, for the concept presented here, handovers of at least some services from the USSP to the vertiport management system need to be designed when the edge of the VTZ is reached. These would mainly be the emergency and the conformance monitoring services. We do not provide definitive answers for these topics and there needs to be future research on integrating these procedures and clearances into UAM operations in a safe and efficient way.

In this study, we discussed the vertiport availability service, a service envisioned from U3 onward, for UAM operations in a U-space environment. We presented the frameworks for the strategic and the tactical phase to be used in upcoming fast-time and human-in-the-loop simulations for validating the service. We suggest to extend the definition of the vertiport availability service within the U-space framework to include all aspects of an arrival or a departure operation. Additionally, this U-space service should not only be a planning service but also provide advisory information and monitor disruptions beyond the initial planning phase. The framework is designed to provide a foundation for extending the service with different alternative concepts. The introduced vertiport availability service, which is one of the services provided by our vertiport management system, VERtiport ManaGER VERTIGER, will be part of a newly created research lab at DLR. In this lab, the service will be used among others to answer questions in the domain of U-space traffic management, e.g., vertiport capacity, vertiport utilization and safe airspace integration.

5.2 U-space Services as a Necessity for Scalable Vertiport Operations

Bianca I. Schuchardt, Enno Nagel, Marzia Corsi and Bernd Bassimir

U-space is a set of new services relying on a high level of digitalization and automation of functions and specific procedures, designed to provide safe, efficient and secure access to airspace for large numbers of unmanned aircraft, operating automatically and even beyond visual line of sight. This kind of concepts of operations (ConOps) of airspace integration for drones and air taxis are also called UTM (Unmanned aircraft system Traffic Management) systems, being U-space the UTM ConOps agreed for Europe. U-space services are under development but commercially not available yet. For demonstration purposes, in the project HorizonUAM, a central U-space cloud service is simulated through a local messaging server using the protocol MQTT (Message Queuing Telemetry Transport). A prototypical vertiport management tool was created to demonstrate the scheduling and sequencing of air taxi flights. The management system of the vertiport (also called vertidrome in the HorizonUAM context) is fully integrated within U-space and receives real-time information on flight plans, including requests for start and landing and emergency notifications, see Figure 5.81-a. Additional information coming from other U-space services (e.g. weather information) can be accessed on request. The integration was demonstrated in a scaled flight test environment with multicopters (<15 kg) representing passenger carrying air taxis, see Figure 5.81-b.

For this purpose, a model city was erected consisting of an urban canyon and several landing pads. The scaled demonstrations proved to be very effective especially as prototypes of full-sized passenger carrying air taxis are still rarely available (Schuchardt et al., 2024). Specifically, the interface evidenced to be a first good approach to the software that would be required in a first implementation phase in which a person-in-the-loop is required to approve or cancel air taxi operations in terms of functionality and information displayed. Furthermore, the process of the eventualities, even with the requirement of a person involved, was quick enough for the drone in the scaled experiment to be able to maneuver on time and execute the rerouting with no risk. U-space services will be

implemented in the near future in Europe and will be made available for new airspace users such as UAS but also for remotely piloted or autonomous air taxis. Specific U-space services as needed for vertiport operations were successfully tested in the reported scaled flight demonstrations. In future research, more emphasis should be placed on the actual vertiport layout and the approach procedures. Capacity and efficiency of different designs should be carefully considered in simulation as well as in flight testing.



(a) (b)

Figure 5.81: (a) Vertiport air traffic management system integrated into U-space; (b) scaled urban air mobility flight demonstration.

Roadmap for the Establishment of an Innovative Air Mobility Control Center Research Lab

In this section, we provide an initial roadmap for establishing an Innovative Air Mobility Control Center (IAM-CC) laboratory at the German Aerospace Center (DLR). The goal of IAM-CC is to serve as a rigorous and reproducible testbed for the evaluation of technical, operational, and human-factor aspects of UAM, as well as to offer an interactive platform for the research and development community interested in UAM.

Growing demand for local and regional air transport along with increasing urbanization drives the development of air taxi and logistic services, which are ultimately expected to operate in U-space, Europe's air traffic management framework for unmanned aviation. In response to the evolving needs of this market, a research laboratory dedicated to the exploration of scalable and technologically advanced air mobility systems is warranted. The laboratory will systematically address the core research questions of flight guidance, U-space, scalability of UAM, human and-automation interaction. The architecture of the IAM-CC laboratory blends a suite of back-end services with a hybrid of web-based operator interfaces and mixed-reality environments. Core components include:

- A Fleet Control Station (FCS) - a web-based user interface for commanding and supervising VTOL flights using U-space services and vertiport management system interfaces.
- Vertiport Management Module (VERTIGER) - a vertiport scheduling and sequencing system that integrates seamlessly with U-space services and air traffic control (ATC) interfaces.
- A Scenarios and Planning Toolkit - enabling the automatic generation of realistic, representative UAM scenarios spanning different densities and complexities.
- U-space simulation modules - emulating the interactions between UAM operations and U-space stakeholders (e.g., Common Information Service Provider (CISP), U-space Service Providers (USSP)).
- Hardware- and mixed-reality simulation tools - including full-sized passenger-cabin simulator, see also Figure 5.82.



(a)



(b)

Figure 5.82: Physical labs used for UAM research at DLR Institute of Flight Guidance, Braunschweig: (a) UASLab; (b) Air taxi cabin simulator UAMSim.

Operational Scenarios and Research Applications

The IAM-CC laboratory will be employed to systematically address the above key research questions through a structured set of operational scenarios, progressing from baseline single-vertiport and single operator scenario to complex multi-stakeholder scenarios and contingency management. The platform is organized around six primary research areas:

1) *U-space service requirements and feasibility:* starting from the baseline use case, it will be assessed which U-space services are strictly necessary, and under what conditions additional services provide measurable operational benefit.
2) *HMI design:* building on established HMI design and evaluation principles, the FCS and VERTIGER interfaces will be assessed in terms of workload, situation awareness, and decision support quality, with particular attention to transitions from nominal to off-nominal conditions.
3) *System efficiency:* metrics such as throughput, delay, slot utilization, and energy consumption will be assessed across scenarios of increasing density and complexity, with the baseline providing a reference point for quantifying the gains introduced by new services or design choices, and for identifying potential bottlenecks.
4) *Procedure design and impact assessment:* using indicators such as U-plan acceptance rates, conflict rates, and human operator intervention frequency, procedures will be evaluated under nominal and of-nominal conditions.
5) *Responsibility allocation and operational efficiency:* as autonomy increases, the appropriate distribution of responsibility between human operators and automated systems becomes a critical design variable. Experiments will examine how different task allocation strategies affect workload, error rates, and system throughput.
6) *Training of personnel:* the controlled IAM-CC lab environment supports the development and evaluation of training protocols, measuring how quickly operators reach proficiency and how performance holds under stress or unfamiliar contingency scenarios.

Under the roadmap described herein, the IAM-CC research laboratory will form a vital enabling component for the future UAM and U-space ecosystem. It will be a dedicated and reproducible testbed for technical, operational, and human-factor evaluations of UAM, offering tangible insights into the safe, efficient, and sustainable deployment of these emerging services.

5.3 Autonomous Conflict Resolution for Drones using Deep Reinforcement Learning

Sasha Vlaskin, Călin Andrei Badea, Emmanuel Sunil, Joost Ellerbroek, Jacco Hoekstra, Dennis Nieuwenhuisen

As drone numbers in European lower airspace continue to grow, through emerging applications such as infrastructure inspection and medical/parcel delivery, drone traffic densities are expected to exceed what human

Air Traffic Controllers can safely manage. For this reason, Autonomous Conflict Detection and Resolution (CD&R) systems are a prerequisite for scalable Urban Air Mobility and drone operations. As required by the European U-space concept (European Union Aviation Safety Agency (EASA), 2026a), these systems must allow for each drone to *self-separate* – that is, use available state information for longer-term evasive maneuvers to avoid unexpected vehicles in their path. Many methods exist for this, from distributed geometric methods to ones fully centralized on the ground. Recently, Reinforcement Learning has been showing great promise for this conflict resolution task, as well as many others such as flow merging at landing sites and altitude layer assignment.

Research up to this point (Groot, Ellerbroek, et al., 2024; Schlichting et al., 2022; Vlaskin et al., 2025) has assumed either single-agent control or fully cooperative multi-agent learning, which presents a research gap. This is because these vehicles should handle not only cooperative traffic, but also priority vehicles that are observable yet unresponsive. Vehicles like this can include medical drones flying high-importance missions that are not expected to deviate from their trajectory, or ones experiencing system faults that broadcast their state but cannot maneuver and participate in conflict detection and resolution. This chapter investigates how the presence of such unresponsive vehicles affects the performance of a learning-based conflict resolution algorithm, and whether explicitly including them in training or adapting the state vector or RL mechanism is necessary for robust operation. A key question for operational deployment is whether a system trained in an idealized, fully cooperative environment will degrade rapidly when unresponsive traffic is added to the vehicle mix.

This work leveraged a fast-time simulation workflow, with the BlueSky ATC simulator and BlueSky-Gym (Groot, Leto, et al., 2024) for RL model training and subsequent fast-time simulation. Fast-time simulation allows for the rapid testing of methods in a representative simulated environment, bypassing costly deployment and allowing for some early methodological insights. The conflict resolution model is trained on a representative environment, and then tested in a similar tested fast-time.

Simulation environment, RL methodology and Baseline

The simulation environment in question models a randomized airspace sector in which vehicles navigate to waypoints on the sector boundary while maintaining separation. This is based on the *SectorCR-Env* from BlueSky-Gym (Groot, Leto, et al., 2024). This is representative for simplified drone tasks, as most autonomous vehicles will be performing GNSS-based waypoint following for most required missions. Resolutions (actions) are constrained to the horizontal plane as to allow for layering and to utilize the restrictive U-space operational ceiling of 120 m AGL, thus consisting of heading and speed changes. All unresponsive vehicles broadcast their state continuously but take no avoidance action, simply following their prescribed path to the waypoint. From this set of vehicle states, compiled from the vehicles in the airspace, an observation is fed to the actor network, or the learning-based conflict resolution agent. Every simulation instance is randomized in order to prevent overfitting, meaning the sector shape, vehicle destination waypoints and positions are all randomly sampled from bounded uniform distributions. The size of the sector in question is randomized, with up to 21 vehicles simulated. The cooperative agents themselves are attention mechanism-based policy actors, sharing a single policy. Their learning is governed by an observation vector encoding airspace state and the states of other drones as input, and an action as output, bounded by their action space. The observation space consists of the ownship state vector, encoding $cos(\delta)$ and $sin(\delta)$ (the drift angle to the waypoint), ground speed v, position (x, y), and velocity components (v_x, v_y), together with a relative state vector computed per intruder, relative position $(\Delta x, \Delta y)$ and relative velocity $(\Delta v_x, \Delta v_y)$, aggregated across a variable number of vehicles via the attention mechanism.

Once the observation is fed forward through the actor network, a resultant action is produced. The corresponding action space, bounded to the horizontal plane as described above, is given by:

Action	*Normalized Range*	*Physical Range*
Heading change	[-1, 1]	±22.5°
Speed change	[-1, 1]	±10 kt

Table 5.27: Allowed actions and their bounds.

The learning itself is shaped by a reward function, which penalizes unsafe and inefficient states numerically, defined as $r=R_{drift}\ \delta+(0$ *if not in intrusion,* -1 *if in intrusion)* where the drift term penalizes heading deviation δ from the direct-to-waypoint course as an efficiency measure, and the intrusion term applies a sparse -1 per timestep spent inside another vehicles protected zone as the safety component. The learning algorithm used is Soft Actor-Critic (SAC) (Haarnoja et al., 2018), implemented in a multi-agent framework with an attention mechanism that allows the model to process a variable number of surrounding vehicles and implicitly weight those posing the greatest conflict risk. This attention-based approach also provides a natural mechanism by which the policy might learn to prioritize avoidance of vehicles that are unlikely to maneuver, even without explicit priority-aware reward shaping. This is the core of the study. The Modified Voltage Potential (MVP) (Ballin et al., 2002) algorithm serves as the classical baseline for the learning-based method. MVP is an iterative geometric method that recomputes avoidance vectors at each timestep, whereby it would be resilient to non-responding traffic if an adequate safety margin is maintained.

Experimental setup and results

Several RL models were trained under different fixed proportions of unresponsive vehicles (0, 4, 8, 12, 16, and 20 out of 21 total), as well as a model trained with the unresponsive count sampled uniformly each episode. Each was evaluated across all unresponsive proportions over 5000 simulation episodes per combination. The central and somewhat surprising result is that the training distribution does not significantly affect the resulting policy's safety performance. As shown in Figure 5.83, neither total intrusion time nor unique loss-of-separation counts show meaningful variation across the different training configurations of the RL model.

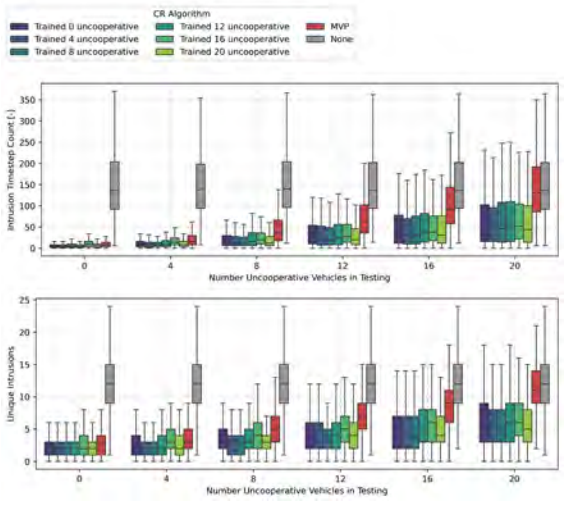


Figure 5.83: Evaluation of all CR algorithm variants across unresponsive vehicle proportions (0–20). Top: intrusion timestep count. Bottom: unique losses of separation. Color indicates training configuration; gray denotes the no-CR baseline. The RL variants (blue–green family) cluster closely together regardless of training condition, and consistently outperform both MVP (red) and the no-CR case (gray) in terms of unique intrusions.

A model trained exclusively on fully cooperative traffic performs comparably to one trained with up to 20 unresponsive vehicles, across all tested conditions. The policy generalizes mixed traffic even without having encountered it in training. The overall airspace state does deteriorate as more unresponsive vehicles are added total intrusion time increases, since those vehicles themselves contribute to losses of separation that no algorithm can prevent. However, when only intrusions involving cooperative vehicles are considered in isolation, the RL model maintains separation at a level consistent with the fully cooperative baseline. The algorithm is effectively shielding its own controlled vehicles from harm even as a growing fraction of the airspace becomes unmanageable.

Compared to MVP, the learning-based models show lower unique intrusion counts across all tested conditions. This advantage persists into high unresponsive proportions, suggesting that the emergent coordinated policy of the attention-based SAC model offers a structural benefit over purely geometric iterative methods when confronted with non-cooperative traffic.

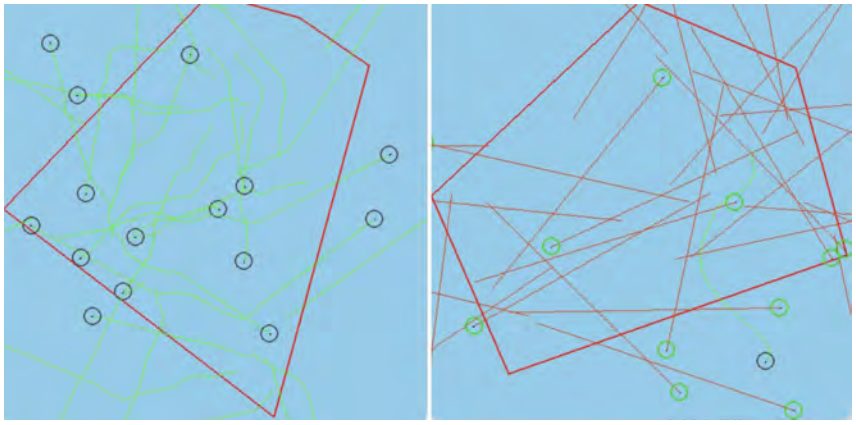


Figure 5.84: Simulated trajectories at episode end for the fully cooperative scenario (left) and a scenario with 20 unresponsive vehicles (right). Cooperative vehicle paths are shown in green; unresponsive paths in red. The single cooperative vehicle in the mixed scenario (bottom right, black) executes sharper avoidance turns to compensate for the absence of reciprocal maneuvers from the surrounding traffic.

The trajectory visualizations in Figure 5.84 reinforce this interpretation. In the fully cooperative case, vehicles share the avoidance burden and execute relatively smooth, distributed maneuvers. In the extreme mixed scenario, the single cooperative vehicle must make sharper, more decisive turns to avoid all unresponsive traffic unilaterally. The policy does adapt its behavior in execution, it simply does not need to be exposed to this scenario during training in order to do so. These results carry practical implications for how conflict resolution algorithms should be trained and certified for deployment in U-space. The finding that training distribution is largely inconsequential, at the tested densities, simplifies one dimension of the algorithm development problem: operators and developers need not curate highly specific mixed-traffic training scenarios in order to achieve robust performance against priority vehicles or faulty drones. A well-trained cooperative model appears to generalize adequately.

This does not, however, eliminate the need for rigorous testing against mixed traffic. Training robustness and test robustness are separate questions. The results presented here suggest that the policy's emergent behavior, enabled by the attention mechanism's ability to weight high-risk neighbors, provides resilience that was not explicitly programmed into the reward function. Understanding the mechanism behind this generalization more deeply, rather than simply observing it, is an important direction for future interpretability work.

A further open question concerns density. The current experiments operate at a fixed total vehicle count. As traffic densities scale toward the upper limits anticipated in mature UAM operations, the available maneuvering room for cooperative vehicles shrinks. The safety headroom that allows the current algorithm to absorb the presence of unresponsive traffic may narrow significantly at higher densities, and preliminary findings suggest this is where the

separation of training conditions may begin to matter. This remains an active area of investigation. Extensions underway include heterogeneous vehicle dynamics among unresponsive intruders, scaling to higher traffic densities where training distribution is expected to matter more, and deeper analysis of attention weights to explain the observed robustness mechanistically.

5.4 Profitability Potential of Urban Air Mobility Operations across Metropolitan Regions

Ansgar Kirste, Eike Stumpf

Motivation and scope

As eVTOL vehicle certification programs advance and demonstration flights validate operational concepts, the research focus on urban air mobility shifts from technical feasibility toward economic viability (Cohen et al., 2021), as part of a growing low-altitude economy (Sun et al., 2025), relies on travel time savings compared to congested ground-based alternatives. However, the costs for infrastructure, fleet operations, and energy currently constrain the achievable market potential, and cost optimization at both strategic and operational levels is required to enable commercially viable services (Kirste & Stumpf, 2025b).

Several studies have assessed UAM market potential across different regions and price assumptions. Mayakonda et al. (2020) apply a willingness-to-pay model across 31 cities and report accelerating demand growth below 0.90 USD/pkm. Asmer et al. (2024) extend this perspective to 990 urban agglomerations and identify a demand threshold around 3 to 4 EUR/pkm beyond which adoption decreases sharply. At the operational level, Lewis et al. (2021) evaluate airport shuttle services in three U.S. metropolitan areas and recommend Los Angeles as a pilot city based on demand volume and route structure. Coppola et al. (2025) survey travelers in Milan and find modal shares below 0.2 percent for intra-city air taxi services. However, the comparability of UAM viability findings remains limited, as most studies address individual metropolitan areas or omit the cost perspective of a fleet operator from the assessment. In particular, three aspects have been identified as recurrent sources of overestimation in earlier UAM market potential analyses: the omission of competing transport modes, the absence of integrated pricing and cost modeling from an operator perspective, and the neglect of vertiport throughput constraints imposed by rotor downwash and outwash effects (Ison, 2024; Muia et al., 2024). A systematic profitability comparison across diverse urban structures that accounts for these factors remains largely unexplored. To address this gap, an integrated simulation and optimization framework is applied to six global metropolitan scenarios: Los Angeles, Rhine-Ruhr, Berlin, Hamburg, Mexico City, and Kyoto, covering a range of urban structures from car-dependent sprawl to compact cities with dense public transport networks.

Demand simulation, surrogate modeling, and profit optimization

The assessment follows a modular framework consisting of three stages (see ***Figure 5.85***): First, UAM demand builds on potential station networks and is simulated using agent-based transport modeling with surrogate model extensions. Second, fleet-level profit is optimized based on total cost of ownership. Third, the resulting scenarios are evaluated from operator, passenger, and system-level perspectives. ***Figure 5.85*** illustrates the modular structure, where eVTOL vehicle design parameters feed into both the demand simulation and the cost model, enabling consistent analysis across different configurations and metropolitan contexts (Kirste & Stumpf, 2026).

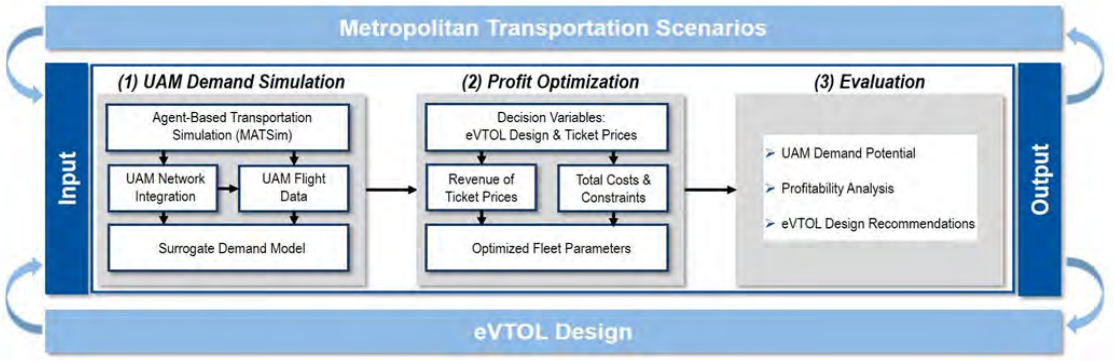


Figure 5.85: Modular framework for comparative UAM demand simulation and profitability assessment. Republishing permitted with attribution to the authors under CC BY 3.0 (Kirste & Stumpf, 2026).

For each simulation scenario, existing ground-based transport networks are processed using MATSim (Horni et al., 2016), a multi-agent transport simulation framework that models individual travel decisions within multi-modal networks (Balac et al., 2019). K-means clustering is applied to mobility routes exceeding 15 km to derive candidate vertiport locations, as UAM provides competitive travel time savings only over medium to long distances. UAM demand is then simulated using the MATSim UAM extension (Rothfeld et al., 2018), where agents iteratively evaluate different transport modes under varying ticket prices, vehicle ranges, and cruise speeds until demand converges. To enable systematic parameter exploration, surrogate demand models are derived from 40 Latin Hypercube samples per scenario across the four-dimensional design space of ticket prices (base fare and variable price), vehicle range, and cruise speed. Each simulation instance is run for 150 MATSim iterations with calibrated replanning settings, and a conservative demand scaling factor is applied to account for potential overestimation in the absence of current real-world validation data. Huber regression is selected for surrogate fitting, as it reduces the influence of outliers from extreme parameter combinations while retaining their partial information. The resulting models express trip count and total flight distance as functions of fixed price, variable price, vehicle range, and cruise speed, with coefficients of determination ranging from 0.6 to 0.9. It should be noted that predictions are reliable only within the sampled parameter space, and coefficient plausibility with respect to expected demand behavior is prioritized alongside statistical fit.

The profit-maximizing fleet configuration for each simulation scenario is determined through mixed-integer linear programming, where the objective function maximizes profit as the difference between total ticket revenue and total operating costs (Kirste & Stumpf, 2025b). The underlying total cost of ownership model captures the following cost components (Kirste & Stumpf, 2025a): energy costs for flight operations (0.30 EUR/kWh on average), fleet maintenance costs (approximately 120 EUR per flight hour, with sensitivities from optimistic drone-specific projections of 50 EUR up to conventional helicopter levels), battery replacement costs (200 to 300 EUR/kWh at approximately 1,000 to 1,500 charge cycles), vehicle acquisition costs scaled by airframe mass and anticipated production volumes (13-year economic lifetime), vertiport infrastructure (1 million EUR upward depending on capacity and urban integration), annual vertiport operating costs allocated per eVTOL vehicle in the fleet (approximately 100,000 EUR per vehicle per year), air traffic management personnel (at least two operators per vertiport), and charging infrastructure at vertiport stations (350 kW chargers for fast turnaround operations). For long-term scenarios, battery energy density is assumed at 400 Wh/kg with 80 percent usable capacity, reflecting projected 2030+ technology. Representative eVTOL configurations are evaluated with configuration-specific energy consumption profiles, covering lift+cruise (Aurora PAV, Beta Alia 250, EHang VT-30, Wisk Gen. 5), Tilt-Rotor (Joby S4, Archer Midnight, Wisk Gen. 6), Tilt-Wing (A3 Vahana, CityAirbus), and Multicopter architectures (EHang 216, VoloCity). Vertiport throughput assumptions are conservative and do not account for high-frequency

simultaneous pad operations, as recent field measurements indicate that eVTOL outwash velocities can exceed 100 km/h at distances of 30 m from the vehicle center (Muia et al., 2024), and theoretical analyses suggest safety areas of up to 110 m around landing pads (Ison, 2024).

The six simulation scenarios are based on openly available MATSim population data and represent heterogeneous metropolitan contexts: Los Angeles as a car-dependent sprawl with over 60 percent car mode share, Rhine-Ruhr as a polycentric agglomeration with substantial inter-city commuting distances, Berlin and Hamburg as compact monocentric cities with moderate to strong public transport, Mexico City as a megacity where the established taxibus system provides low-cost ground alternatives, and Kyoto as a compact metropolitan area with dense and competitive rail-based public transport.

Key findings and implications

Table 5.28 summarizes the profitability assessment across all six simulation scenarios. Profit optimization indicates that only Los Angeles and Rhine-Ruhr achieve viable operations under the analyzed assumptions and parameter ranges. Both profitable scenarios share structural characteristics: large metropolitan populations with car-dependent mobility patterns and substantial volumes of commuting trips exceeding 15 km, where existing public transport cannot fully compete and UAM travel time savings become a relevant factor (Goyal et al., 2018).

Scenario	*Demand Potential**	*UAM Profitability***	*Mobility characteristic*
Los Angeles	*Substantial*	*Viable (piloted & auton.)*	*Car-dependent, large medium-distance pool*
Rhine-Ruhr	*Relevant*	*Viable (auton., long-term)*	*Polycentric inter-city commuting*
Hamburg	*Limited*	*Non-viable*	*Compact city, limited trip distances*
Berlin	*Limited*	*Non-viable*	*Compact city, limited trip distances*
Mexico City	*Limited*	*Non-viable*	*Low-cost taxibus competition*
Kyoto	*Limited*	*Non-viable*	*Small network, competitive public transport*

** Demand potential at optimized pricing of 1.50 to 2.00 EUR/pkm. Substantial: demand volume sufficient for network-level operations independent of competing mode prices. Relevant: viable demand contingent on scenario-specific pricing and vehicle technology. Limited: insufficient demand to offset infrastructure-related fixed costs under any analyzed configuration.*
*** Viable (piloted and autonomous): profitability under both piloted and autonomous operations with current eVTOL technology projections. Viable (autonomous, long-term): requires autonomous flight approval, battery energy density of 400 Wh/kg, and scenario-specific dynamic pricing* (Kirste & Stumpf, 2024)*. Non-viable: negative operating margins under all analyzed configurations.*

Table 5.28: Comparative profitability assessment across six metropolitan UAM simulation scenarios.

In the four remaining simulation scenarios, the infrastructure-related fixed costs required for adequate network coverage consistently exceed the revenue achievable under any pricing strategy. Vertiport construction, personnel for air traffic management, and network operations account for the dominant cost shares, while the optimizer responds by reducing prices to their lower bounds to maximize demand volume without achieving sufficient total revenue.

The following observations can be drawn from the comparative analysis:

- *UAM commuter demand.* Profitability beyond niche applications such as VIP shuttles or route specific sight-seeing requires network-level demand that can only emerge through large-scale implementation. The results indicate that car-dependent metropolitan regions where public transport is either inefficient or already partly operating near capacity provide the necessary demand basis. In addition, scenario size directly affects the achievable demand volume, as smaller metropolitan regions such as Kyoto yield substantially fewer candidate trips and therefore benefit less from the network effects that enable near-term or long-term cost-efficient operations. This finding complements rather than contradicts initial market entry strategies via dedicated high-value

routes and airport shuttles (Lewis et al., 2021), but suggests that long-term viability depends on scaling beyond these early services.

- *Vehicle technology.* Tilt-Rotor configurations systematically outperform alternative architectures through their combination of cruise speed, aerodynamic efficiency, and multi-passenger capacity that enables passenger pooling. Multicopter configurations remain constrained by limited range and are more applicable to short-distance logistics or specialized operations than to network-scale passenger transport (see also Chapter 2 for the corresponding UCM reference vehicles). The optimization consistently selects maximum available range across all profitable scenarios, indicating that extended operational reach is a primary driver of revenue generation.
- *Autonomous operations.* After infrastructure-related fixed costs, crew costs represent the largest cost lever, making autonomous flight the most important technology enabler for long-term UAM applications. Only Los Angeles achieves positive operating margins under piloted operations across all analyzed scenarios.
- *Pricing and infrastructure.* Scenario-specific ticket pricing emerges as a decisive factor for profitability. Los Angeles supports premium pricing at approximately 20 EUR fixed fare and 2.00 EUR/pkm, while Rhine-Ruhr requires moderate fares around 12 EUR fixed and 1.00 EUR/pkm combined with dynamic pricing strategies to balance demand peaks and fleet utilization (Kirste & Stumpf, 2024). Vertiport infrastructure, while necessary for operations, can be deployed incrementally and is therefore less time-critical than vehicle certification and autonomy approval.

Further calibration of the demand and cost models against real-world UAM operations is required once commercial flight test data becomes available. From a sustainability perspective, the contribution of UAM networks is less ecological than economic, as electrified ground-based alternatives can be expected to achieve lower energy consumption per passenger-kilometer for intra-city distances (Kirste et al., 2023). Consequently, public acceptance at the low mode shares identified across all scenarios represents a critical factor for scaling UAM from initial niche services toward the network-level operations required for long-term profitability (Sun et al., 2025).

6 Cross-Cutting Challenges and Directions Toward a Vertical Future

The preceding chapters moved deliberately outward: from reference vehicles, through the aerodynamics and aeroacoustics of their rotors, to urban noise and vertiports, and finally to the operations and airspace that tie a fleet together. Read in isolation, each contribution answers a bounded technical question. Read together, they describe something larger and more demanding — a system in which a decision made about a propeller blade propagates all the way to a noise contour over a residential street, and a constraint set by an urban planner reaches back to reshape an aircraft's design requirements. This closing chapter draws out those connections, names the challenges that cut across every chapter, and sets out where the field should go next.

6.1 The value is in the connections

If there is a single argument running through this edited book, it is that the hard problems of urban air mobility live in the couplings between disciplines, not within them. Chapter 2 established common reference vehicles, lift+cruise, tiltrotor, and multicopter configurations so that aerodynamic, acoustic, and operational studies could speak a shared language. Chapter 3 then showed how rotor performance and noise cannot be predicted from isolated-blade intuition once installation and interaction effects are admitted. Chapter 4 carried the noise produced at the source out into the city and turned it into something a planner can act on. Chapter 5 placed the resulting aircraft into a dense, regulated airspace where throughput, safety, and human oversight become the binding constraints.

6.2 Three cross-cutting challenges

Three themes introduced at the outset of this book, interaction, scalability, and commonality, recur in every chapter, and each is better understood now that the contributions can be read against one another.

Interaction, scalability and commonality

eVTOL aircraft are interaction-driven in a way conventional aircraft are not. Their propellers operate in the disturbed wakes of other rotors, wings, pylons, and fuselages; their noise is shaped by unsteady inflow rather than clean, steady operation; and their vertiports are not isolated pads but nodes embedded in urban wind fields and intermodal transport networks. The aerodynamic studies in Chapter 3, body-force and mid-fidelity methods, multirotor interaction analyses, and propeller–pylon optimization, repeatedly find that isolated-component estimates are insufficient, sometimes dangerously so, once the full configuration is assembled. The lesson generalizes: across this book, performance depends less on optimizing parts than on understanding how parts disturb one another. Designing for interaction, rather than designing parts and discovering the interaction later, is the first cross-cutting imperative. Many solutions that succeed at prototype scale fail when multiplied. A rotor that is acceptably quiet in a single flyover may still produce an unacceptable cumulative noise climate when dozens of operations cross a neighborhood each hour. A conflict-resolution algorithm that performs well between a handful of aircraft must still be shown to hold as traffic density grows and as human controllers are kept meaningfully in the loop. The operations and U-space contributions in Chapter 5, vertiport availability and slot management, the case for U-space services, and learning-based conflict resolution, are fundamentally about this transition from demonstration to deployment. Scalability is not a property a technology has on its own; it is a property of the technology together with the infrastructure and the operational concept around it. Comparison and validation require shared references. The common-model philosophy of Chapter 2 gives the community vehicles that different groups can size, simulate, and measure against a single definition, so that results become commensurable rather than anecdotal. The same logic applies to shared benchmark cases for installed propellers, tandem configurations, and urban noise prediction. Open, traceable, and reproducible baselines are not housekeeping; they are what allow a

distributed research community, and, later, certifying authorities, to trust that a claimed improvement is real. Sustaining and extending these common models and datasets delivers disproportionate returns to the whole community.

6.3 The societal dimension

Urban air mobility will be judged not by efficiency curves but by whether communities accept aircraft operating above their homes. Five societal threads run through this edited book and deserve to be made explicit.

Community noise and acceptance

Noise is the thread that connects almost every chapter, and it is the dimension on which public acceptance most plainly turns. The aeroacoustic work of Chapter 3 attacks the problem at the source, predicting tonal and broadband noise under unsteady inflow, and exploring blade concepts that trade efficiency against sound. Chapter 4 carries that source noise into the urban environment and, crucially, turns it into a planning instrument: the Noise-Adjusted Obstacle-Free Volume introduced there extends the regulator's purely geometric safety envelope so that local noise limits help shape the very corridors aircraft are allowed to fly. That is the right pattern for the whole field, noise treated not as a downstream nuisance to be measured after the fact, but as a design and planning constraint embedded from the start, with the affected public's thresholds written into the geometry of operations.

Safety, equity and sustainability

Public trust is earned through demonstrable safety, and safety in this domain is unusually multidimensional. Chapter 3's analysis of dynamic rollover hazards addresses a vehicle-level failure mode peculiar to multirotor configurations; Chapter 5's conflict-resolution and U-space work addresses safety at the level of the airspace system. Both sit beneath an evolving certification landscape, the special conditions for VTOL aircraft and the powered-lift rules now emerging from European and United States authorities. The recurring requirement is continued safe flight and landing under failures, and the recurring difficulty is that these aircraft are novel enough that historical safety data are thin. Building public trust will require not only safe systems but transparent evidence that they are safe. Where vertiports are placed determines who benefits. The vertiport contributions in Chapter 4 on holistic design, on localization through intermodality, and on the interdisciplinary nature of the problem, make clear that infrastructure siting is simultaneously an engineering, planning, and social-equity decision. A network optimized only for premium point-to-point travel will entrench existing inequalities; one designed around intermodal hubs and genuine public connectivity can widen access. Because vertiports also impose their constraints back onto aircraft design and operations, these siting choices are not peripheral, they are among the earliest and most consequential decisions in the whole system, and they belong to cities as much as to engineers. The environmental case for electrification depends on more than zero tailpipe emissions. Battery performance and degradation, addressed in the previous chapters through state-of-health prediction for the lithium-ion packs that power these aircraft, bear directly on safety, operating economics, reserve margins, and the lifecycle footprint of a fleet. Aerodynamic and acoustic efficiency, the subject of much of Chapters 2 and 3, translates into energy consumed per passenger-kilometer. A credible sustainability claim for urban air mobility must account for manufacturing, battery lifetime and replacement, grid demand, and end-of-life, not flight emissions alone. Several contributions in this book turn to machine learning, transformer models for rotor aeroacoustics and for city-scale urban noise mapping, and reinforcement learning for conflict resolution. These methods offer something the field badly needs: speed, enabling rapid assessment where high-fidelity simulation is too slow for design or operational use. But they introduce a governance question. Surrogate and learning-based models must be validated, bounded, and explainable enough to be trusted in safety-relevant and public-facing decisions, and automated airspace

functions must preserve meaningful human oversight. The promise of automation is scalability; its price is a heightened obligation to demonstrate reliability and to keep accountability legible.

6.4 Directions

The following priorities are drawn directly from the gaps surfaced in this volume.

Interaction-resolved physics. Predicting installed aerodynamic and aeroacoustic behavior, rotor-on-rotor, rotor-on-airframe, and unsteady-inflow effects with validated mid-fidelity methods fast enough to use inside a design loop, not only in final verification.

Trustworthy data-driven modeling. Machine-learning surrogates for aeroacoustics and propagation that come with quantified uncertainty, physical consistency, and demonstrated generalization beyond their training conditions, so they can be used responsibly in certification-adjacent decisions.

Open benchmarks and reference data. Continued development of shared common-model vehicles, installed-propeller and tandem benchmark cases, and openly published measurement datasets against which methods can be calibrated and compared.

Quiet-by-design rotors and configurations. Maturing the low-noise blade and propulsor concepts explored here, including swept and unconventional geometries and the control of distributed propulsion, with community noise as a first-order objective rather than a constraint applied late.

Integrated design tooling. Coupling fast aerodynamic, acoustic, energy, and operational models into design environments, ultimately models of vehicle and vertiport, so that cross-disciplinary trade-offs can be explored early and cheaply.

Noise-aware, intermodal vertiport networks. Siting and designing vertiports as connected public infrastructure, with acoustic and wind constraints, obstacle-free and noise-adjusted volumes, and intermodal access treated together from the outset.

Scalable, accountable airspace operations. Maturing U-space services, slot and availability management, and automated conflict resolution to high traffic densities while preserving human oversight and a clear chain of accountability.

Certification and public engagement in step. Advancing the special-condition and powered-lift certification frameworks alongside genuine community engagement, so that acceptance is built with the public rather than assumed of it.

6.5 Outlook toward the next cycle

Across the 2022–2026 cycle, DICUAM tracked a field maturing from component-level curiosity to system-level responsibility. The contributions gathered here show that the core technical questions: how small rotors behave, how they sound, how vehicles should be sized, how vertiports should be placed, how airspace should be managed, are increasingly tractable, and increasingly connected. What remains open is largely integration: turning credible parts into a system that a city will accept, a regulator will certify, and a community will welcome overhead.

That is the agenda for the cycles to come. The most valuable next steps are not single breakthrough results but shared infrastructure: common models, validated fast methods, noise and safety constraints built in from the start, and governance frameworks that keep accountability legible. A vertical future is not inevitable, it is a choice that

cities, regulators, and communities will make. The purpose of this edited book is to make that choice better informed.

Bibliography

Ali, M., Piccolo, A., Zamponi, R., Ragni, D., & Avallone, F. (2025). On the impact of turbulent inflow on the noise generated by a propeller operating at low Reynolds number. *Proceedings of the 11th Convention of the European Acoustics Association Forum Acusticum, EuroNoise 2025*, 1737–1744. https://doi.org/10.61782/fa.2025.0647

Amiet, R. K. (1978). Noise due to rotor-turbulence interaction. In *Helicopter Acoustics*. (NASA Conference Publication No. 2052, pp. 109-126). Nasa Langley Research Center. https://ntrs.nasa.gov/citations/19780024880

Asmer, L., Jaksche, R., Pak, H., & Kokus, P. (2024). A city-centric approach to estimate and evaluate global Urban Air Mobility demand. *CEAS Aeronautical Journal*, *16*(3), 697–712. https://doi.org/10.1007/s13272-024-00742-w

Atte, A., Wylie, D., & Rauleder, J. (2022, May 10-12). *Experimental evaluation of multi-rotor aerodynamic interactions* [Paper Presentation]. Vertical Flight Society 78th Annual Forum & Technology Display, Fort Worth, TX, United States. https://doi.org/10.4050/f-0078-2022-17467

Baars, W. J., & Ragni, D. (2024). Low-frequency intensity modulation of high-frequency rotor noise. *AIAA Journal*, *62*(9), 3374–3390. https://doi.org/10.2514/1.j063610

Balac, M., Vetrella, A. R., Rothfeld, R., & Schmid, B. (2019). Demand estimation for aerial vehicles in urban settings. *IEEE Intelligent Transportation Systems Magazine*, *11*(3), 105–116. https://doi.org/10.1109/mits.2019.2919500

Ballin, M. G., Hoekstra, J. M., Wing, D. J., & Lohr, G. W. (2002). NASA Langley and NLR research of distributed air/ground traffic management. In *AIAA's Aircraft Technology, Integration, and Operations (ATIO) 2002 Technical Forum* (Article AIAA 2002-5826). American Institute of Aeronautics and Astronautics. https://doi.org/https://doi.org/10.2514/6.2002-5826

Bao, H., Tan, Q., Zhou, P., Chen, W., Zhang, X., & Zhong, S. (2025). On the Gaussian beam tracing method for long-distance sound wave propagation in non-uniform mean flows. *Proceedings of the Royal Society A: Mathematical, Physical and Engineering Sciences*, *481*(2307), Article 20240485. https://doi.org/10.1098/rspa.2024.0485

Bergmann, O., Möhren, F., Braun, C., & Janser, F. (2024). Influence of aeroelasticity on aeroacoustics of lifting propellers with swept planforms. *SSRN Electronic Journal*. https://doi.org/10.2139/ssrn.4980332

Bills, K., Costello, L., & Cattani, M. (2026). Aviation accident investigation analysis methodologies used by 12 government Safety Investigation Authorities. *Journal of Safety Research*, *97*, 112–129. https://doi.org/10.1016/j.jsr.2026.02.001

Blanes, N., Houthuijs, D., Swart, W., Sainz de la Maza, M., Ramos, M., Castell, N., & Van Kempen, E. (2017). Noise in Europe 2017: Updated assessment. *European Topic Centre on Air Pollution and Climate Change Mitigation*, *13*(6), 200–203. https://www.eionet.europa.eu/etcs/etc-atni/products/etc-atni-reports/etcacm_tp_2016_13_noiseineurope2017

Bresciani, A. P. C., Vardanyan, A., Christophe, J., & Schram, C. (2025). *eVTOLUTION-Experimental dataset-Configuration A1-VKI* [Dataset] Zenodo. https://doi.org/10.5281/zenodo.17941588

Brown, M. J., Williams, M. D., Nelson, M. A., & Werley, K. A. (2016). QUIC transport and dispersion modeling of vehicle emissions in cities for better public health assessments. *Environmental Health Insights*, *9*(1), Article 55. https://doi.org/10.4137/EHI.S1566

Bureau of Transport Statistics. (2026). *On-time performance marketing carrier annual data*. U.S. Department of Transportation. Retrieved in October 30, 2026 the data from year 2018 to 2026, from https://transtats.bts.gov/Marketing_Annual.aspx

Casalino, D., Grande, E., Romani, G., Ragni, D., & Avallone, F. (2021). Definition of a benchmark for low Reynolds number propeller aeroacoustics. *Aerospace Science and Technology*, *113*, Article 106707. https://doi.org/10.1016/j.ast.2021.106707

Chahba, S., Sehab, R., Morel, C., Krebs, G., & Akrad, A. (2023). Fast sizing methodology and assessment of energy storage configuration on the flight time of a multirotor aerial vehicle. *Aerospace*, *10*(5), Article 425. https://doi.org/10.3390/aerospace10050425

Città Metropolitana di Milano. (2021). *Piano urbano della mobilità* [Urban mobility plan]. https://www.comune.milano.it/argomenti/mobilita/piano-urbano-della-mobilita

Città Metropolitana di Milano. (2023). *Piano Territorio Metropolitano (PTM)* [Metropolitan territorial plan]. http://www2.cittametropolitana.mi.it/aree-tematiche/pianificazione-territoriale/ptm-piano-territorio-metropolitano/

Cohen, A. P., Shaheen, S. A., & Farrar, E. M. (2021). Urban air mobility: history, ecosystem, market potential, and challenges. *IEEE Transactions on Intelligent Transportation Systems*, *22*(9), 6074–6087. https://doi.org/10.1109/tits.2021.3082767

Colleoni, M. (2019). *Mobilità e trasformazioni urbane : la morfologia della metropoli contemporanea* [Mobility and urban transformations: the morphology of the contemporary metropolis]. Franco Angeli. https://hdl.handle.net/10281/220747

Combey, K., Elsayed, O. A., Magrini, A., Ramirez, F. N., Wang, S., Qaissi, K., Chouiyakh, H., Pereira, L. T. L., & Ragni, D. (2026). Aerodynamic and aeroacoustic interactions in multirotor aircraft for urban air mobility: A review. *Physics of Fluids*, *38*(1), Article 011301. https://doi.org/10.1063/5.0311473

Combey, K., Elsayed, O. A., Qaissi, K., Chouiyakh, H., & Mustapha, F. (2025). Numerical analysis of multirotor aerodynamic interactions in forward and transition flight. *Journal of Aircraft*, *63*(3), 1–17. https://doi.org/10.2514/1.c038518

Comune di Milano. (2020). *PGT - Territorial Government Plan - Current*. https://www.comune.milano.it/en/argomenti/rigenerazione-urbana/pgt-piano-di-governo-del-territorio-2020-vigente

Coppola, P., De Fabiis, F., & Silvestri, F. (2025). Urban air mobility demand forecasting: modeling evidence from the case study of Milan (Italy). *European Transport Research Review*, *17*(2), 1–17. https://doi.org/10.1186/s12544-024-00700-x

Dabaghian, P. H., Mitsingas, C. M., & Halder, A. (2025). A hybrid machine learning framework for rotor performance prediction. *Physics of Fluids*, *37*(7), Article 77194. https://doi.org/10.1063/5.0271761

Diaz, P. V., & Yoon, S. (2020). Computational study of NASA's quadrotor urban air taxi concept. In *AIAA Scitech 2020 Forum*, (Article AIAA 2020-0302). American Institute of Aeronautics and Astronautics. https://doi.org/10.2514/6.2020-0302

Doo, J., Pavel, M., Didey, A., Hange, C., Diller, N., Tsairides, M., Smith, M., Bennet, E., Bromfield, M., & Mooberry, J. (2021). *NASA electric vertical takeoff and landing (eVTOL) aircraft technology for public services - a white paper: NASA transformative vertical flight working group 4 (TVF4)*. National Aeronautics and Space Administration. https://research.birmingham.ac.uk/en/publications/nasa-electric-vertical-takeoff-and-landing-evtol-aircraft-technol/

Duda, H., Sachs, F., Seewald, J., & Lorenz, S. (2022). Dynamic rollover of gyroplanes during landing - cause and prevention. *CEAS Aeronautical Journal*, *13*(2), 521–533. https://doi.org/10.1007/s13272-022-00575-5

European Union Aviation Safety Agency (EASA). (2021). *Vertical take-off & landing - VTOL*. https://www.easa.europa.eu/en/domains/rotorcraft-vtol/VTOL

European Union Aviation Safety Agency (EASA). (2022). *Vertiports in the urban environment.* https://www.easa.europa.eu/en/light/topics/vertiports-urban-environment

European Union Aviation Safety Agency (EASA). (2026a). *Easy access rules for unmanned aircraft systems*. https://www.easa.europa.eu/en/document-library/easy-access-rules/easy-access-rules-unmanned-aircraft-systems

European Union Aviation Safety Agency (EASA). (2026b). *Special condition for VTOL and means of compliance*. https://www.easa.europa.eu/en/document-library/product-certification-consultations/special-condition-vtol

Federal Aviation Administration (FAA). (2002). *Noise standards: Aircraft type and airworthiness certification (14 C.F.R. Part 36). Code of Federal Regulations.* https://www.ecfr.gov/current/title-14/chapter-I/subchapter-C/part-36

Federal Aviation Administration (FAA). (2024). *Integration of powered-lift: pilot certification and operations; miscellaneous amendments related to rotorcraft and airplanes*. https://www.faa.gov/newsroom/integration-powered-lift-pilot-certification-and-operations-miscellaneous-amendments

Ffowcs Williams, J. E., & Hawkings, D. L. (1969). Theory relating to the noise of rotating machinery. *Journal of Sound and Vibration*, *10*(1), 10–21. https://doi.org/10.1016/0022-460x(69)90125-4

Gallo, E., De Decker, J., Bresciani, A., Haezebrouck, P., Garone, E., & Schram, C. (2025). Development and commissioning of an aeroacoustic test bench for the investigation of single and coaxial propeller noise. *Acta Acustica*, *9*, Article 16. https://doi.org/10.1051/aacus/2024085

Gill, H., & Lee, S. (2024). Development of new empirical rotor broadband noise prediction models for urban air mobility applications. In *AIAA SciTech 2024 Forum and Exposition* (Article AIAA 2024-2473). American Institute of Aeronautics and Astronautics. https://doi.org/10.2514/6.2024-2473

Glegg, S. & Devenport, W. (2017). *Aeroacoustics of low mach number flows.* Elsevier. https://www.sciencedirect.com/book/monograph/9780128096512/aeroacoustics-of-low-mach-number-flows

Go, S. T., Kingan, M. J., Bowen, L., & Azarpeyvand, M. (2024). Noise of a shrouded propeller due to ingestion of grid-generated turbulence. *Journal of Sound and Vibration*, *571*, Article 118044. https://doi.org/10.1016/j.jsv.2023.118044

Gojon, R., Parisot-Dupuis, H., Mellot, B., & Jardin, T. (2023). Aeroacoustic radiation of low Reynolds number rotors in interaction with beams. *The Journal of the Acoustical Society of America*, *154*(2), 1248–1260. https://doi.org/10.1121/10.0020672

Goyal, R., Reiche, C., Fernando, C., Serrao, J., Kimmel, S., Cohen, A., & Shaheen, S. (2018). *Urban Air Mobility (UAM) market study* (Report No. NASA/CR-2018-220072). National Aeronautics and Space Administration. https://ntrs.nasa.gov/citations/20190001472

Grande, E., Romani, G., Ragni, D., Avallone, F., & Casalino, D. (2021). Aeroacoustic investigation of a propeller operating at low Reynolds numbers. *AIAA Journal*, *60*(2), 860–871. https://doi.org/10.2514/1.J060611

Groot, D. J., Ellerbroek, J., & Hoekstra, J. M. (2024). Analysis of the impact of traffic density on training of reinforcement learning based conflict resolution methods for drones. *Engineering Applications of Artificial Intelligence*, *133*, Article 108066. https://doi.org/10.1016/j.engappai.2024.108066

Groot, D. J., Leto, G., Vlaskin, S., Moëc, A. A. G., & Ellerbroek, J. (2024). BlueSky-Gym: reinforcement learning environments for air traffic applications [Paper Presentation]. 14th SESAR Innovation Days, Rome, Italy. https://research.tudelft.nl/en/publications/bluesky-gym-reinforcement-learning-environments-for-air-traffic-a/

Haarnoja, T., Zhou, A., Hartikainen, K., Tucker, G., Ha, S., Tan, J., Kumar, V., Zhu, H., Gupta, A., Abbeel, P., & Levine, S. (2018). Soft actor-critic algorithms and applications. *ArXiv*. https://doi.org/10.48550/arXiv.1812.05905

Hanson, D. B. (1985). Noise of counter-rotation propellers. *Journal of Aircraft*, *22*(7), 609–617. https://doi.org/10.2514/3.45173

Hanson, D. B. (1993). *Theory for noise of propellers in angular inflow with parametric studies and experimental verification*. (NASA Contractor Report No. 4554) National Aeronautics and Space Administration, Scientific and Technical Information Program. https://ntrs.nasa.gov/citations/19930015905

Heidt, A., Kapolke, M., Liers, F., Fürstenau, N., & Helmke, H. (2014). *Pre-tactical time-slot assignment: runway utilization and the impact of uncertainties* [Paper Presentation]. 4th SESAR Innovation Days, Madrid, Spain. http://www.sesarinnovationdays.eu

HeliOffshore. (2025). *Accident occurrence categories by CICTT definition*. https://www.helioffshore-industry-report.org/accident-types

Horni, A., Nagel, K., & Axhausen, K. W. (Eds.). (2016). *The multi-agent transport simulation MATSim.* Ubiquity Press. https://doi.org/10.5334/baw

Hwang, U. J., Park, J. S., & Lee, M. K. (2024). Performance, vibration, load, and whirl flutter stability analyses of tiltrotors with swept-back blades. *International Journal of Aeronautical and Space Sciences*, *26*(4), 1632–1648. https://doi.org/10.1007/s42405-024-00815-4

International Civil Aviation Organization (ICAO). (1993). *Procedures for air navigation services (PANS) - Aircraft operations - Volume I. Flight procedures* (Doc 8168, 4th ed.). https://store.icao.int/en/procedures-for-air-navigation-services-pans-aircraft-operations-volume-i-flight-procedures-doc-8168

International Civil Aviation Organization (ICAO). (2017). *Annex 16 to the Convention on International Civil Aviation: Environmental protection - Volume I: Aircraft noise* (7th ed.). https://store.icao.int/en/annex-16-environmental-protection-volume-i-aircraft-noise

International Organization for Standardization (ISO). (2024). *Acoustics - Attenuation of sound during propagation outdoors - Part 2: Engineering method for the prediction of sound pressure levels outdoors*. (ISO Standard No. 9613-2:2024). https://www.iso.org/standard/92873.html

Ison, D. (2024). Analysis of VTOL downwash and outwash to establish vertiport safety standards: a theoretical approach. *The Collegiate Aviation Review International*, *42*(2), 17–40. https://doi.org/10.22488/okstate.24.100236

Jamaluddin, N. S., Celik, A., Baskaran, K., Rezgui, D., & Azarpeyvand, M. (2021). Aeroacoustic performance of propellers in turbulent flow. In *AIAA AVIATION 2021 Forum* (Article AIAA 2021-2188). American Institute of Aeronautics and Astronautics. https://doi.org/10.2514/6.2021-2188

Jeracki, R. J., Mikkelson, D. C., & Blaha, B. J. (1979). *Wind tunnel performance of four energy efficient propellers designed for Mach 0.8 cruise*. (NASA Technical Memorandum No. 79124). National Aeronautics and Space Administration. https://ntrs.nasa.gov/search.jsp?R=19790052746

Jeracki, R. J., & Mitchell, G. A. (1981). *Low and high speed propellers for general aviation: Performance potential and recent wind tunnel test results.* (NASA Technical Memorandum No. 81745). National Aeronautics and Space Administration. https://ntrs.nasa.gov/citations/19810058354

Jia, H., Lin, C., Iwabuchi, M., & Kikumoto, H. (2026). Ten questions concerning urban wind environments for the safe utilization of urban air mobility. *Building and Environment*, *290*, Article 114136. https://doi.org/10.1016/J.BUILDENV.2025.114136

Johnson, W., & Silva, C. (2022). NASA concept vehicles and the engineering of advanced air mobility aircraft. *The Aeronautical Journal*, *126*(1295), 59–91. https://doi.org/10.1017/aer.2021.92

Katz, J., & Plotkin, A. (2001). *Low-speed aerodynamics (2nd ed.)*. Cambridge University Press.

Kelley, N. D., & Jonkman, B. J. (2007). *Overview of the TurbSim stochastic inflow turbulence simulator: version 1.21*. (Report No. NREL/TP-500-41136). National Renewable Energy Laboratory. https://doi.org/10.2172/903073

Kim, H. D. (2020). *Progress in distributed electric propulsion vehicles and technologies*. (Report No. AFRC-E-DAA-TN76298). National Aeronautics and Space Administration. https://ntrs.nasa.gov/citations/20200011461

Kim, H. D., Perry, A., & Ansell, P. (2018). A review of distributed electric propulsion concepts for air vehicle technology. In *2018 AIAA/IEEE Electric Aircraft Technologies Symposium (EATS)*, 1–21. IEEE. https://doi.org/10.2514/6.2018-4999

Kim, Y., & Lee, S. (2024). Deep learning based prediction of urban air mobility noise propagation in urban environment. *The Journal of the Acoustical Society of America*, *155*(1), 171–187. https://doi.org/10.1121/10.0024242

Kirste, A., Husemann, M., & Stumpf, E. (2023). Analysis of sustainability specifications of urban air mobility fleet operations using agent-based transportation simulation. In *AIAA AVIATION 2023 Forum* (Article AIAA 2023-3264). American Institute of Aeronautics and Astronautics. https://doi.org/10.2514/6.2023-3264

Kirste, A., & Stumpf, E. (2024). Modeling and analysis of dynamic pricing potential for urban air mobility operations. In *AIAA AVIATION FORUM AND ASCEND 2024* (Article AIAA 2024-3938). American Institute of Aeronautics and Astronautics. https://doi.org/10.2514/6.2024-3938

Kirste, A., & Stumpf, E. (2025a). Development of a generalized eVTOL vehicle cost model for urban air mobility operations. *Journal of the Air Transport Research Society*, *5*, Article 100082. https://doi.org/10.1016/j.jatrs.2025.100082

Kirste, A., & Stumpf, E. (2025b). Multidisciplinary optimization of advanced air mobility fleet operations. In *AIAA SCITECH 2025 Forum* (Article AIAA 2025-2170). American Institute of Aeronautics and Astronautics. https://doi.org/10.2514/6.2025-2170

Kirste, A., & Stumpf, E. (2026). Comparing UAM demand, eVTOL design, and profitability across metropolitan regions using simulation and optimization. *Materials Research Proceedings*, *69*, 94–98. https://doi.org/10.21741/9781644904251-17

Kleinbekman, I. C., Mitici, M. A., & Wei, P. (2018). eVTOL arrival sequencing and scheduling for on-demand urban air mobility. In *2018 IEEE/AIAA 37th Digital Avionics Systems Conference (DASC)* (pp. 1–7). IEEE. https://doi.org/10.1109/dasc.2018.8569645

Krone, N. J. (1980). Forward swept wing flight demonstrator. In *AIAA Aircraft Systems and Technology Meeting* (Article AIAA 1980-1882). American Institute of Aeronautics and Astronautics. https://doi.org/10.2514/6.1980-1882

Lee, C., Bae, B., Lee, Y. L., & Pak, T. Y. (2023). Societal acceptance of urban air mobility based on the technology adoption framework. *Technological Forecasting and Social Change*, *196*, Article 122807. https://doi.org/10.1016/J.TECHFORE.2023.122807

Lee, H., & Lee, D. J. (2020). Rotor interactional effects on aerodynamic and noise characteristics of a small multirotor unmanned aerial vehicle. *Physics of Fluids*, *32*(4), Article 047107. https://doi.org/10.1063/5.0003992

Lewis, E., Ponnock, J., Cherqaoui, Q., Holmdahl, S., Johnson, Y., Wong, A., & Oliver Gao, H. (2021). Architecting urban air mobility airport shuttling systems with case studies: Atlanta, Los Angeles, and Dallas. *Transportation Research Part A: Policy and Practice*, *150*, 423–444. https://doi.org/10.1016/J.TRA.2021.06.026

Li, J., Zhang, H., Yi, J., Deng, C., & Zhou, J. (2025). Capacity assessment of vertiports with a scheduling algorithm considering quality of service. *The Aeronautical Journal*, *129*(1337), 1791–1809. https://doi.org/10.1017/aer.2024.152

Li, S., & Lee, S. (2020). A machine learning-based fast prediction of rotorcraft broadband noise. In *AIAA AVIATION 2020 Forum* (Article AIAA 2020-2588). American Institute of Aeronautics and Astronautics. https://doi.org/10.2514/6.2020-2588

Lima Pereira, L. T., Wang, S., & Ragni, D. (2024). A preliminary design framework for performance and noise assessment of urban air mobility vehicles. In *30th AIAA/CEAS Aeroacoustics Conference (2024)* (Article AIAA 2024-3334). American Institute of Aeronautics and Astronautics. https://doi.org/10.2514/6.2024-3334

Lopes, D., & Silva, J. (2023). Urban air mobility (UAM) in the metropolitan region of São Paulo: Potential and threats. *Journal of Airline and Airport Management, 13*, 1–19. https://doi.org/10.3926/jairm.345

Lowson, M. V. (1965). The sound field for singularities in motion on JSTOR. *Proceedings of the Royal Society of London. Series A, Mathematical and Physical Sciences*, *286*(1407), 559–572. https://www.jstor.org/stable/2415351

Mao, Y., Gu, Y., Qi, D., & Tang, H. (2012). An exact frequency-domain solution of the sound radiated from the rotating dipole point source. *The Journal of the Acoustical Society of America*, *132*(3), 1294–1302. https://doi.org/10.1121/1.4742972

Mayakonda, M. P., Justin, C. Y., Anand, A., Weit, C. J., Wen, J. T., Zaidi, T. A., & Mavris, D. N. (2020). A top-down methodology for global urban air mobility demand estimation. A top-down methodology for global urban air mobility demand estimation. In *AIAA AVIATION 2020 Forum* (Article AIAA 2020-3255). American Institute of Aeronautics and Astronautics. https://doi.org/10.2514/6.2020-3255

Menter, F. R., Kuntz, M., & Langtry, R. (2003). Ten years of industrial experience with the SST turbulence model. *Turbulence Heat and Mass Transfer*, *Turbulence, Heat and Mass Transfer*, *4*, 625–632.

Meteomatics. (2026). *OpenWeather APIs for weather, energy, and environment*. https://openweathermap.org/

Moorhouse, D. J., & Woodcock, R. J. (1982). *Background information and user guide for Mil-F-8785B (ASG), military specification - Flying qualities of piloted airplanes*. (Report No. AFWAL-TR-81-3109). Air Force Wright Aeronautical Laboratories. https://apps.dtic.mil/sti/citations/AD0860856

Muia, M. J., Stanley, J., Anderson, T., Hall, D., Shuman, Z., Goericke, J., Batther, J. B., Habana, Z., He, C., & Saberi, H. (2024). *Electric vertical takeoff and landing (eVTOL) downwash and outwash Surveys*. (Report No. DOT/FAA/TC-24/18). Federal Aviation Administration. https://www.airporttech.tc.faa.gov/Products/Airport-Pavement-Papers-Publications/Airport-Pavement-Detail/electric-vertical-takeoff-and-landing-evtol-downwash-and-outwash-surveys

Nithya, D. S., Monteleone, F., Quaranta, G., Liang, M., & Muscarello, V. (2025). Development and validation of a custom stochastic microscale wind model for urban air mobility applications. *Drones 2025*, *9*(12), Article 863. https://doi.org/10.3390/DRONES9120863

Nithya, D. S., Rylko, A., Muscarello, V., Liang, M., & Quaranta, G. (2025). Towards determining wind disturbance levels for an urban air mobility aircraft through simulation-based flight testing. In *Proceedings of the 51st European Rotorcraft Forum.* European Rotorcraft Forum. https://hdl.handle.net/20.500.11881/4774

Northeast UAS Airspace Integration Research Alliance (NUAIR). (2021). *High-density automated vertiport concept of operations*. https://lowaltitudeeconomy.aero/directory/white-papers/advanced-air-mobility-aam/high-density-automated-vertiport-concept-of-operations

OpenStreetMap. (2026). *Map database* [Data set]. OpenStreetMap Foundation. https://www.openstreetmap.org/#map=8/52.154/5.29

Owen, A. B. (2013). *Monte Carlo theory, methods and examples*. Stanford University. https://artowen.su.domains/mc/

Palmerton, D. (2005). *Fatality and injury rates for two types of rotorcraft accidents*. https://www.govinfo.gov/app/details/GOVPUB-TD4_200-PURL-LPS66043

Papa, L., Russo, P., Amerini, I., & Zhou, L. (2024). A survey on efficient vision transformers: algorithms, techniques, and performance benchmarking. *IEEE Transactions on Pattern Analysis and Machine Intelligence*, *46*(12), 7682–7700. https://doi.org/10.1109/tpami.2024.3392941

Park, J., Elfar, M., Fleming, C., & Shoukry, Y. (2025). Certified learning-enabled noise-aware motion planning for urban air mobility. *ArXiv*. https://arxiv.org/pdf/2509.20306

Pavel, M. D., White, M., Padfield, G. D., Roth, G., Hamers, M., & Taghizad, A. (2013). Validation of mathematical models for helicopter flight simulators past, present and future challenges. *The Aeronautical Journal*, *117*(1190), 343–388. https://doi.org/10.1017/s0001924000008058

Pesaresi, M., Florczyk, A., Schiavina, M., Melchiorri, M., & Maffenini, L. (2019). *GHS-SMOD R2019A - GHS settlement layers, updated and refined REGIO model 2014 in application to GHS-BUILT R2018A and GHS-POP R2019A, multitemporal (1975-1990-2000-2015)* [Data set]. European Commission, Joint Research Centre. https://doi.org/10.2905/42e8be89-54ff-464e-be7b-bf9e64da5218

Piccinini, R., Tugnoli, M., & Zanotti, A. (2020). Numerical investigation of the rotor-rotor aerodynamic interaction for eVTOL aircraft configurations. *Energies*, *13*(22). https://doi.org/10.3390/en13225995

Piccolo, A., Zamponi, R., Avallone, F., & Ragni, D. (2025). Modification of Amiet's model for turbulence-ingestion noise prediction in rotors. *The Journal of the Acoustical Society of America*, *158*(1), 461–475. https://doi.org/10.1121/10.0037185

Porter, M. B., & Bucker, H. P. (1987). Gaussian beam tracing for computing ocean acoustic fields. *The Journal of the Acoustical Society of America*, *82*(4), 1349–1359. https://doi.org/10.1121/1.395269

Preis, L. (2021). Quick sizing, throughput estimating and layout planning for VTOL aerodromes - A methodology for vertiport design. In *AIAA AVIATION 2021 Forum* (Article AIAA 2021-2372). American Institute of Aeronautics and Astronautics. https://doi.org/10.2514/6.2021-2372

Prince, J. (2025). *Feasibility and scalability of midterm UAM operations in cooperative airspace: Class B airspace simulation evaluation*. (NASA Technical Memorandum No. 2025-0001234). National Aeronautics and Space Administration, Langley Research Center. https://catalog.princeton.edu/catalog/99131831737806421

Putnam, J., & Littell, J. (2023). Simulation and analysis of NASA Lift+Cruise eVTOL crash test [Paper presentation]. Vertical Flight Society 79th Annual Forum and Technology Display, West Palm Beach, FL, United States. https://doi.org/10.4050/f-0079-2023-18019

Raposo, H., & Azarpeyvand, M. (2024). Turbulence ingestion noise generation in rotating blades. *Journal of Fluid Mechanics*, *980*, Article A53. https://doi.org/10.1017/jfm.2024.7

Regione Lombardia. (2016). *Programma regionale della mobilità e dei trasporti* [Regional Mobility and Transport Programme]. https://www.regione.lombardia.it/infrastrutture-trasporti-e-mobilita/infrastrutture-stradali-e-ciclabili/red-prmt

Ren, P., Pu, Y., Zhang, J., & Yang, L. (2025). Modeling and equilibrium analysis of civil aircraft crosswind landing under gradient wind field conditions. *Lecture Notes in Electrical Engineering*, *1347*, 118–127. https://doi.org/10.1007/978-981-96-2240-5_12

Rete Ferroviaria Italiana. Gruppo Ferrovie dello Stato. (2024). *Le nostre stazioni: classificazione, numeri e performance che le identificano* [Our stations: classification, figures, and performance metrics that define them]. https://www.rfi.it/it/stazioni/pagine-stazioni/le-nostre-stazioni-classificazione-numeri-e-performance-che-le-identificano.html

Riboldi, C. E. D., & Gualdoni, F. (2016). An integrated approach to the preliminary weight sizing of small electric aircraft. *Aerospace Science and Technology*, *58*, 134–149. https://doi.org/10.1016/j.ast.2016.07.014

Rizzi, S. A., Henderson, B. S., Lopes, L. V, Bain, J. J., Cluts, J. D., McCarthy, P., Krishnamurthy, S., Merino-Martinez, R., He, H., & Snider, R. (2026). *Urban air mobility noise: 2025 update on current practice, gaps, and recommendations* (NASA Technical Publication No. 2026-219000). National Aeronautics and Space Administration. http://www.sti.nasa.gov

Roger, M., & Kucukcoskun, K. (2019). Near-and-far field modeling of advanced tail-rotor noise using source-mode expansions. *Journal of Sound and Vibration*, *453*, 328–354. https://doi.org/10.1016/j.jsv.2019.02.007

Roger, M., & Moreau, S. (2020). Tonal-noise assessment of quadrotor-type UAV using source-mode expansions. *Acoustics*, *2*(3), 674–690. https://doi.org/10.3390/acoustics2030036

Roskam, J. (1987). *Airplane design part VI: preliminary calculation of aerodynamic, thrust and power characteristics*. DARcorporation. https://books.google.com/books/about/Airplane_Design.html?id=L60uqKL2q10C

Rothfeld, R. L., Balac, M., Ploetner, K. O., & Antoniou, C. (2018). Agent-based simulation of urban air mobility. In *AIAA Modeling and Simulation Technologies Conference* (Article AIAA 2018-3891). American Institute of Aeronautics and Astronautics. https://doi.org/10.2514/6.2018-3891

Saleh, J. H., Xu, Z., Guvir, A. I., Margousian, A., Zhang, W., & Ma, M. (2022). Data-driven analysis and new findings on the loss of tail rotor effectiveness in helicopter accidents. *Scientific Reports*, *12*(1), Article 2854. https://doi.org/10.1038/s41598-022-06647-0

Schlichting, M. R., Notter, S., & Fichter, W. (2022). Long short-term memory for spatial encoding in multi-agent path planning. *Journal of Guidance, Control, and Dynamics*, *45*(5), 952–961. https://doi.org/10.2514/1.g006129

Schmerwitz, S., Dautermann, T., Lenz, H., & Lueken, T. (2019). *GNSS solutions for increased GA and rotorcraft airport accessibility demonstration* [Paper presentation]. 9th SESAR Innovation Days, Athens, Greece. https://www.sesarju.eu/node/3268

Schuchardt, B. I., Devta, A., & Volkert, A. (2024). Integrating vertidrome management tasks into U-space. *CEAS Aeronautical Journal*, *16*(3), 857–872. https://doi.org/10.1007/s13272-024-00747-5

Schuchardt, B. I., Vu, T. H., Mangas, A., Nava, C., Riccardi, G., Kolago, M., Abdullah, A. H., Cappello, P., & Omeri, M. (2025). How to integrate vertiport operations into the airspace? Introducing the EUREKA project. In *AIAA SCITECH 2025 Forum* (Article AIAA 2025-2370). American Institute of Aeronautics and Astronautics. https://doi.org/10.2514/6.2025-2370

Schweiger, K., Knabe, F., & Korn, B. (2022). An exemplary definition of a vertidrome's airside concept of operations. *Aerospace Science and Technology*, *125*, Article 107144. https://doi.org/10.1016/j.ast.2021.107144

Seitz, A., Kruse, M., Wunderlich, T., Bold, J., & Heinrich, L. (2011). The DLR Project LamAiR: Design of a NLF forward swept wing for short and medium range transport application. In *29th AIAA Applied Aerodynamics Conference* (Article AIAA 2011-3526). American Institute of Aeronautics and Astronautics. https://doi.org/10.2514/6.2011-3526

SESAR Joint Undertaking. (2023). *U-space CONOPS and architecture 4th Edition*. https://www.sesarju.eu/node/4544

Sikirica, A., Carija, Z., Kranjcevic, L., & Lucin, I. (2019). Grid type and turbulence model influence on propeller characteristics prediction. *Journal of Marine Science and Engineering*, *7*(10), Article 374. https://doi.org/10.3390/jmse7100374

Silva, C., Johnson, W., Antcliff, K. R., & Patterson, M. D. (2018). VTOL urban air mobility concept vehicles for technology development. In *2018 Aviation Technology, Integration, and Operations Conference* (Article AIAA 2018-3847). American Institute of Aeronautics and Astronautics. https://doi.org/10.2514/6.2018-3847

Solanki, D. T., & Sharma, D. S. (2022). Potential flow around polygonal shaped cylinders using hypotrochoidal mapping function. *International Journal of Mechanical Sciences*, *226*, Article 107395. https://doi.org/10.1016/j.ijmecsci.2022.107395

Stokkermans, T. C. A., Usai, D., Sinnige, T., & Veldhuis, L. L. M. (2021). Aerodynamic interaction effects between propellers in typical eVTOL vehicle configurations. *Journal of Aircraft*, *58*(4), 815–833. https://doi.org/10.2514/1.c035814

Stoll, K., Lloyd, S. (2010). *Infrastructure as architecture: designing composite networks*. Jovis. http://hdl.handle.net/20.500.11850/62091

Sun, X., Wang, S., Zhang, X., & Wandelt, S. (2025). LAERACE: Taking the policy fast-track towards low-altitude economy. *Journal of the Air Transport Research Society*, *4*, Article 100058. https://doi.org/10.1016/j.jatrs.2025.100058

Tinney, C. E., & Sirohi, J. (2018). Multirotor drone noise at static thrust. *AIAA Journal*, *56*(7), 2816–2826. https://doi.org/10.2514/1.j056827

Tugnoli, M., Montagnani, D., Syal, M., Droandi, G., & Zanotti, A. (2021). Mid-fidelity approach to aerodynamic simulations of unconventional VTOL aircraft configurations. *Aerospace Science and Technology*, *115*, Article 106804. https://doi.org/10.1016/j.ast.2021.106804

Vahdat-Nejad, H., Ramazani, A., Mohammadi, T., & Mansoor, W. (2016). A survey on context-aware vehicular network applications. *Vehicular Communications*, *3*, 43–57. https://doi.org/10.1016/j.vehcom.2016.01.002

Vascik, P. D., & Hansman, R. J. (2019). Development of vertiport capacity envelopes and analysis of their sensitivity to topological and operational factors. In *AIAA Scitech 2019 Forum* (Article AIAA 2019-0526). American Institute of Aeronautics and Astronautics. https://doi.org/10.2514/6.2019-0526

Vella, E., Gojon, R., Parisot-Dupuis, H., Doué, N., Jardin, T., & Roger, M. (2024). Mutual interaction noise in rotor-beam configuration. In *30th AIAA/CEAS Aeroacoustics Conference 2024* (Article AIAA 2024-3318). American Institute of Aeronautics and Astronautics. https://doi.org/10.2514/6.2024-3318

Vlaskin, S., Fazlur Rahman, M., Sunil, E., Ellerbroek, J., Hoekstra, J., & Nieuwenhuisen, D. (2025). *Deep reinforcement learning for drone conflict resolution under uncertainty* [Paper presentation]. 15th SESAR Innovation Days. https://hdl.handle.net/10921/1837

Wang, S., Lima Pereira, L. T., & Ragni, D. (2025). Design exploration of UAM vehicles. *Aerospace Science and Technology*, *160*, Article 110058. https://doi.org/10.1016/J.AST.2025.110058

Wang, Y., Deng, Y., Zheng, Y., Chattopadhyay, P., & Wang, L. (2025). Vision transformers for image classification: a comparative survey. *Technologies*, *13*(1), Article 32. https://doi.org/10.3390/technologies13010032

Weitsman, D., Stephenson, J. H., & Zawodny, N. S. (2020). Effects of flow recirculation on acoustic and dynamic measurements of rotary-wing systems operating in closed anechoic chambers. *The Journal of the Acoustical Society of America*, *148*(3), 1325–1336. https://doi.org/10.1121/10.0001901

White, M. D., Padfield, G. D., Lu, L., Advani, S., & Potter, M. (2021). Review of flight simulation fidelity requirements to help reduce 'rotorcraft loss of control in-flight' accident rates. *CEAS Aeronautical Journal*, *12*(4), 701–721. https://doi.org/10.1007/s13272-021-00542-6

Wojno, J. P., Mueller, T. J., & Blake, W. K. (2002). Turbulence ingestion noise, Part 2: rotor aeroacoustic response to grid-generated turbulence. *AIAA Journal*, *40*(1), 26–32. https://doi.org/10.2514/2.1637

Wu, Y., Kingan, M. J., & Go, S. T. (2022). Propeller-strut interaction tone noise. *Physics of Fluids*, *34*(5), Article 057106. https://doi.org/10.1063/5.0090187

Yunus, F., Casalino, D., Avallone, F., & Ragni, D. (2023a). Efficient prediction of airborne noise propagation in a non-turbulent urban environment using Gaussian beam tracing method. *The Journal of the Acoustical Society of America*, *153*(4), 2362–2362. https://doi.org/10.1121/10.0017825

Yunus, F., Casalino, D., Avallone, F., & Ragni, D. (2023b). Efficient prediction of urban air mobility noise in a vertiport environment. *Aerospace Science and Technology*, *139*, Article 108410. https://doi.org/10.1016/j.ast.2023.108410

Zamponi, R., Beni, A., Zarri, A., & Christophe, J. (2026). Prediction of potential interaction noise in a generic rotor–strut arrangement. *Journal of Sound and Vibration*, *637*, Article 119805. https://doi.org/10.1016/j.jsv.2026.119805

Zanotti, A., & Algarotti, D. (2022). Aerodynamic interaction between tandem overlapping propellers in eVTOL airplane mode flight condition. *Aerospace Science and Technology*, *124*, Article 107518. https://doi.org/10.1016/j.ast.2022.107518

Zarri, A., Dell'Erba, E., Munters, W., & Schram, C. (2022). Aeroacoustic installation effects in multi-rotorcraft: numerical investigations of a small-size drone model. *Aerospace Science and Technology*, *128*, Article 107762. https://doi.org/10.1016/j.ast.2022.107762

Zawodny, N., & Douglas Boyd Jr, D. (2020). *Investigation of rotor-airframe interaction noise associated with small-scale rotary-wing unmanned aircraft systems* [Paper presentation]. 73rd Annual Forum & Technology Display, Virginia Beach, VA, United States.

Zelinski, S. (2020). Operational analysis of vertiport surface topology. In *2020 IEEE/AIAA 39th Digital Avionics Systems Conference (DASC)* (pp. 1–8). IEEE. https://doi.org/10.1109/dasc50938.2020.9256794

Zhang, J. (2021). Modern Monte Carlo methods for efficient uncertainty quantification and propagation: A survey. *Wiley Interdisciplinary Reviews: Computational Statistics*, *13*(5), Article e1539. https://doi.org/https://doi.org/10.1002/wics.1539

Zhong, S., Zhang, X., Gill, J., Fattah, R., & Sun, Y. (2018). A numerical investigation of the airfoil-gust interaction noise in transonic flows: Acoustic processes. *Journal of Sound and Vibration*, *425*, 239–256. https://doi.org/10.1016/j.jsv.2018.04.010

Zhou, B. Y., Hanson, L., Pullin, S. F., Zang, B., Hauth, J., & Huan, X. (2025). Data-driven propeller noise prediction approach with transfer and active learning. *AIAA Journal*, *63*(12), 5393–5404. https://doi.org/10.2514/1.j065406